Assessment of future stratification induced by opening of Haringvliet sluices

Jouke G. Binsma

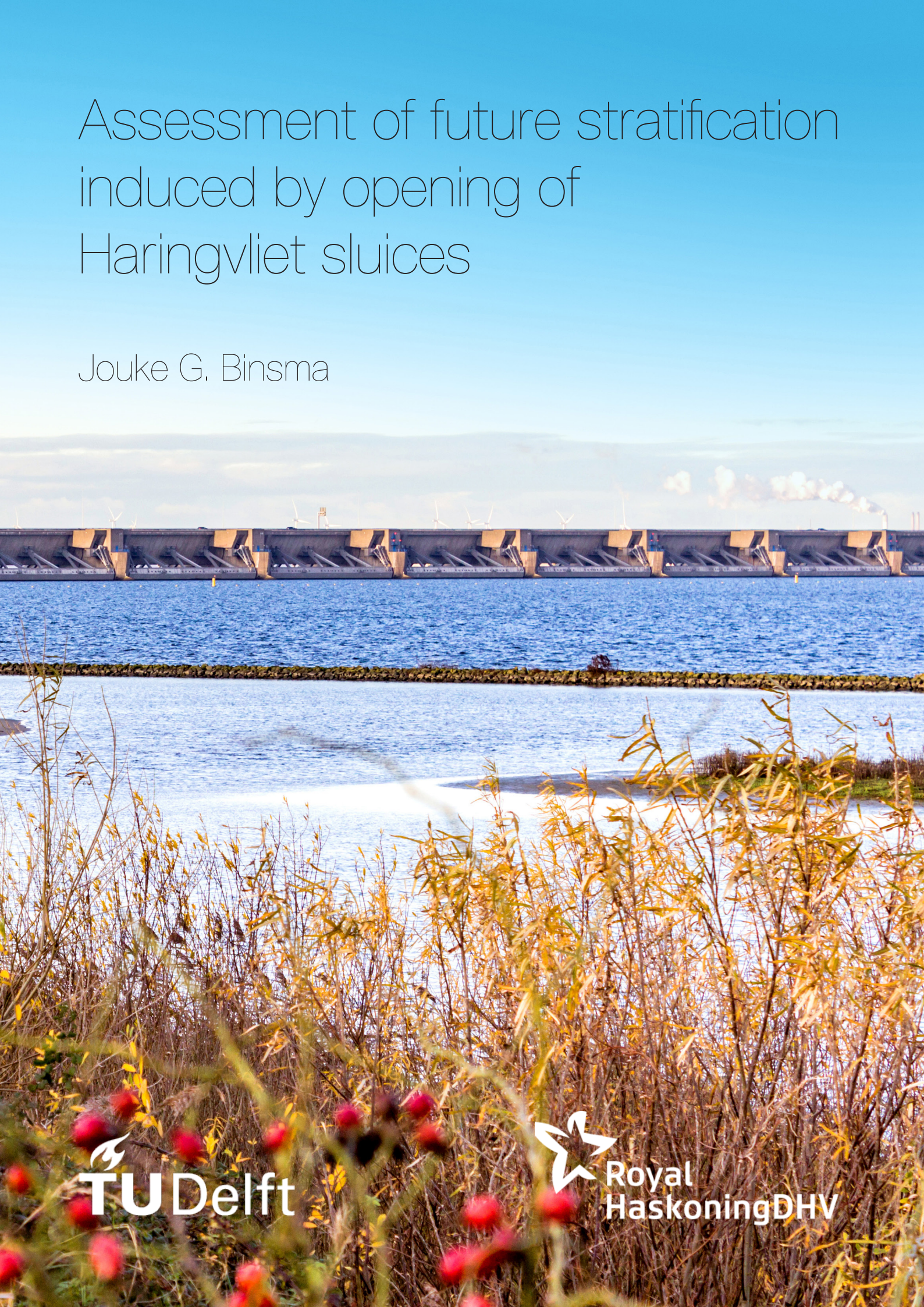

Assessment of future stratification induced by opening of Haringvliet sluices

by

Jouke G. Binsma

to obtain the degree of Master of Science
at the Delft University of Technology,
to be defended publicly on Friday March 19, 2021 at 11:00 AM.

Student number:	4375033	
Project duration:	May 11, 2020 – March 19, 2021	
Thesis committee:	Prof. dr. J. D. Pietrzak,	TU Delft, supervisor
	Dr. C. D. Katsman,	TU Delft
	Prof. dr. S. G. J. Aarninkhof,	TU Delft
	Ir. J. Daniëls,	Royal HaskoningDHV
	Dr. M. Busnelli,	Royal HaskoningDHV

TU Delft

Royal HaskoningDHV
Enhancing Society Together

Nomenclature

Abbreviations

2SIPS	Secondary SIPS
ADI	Alternating Direction Implicit scheme
EoS	Equation of State
ETM	Estuarine Turbidity Maximum
HD	Hollands Diep
HoH	Hook of Holland
HV	Haringvliet
HW	High Water
HWS	High Water Slack
KWA	Kleinschalige Wateraanvoer
LW	Low Water
LWS	Low Water Slack
MSL	Mean Sea Level
MWL	Mean Water Level
NAP	Normaal Amsterdams Peil
NS	North Sea
NWW	Nieuwe Waterweg
OPEX	Operating Expenditures
OSR-HV	Operationeel Stromingsmodel Rotterdam - Haringvliet
POA	Permanente Oostelijke Aanvoer
PoR	Port of Rotterdam
PSU	Practical Salinity Units
RD	Rijksdriehoekscoördinaten (Dutch coordinates)
RMB	Rhine-Meuse Basin
RMS	Root Mean Square
ROFI	Region of Freshwater Influence
RWS	Rijkswaterstaat
RWW	Rotterdam Waterways

SDS	SIMONA Data Storage
siminp	SIMONA Input
SIMONA	SImulatie MOdellen NAtte waterstaat
SIPS	Strain-Induced Periodic Stratification
SLR	Seal Level Rise
SPM	Suspended Particulate Matter
SWE	Shallow Water Equations

Greek symbols

Δt	Numerical time step	$[s]$
η	Across-estuary curvilinear grid coordinate	$[-]$
η	Tidal amplitude at estuary mouth	$[m]$
ν_h	Horizontal eddy viscosity	$[m^2/s]$
ν_t	Turbulent eddy viscosity	$[m^2/s]$
ν_v	Vertical eddy viscosity	$[m^2/s]$
ω	Eigen frequency	$[rad/s]$
ϕ	Latitude	[]
ρ	Water density	$[kg/m^3]$
ρ_0	Water reference density	$[kg/m^3]$
τ_b	Bed shear stress	$[N/m^2]$
τ_w	Wind shear stress	$[N/m^2]$
$\tau_{i,i}$	Normal (viscous) stress	$[N/m^2]$
$\tau_{i,j}$	Turbulent stress	$[N/m^2]$
ε	Relative density	$[-]$
ε	Turbulent kinetic energy dissipation	$[m^2/s^3]$
ξ	Along-estuary curvilinear grid coordinate	$[-]$
ζ	Water surface deflection w.r.t. mean level	$[m]$

Roman symbols

$\hat{u}$	Maximum tidal velocity at estuary mouth	$[m/s]$
a	Opening height Haringvliet sluice caisson	$[m]$
A_c	Water conveying cross-section	$[m^2]$
b	Buoyancy	$[m/s^2]$
C	Courant number	$[-]$
c	Phase speed	$[m/s]$
C_d	Wind drag coefficient	$[-]$
c_f	Bottom friction coefficient	$[-]$
C_{2D}	Two-dimensional Chézy coefficient	$[m^{1/2}/s]$
C_{3D}	Three-dimensional Chézy coefficient	$[m^{1/2}/s]$
d	Water depth	$[m]$
$D_{x,y}$	Horizontal diffusion coefficient	$[m^2/s]$
f	Coriolis parameter	$[rad/s]$
g	Earthly gravitational acceleration	$[m/s^2]$
g'	Reduced gravity	$[m/s^2]$
h	Water level	$[m]$
k	Sigma layer number	$[-]$

k	Turbulent kinetic energy production	$[m^2/s^2]$
L_{max}	Maximum intrusion length	$[m]$
N	Brunt-Väisälä frequency	$[s^-1]$
n	Manning roughness coefficient	$[m^{-1/3}s]$
p	Pressure	$[N/m^2]$
q	Specific discharge	$[m^2/s]$
Q_{ad}	Automatically distributed discharge	$[m^3/s]$
Q_f	Freshwater discharge	$[m^3/s]$
Q_{HV}	Discharge Haringvliet	$[m^3/s]$
Q_{Lobith}	Freshwater discharge Rhine at Lobith	$[m^3/s]$
R_D	External Rossby radius of deformation	$[m]$
R_I	Internal Rossby radius of deformation	$[m]$
Ri_E	Estuarine Richardson number	$[-]$
S	Salinity	$[PSU]$
Si	Simpson number	$[-]$
T	Temperature	$[C]$
u	Flow velocity (x)	$[m/s]$
u_T	Root mean square tidal velocity at estuary mouth	$[m/s]$
U_{max}	Domain-wide maximum flow velocity	$[m/s]$
v	Flow velocity (y)	$[m/s]$
W	Local estuary width	$[m]$
w	Vertical flow velocity	$[m/s]$
W_{10}	Ten-minute averaged wind speed at 10m height	$[m/s]$

Preface

The following study is performed in cooperation with Royal HaskoningDHV (RHDHV), a non-listed engineering consultancy firm with an international character based in the Netherlands. Intellectual, material and financial support was offered by RHDHV to enable the timely completion of this thesis.

This subject is part of a greater framework of nearly fifty MSc. thesis works. No subject within the scope of this project can be treated as standalone and monthly meetings with other graduate candidates were held to warrant consistency within the framework.

A word of gratitude to Prof. dr. Julie Pietrzak for trusting and aiding me in working on this thesis. Her passion for stratified fluid dynamics was transferred to me effortlessly and to Dr. Caroline Katsman and Prof. dr. Stefan Aarninkhof for reserving time to assess my work and provide me with valuable feedback.

A great thanks to my supervisors at Royal HaskoningDHV, ir. Jeroen Daniëls and Dr. Marcela Busnelli, for months of close cooperation and support. Not only on a professional level but also for involving me in the social dynamics of the work floor which was especially valuable to me being homebound during the CoVid-19 pandemic.

Furthermore, I acknowledge Lambèr Hulsen (PoR) for providing the extensive and intricate OSR-HV model which proved to be a powerful tool in this research. Meinard Tiessen, Firmijn Zijl (Deltares) and Lennart Keyzer (TUD) for providing help on important modelling aspects throughout various stages of the thesis. Last (but certainly not least), Huub Lavooij and Leen Berke, for involving me in the Delta21 framework.

Jouke G. Binsma
Delft, February 2021

Abstract

Key Points

- Pre-closure salinity intrusion into Haringvliet-Hollands Diep is known to have reached Biesbosch National Park at flood tide. Post-Delta21 salinity intrusion is projected to be less extensive than pre-closure. Maximum intrusion is estimated to reach the westernmost Moerdijk ports mainly due to diminished tidal flow at the estuary mouth.
- Freshwater intake in the Haringvliet is projected to be compromised for the majority of the year whereas freshwater intake in Hollands Diep is compromised during prolonged drought.
- Salinity outwash from the Haringvliet on ebb tide is projected to be poor under both drought and normal conditions due to widespread salinity diffusion in lateral and vertical directions on flood tide.

Salinity has a major impact on ecology, chemistry, water quality and sedimentary processes in estuarine environments. Climate change effects such as Sea Level Rise (SLR) and more frequent prolonged droughts are known to promote salinity intrusion into estuaries which makes it a relevant topic to be studied.
The Delta21 framework, in which this study is positioned, aims at increased flood safety and ecological restoration of the Haringvliet, a former estuary in the Dutch southwestern delta that has been closed as part of the Delta works. To achieve this, Delta21 proposes to reopen the Haringvliet freshwater basin to tidal effects in an attempt to restore its estuarine character. Implementation of Delta21 introduces the risk of compromising agricultural and industrial activities around the Haringvliet-Hollands Diep by reintroducing salinity and tidal movement in the basin. The central problem lies in quantifying the extent and stability of the expected periodic salt intrusion post-Delta21. This has been done by projecting a geographical bandwidth of salinity intrusion patterns depending on the severity of SLR (2020-2100) and low-to-mean Rhine-Meuse discharges (in 2100 CE) using a numerical model. Mitigation strategies are then recommended based on these numerical results.

The OSR-HV model (owner: Port of Rotterdam) is used to run predictive scenarios of salinity intrusion for the lower reaches of the Rhine-Meuse basin. OSR-HV runs in TRIWAQ (Rijkswaterstaat), which is 3D numerical modelling software that employs coupled hydrodynamics and constituent transport thereby resolving salinity transport. An upper-end critical scenario consists of a Rhine (Lobith) discharge averaging 1000 m^3/s for 31 days combined with 85cm SLR in 2100. This resulted in an intrusion pattern reaching the westernmost port of Moerdijk in Hollands Diep. Results show that the basin geometry, possibly nudged by Coriolis deflection, initially causes a preferential path of salinity intrusion along the southern bank of the Haringvliet. Lateral and vertical mixing is extensive in the western part of Haringvliet which is thought to be a combined effect of weakened tidal flow at the estuary mouth and robust and erratic geometry of the basin. Further up-estuary, the historical flood-ebb tidal channel structures is the main transporter of salinity. The Haringvliet shows distinctly different estuarine behaviour compared to the neighbouring Rotterdam Waterways where stratification is more stable, causing less up-estuary diffusion. The relative robustness of the Haringvliet and mild freshwater forcing give rise to extensive 3D mixing which subsequently limits the maximum horizontal excursion of salinity. Salinity intrusion into the Old Meuse is observed to aggravate upon opening of the Haringvliet sluices due to

flow reversal in Spui which connects Haringvliet with the Rotterdam Waterways. This effect can even result in salt intrusion from the Rotterdam Waterways via Old Meuse and Spui back into the Haringvliet, causing a secondary spike in salinity on ebb tide there.

Finally, height-limitation of the Haringvliet sluice gates is somewhat effective in countering horizontal excursion of salinity but runaway diffusion in the Haringvliet results in similar salinity profiles compared to full opening of the sluice gates.

A shipping channel that crosses the current Haringvliet front delta is included in Delta21. This deep feature promotes advection of salt through the Haringvliet sluices. Subsequent diffusion patterns cause for poor washout of salinity from the basin upon ebb tide. Limiting the depth of this channel is recommended if salt intrusion is to be reduced. Full opening of the Haringvliet sluices furthermore causes approx. 0.50m lowering of Mean Low Water (MLW) near Moerdijk which affects busy shipping routes between Rotterdam-Moerdijk-Scheldt. Partial reduction of the conveying area of the Haringvliet sluices may be used to suppress the tidal wave penetration into Haringvliet-Hollands Diep. Significant gain in ecological value is likely post-Delta21 due to addition of approx. 1900 ha of intertidal areas and a 40 km salinity gradient (excl. front delta).

Ample recommendations on further research have been made in this exploratory study. It is recommended to further study the effects of Delta21 interventions on macro hydrodynamics of the Dutch coastal shelf. The interconnected nature of the region requires a larger modelling domain to prevent the occurrence of non-physical effects obtained from the current numerical schematization. Furthermore, hydrological relations and bathymetry were generated from 2020 data. It is therefore recommended to precede the assessment of salinity intrusion into the Haringvliet with numerical projections on change to these environmental factors. Lastly, significant gain in accuracy may be obtained from applying spatially varying temperature and wind to the domain to better replicate baroclinic flows and turbulent mixing.

Samenvatting

Kernpunten

- Zoutindringing in het Haringvliet-Hollands Diep reikte voor de afsluiting tot de Biesbosch bij vloed. Zoutindringing Post-Delta21 wordt als minder wijdverspreid geschat dan voor de sluiting. De maximale indringingslengte De maximale indringingslengte is geschat tot de meest westelijke Moerdijkhaven voornamelijk door afgeknepen getijdestroming bij de estuariummonding.
- Post-Delta21 zoetwaterinname aan het Haringvliet wordt onmogelijk geacht voor het grootste deel van het jaar terwijl zoetwaterinname aan het Hollands Diep in het geding komt gedurende aanhoudende droogte.
- Het uitspoelen van zout uit het Haringvliet gedurende eb is ingeschat als pover onder zowel droogte als gemiddelde condities door de wijdverspreide diffusie van zout in de dwarsrichting en verticaal gedurende vloed.

De zoutgraad van water heeft een nadrukkelijk effect op ecologie, watersamenstelling, waterkwaliteit en sedimentaire processen in estuariene omgevingen. Gevolgen van klimaatverandering zoals zeespiegelstijging en frequentere periodes van aanhoudende droogte staan bekend om hun bijdrage aan zoutindringing in estuaria wat het een relevant onderzoeksonderwerp maakt.

Het Delta21 kader, waarin dit onderzoek zich bevindt, mikt op een toename van de overstromingsveiligheid en ecologisch herstel in het Haringvliet, een voormalig estuarium in de Nederlandse zuidwestelijke delta dat gesloten is als onderdeel van de Deltawerken. Delta21 stelt voor om het zoete Haringvliet basin te heropenen voor getijdeinvloed in een poging om het estuariene karakter te herstellen. Implementatie van Delta21 introduceert het risico dat de landbouw en industrie door de herintroductie van zout en getijdebweging in het basin belemmerd worden in hun activiteiten rondom het Haringvliet-Hollands Diep. Het kernprobleem in dit onderzoek is het kwantificeren van de mate en stabiliteit van de verwachte periodieke zoutindringing post-Delta21. Dit is gedaan middels een geografische projectie van zoutindringingspatronen afhankelijk van de mate van zeespiegelstijging (2020-2100) en lage tot gemiddelde Rijn-Maas afvoeren (in 2100) door middel van een numeriek model. Vervolgens zijn er mitigatie strategieën aanbevolen.

Het OSR-HV model (Havenbedrijf Rotterdam) is gebruikt om voorspellende scenarios door te rekenen voor zoutindringing in de Rijnmaasmonding. OSR-HV rekent in TRIWAQ (RWS), een 3D numeriek softwarepakket dat gebruik maakt van gekoppelde hydrodynamica en massatransport en daarmee zouttransport oplost. Een kritiek scenario bestaat uit een Rijnafvoer (Lobith) van gemiddeld 1000 m^3/s gedurende 31d gecombineerd met 85cm zeespiegelstijging in 2100. Dit resulteerde in een indringingspatroon reikende to de meest westerlijke Moerdijkhaven in het Hollands Diep. Resultaten laten zien dat de basingeometrie, mogelijk aangespoord door Coriolisafbuiging, zorgt voor een voorkeurspad van zoutindringing langs de zuidelijke oever van het Haringvliet. Laterale en verticale menging is wijdverspreid in het westelijke Haringvliet. Dit wordt mogelijk veroorzaakt door een combinatie van verzwakte getijstroming bij de monding en robuuste, grillige bathymetrie van het basin. Stroomopwaarts neemt de historische structuur van eb- en vloedkanalen de zouttransportfunctie over. Het Haringvliet toont duidelijk verschillend estuarien gedrag vergeleken met de Rotterdamse Waterwegen waar

gelaagdheid stabieler is en resulteert in minder stroomopwaartse menging. De relatieve robuustheid van het Haringvliet en de milde zoetwaterforcering leiden tot grote mate van 3D menging wat derhalve de meximale horizontale excursie van zout limiteert. Verergering van zoutindringing in de Oude Maas is waargenomen ten gevolge van het openen van de Haringvlietsluizen door het omkeren van de stroomrichting in het Spui. Dit effect kan er zelfs voor zorgen dat zout het Haringvliet binnendringt via Oude Maas-Spui wat zorgt voor een secundaire piek in zoutgraad tijdens eb in het Haringvliet. Ten slotte zorgt hoogtebeperking van de Haringvlietsluisdeuren voor beperking van de horizontale excursie van zout maar onbeheersbare diffusie in het Haringvliet resulteert in gelijkwaardige zoutprofielen t.o.v. volledig geopende sluisdeuren.

Een scheepskanaal dat de Haringvliet voordelta doorkruist is opgenomen in Delta21. Dit diepere gedeelte bevordert stroming van zout door de Haringvlietsluizen. Daaropvolgende difussiepatronen zorgen voor povere uitstroming van zout uit het basin gedurende eb. Diepte limitatie van dit kanaal is aangeraden als zoutindringing moet worden gereduceerd. Volledig openen van de Haringvlietsluizen zorgt bovendien voor een ca. 0.50m verlaging van gemiddeld laagwater nabij Moerdijk extra druk levert op scheepsroute Rotterdam-Moerdijk-Schelde. Reductie van het doorstroomoppervlak van de Haringvlietsluizen kan worden gebruikt om de penetratie van de getijdegolf in het Haringvliet-Hollands Diep te onderdrukken. Verder is de winst in ecologische waarde hoogstwaarschijnlijk door de toevoeging van ca. 1900 ha intergetijdegebied en een zoutgradient van 40 km (excl. voordelta).

Aanbevelingen voor vervolgonderzoek zijn uitvoerig gedaan in deze beginstudie. Het is aanbevolen om de effecten van Delta21 interventies op grootschalige waterbeweging aan de Nederlandse kust nader te bestuderen. De vervlochten aard van de regio vereist een groter modeldomein om niet-fysische effecten ten gevolge van de modelschematisatie te voorkomen. Verder zijn hydrologische relaties en bathymetry gebaseerd op data uit 2020. Het is aangeraden om verandering van deze omgevingsfactoren in te schatten alvorens zoutindringingsprojecties te doen in het Haringvliet. Ten slotte is er significante winst in nauwkeurigheid te behalen door toepassing van ruimtelijk varierende temperatuur en wind in het domein om de dichtheidsstromen en turbulente menging better na te bootsen.

Contents

1 Introduction

Section 1.1 and Section 1.2 are used to establish the relevance and societal background of the following study. Section 1.3 then elaborates on what problems may be expected considering this background. Then, in Section 1.4, the scientific and geographical scopes are limited. The main research question and sub-questions are defined following this scope limitation. Section 1.5 delineates the strategy to answering the research questions. Section 1.6 can be used to discern the line of thought of this study.

1.1 Motivation

Salinity transport in aquatic environments has a major impact on ecology, water chemistry, water quality and sedimentary processes in estuarine and coastal environments (Geyer and Signell (1992)). Climate change effects such as Sea Level Rise (SLR) (Church et al. (2013)) and more frequent and intense storms and droughts (ter Maat (2015)) are thought to exceedingly contribute to salt intrusion in the future (Mahmuduzzaman et al. (2014)). This, in turn, poses risks to human activities regarding the use of freshwater resources for agriculture, industry and municipal purposes.

On the contrary, positive effects for biodiversity are to be expected upon reintroduction of salinity dynamics in freshwater systems due to a smoother transition from marine to freshwater ecotopes (Wijsman et al. (2018), Tuomi et al. (2012)).

Using this knowledge, one can see that the current climate trends (Church et al. (2013)) and ever more densely populated water-land interfaces (van Koningsveld et al. (2008)) motivate researching salt intrusion near population centres.

1.2 Framework: Delta21

Future peak river discharges (Q_{Lobith}=15.000 m^3/s, ter Maat (2014)) in the Dutch Rhine-Meuse basin (RMB) threaten the surrounding landscape and infrastructure. To reduce this flood risk to acceptable levels, one would suggest to increase the river dike elevations throughout the system. Such an undertaking is however costly (order €10 billions), extensive (≈600 km) and requires increased maintenance as land subsidence continues in the river region (Lavooij and Berke (2019)).

Delta21 focuses on an alternative future-proofing of the RMB by installing pumps (Q_{max}=10.000 m^3/s) to amplify river discharge in case of imminent flooding. Delta21 was conceived because strengthening of river dikes on its own is deemed insufficient to combat peak future river discharges. Moreover, heightening of the dike system would pose a serious threat to the wider river environment by alteration of the historical landscape (Lenders et al. (1999)). Lastly, Delta21 offers a significant reduction in execution costs of €5-10 billion compared to dike reinforcement (Lavooij and Berke (2019)) while addressing other pressing concerns such as the transition to full use of renewable energy and ecological restoration as well.

Figure 1.1a shows the geographical location of Delta21 in the Dutch southwestern delta. Figure 1.1b points out the main interventions included in Delta21. An energy storage lake southwest of Maasvlakte II (blue left arrow) and a new storm surge barrier further west (green 2nd right arrow) jointly create a tidal lake (red 2nd left arrow) in the current HV front delta. The now near-permanently opened 'former' HV sluices (black right arrow) allow for intrusion of marine water into the Haringvliet-Hollands Diep (HV-HD). Studying this consequence of implementing Delta21 is the central theme of this thesis. The HV sluices retain their current function as water level and salinity regulator and furthermore add redundancy to the flood safety of the system as secondary storm surge barrier.

(a) (b)

Figure 1.1: **(a)** Artist impression of what the Delta21 interventions would look like on the study domain (also see Figure 1.3): I - energy storage lake and pumps, II - new navigation channel and storm surge barrier, III - raised sill Haringvliet bridge, IV - new freshwater intake Strijensas. **(b)** Delta21 in bird's flight, left-to-right: energy storage lake, brackish tidal lake, Delta21 storm surge barrier and Haringvliet sluices. Source: Lavooij and Berke (2019)

Contribution of Delta21 to the transition to renewable energy is done by storage of potential energy (Figure 1.1a-I). Continued navigation and flood safety in the area is warranted by a shipping channel and storm surge barrier (Figure 1.1a-II). An attempt at prevention of excessive salt intrusion in Hollands Diep is made by locally raising the bottom under Haringvliet bridge (Figure 1.1a-III) which marks the border between the HV and Hollands Diep (HD), in this study often referred to as one entity: Haringvliet-Hollands Diep (HV-HD). Relocation of the westernmost surface water intakes for freshwater to the east (Figure 1.1a-IV) is included in Delta21 as well. Important to note is that the flood protection function is now fulfilled by the new Delta21 storm surge barrier. Prevention of extreme salt intrusion into the HV is regulated using the old HV sluices by closure at Q_{Lobith}<1000 m^3/s (Figure 1.2). More information on Delta21 can be found in Appendix A and Lavooij and Berke (2019).

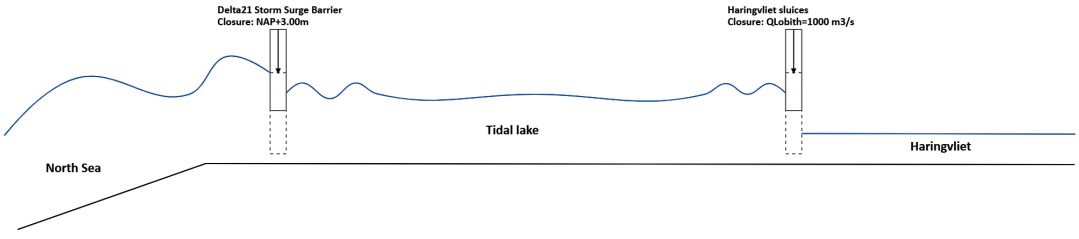

Figure 1.2: Closure thresholds of the two system barriers shown in Figure 1.1b on the right

1.3 Problem statement

A key factor in undoing of peak river flows in the Dutch southwestern delta today is the Haringvliet (HV), the former estuary was closed off from the North Sea in 1970 as part of the Delta Works. This closure work will from here on be referred to as 'HV sluices' as coined by (Ferguson (1971)). Subsequently, a deterioration of the estuarine ecology was observed (Wijsman et al. (2018)). A first attempt at improving this situation is the 'Kierbesluit', initiated per January 16th 2019, which meant that the HV sluices would be opened slightly during flood to allow for upstream fish migration, tidal exchange and stratification no further than Spui-Middelharnis (≈13 km upstream) (Wit et al. (2011), Wijsman et al. (2018)). Delta21 proposes to reinstate the pre-1970 open sea connection of the HV to relieve the system of future extreme river discharges by means of large capacity pumps (8000-10.000 m^3/s) and increase the ecological value of the region. Then, the 'old' HV sluices only close at low river discharge (Q_{Lobith}<1000 m^3/s) to prevent extreme salt intrusion.

The effects of global acceleration of Relative Sea Level Rise (RLSR) (Church and White (2006), Church et al. (2013), Oppenheimer et al. (2019)) are likely to promote salt intrusion in estuaries worldwide. Change in local ecosystems (Hong and Shen (2012)), destruction of agricultural resources (Mahmuduzzaman et al. (2014), Wassmann et al. (2019))), and increased cost of water treatment (Kleinman and Brown (1980)) are all associated with salt intrusion. Therefore, salt intrusion is a relevant subject for coastal societies in various ways. For the HV-HD, nature organizations and aquaculture businesses are known to favour such plans whereas industries and agriculture which rely on freshwater intakes along the HV-HD will be more sceptical (Lavooij and Berke (2019)).

Central to the the problem is judgment on the extent of salt intrusion resulting from predictive scenarios. Relaxation of salinity requirements, infrastructure relocation or overall sacrifice of assets are to be considered as part of mitigation strategies. The problem is thus stated as follows:

Problem Statement:

To quantify the extent and stability of stratification of the HV resulting from an operational Delta21 plan under different climate scenarios and offer mitigating measures for affected activities in the area.

1.4 Scope & objective

The HV-HD is situated within the larger interconnected region of the RMB in the southwest of the Netherlands. The latter is defined from the point where the Rhine river enters the country near Lobith ($\bar{Q}_{year}$=2200 m^3/s, Klijn et al. (2011)), continuing as the Waal shortly thereafter and joined by the Meuse (Dutch: Maas), before it debouches into the North Sea. The area of interest is found at the southern half of the RMB running from south of Maasvlakte II in the west to the Biesbosch in the east (Figure 1.3).

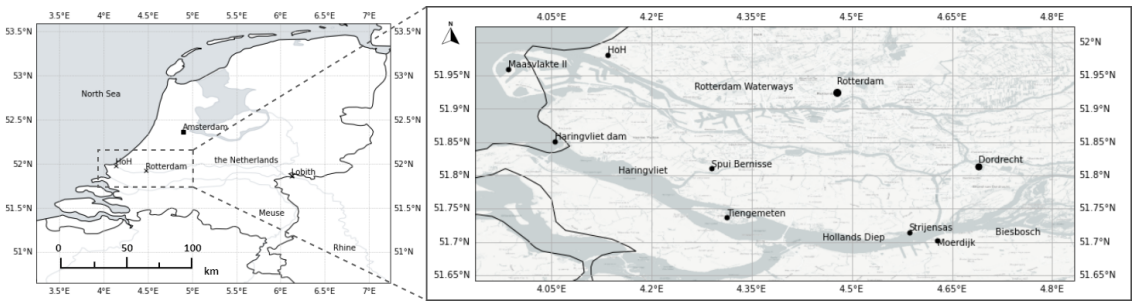

Figure 1.3: Rhine-Meuse basin in the Netherlands (left) and in the scope area (right) including locations of importance to this study

The HV sluices, one of the delta works (Subsection 3.1.1), remain functional as emergency stop in case of extremely low river discharges (Q_{Lobith}<1000 m^3/s) within Delta21 (Lavooij and Berke (2019)). This is to counter extreme salt intrusion of the HV-HD at flood. When opened however, the situation greatly differs from the pre-1970 estuary in terms of mouth conveyance area ($A_{c,m}$) and orientation (compare Figures 1.1a and 1.3). Tidal flow interaction with the basin will be present but weakened. Inherent to the objective is assessment of this new North Sea ⇔ HV tidal interaction.

The research objective consists of simulating Delta21 conditions using a numerical tool capable of reproducing salinity transport in the RMB. Results from this study can then be used to recommend strategies in handling periodic movement of salinity in the HV-HD. Note that morphological and ecological assessments are not part of the scope. Hydrodynamics are assessed at the meso-scale meaning that developments in e.g. North Sea hydrodynamics (macro) or details of local flow structures (micro) are not included in the assessments. The problem statement from Section 1.3 is used to formulate a main research question (RQ) and three associated sub-questions (SQ) as follows:

- **RQ:** How does opening of the Haringvliet sluices impact the spatiotemporal salinity distribution in the Haringvliet-Hollandsch Diep for relevant climate projections post-Delta21?
- **SQ1:** On what timescales does the new dynamic salinity equilibrium form, if it forms at all?
- **SQ2** Is the extent of salt intrusion acceptable with regard to existing regional regulations, and if not, are mitigation strategies viable?
- **SQ3:** What are the effects on salt intrusion of varying the conveyance cross section of the Haringvliet dam?

1.5 Methodology

Net landward dispersion of salinity is a process driven by residual flows (Section 2.3). A theoretical framework is offered in Chapter 2 to understand the relevant processes responsible for these residual flows driving salt intrusion into estuaries. Chapter 3 then applies the theoretical framework to the system studied here.

Modelling of salt intrusion for relevant prospective scenarios allows for assessment of these effects post-Delta21. Quantification of the horizontal extent of salt intrusion and salinity gradients is most relevant to (potential) estuarine biodiversity (Wijsman et al. (2018)) while vertical mixing of salinity is of more concern to freshwater consumers (HydroLogic (2015)). Lateral mixing of salinity occurs within relatively wide estuaries (B≫h) and can be an important sink of turbulent kinetic energy (Saveneije (2006)). Three-dimensional hydrodynamics and salinity transport resolving software has therefore been used to capture the advective and diffusive processes driving salt intrusion, see Section 4.2.

Civil engineering works built in the marine environment can significantly alter hydrodynamics and mass transport on the coastal shelf (van Koningsveld et al. (2008)). An example of this in the proximity of Delta21 is Maasvlakte II (Stolk and Dijkshoorn (2009)), a seaward extension of the Port of Rotterdam (PoR), see Figures 1.1 and 1.3. Delta21 includes such seaward works as well, therefore its effect on the hydrodynamics in the model domain have been assessed as a prologue to the main modelling study. The selection, acquisition and salinity reproduction quality are grouped under 'Model quality assessment' in Figure 1.4. The total assessment consists of three parts: validation of the model using field data, a comparison of pre- and post-Delta21 salinity transport behaviour and finally a comparison of numerical performance to an example found in literature (de Nijs et al. (2011)) for the Rotterdam Waterways (RWW), on which salinity transport in the HV-HD is highly dependent. This way, more confidence is gained in salinity reproduction skill of the model.

Acceleration in global sea level rise (Church and White (2006), Church et al. (2013)), increasing storm frequency and intensity (Katsman et al. (2011), ter Maat (2015)) and prolonged periods of drought are known to promote salt intrusion into estuaries (Section 2.1). Each has its associated uncertainty, especially for long-term predictions. Hence, several scenarios have been composed to assess the combined effects of (relevant) promoters of salt intrusion into the HV-HD (Subsection 4.6.2). Composition of scenarios and further model alterations following model quality assessment are found in the

middle column of Figure 1.4. These scenarios are then implemented as boundary conditions in a 3D hydrodynamic model with mass transport coupling (Subsection 4.6.1).

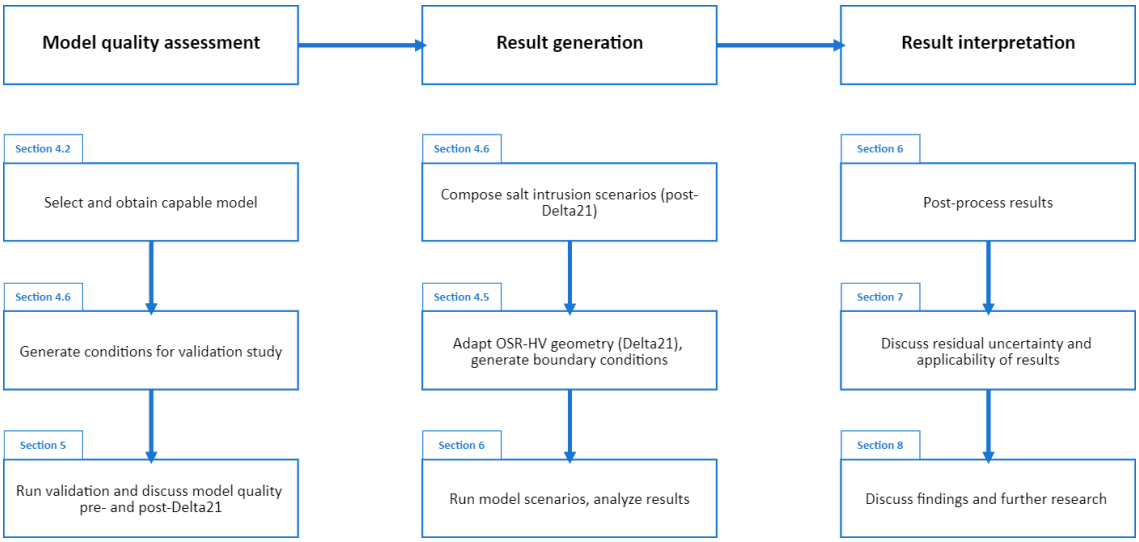

Figure 1.4: Methodology to answering research questions from Section 1.4

1.6 Thesis outline

- Chapter 2 - explains useful background concepts related to the physical behaviour of estuaries that may not be familiar to the reader. Moreover, an expectation about the dynamics of a future HV estuary is sketched using Estuary Richardson and Simpson numbers.
- Chapter 3 - sketches the scope area, offers an inventory of current system values and the way in which Delta21 affects these values. Additionally, system forcing and salinity dynamics are discussed.
- Chapter 4 - provides details on the modelling study. The choice for a numerical model that has been used to assess salt intrusion is motivated. The most important functionalities, assumptions and parametrizations are described first. Input in the form of climate scenarios is then described. Five (4+1) climate scenarios are introduced. The first four scenarios aim to quantify salt intrusion for average to critical conditions (Research question, sub-questions I&II). The last scenario focuses on the effectiveness of the HV sluices in suppressing horizontal salt intrusion (sub-question III). The way in which output is described concludes the model set-up chapter.
- Chapter 5 - aims at gaining confidence in capabilities of the numerical model chosen in this study. A reference case is setup which contains the unaltered (2019) system geometry. Then, the influences of Delta21 on the modelling domain are inspected by comparing reference cases in- and excluding the interventions. Further model assessment is then done by comparing Kierbesluit data and to numerical results in the HV front delta and basin. The validation chapter concludes with a comparison of model performance to that found in literature for the well-studied Rotterdam Waterways.
- Chapter 6 - discusses the outcomes from the modelling study. First, along-estuary bottom and surface profiles are plotted to compare results from climate scenarios. Then, salinity anomaly maps are shown (bottom and surface) to stress the relatively importance of Sea Level Rise and freshwater discharge. Additionally, salinity movement achieved per tidal phase are visualised using maps at the end of flood and ebb respectively. Thereafter, an assessment of along-estuary salinity contours is done to show the characteristics of stratification per scenario. Some comments on the effects of height-limiting of the Haringvliet sluice gates are provided as well. This is done using the same figures as mentioned above. Aggregation of all the results with emphasis on functionalities described in Chapter 3 follows. The final paragraph discusses the results and how the results relate to the theoretical framework (Chapter 2).
- Chapter 7 - discusses the dominant residual uncertainties in this study and the way in which results should be interpreted.
- Chapter 8 - key findings from the study are summarized and recommendations for enhancing model qualities and further research are offered.

2

Theoretical framework

This chapter deals with definitions of parameters and physical phenomena important to understanding the modelling study, results and conclusions as discussed in this study. Section 2.1 explains the terminology surrounding water salinity. Section 2.2 explains the classification of transition zones from the marine to riverine domain. Section 2.3 then discusses the ways in which salinity is transported within such systems.

2.1 Salinity theory

Salinity norms for freshwater intake in the Netherlands are generally defined using chlorinity [mg/l Cl^-]. Landward data stations of RWS therefore express salinity by measure of chlorinity as well. This study makes use of Practical Salinity Units (PSU), a measure of the Total Dissolved Solids (TDS) in water, to define the salt content of water (Lewis (1980)). Reference is made to the more modern, standardized approach of TEOS-10 which relies on absolute salinity (S_A), conservative temperature (Θ) and pressure (p) for describing density (McDougall and Barker (2011)). The choice for describing salinity in PSU in this study is one of convenience. This is mainly due to the fact that historical data (1970-2019) used in the model validation study (Chapter 5) often preceded the introduction of TEOS-10 (2010) and was therefore expressed in PSU (or antecedent units) for the marine domain.

The chemical composition of salt ions in seawater shows little variation which is known as Dittmars relationship (Pietrzak and Katsman (2019)). This fact can be exploited to convert chlorinity data to PSU. The standard prevalence of chlorine in seawater amounts to approx. 55% which leads to Equation 2.1. It thus follows that 1.0 PSU ≅ 1806.6 mg/L Cl^-.

$$S = \frac{[Cl^-]}{0.5535} = [Cl^-] \cdot 1.8066 \tag{2.1}$$

Salt intrusion into estuaries becomes problematic when it compromises human activities[1]. This is a problem ever more likely to occur given the growth of urban centres, often in or near estuaries and deltas (Meyer et al. (2014)). Agricultural water salinity norms in the Netherlands are in the range of 150-300 mg/L (Huismans (2018)). A typical river background chlorinity of the downstream Rhine-Meuse system

[1] Salt intrusion can also cause the destruction of habitats, though in the scope of this research consensus is that salt intrusion benefits ecology (Lavooij and Berke (2019))

is 50 mg/L. Hence, only little added salinity is needed to exceed these norms. In fact, only about 1:100 part North Sea water per unit river water is needed to do so (ter Maat (2015)). This indicates that a slight increase in marine forcing can lead to exceedance of salinity standards.

2.2 Estuary classification

Intuitively, one would define an estuary as there 'where the river meets the sea' (Saveneije (2006)) or more specifically as a body of water which has a free connection with the open sea and within which seawater is measurably diluted with freshwater derived from land drainage (Pritchard (1967)). Further nuance can be applied by recognising that tidal dominance characterises estuaries which is expressed in the upstream fining of marine sediment (Bosboom and Stive (2015)). The maximum landward excursion of salinity and sediment in estuaries are often found to coincide (de Nijs et al. (2011)).

The simplest case of interaction between river and tidal forcing in an estuary is where the (usually) denser marine water moves in and out underneath the fresher river discharge each tidal cycle without the exchange of properties. In natural systems however, salt-fresh mixing processes occur at various spatiotemporal scales leading to a less binary distribution of salinity. Asymmetries in along-channel momentum transport during a tidal cycle give rise to residual flows (MacCready (2004)). Residual flows, despite being of O(0.1 m/s) at maximum, are largely responsible for the dispersion (macro-diffusion) of salinity as they potentially appear as leading terms in the Eulerian tidally averaged along-channel momentum balance (Geyer and Signell (1992)). According to Geyer and MacCready (2014) the following regimes can be distinguished in estuaries worldwide, see Table 2.1 below. The term 'halocline' refers to an interface between two vertical positions in the water column with distinctly different salinity (Pietrzak and Katsman (2019)).

Table 2.1: Four spatial estuary regimes recognized by Geyer and MacCready (2014)

Regime	**Halocline**	**Example**
Salt wedge	Single, sharp	Ebro, Fraser, Mississippi
Stratified	Multiple, sharp	Chesapeake Bay, Hudson
Partially mixed	Gentle	James, Narragansett Bay
Well-mixed	Near-uniform salinity, absent	Conwy, Tamar, Skagit

Note that the regimes above are defined based on spatial distribution of salinity. Factors such as spring-neap cycles, storms and droughts allow for temporary mobility between the regimes in an estuary. Starting top-left and decreasing the river flow counterclockwise, Figure 2.1 shows that vertical salinity profiles become more homogeneous compared to the salt wedge when tidal forcing gains in relative magnitude. Black arrows denote barotropic forcing (external, entire water column) whereas baroclinic forcing (internal, density flows) may occur in presence of horizontal density gradients (Subsection 2.3.1). Less apparent from Figure 2.1 is that not only mixing over the vertical takes place but in upstream direction as well. This leads to a migration of salinity much further upstream for better mixed estuary types (Saveneije (2006)). The classification of estuarine regimes is often done using dimensionless numbers. Here, the Estuary Richardson (Ri_E) and Simpson (Si) numbers have been used as a first assessment of the estuarine character of a reopened HV in the future.

Ri_E (Equation 2.6) is a dimensionless number (ratio) which compares the amount of work needed to mix a fluid (εq_f) to the kinetic energy available to do so (u_T^3). In other words, the buoyant input versus the marine forcing. Note that surface shearing by wind is excluded. Parameter u_T describes the Root Mean Square (RMS) of the tidal velocity near the estuary mouth (de Nijs et al. (2011)) and is found from the peak tidal velocity (Equation 2.2) by mathematical relation (Equation 2.3). The tidal amplitude at the Haringvliet mouth (η) for fully opened HV sluices equals approx. 0.78m (Table 3.3). A typical water level (h) near the Haringvliet mouth is 10m. Various other dimensionless numbers have been defined in the past such as the gradient (Ri_g), flux (Ri_f) and bulk (Ri_b) Richardson numbers and the (inverse) Strouhal number (e.g. Burchard and Hetland (2010), Tuomi et al. (2012), Scully and Geyer (2012)).

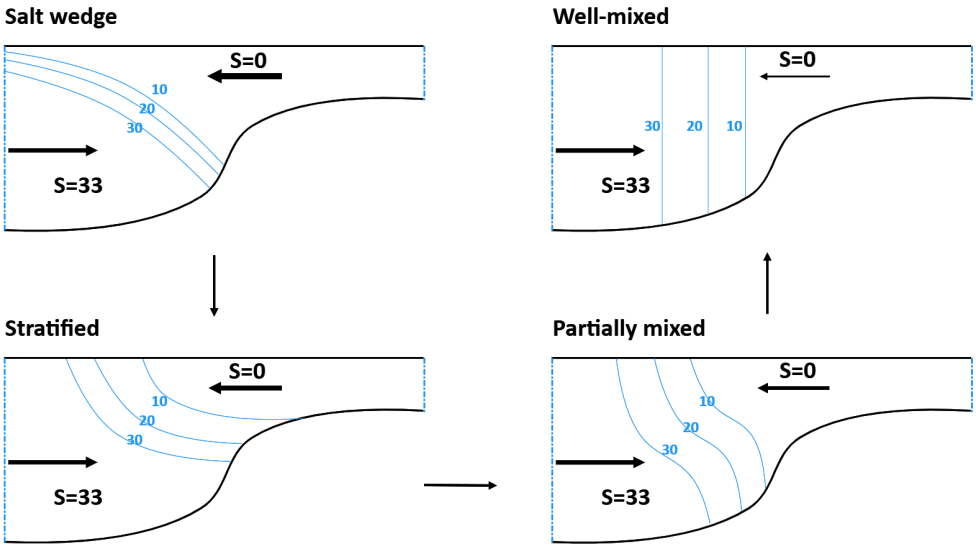

Figure 2.1: Types of estuaries based on degree of salt-fresh mixing, based on Pietrzak (2020), numbers denote salinity in Practical Salinity Units [PSU]

Their importance to analysing existing tidal systems is recognised but their application as parameters for predicting estuarine behaviour is deemed of limited value here.

Density differences ($\Delta\rho$) between two stratified layers were found to vary from approx. 0.5 to 5 PSU at sea leading to $\varepsilon = 5 \cdot 10^{-4} - 5 \cdot 10^{-3}$ [-]. A typical pre-closure HV discharge was 1100 m^3/s, (Subsection 3.1.4). Post-closure, the maximum conveyance area of the HV sluices amounts to 6000 m^2 and has a maximum conveyance height (h_c) of 5.50 m (Jacobs et al. (2003)). The HV mouth conveyance width (W_c) thus amounts to approx. 1100 m leading to a freshwater specific discharge (q_f, Equation 2.5) of approx. 1.0 m^2/s given mean freshwater discharge (assumed: perfect weir).

$$\hat{u} = \eta\sqrt{\frac{g}{h}} = 0.78 \cdot \sqrt{\frac{9.81}{10}} = 0.77\ m/s \tag{2.2}$$

$$u_T = \sqrt{\frac{1}{T}\int_0^T \hat{u}^2 \sin^2(\omega t)dt} = \frac{\hat{u}}{\sqrt{2}} = 0.55\ m/s \tag{2.3}$$

$$\varepsilon = \frac{\Delta\rho_{1,2}}{\rho_1} = \{5 \cdot 10^{-4}, 5 \cdot 10^{-3}\}\ [-] \tag{2.4}$$

$$q_f = \frac{Q_{HV}}{W_c} = \frac{Q_{HV}}{A_c {h_c}^{-1}} = \frac{1.1 \cdot 10^3}{6 \cdot 10^3 \cdot 5.5 \cdot 10^{-1}} \approx 1.0\ m^2/s \tag{2.5}$$

$$Ri_E \equiv g\frac{\varepsilon q_f}{u_T^3} = \frac{g' q_f}{u_T^3} = 10 \cdot \frac{\{5 \cdot 10^{-4}, 5 \cdot 10^{-3}\}}{0.55^3} = \{0.03, 0.30\}\ [-] \tag{2.6}$$

It follows that a likely range for Ri_E after opening of the HV sluices amounts to 0.03-0.30. The value of Ri_E enables to broadly indicate the expected type of estuary (Figure 2.1) as follows (Burchard and Hetland (2010)):

- Ri_E < 0.08 - well-mixed estuary
- 0.08 < Ri_E < 0.80 - partially stratified estuary
- Ri_E > 0.80 - salt wedge estuary

The result of Equation 2.6 suggests that the HV, especially near the estuary mouth, is likely to exhibit partially mixed behaviour and that a shift towards well-mixed behaviour may be observed upon weak strafication of the shelf sea. Note however, that Ri_E can vary significantly in space and time. At spring tide (η=0.98 m), shallow depth (h≤5 m), ε=10^4 and low-precipitation flow regime (Q=600 m^3/s) the Ri_E is exclusively below 0.08 indicating well-mixed conditions. Figure 2.2a shows that low to mean flows through the HV quickly approach well-mixed conditions. Moreover Figure 2.2b shows that, at depths of 5-10m, the water column will likely be well-mixed too. This leads to the conclusion that the 'newly created' estuary will likely exhibit a more diffusive salt flux.

Though useful in itself, Ri_E excludes the effects of horizontal buoyancy gradients ($\frac{\partial b}{\partial x}$) that drive tidal straining, see Figure 2.4b. The ratio of potential energy change due to straining compared to the production of kinetic (mixing) energy was coined the Simpson number (Si, Burchard and Hetland (2010)), sometimes named the horizontal Richardson number (Geyer and MacCready (2014)). For small Si, the turbulent kinetic energy ($c_f\ u_T^2$) can overcome the stabilizing influence of tidal straining (during ebb tide) which leads to vertically well-mixed conditions. A rule of thumb is that Si>0.2 is indicative for runaway stratification (Stacey and Ralston (2005)).

$$Si \equiv \frac{\frac{\partial b}{\partial x} h^2}{c_f u_T^2} \quad ; \quad b = -g\frac{\rho - \rho_0}{\rho_0} \tag{2.7}$$

Figure 3.5 shows a bottom salinity at HW running from 15 g/L at the HV sluices to 3 g/L at Moerdijk bridge. This amounts to roughly 27 PSU (b=-0.26 m/s^2) to 5.5 PSU (b=-0.05 m/s^2) (Wallace (1974)), assumption is that the future bottom salinity of the HV basin develops similarly to that of the pre-closure estuary. Taking L_{HV} = 45 km a horizontal buoyancy gradient of $\partial b/\partial x \approx 4.7 \cdot 10^{-6}$ s^{-2} is found. Bottom roughness (c_f) for the HV historical flood channel sections can be estimated at approx. $2{\cdot}10^{-3}$ [-] (Uittenbogaard et al. (2005)).

For mean situations (Q=1100 m^3/s, η=0.78 m, u_T=0.39 m/s, H=10 m) periodic stratification (SIPS, Section 2.2) of the HV basin is likely to occur, this is depicted in Figure 2.2b alongside the Ri_E. In theory, the lower Si values indicate complete de-stratification during flood tide and partial re-stratification on ebb tide but this assumes perfect mixing efficiency which is often not the case (Geyer and MacCready (2014)). Deeper parts (H=15-20 m) found near the HV sluices are likely to remain stratified for normal tidal conditions. Lastly, runaway stratification is expected during neap tides (low η, u_T) and enhanced mixing during spring tide (high η, u_T).

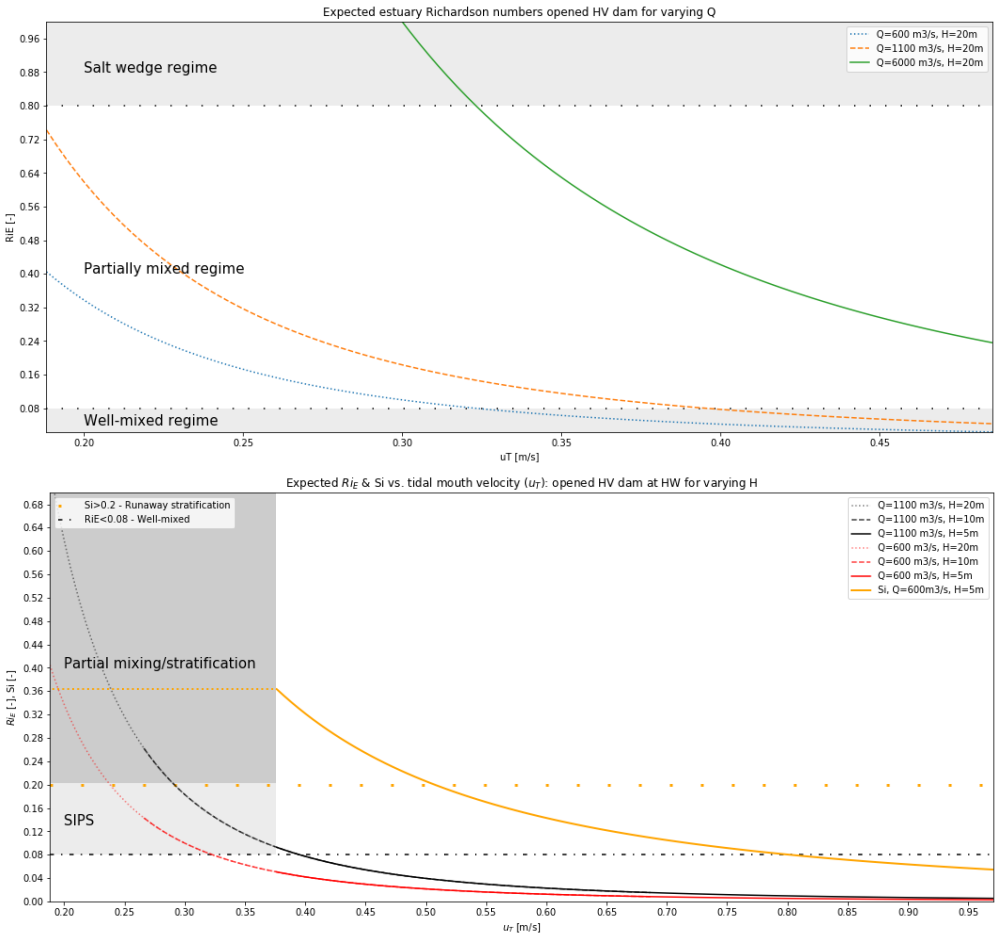

Figure 2.2: **Top:** Estuarine Richardson number HV for local discharge during drought (Q=600 m^3/s), mean flow (Q=1100 m^3/s) and river floods (Q=6000 m^3/s) based on 'Warm 2100' scenario (ter Maat (2014)). **Bottom:** Estuarine Richardson number (lower two lines) for relatively deep (H=20m), mean (H=10m) and shallow (H=5m) depth in HV vs. tidal velocity at the mouth. Rule-of-thumb for well-mixed conditions plotted at Ri_E=0.08. Simpson number (upper line) for H=5m vs. tidal velocity at the mouth. Rule-of-thumb for runaway stratification plotted at Si=0.2. Si only plotted at Q=600 m^3/s and corresponding u_T. Shaded areas for partial mixing and SIPS regimes (Subsection 2.3.2)

2.3 Transport phenomena

Stratification occurs due to downward (gravitational) transport of denser saline water which is countered by vertical diffusion. Estuarine dynamic salinity equilibria are therefore determined by the relative intensities of mixing and re-stratification (de Nijs et al. (2011)). Subsection 2.3.1 treats how density differences contribute to transport phenomena, this knowledge is applied to estuaries for the along-estuary direction (Subsection 2.3.2) and cross-channel direction (Subsection 2.3.3). Finally, disturbances of salinity profiles by flow instabilities are treated in Subsection 2.3.4.

Key points:

- Up-estuary displacement of salinity is promoted, in presence of a horizontal salinity gradient, via the dispersion of particles in longitudinal direction due to asymmetries in the tidally-averaged flow.
- Second-order circulation can have a pronounced effect on salinity in deep, narrow tidal channels
- Turbulent mixing arises from shear instabilities in the flow and gives rise stratification breakdown and more limited up-estuary salt dispersion

2.3.1 Density-driven flow

The hydrostatic pressure of an arbitrary body of water with instantaneous water depth h is defined through Equation 2.8. It now follows that for any point of equal h but different density ρ a pressure difference arises. Equation 2.9 shows that internal pressure differences can arise for two locations of equal instantaneous water level. The resulting internal pressure gradient is, like for an external pressure gradient, diminished by a flow from high to low pressure. This is referred to as baroclinic flow as opposed to barotropic flow for movement by external pressure gradients.

$$p = \rho g h \tag{2.8}$$

$$\Delta p = p_2 - p_1 = (\rho_2 - \rho_1) g h \tag{2.9}$$

The order of magnitude of baroclinic (density-driven) flows is generally lower compared to mean tidal velocities but can become significant upon tidal reversal. The cause of this weaker character lies in that baroclinic flows are driven by relative density differences across interfaces. The principle of reduced gravity (Equation 2.10) allows for calculation of baroclinic flows via (implicit) inclusion in the mathematical framework of numerical models see e.g. E.14 in Appendix E.

$$g' = \varepsilon g = \frac{\rho_2 - \rho_1}{\rho_2} g \tag{2.10}$$

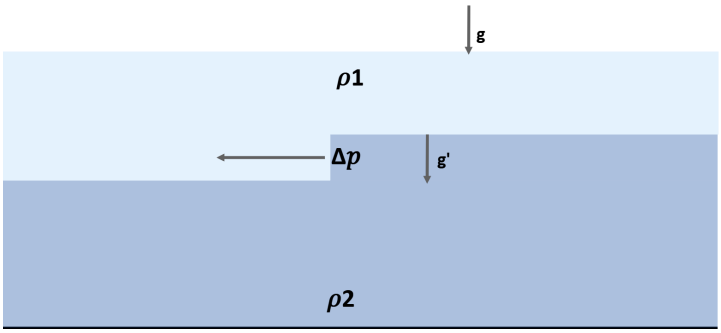

Figure 2.3: Concept sketch of internal pressure gradient giving rise to an equilibrium-restoring baroclinic flow. Flow magnitude determined by principle of reduced gravity (g'), adaptation from Gill (1982), Pietrzak (2020).

2.3.2 Estuarine circulation

The estuarine circulation denotes totality of all process responsible for the bi-directional exchange flow between sea and river in estuaries (Simpson (1997), Geyer and MacCready (2014)). This exchange is most conveniently observed over a tidal cycle, which typically constitutes to the period of forcing (Saveneije (2006). For a perfect estuary, bulk motion (advection) on flood and ebb tide are equal and therefore leads to no exchange of transported constituents. More complex, natural estuaries tend to import constituents (Bosboom and Stive (2015)) via residual (=sub-tidal) fluxes. Variable system boundary conditions, geometry, meteorological events etc. can lead to residual along-estuary advection and diffusion processes and subsequent migration of salinity (Burchard and Hetland (2010)). Upstream excursion of salinity generally increases for increasing sea level and for decreasing freshwater discharge but identification of individual processes and their relative contribution to the estuarine circulation remains a complex exercise (Geyer and MacCready (2014)).

The estuarine circulation relies on a balance between the horizontal density gradient caused by buoyancy forcing and production/dissipation of turbulent kinetic energy by tidal currents and wind (Geyer

and Signell (1992), MacCready (2004)). Meteorological phenomena such as differential heating, precipitation, freezing and evaporation may contribute to this balance as well (Saveneije (2006)) but are not addressed here.

Two asymmetries that are ubiquitous for estuaries are the gravitational circulation (Figure 2.4a) and tidal straining (Figure 2.4b) which, once superimposed, are generally the dominant constituents of the estuarine circulation (Burchard and Hetland (2010)). The gravitational circulation relies on the interplay between pressure due to position of the free surface (barotropic) and the horizontal density gradient (baroclinic). It can be seen that the barotropic signal is pointed seawards whereas the pressure due to the horizontal density gradient (=baroclinic) is directed up-estuary. Superimposition of these signals yields a circulatory flow pattern over depth known as the gravitational circulation (Simpson (1997)), see Figure 2.4a. The gravitational acceleration on its own would yield a constantly stratified estuarine character for all estuaries which is not observed in nature. Simpson et al. (1990) shows that breakdown of stratification can be achieved when the water column becomes unstably stratified on flood tide (Figure 2.4b). High shear flow on ebb tide can then potentially resharpen the pycnocline. This means that periodic breakdown and generation of stratification may be observed in estuaries and was therefore coined Strain Induced Periodic Stratification (SIPS), Simpson et al. (1990).

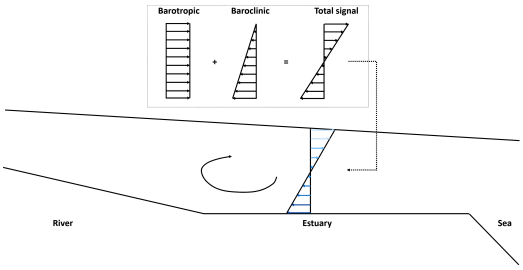

(a) Gravitational circulation: lighter river water is transported down-estuary by a water level gradient. Denser shelf seawater is drawn in to complete the mass balance thereby increasing stratification (Simpson (1997))

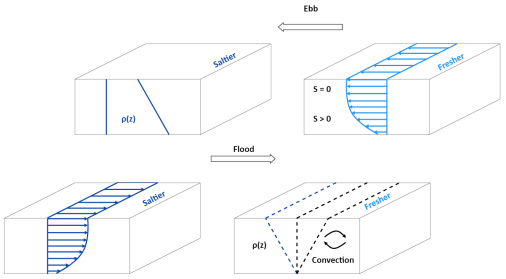

(b) Tidal straining: offshore velocities on ebb tide cause strong shear and stable stratification. Reversal of the velocity signal on flood tide causes unstable stratification and thereby stratification breakdown (Simpson et al. (1990), Pietrzak (2020))

Figure 2.4: Concept drawings of two first order contributors to the estuarine circulation: gravitational circulation driven by longitudinal density gradient (a) and periodic tidal straining by flow reversal in a tidal cycle (b).

Finally, two physical process that are likely to affect intrusion into the HV-HD are tidal pumping and trapping. For tidal pumping, the difference in inflow (hemispherical) and outflow (jet-like) is responsible for increased mixing on either side of the estuary mouth depending on the tidal phase. See e.g. Jacobs et al. (2003) for an elaboration. Tidal trapping arises from phase lags between filling and emptying of shallow and deep features (e.g. tidal gullies and flats) which also applies to the system studied here (Subsection 3.1.1). Internal asymmetries in stratification and hydrodynamics can further contribute to mixing by affecting baroclinic pressure gradients in the system (de Nijs et al. (2011)) which is discussed in the following parts.

2.3.3 Lateral circulation

Lerczak and Geyer (2004) recognise that along-channel tidal currents generally are strongest along the thalweg (pathway of maximum depth) and weaker in shallow zones. This differential advection is a transport phenomenon in itself and furthermore causes lateral shearing of along-channel flow resulting in transverse channel density gradients which is shown on the foreground of Figure 2.5. This density gradient leads to a baroclinic pressure gradient driving lateral flow typically of one order of magnitude lower than the main flow (Subsection 2.3.1). It is therefore sometimes referred to as secondary circulation. At flood tide, this lateral flow is directed outward. Mass continuity demands replacement of the displaced fluid by water from higher up in the water column leading to a downwelling of surface water. This is shown on the background of Figure 2.5. This displacement of lower salinity water to the channel fringes and downwelling of locally higher salinity water contributes to re-stratification. This

re-stratifying effect reminds of SIPS (Subsection 2.3.2) and was therefore coined 2SIPS (secondary SIPS) by Schulz et al. (2015).

Lerczak and Geyer (2004) also found that stratification suppresses the lateral circulation. The circulation was observed to only (weakly) occur below the pycnocline in case of strong stratification. Lateral circulation is therefore strengthened by mixed conditions of the water column in contrast to SIPS (Subsection 2.3.2). Nunes and Simpson (1985) studied the well-mixed Conwy estuary (Table 2.1) and found no in-field evidence of lateral circulation on ebb tide there. The extent of re-stratification on ebb tide therefore influences the degree to which the lateral circulation influences salinity transport on flood tide. Note that the lateral circulation as described in Figure 2.5 makes use of an idealised channel cross-section and further assumes no external sources of mass such as Saltwater Spillover (SSO) from other channels Lyu and Zhu (2018).

Schulz et al. (2015) continued the work of Lerczak and Geyer (2004) by studying channel geometry influences on lateral circulation. The latter hypothesised a strengthening of the circulation for narrower estuaries. The key parameter used by Schulz et al. (2015) was the depth-to-width or aspect ratio (d/W). Low aspect ratios (d/W<0.002) showed very weak lateral circulation and dominance of tidal straining with a secondary contribution of gravitational circulation. Medium aspect ratio channels (0.002<d/W<0.015) showed a maximum contribution of tidal straining and gravitational circulation to the estuarine circulation. For narrow and deep (d/W>0.015) channels, cross-channel density gradients are stronger which therefore causes a pronounced effect of 2SIPS. The important nuance added to the work of Lerczak and Geyer (2004) by Schulz et al. (2015) is therefore that influence of lateral straining depends on both channel depth and width rather than width only. Normal, longitudinal SIPS then adds to the stratifying effect but increased levels of shear cause turbulence production and subsequent stratification breakdown which is treated next.

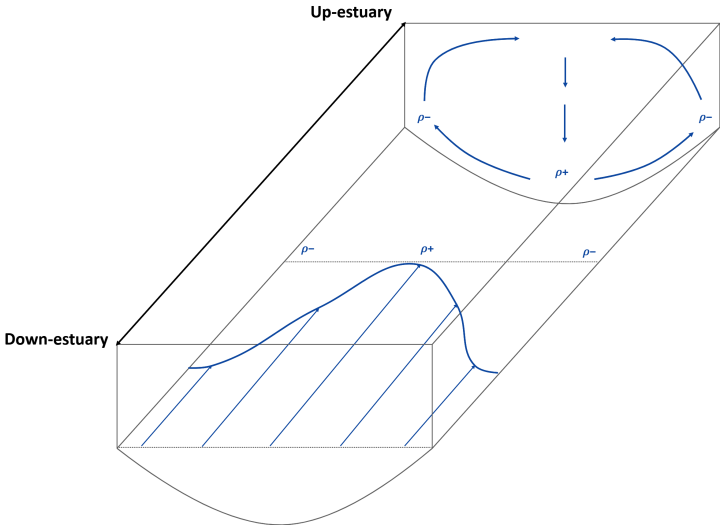

Figure 2.5: Downwelling of surface water due to a cross-channel density gradient caused by differential advection in a tidal channel on flood tide. Based on Lerczak and Geyer (2004). Note that asymmetries in the parabolic channel cross-section can obscure the lateral circulation.

2.3.4 Turbulence

Turbulence arises from non-linear instabilities in the flow field and is amply described in literature, e.g. Nieuwstadt et al. (2016). The instabilities transfer energy from the mean flow through three-dimensional eddy motion. These eddies transfer energy to ever smaller length-scales until molecular viscosity is able to convert the kinetic energy into heat. This turbulent transport of mass, energy and momentum is conjointly called mixing here. The wide variety of length and timescales of these motions often calls for a simplified description of turbulence.

In numerical representations, turbulence is often represented as a diffusion-like process using the eddy viscosity concept (ν [m^2/s]), see Appendix E. This should be interpreted as a measure for the turbulent transport by an eddy of characteristic length (L [m]) and velocity gradient scale (U [m/s]) of flow instabilities (Equation 2.11).

$$\nu_t \sim U \cdot L \tag{2.11}$$

The bi-directional nature of the tidal signal causes a reversal of shear (Geyer and MacCready (2014)) and therefore a varying eddy viscosity in both space and time. It can be seen in Figure 2.4b that ebb tide creates a sharp pycnocline due to the associated stable stratification. Free shear instabilities such as Kelvin-Helmholtz instabilities (Thorpe's experiment, Pietrzak (2020)) may develop on the pycnocline though buoyant and gravitational forces act to restore stratification (Figure 2.6). In doing so, a displaced fluid parcel tends to 'overshoot' into an unstable surrounding several times. The frequency of this oscillation is known as the Brunt-Väisälä or buoyancy frequency (N), see Equation 2.12.

$$N^2 = -\frac{g}{\rho_0}\frac{\partial \rho}{\partial z} \tag{2.12}$$

For z positive upwards from the bed in Figure 2.6, it can be seen that oscillations (i.e. re-stratification) will be fast for $\rho_2 \gg \rho_1$. Marked vertical density gradients (i.e. sharp pycnoclines) therefore tend to quickly dissipate instabilities in the vertical density profile. This is known as turbulence damping which can confine sediment below pycnoclines in port systems as observed by e.g. de Nijs et al. (2011).

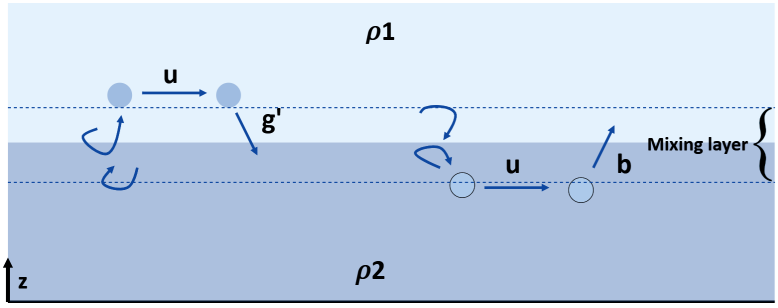

Figure 2.6: Restoration of pycnocline in a stably stratified ($\rho_1 < \rho_2$) fluid caused by vertical density difference. Full restoration is not achieved due to formation of a mixing layer. Turbulence suppression is caused by the diminished vertical density gradient within the mixing layer.

The gravitational circulation (Figures 2.4a) is weakened as mixing processes reduce stratification by smoothing longitudinal density gradients. This limits the maximum intrusion length (L_{max}). The superimposed effects of tidal forcing, buoyant forcing, wind forcing and geometry determine the amount of mixing in estuaries (HydroLogic (2015)). Mixing processes can occur in longitudinal, lateral and vertical sense (Scully and Geyer (2012)). The underlying physical principle is the Second Law of Thermodynamics which states that the entropy of a system can never decrease over time (Sestak (2005)) i.e. globally, no indefinite buildup of salinity will be observed and extremes will be smeared out. This does not rule out local extremes in e.g. deep pits. In literature, a wide range of mixing processes have been identified (e.g. Pietrzak and Labeur (2004), Geyer and MacCready (2014), Wei et al. (2016), Haddout et al. (2019)) which makes distinction of individual in-field mixing processes laborious or even unattainable (Saveneije (2006)).

Streamwise mixing generally has the largest geographical extent due to estuarine geometry. Lateral and vertical mixing can then be seen as inhibitors to streamwise mixing by extraction of kinetic energy to fuel these turbulent mixing processes. Lateral mixing is relatively important in stratified bodies with wide and irregular cross sections (West and Cotton (1981), Geyer and Signell (1992)) which applies to the HV (Appendix F). Mixing by wind and bed-generated turbulence are generally of lower order in estuaries than the process mentioned above (Saveneije (2006)) but have increasing significance regarding stratification for decreasing depth.

3

System analysis

Section 3.1 describes the hydrological network of the RMB. Subsection 3.1.1 then offers historical context regarding the HV-HD subsystem. The three main basin functionalities associated with salt intrusion are then treated in the order: freshwater intake (Subsection 3.1.2), navigation (Subsection 3.1.3) and ecology (Subsection 3.1.4). Section 3.2 proceeds to describe in which way the system is forced by: salinity (Subsection 3.2.1), marine influence (Subsection 3.2.2), wind (Subsection 3.2.3) and freshwater input (Subsection 3.2.4).

3.1 Rhine-Meuse basin

The Rhine-Meuse basin describes the lower reaches of Rhine and Meuse rivers in the Netherlands (Figure 1.3). The majority of the hydrological system is controlled by hydraulic engineering works (Huismans (2018)). Figure 3.1 shows the main connections within the hydrological network as well as the engineering works currently responsible for controlling salinity levels of the lower RMB. Currently (2020-21), most riverine discharge into the North Sea takes places through the New Waterway (Dutch: Nieuwe Waterweg), Hartel- and Beer canals and the HV sluices. The latter periodically sluice at ebb to regulate inland water levels depending on Q_{Lobith} (ter Maat (2015)). Flow through Spui and Dordtse Kil is directed northward when HV sluices are closed (HydroLogic (2015)). A flow reversal in these branches upon opening of the HV sluices is confirmed by results of this study (Chapter 6).

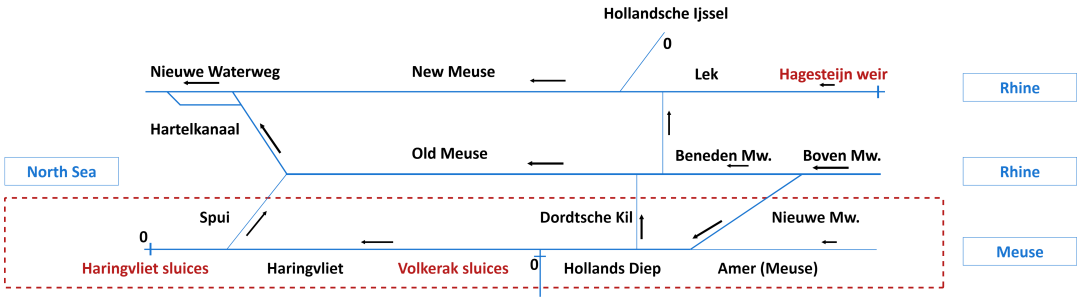

Figure 3.1: Network chart of the Rhine Meuse basin, area of interest shown by the dashed line. Salinity controlling structures in red. Nieuwe Waterweg is currently the only open sea connection of the RMB. Directions and relative magnitude of flow indicated for drought scenario: Q_{Lobith}=1000 m^3/s. Based on ter Maat (2015).

Table 3.1: Main hydrological system components RMB within the project scope (Section 1.4)

Water body	Description
Haringvliet	Former estuary turned freshwater body with micro-tidal conditions. Largely Natura2000 area
Hollands Diep	Houses Moerdijk industrial area and runs from the HV bridge (west) to the Biesbosch (east)
Spui	Connects HV and Oude Maas, Hook of Holland tide penetrates HV through here
New Meuse	Runs through Rotterdam and forms a major industrial and municipal artery
Old Meuse	Dominant discharging tidal river branch, join New Meuse to form New Waterway (NWW)
Dordtsche Kil	Connects Hollands Diep and Old Meuse, runs along the flood-prone Dordrecht historical centre
Merwedes	Boven Merwede bifurcates to Beneden and Nieuwe Merwede to supply north and south of RMB

3.1.1 Haringvliet-Hollands Diep

The Great Reclamations (Dutch: Grote Ontginningen) mark the era in which poldering and dewatering of low-lying peat landscapes allowed more extensive habitation and exploitation of the Dutch landscapes. These campaigns ran from the 10th to late 13th centuries. This did however mean that many of the newly settled people lived close to (or even below) mean sea level (Blom and Lamberts (1999)).

This vulnerability to flooding became a recurring issue. For instance in 1421, when years of neglectant dike management gave way to the St. Elisabeth's Flood which claimed over 2000 victims. The HV-HD was formed after the river flood receded. Estuaries like the HV-HD continued to be critical factors in minor and major floodings throughout the following centuries (de Kraker (2006)). It was not until the 1930s that purposeful studies into closure of the HV were conducted to improve water safety, fresh water availability and navigability in the area (Ferguson (1971), Wit et al. (2011)).

A first concrete proposal for closure of the HV estuary came in 1952, one year before the impactful 1953 North Sea flood (Dutch: Watersnoodramp). The flood claimed over 2500 lives around the North Sea, most of them in the Netherlands, and accelerated closure of the HV as part of the Delta Works. Three years of planning and fourteen years of construction meant that the HV was closed off from the North Sea in 1970 (Ferguson (1971)).

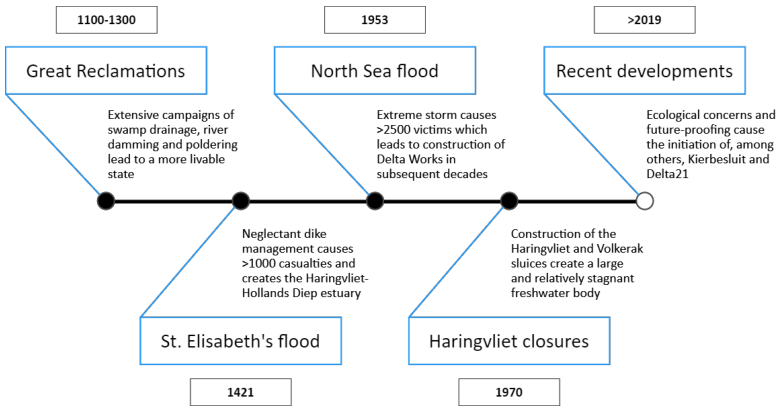

Figure 3.2: Historical developments that have influenced the present-day layout of HV-HD

The 1 km closure work has caused permanent submersion of the majority of tidal flats and changed the basin into a stagnant body of fresh water causing deterioration of the estuarine ecology (3.1.4). Some species of fish were now denied access to their spawning grounds (Wit et al. (2011)). Further deterioration occurred due to settlement of polluted river silt (Wijsman et al. (2018)) and a reduction in tidal range from roughly 2.00m to 0.30m which permanently exposed or submerged different ecotopes (Storm et al. (2006), Marks et al. (2014)). The historical structure of tidal channels and shoals has been preserved but submitted to gradual infilling by sediment from upstream (Tönis et al. (2002)).

The HV sluices play a major role in the hydrological system of the RMB. Comprising of a series of 17 sluice caissons, the closure work has been responsible for the creation of a robust fresh water reservoir in a coastal environment. The operational scheme of the HV sluices (Appendix B) is regulated by a hierarchy of three criteria:

- Prevent (excessive) salt intrusion Hollandsche Ijssel (Figure 3.1)
- Prevent (excessive) salt intrusion into Spui (Figure 3.1)
- Retain navigability at Moerdijk industrial zone (Figure 1.3)

The water quality of the Hollandsche Ijssel to the north (Figure 3.1) is prioritized as it houses the Gouda freshwater intake which is essential to the Rijnland region. A solution to (possible) future problems regarding Hollandsche Ijssel is under development as well, this is called the 'Permanent Easterly Supply' (Dutch: Permanente Oostelijke Aanvoer, POA). Reference is made to Mens (2018). Salt intrusion into HV-HD and navigability at Moerdijk are focal points to this research, see Subsections 1.3 and 1.4.

An increasing social awareness with respect to ecological value in the 1970s lead to the calls for opening the HV once again (Roels (2020)). It was not until 2000 that a final decision was made for the Kierbesluit, which states that the old HV sluice program is adapted to allow slight tidal interaction. Specifics of this new program can be found in Appendix B. Inertia in policy-making caused further postponement of the new sluice program (Marks et al. (2014)) until it initiated in January 2019 (Communications: RWS). The implementation is done step-wise to gain experience in tuning the HV sluices to comply with salinity requirements (Dutch: Lerend Implementeren), (Paalvast (2016), Wijsman et al. (2018)). The Delta21 plan has been developed since 2015 and is ongoing at the time of writing (2020-21).

3.1.2 Freshwater intake

Periods of low precipitation and Q_f require increased usage of freshwater sources for water supply in the RMB. The nature of freshwater bodies in the RMB is robust. Therefore, freshwater shortages in the RMB are often not a problem of quantity but rather quality of the stored water (HydroLogic (2015)). salt intrusion is responsible for episodes of low water quality which reduces overall availability of fresh water in the downstream RMB (ter Maat (2015)). The function of the HV sluices changes from a closure work with sluicing program (Appendix B) to, essentially, a safety stop when river discharges become extremely low (Q_{Lobith}<1000 m^3/s). This is done to prevent extreme salt intrusion into HV-HD. Refer to Subsection 3.2.1 for the response of salinity to low Q_{Lobith}. The situation in which Q_{Lobith} =1000 m^3/s but the HV remains opened thus forms a critical scenario to the RMB freshwater buffering bodies. On macro-level, the RMB has 5 bodies for freshwater supply (HydroLogic (2015)), see Table 3.2. The Brielse Meer receives its water from intake Bernisse Zuidland discussed in Subsection 3.2.1.

Table 3.2: Macro-level storage and supply of fresh water in the lower RMB. HV-HD and the Brielse Meer which is connected to Spui (Figure 3.1) are focus areas within this study. Majority of the consumption is for agricultural purposes (Mens (2018)).

Water body	**Supplies to**
Brielse Meer	Hollandse Delta, Delfland, Evides, PoR
HV-HD	Hollandse Delta, Brabantse Delta, Volkerak-Zoommeer
Volkerak-Zoommeer	Hollandse Delta, Brabantse Delta, Scheldestromen
Hollandsche Ijssel	Rijnland, Schieland, Krimpenerwaarden, Stichtse Rijnlanden
Lek	Stichtse Rijnlanden, Krimpenerwaard, Rivierenland

The current (2020) salt intrusion mechanisms (Figure 3.6) have already necesitated relocation of the westernmost freshwater intakes Stellendam-Scheelhoek, Zuidland and Hellevoetsluis in 2017 which were moved east to Middelharnis (Communications: TU Delta). This leaves Bernisse intake in the Spui (left circle Figure 3.3) as the next critical point for fresh water intake (HydroLogic (2015)). For the current climate scenarios (Bruggeman et al. (2011)), Bernisse intake is at risk of more frequent salinity norm exceedance in 2100 (Marchand et al. (2012)). Investments have already been made to draw water for Bernisse from the Old Meuse rather than Spui. Though the results of this intervention are doubtful as water supplier Evides already had to admix water to comply with salinity standards

in the dry summer of 2018 (Roels (2020)). Hence, Delta21 proposes to relocate the Bernisse intake (supplies: Brielse Meer) to the east as well. The new inlet will be located roughly 28 km to the east at Strijensas (Lavooij and Berke (2019)), see Figure 1.3. From there, a pumping station (20 m^3/s) drives the intake flow towards the Brielse Meer via Keen, Binnenbedijkte Maas and Piershilse Gat. This route has been drawn in Figure 3.3. There, 10^7 m^3 of storage is added to guarantee freshwater availability during droughts. A similar solution is found for the supply of fresh water to Noord-Brabant through Roode Vaart, albeit with $5 \cdot 10^6$ m^3 storage (Lavooij and Berke (2019)).

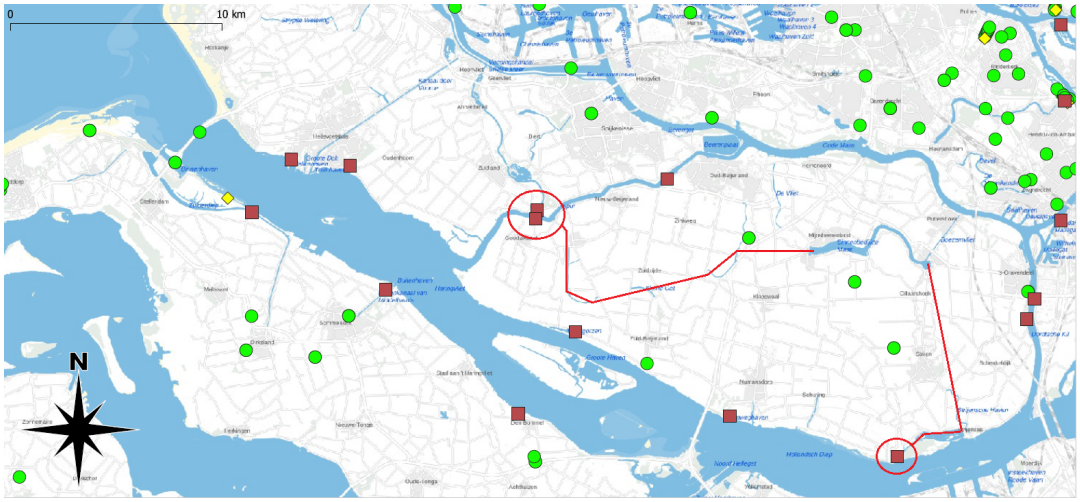

Figure 3.3: Drinking water intakes (yellow diamond), irrigation water intakes (brown square) and intakes for municipal water treatment (green circle) along the HV-HD. Relocation of Bernisse intake to the east indicated in red. Source: PDOK geodata.

WNF has argued that fresh water storage has become the main functionality of the HV-HD thereby replacing water safety as priority (Roels (2020)). It is implicated that the stagnant nature of the basin is maintained for freshwater extraction at the expense of biodiversity (Subsection 3.1.4). Redesigning water management in the west of the Netherlands is therefore deemed necessary to regain ecological values (HydroLogic (2015)). Essential steps in terms of countering anthropogenic land subsidence through groundwater management have already been undertaken in the Netherlands (Herrera-García et al. (2021)), these strategies are ideally extended to the management of surface water salinity as well.

3.1.3 Navigation

The HD houses Moerdijk industrial zone on its southern bank (province of Noord-Brabant). This area was purchased by Royal Dutch Shell in the 1970s to allow for expansion of their activities in the Netherlands. The main activities in the area are of petrochemical nature. The Moerdijk ports form the largest inland transshipment area in the Netherlands and it can be reached by vessels of up to 9 metres draught. Parties in the area benefit from the effect of economies-of-scale. This implies that exceeding benefits are obtained from employing ever larger ships as long as product demand keeps up. Larger ships have a larger draught and therefore require larger navigational depth for which ports and navigation channels need more frequent dredging.

The North Sea tidal signal reached 50 km inland (Biesbosch National Park) before closure of the HV (Tönis et al. (2002)). Reopening of the HV sluices is expected to widen the current tidal range of 0.30m to approx. 1.30m locally (Paalvast et al. (1998)). Mean Low Water (MLW) near the Moerdijk ports will hence be lowered by approx. $\frac{1}{2}$(1.30-0.30)=0.50m on average. One effect is that tidal windows in which large draught vessels are able to reach/pass the Moerdijk ports will therefore become narrower. This affects port operations and traffic intensity on the shipping route Scheldt-Moerdijk-Rhine. Moreover, the newly introduced effects of tidal filling and baroclinic exchange near the port mouths will likely lead to a net increase of sediment import (Tönis et al. (2002)).

The main considerations for navigation purposes are as expected of a commercial nature. Problems surrounding a reintroduced tidally dynamic regime near Moerdijk port entrances are twofold for the local parties:

- Negative deflection w.r.t. Mean Water Level (MWL) for 12 hours per day narrows tidal windows
- Net fine sediment import into port basins requires more frequent maintenance dredging

The former necessitates either the imposition of narrower tidal windows for ships or the use of ships with smaller draught altogether both of which are economically disadvantageous for the producer. The latter increases the cost of port dredging which, depending on the port design and near-entrance morphodynamics can be a significant addition to the Operating Expenses (OPEX).

In a Haringvliet Flows debate (TU Delta, June 2019), it is argued though that tidal windows for industrial shipping should not be seen as rigid constraints. The deepening of ports are often paid for by the community but benefit the corporations that add ever larger ships to their fleet. One of the outcomes of this debate is that concessions can therefore be made by the industries. This includes e.g. more frequent movement by smaller draught vessels or increased use of facilities at Maasvlakte II (Figure 1.3).

3.1.4 Estuarine ecology

The focal point of Delta21 is offering flood safety while benefiting the natural landscape (Section 1.2). Strong spatiotemporal variability in salinity, like in estuaries, cause for low biodiversity as species struggle to maintain their populations under such conditions. The (re)-development of estuarine ecology in the HV-HD is therefore dependent on smoothness of the horizontal salinity gradient (S_x), which is preferably of (O(0.1)) PSU/km. This allows for the development of a species-rich system despite the theoretically poor conditions for organisms to live under (Wijsman et al. (2018)).

Estuarine ecology develops along a chain of requirements, see Figure 3.4. Starting point is the periodic movement of salt, though estuarine ecology cannot be obtained without the movement of sediment and water ('Processes'), appropriate habitats ('Ecotopes') and habitation ('Species'). Estuarine ecology is characterised by habitation on the interfaces of permanently submerged (aquatic) and emerged (terrestrial) ecotopes known as intertidal areas (or flats). For many species of fish, however, mobility across the estuary mouth is important too. Marine juveniles, dwellers and foragers are categorisations of fish species that need unhindered access to the estuarine environment. Allowing salt to enter an inland basin therefore does not guarantee development of estuarine characteristics (Paalvast et al. (1998), Wijsman et al. (2018), Roels (2020)).

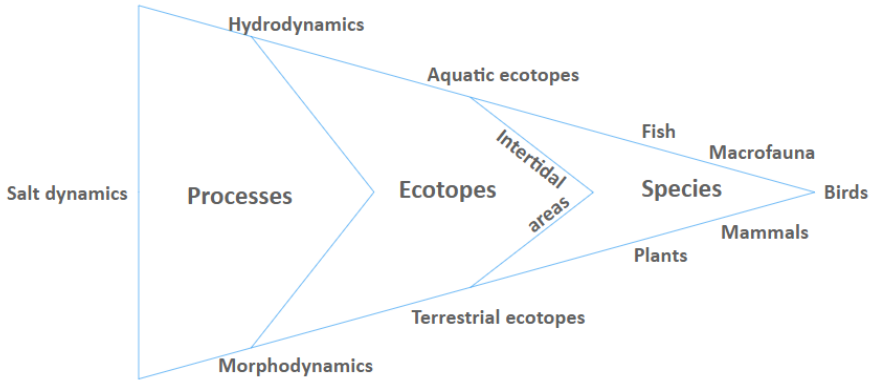

Figure 3.4: Convergence of physical processes to ecosystem in an estuary, based on Paalvast et al. (1998)

Like in the rest of the Netherlands, reclamations of the areas surrounding the HV started as early as the 12th century CE (Subsection 3.1.1) which has led to the disappearance of extensive intertidal areas important to the connection of terrestrial and aquatic ecotopes (Figure 3.4). Deterioration of estuarine ecology has been observed after closure of the HV in 1970 (Paalvast et al. (1998)). Of the 13.700 ha of intertidal areas, 1.850 ha was turned to dry land and 11.850 ha was submerged near-permanently. Moreover, an accumulation of polluted river sediment contributes to an overall decline in

ecological value in the Hollands Diep (Wijsman et al. (2018)). Figure 3.5 shows that the HV was the dominant debouching river branch at Q_{Waal}=2200 m^3/s, this discharge distribution is assumed to not differ significantly post-Delta21 as the mean Q_{Lobith} is expected to remain approx. the same in 2100 (ter Maat (2014)). Explanation for the invariability of the Rhine-Meuse mean discharge is the fact that the increased frequencies of droughts and heavy rainfall in 2100 almost equally contribute to variability around Q_{Lobith}.

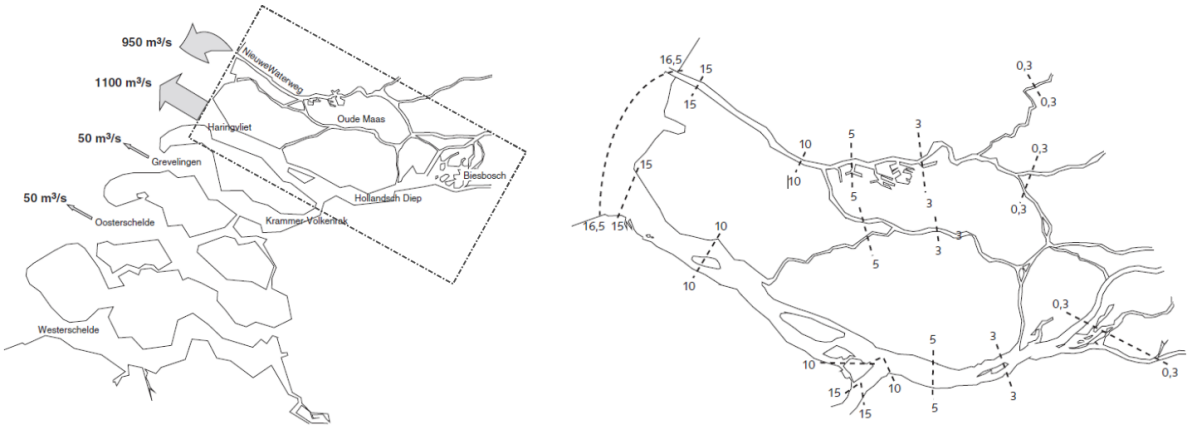

Figure 3.5: Pre-closure RMB based on Paalvast et al. (1998). **Left:** characteristic discharge distribution debouching sea arms (Q_{Rhine}+Q_{Meuse}) of 2150 m^3/s. **Right**: characteristic bottom salinity shown by isohalines in g/L Cl^- for Q_{HV}=600 m^3/s at High Water (HW). Conversion factor: 1.0 PSU ≈ 1.80655 x g/L Cl^- (Pietrzak and Katsman (2019))

Figure 3.5 shows that, at HW and low river flow (Q_{Lobith}=600 m^3/s), mean bottom water salinity diminished from 15 g/L Cl^- (27.1 PSU) to 3 g/L Cl^- (5.4 PSU) at Moerdijk industrial area. Three classess of brackishness can be distinguished (Paalvast et al. (1998), Wijsman et al. (2018)): polyhaline (18-31 PSU) from HV sluices to Tiengemeten ($\partial S/\partial x$=-0.45 PSU/km), mesohaline (5.5-10 PSU) from Tiengemeten to Moerdijk (($\partial S/\partial x$=-0.63 PSU/km) and oligohaline (0.55-5.50 PSU) from Moerdijk to Nieuwe Merwede ($\partial S/\partial x$=-0.33 PSU/km). The length of brackish zone then serves as accommodation space for species thriving under the specific conditions.

A 1994 test showed that passage of migratory fish occurred by slightly opening the HV sluices at flood. In July 2020, shad (fish) was observed to have passed the HV sluices, a species thought to have gone extinct in the Rhine area (Rijnmond Nieuws (2020)). RWS estimates that $O(10^7)$ fishes passed the HV sluices since the Kierbesluit came in effect. Ecologically valuable functions can thus be retrieved by reopening of the HV sluices but it is important to note that the ecological timescale is decadal.

Delta21 is not thought to reverse the ecological timeline of the HV in the sense that pre-1970 conditions are recovered. This is attributed to the constricted estuary mouth (6.000/17.000 m^2) which weakens tidal flow by energy losses and possibly affects the import of marine sediment. Consensus is that the impact of fully opening the HV sluices will be positive with regard to ecology in the estuary though (communications: TU Delta). A comparison made by Paalvast et al. (1998) shows some ecological parameters of the HV for the Kierbesluit situation (2019 onwards) and fully opened HV sluices, see Table 3.3.

Some critical notes must be made here as well. Delta21 proposes to construct engineering works in a protected Natura2000 area (Appendix C). This seaward area was assigned as ecological compensation for constructing Maasvlakte II (Tulp et al. (2016)). The future situation then resembles that of the Eastern Scheldt in which tidal flow is choked by the Eastern Scheldt storm surge barrier (Oosterscheldekering). This has led to ongoing tidal flat erosion in the Eastern Scheldt (Bosboom and Stive (2015)). Moreover, the proposed system (Appendix A) is likely to separate the HV contribution to the Rhine ROFI (de Boer (2009)) by diverting HV discharge away from thee RWW contribution. The Rhine ROFI is an extensive system running from Zealand to the Danish coast and functions as an important ecological route (Appendix C).

Table 3.3: Estuarine eco-parameters HV-HD: Kierbesluit vs. Opened HV dam. Note that opening the HV dam results in a loss of intertidal areas in the front delta due to emergence/submergence by diminished tidal range.

Parameter	**Kierbesluit HV**		**Opened HV dam**	
	Value	Unit	Value	Unit
Tidal range (mouth)	2.15	m	1.55	m
Tidal range (Haringvliet)	0.35	m	0.90	m
Tidal range (Biesbosch)	0.40	m	1.30	m
Morphodynamics	0		++	
Anoxicity	1/7	per year	0	per year
Salinity gradient	0-13	km	18-35	km
Intertidal areas (mouth)	1100	ha	700	ha
Intertidal areas (basin)	500	ha	2250	ha
Estuarine ecotopes (mouth)	12		12	
Estuarine ecotopes (basin)	9		25	

3.2 System forcing

System salinity relies on a balance between turbulent buoyant input. Subsection 3.2.1 describes the current mode of salinity transport in the RMB. Subsection 3.2.2 and Subsection 3.2.3 describe the marine and wind forcing in the RMB. Subsection 3.2.4 describes the effect of the buoyant input from the Rhine-Meuse branches.

3.2.1 System salinity

Regulation of salinity in the RMB is predominantly done by three 'control stations', being: HV sluices, Hagesteijn weir and Volkerak sluices (Figure 3.1). Post-closure, episodic events of salt intrusion have occurred in the HV basin mainly due to backwards intrusion through the Spui. This mechanism is activated when a water level set-up at PoR, e.g. due to a storm, drives a north-to-south flow through the Spui. These events cause a short spike in salinity at the Bernisse fresh water intake situated along the Spui (3.2.4). Such short salinity peaks are not problematic as the storage lake, at Brielle, has sufficient buffering capacity (Huismans (2018)). The slow and less intense feedback of salinity from the HV to the Spui is in indicated in Figure 3.6 as 'post-supply'. This feedback mechanism *can* be harmful as it can persist for weeks. Subsequent chlorinity values have been observed to exceed the 150 mg/L Cl^- norm. Figure 3.7 shows an observed example of these events from the winter of 2013.

The salinity levels in the current HV vary slowly throughout the year depending on the imposed discharge from upstream (Equation 3.1). Spikes in salinity do not occur in the HV due to the robust nature of the basin and the limited implementation of the Kierbesluit. The river background concentration averages 50 mg/L Cl^- which is lower than before 2009 due to the closure of upstream potash mines (Huismans (2018)). The background salinity increases for low discharges (Equation 3.1, ter Maat (2015)). The bandwidth of background concentrations is 122.4 mg/L or 0.07 PSU (Q_{Lobith}) to 51.9 mg/L or 0.03 PSU (Q_{Lobith}=15.000 m^3/s). Hence, Lavooij and Berke (2019) propose to close the HV sluices at Q_{Lobith} to prevent exceedance of the 150 mg/L Cl^- agricultural norm (Huismans (2018)). Lastly, minor intrusion occurs during cases when the Kierbesluit is in effect, which has been the case for a total of 16 days between January 2019 - February 2020 (Data: Rijkswaterstaat). Inherent to the Kierbesluit is anticipatory 'rinsing' (Dutch: zoetspoelen) of the HV before periods of low Q_{Lobith}. This is done to prevent runaway intrusion of salinity by diffusive processes as residual flow towards the North Sea diminish in these periods (ter Maat (2015)).

Regulation of salinity in the RMB is predominantly done by three 'control stations', being: HV sluices, Hagesteijn weir and Volkerak sluices (Huismans (2018)). Post-closure, episodic events of salt intrusion have occurred in the HV basin mainly due to backwards intrusion through the Spui (Figure 3.1). This

mechanism is activated when a water level set-up at HoH, e.g. due to a storm, drives a north-to-south flow through the Spui. These events cause a short spike in salinity at the Bernisse fresh water intake situated along the Spui (Subsection 3.1.2). Such short salinity peaks are not problematic as the freshwater reservoir, at Brielle, has sufficient buffering capacity (Huismans (2018)). The slow and less intense feedback of salinity from the HV to the Spui is in indicated in Figure 3.6 as 'post-supply'. This feedback mechanism *can* be harmful as it can persist for weeks. Subsequent chlorinity values have been observed to exceed the 150 mg/L Cl^- norm (ter Maat (2015)). Figure 3.7 shows an observed example of these events from the winter of 2013.

The salinity levels in the current HV are stable apart from the previously indicated promoters of salinity (average 6 days per year). The river background concentration averages 50 mg/L Cl^- which is lower than before 2009 due to the closure of upstream potash mines (Huismans (2018)). The background salinity increases for low discharges (Equation 3.1, ter Maat (2015)). The bandwidth of background concentrations is 122.4 mg/L or 0.07 PSU (Q_{Lobith}=1000 m^3/s) to 51.9 mg/L or 0.03 PSU (Q_{Lobith}=15.000 m^3/s). Note that the freshwater intake norm at Spui Bernisse is 150 mg/L Cl^- (Huismans (2018)).

$$C(t) = 46.9 + 1000 \times 75,532/Q(t) \tag{3.1}$$

Lastly, minor intrusion occurs during cases when the Kierbesluit is in effect, which has been the case for a total of 16 days between January 2019 - February 2020 (Data: Rijkswaterstaat). Inherent to the Kierbesluit is anticipatory 'rinsing' (Dutch: zoetspoelen) of the HV before periods of low Q_{Lobith}. This is done to prevent runaway intrusion of salinity by diffusive processes as residual flow towards the North Sea diminish in these periods (ter Maat (2015)).

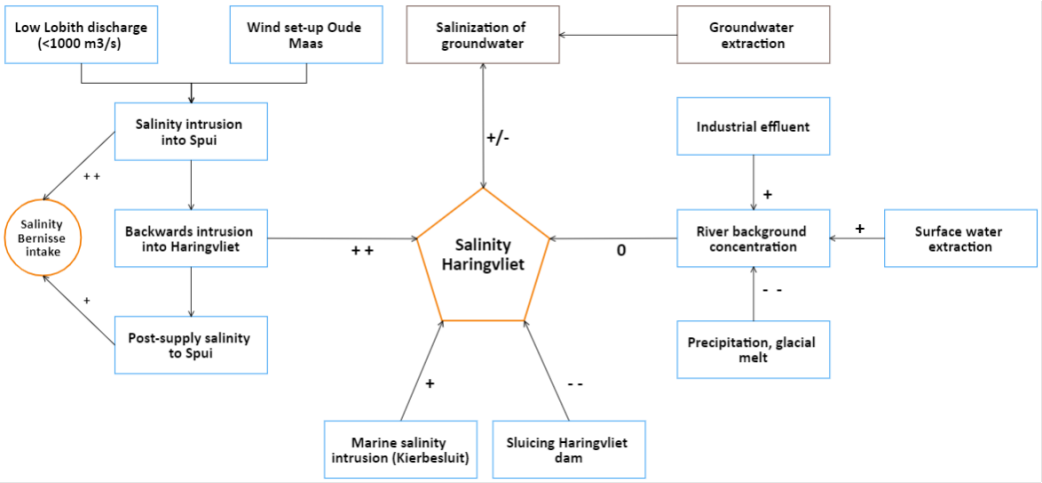

Figure 3.6: Current (2020) sources and sinks of salinity in the HV basin based on ter Maat (2015)

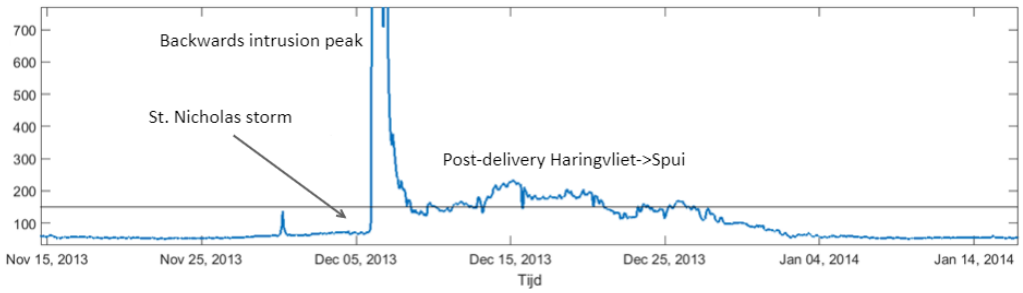

Figure 3.7: Graph showing short-lived peak of salinity near Zuidland (Bernisse) freshwater intake due to December 2013 storm followed by three week long post-supply by HV, adapted from Huismans (2018). Water intake norm shown at 150 mg/Cl^-.

The current (infrequent) salt intrusion mechanisms are show to be eclipsed by large scale salt intrusion post-Delta21 (Section 6.2). Paalvast et al. (1998) estimates that the 300 mg/L Cl^- bottom isohaline will be found approx. halfway the island of Tiengemeten (Figure 1.3). This was assessed using 1D SOBEK models and therefore recommended for further research. Moving the Spui Bernisse freshwater intake eastwards, to Strijensas (Figure 1.3), is deemed inevitable according to Lavooij and Berke (2019) and is inherent to the definition of Delta21 due to the sensitivity of this intake to episodes of salt intrusion.

3.2.2 Tidal signal

The tidal signal is the ubiquitous form of marine forcing for estuaries worldwide. It controls the vector of water motion (water levels, velocities) but does not dominate overall riverine discharge (Bosboom and Stive (2015)). The mouth of the RMB experiences an asymmetrical semi-diurnal tide (Appendix G) with a tidal period of approx. 12h25min. The spring-neap tidal period amounts to 14.5 days (ter Maat (2015)). Marine forcing of salinity depends on depth-averaged pressure gradients, or barotropic pressures and internal pressure gradients or baroclinic pressures direct against the outflowing buoyant flux (Subsection 3.2.4). These pressure gradients arise from the momentary water level at the estuary mouth and vertical gradients of density on the shelf sea. Tidal amplitudes and ranges are shown in Table 3.4. Contributions by wind-induced set-up and flow may also play a role, see Subsection 3.2.3.

Table 3.4: Tidal deflections of the water surface at HoH and HV front delta. MLW: Mean Low Water, MHW: Mean High Water. Source: ter Maat (2015).

Hook of Holland	**MLW [m+NAP]**	**MHW [m+NAP]**	**Mean tidal range [m]**
Neap tide	-0.60	0.88	1.48
Mean tide	-0.63	1.11	1.74
Spring tide	-0.60	1.30	1.90
Haringvliet front delta	**MLW [m+NAP]**	**MHW [m+NAP]**	**Mean tidal range [m]**
Neap tide	-0.77	1.08	1.85
Mean tide	-0.86	1.49	2.35
Spring tide	-0.99	1.82	2.72

From a human point of view, increasing sea levels by e.g. by waves (T=seconds), short-term tides (T=hours) and storms (T=days) can be visually observed but multi-annual timescales play an equally important role for engineering designs. Sea Level Rise (SLR) is an important contributor to the increase of barotropic forcing on estuaries (Burchard and Hetland (2010)). Eustatic and isostatic changes are mainly responsible for absolute SLR whereas regional effects and tectonics affect relative SLR (Bosboom and Stive (2015)). A well-studied threat to metropolitan areas caused by such effects is land subsidence which has more direct implications for flood risk (Herrera-García et al. (2021)). A range of factors have recently accelerated the process of globally averaged SLR which is well-documented in Church et al. (2013). Bruggemann et al. (2013) offer a clear description of estimated long-term local SLR for the Dutch coast and base their 35-85cm SLR range in 2100 on the official IPCC reports of the same year (Church et al. (2013)).

The increase of marine forcing on an estuary can be found by superimposing short term effects (tides, surge) and long term effects (SLR, nodal tide (Hollebrandse et al. (2005)) etc.). To that end, SLR scenarios described by Bruggemann et al. (2013) are consistently used here in combination with an analytical forecast of the tidal signal (Appendix G).

Furthermore, the correct representation of marine forcing in the near-coast environment plays a major role in predicting estuarine dynamics. North Sea flow in along the Dutch coast for instance is subject to a complex superimposed pattern of: stratified flows (salinity, heating), rotation (Coriolis) and friction-induced flows at the surface and bed (Ekman spirals). Elaboration can be found in de Boer (2009). Ideally, all of these effects are included at marine boundaries to correctly model salinity dynamics in the HV front delta and thereby intrusion into the estuary. For the HV-HD, flow is dominated by bi-directional tidal flow, river discharge and diffusion further inland (Kranenburg and Schueder (2015)).

Sub-tidal flows induced by geometry and stratification dominate around slack tides as the main flow and residual flows become comparable in order of magnitude (Burchard and Hetland (2010)).

3.2.3 Wind

Wind will induce a shear stress on the water column in the presence of a velocity gradient with respect to the water. Initially, this drives near-surface flow (Figure 3.8b). The depth of the wind-driven flow profile increases as time progresses until a pycnocline is reached and velocity is significantly damped. For spatially limited bodies, the transport by wind is influenced by the boundaries which creates a set-up (Figure 3.8a). This set-up increases the pressure in the surface layer and therefore causes a set-down of the pycnocline for a stratified body (Pedersen (2012), Pietrzak (2020)). This internal mode contributes to the baroclinic flows introduced in Subsection 2.3.1. Wind can be the dominating forcing of mixing in closed systems i.e. when tidal influences are absent but can be significant on coastal systems as well as wind surge drives landward flows (ter Maat (2015)).

Two more known effects of wind on flow are associated with surface instabilities (waves) shown in Figures 3.8c-3.8d for completeness. Wave effects have more implications for morphology (bed stirring, shock erosion) than for advection and diffusion of salinity. Instabilities of flow at pycnoclines may give rise to internal wave phenomena, reference is made to Pietrzak et al. (1991) and Pietrzak and Labeur (2004) for more on these non-linear effects.

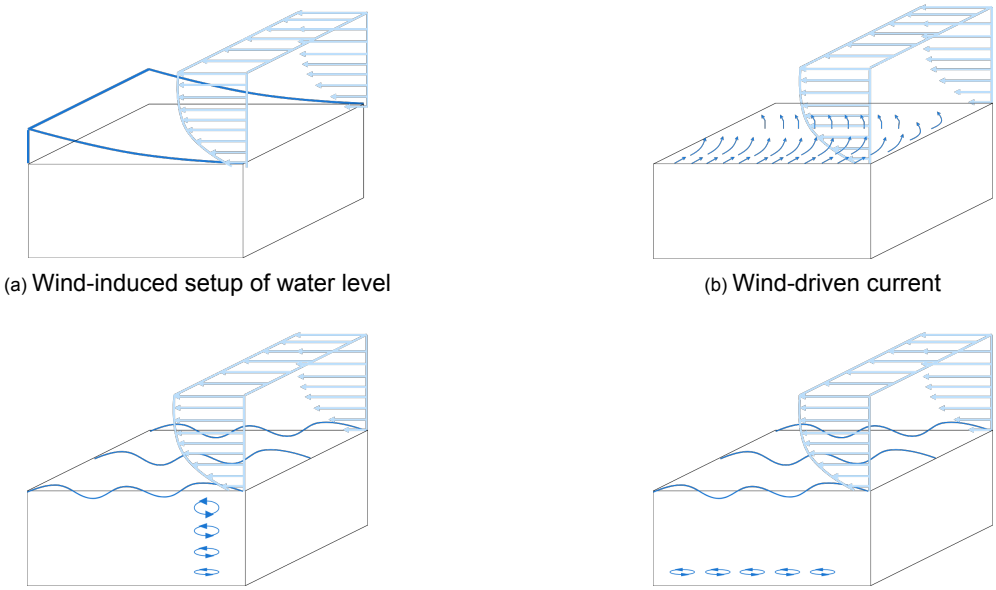

(a) Wind-induced setup of water level

(b) Wind-driven current

(c) Wind wave orbital velocities

(d) Wind wave bottom streaming

Figure 3.8: Four (possible) effects of wind on hydrodynamics based on Pedersen (2012)

The relative contribution of wind to the velocity scale (r_u) is defined using Equation 3.2 (Burchard and Hetland (2010)). It can be seen that for a typical non-storm wind at HoH of W_{10}=10 m/s (4.3), ρ_a=1.225 kg/m^3, ρ_0=1000 kg/m^3 and U_{max}=1.21 m/s, $r_U \approx 8\%$. Using the denominator of Equation 3.2 in the definition of u_T for determining Ri_E (Equation 2.6) and Si (Equation 2.7) it can be seen that both dimensionless numbers decrease for landward directed wind which indicates less persistent stratification and increased mixing. Inclusion of a realistic wind field is therefore an important aspect to modelling salinity transport.

$$r_u = \frac{\frac{\rho_a}{\rho_0} W^2}{U_{\max}^2 + \frac{\rho_a}{\rho_0} W^2} \tag{3.2}$$

The Royal Dutch Institute for Meteorology (KNMI) supplies data for various stations around the Netherlands. In this study, no storm events are assessed as these would constitute to closure of the HV sluices post-Delta21 (Section 1.2). Most hydrodynamic models use a simple relation (Appendix F) to include wind-induced shearing of the free water surface by using measurements for a single representative location for the entire geographic scope (Figure 4.12). This representation of wind introduces some modelling uncertainty which is treated in Chapter 7.

3.2.4 Freshwater discharge

Strictly speaking, river forcing (Figure 2.1) is not the only term affecting salt intrusion into estuaries. The term 'buoyancy forcing' is preferred to account for all fluxes that change stratification such as irradiation, precipitation and evaporation. Buoyancy effects arise from differences in density between two compounds, in this case water of different origin (Pickover (2008)). Salinity tends to dominate density, and therefore buoyancy, within systems of relatively small surface areas such as estuaries (Lyu and Zhu (2018)). Water density (ρ) is thus considered to be a function of two parameters here: salinity (S) and pressure (p). Morphological and oceanographic studies may include other parameters such as suspended matter (SPM) and temperature (T). Density is thus described by an equation of state (EoS) which indicates that bodies of fluid with different parameters but identical state do not interact. The omission of temperature from the EoS is treated in Chapter 7.

Figure 3.9 shows a cross-section of a shelf sea and the processes that affect stratification locally. This relatively shallow area (depth of O(10-100m)) forms the gently sloping submerged area between coastline and the ocean (depth of O(1km)). Here, surface heating (i.e. buoyancy input) during summer can sustain thermal fronts. The area in which rivers measurably dilute the shelf sea are called Regions of Fresh water Influence (ROFI). The ROFI transits into the estuary, which one could inversely denote as the Region of Salt water Influence, though this term has never been coined.

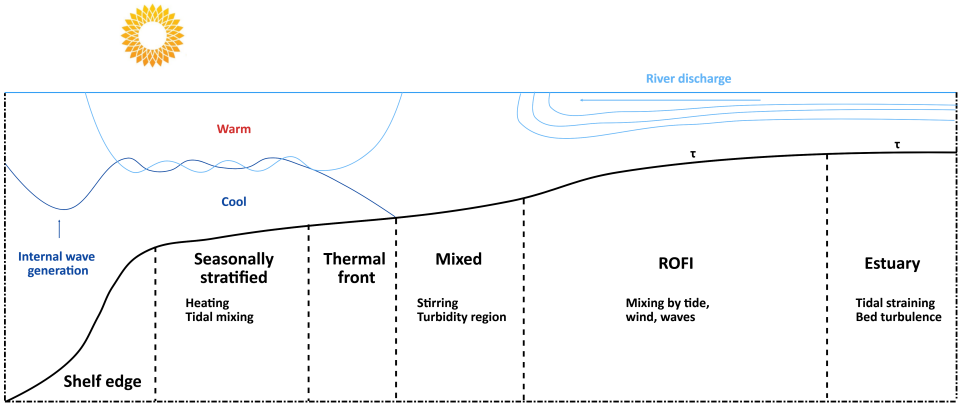

Figure 3.9: Overview of dominant baroclinic processes on the continental shelf, adapted from Simpson (1997). ROFI: Region of Freshwater Influence (de Boer (2009)).

Stronger stratification is associated with relatively high buoyancy forcing, see Figure 2.1. This is attributed to the shear stress induced by the fresh water discharge which stabilises and suppresses the slope of the saline wedge by transporting salt downward (Saveneije (2006)). Intense irradiation of shelf seas can lead to stratification as well, see Figure 3.9. The North sea is an example of a shelf sea that shows seasonal thermal front formation (Pietrzak et al. (2011)). It is observed that the Dutch coastal salinity profile is well-mixed during winter. Reference is made to de Boer (2009) for the associated frictionless rotational flow physics known as thermal wind.

Especially episodes of low buoyancy forcing are of interest to study salt intrusion due to increased 3D mixing and weak re-stratification on ebb tide. For the RMB this corresponds to months of extremely low river discharge (i.e. periods of low precipitation) which are thought to occur both more frequently and extremely in the next century (Bruggeman et al. (2011)). Buoyancy forcing in the geographical scope (Figure 1.3) is thus dominated by: Rhine discharge through the Rotterdam Waterways, discharge of the HV sluices at ebb and heating of the North Sea.

4

Model set-up

The strengths of numerical modelling are ubiquitous. If well-employed, its use leads to a great increase in labour efficiency and understanding of physical processes. Section 4.1 deals with describing steps to successfully employing a numerical model and serves as a reading guide as well.

4.1 Good Modelling Practice

Estuarine salt intrusion is a continuous, complex physical process which often has a dynamic equilibrium at best. Attempts at proposing analytical or 1D numerical models to describe intrusion have been made but results were mostly unsatisfactory or not universally applicable (e.g. Savenije (1986), Geyer and Signell (1992), MacCready (2004)). Here, the 3D Shallow Water Equations (SWE) with coupling to a transport equation (Appendix E) form the mathematical basis of the problem. An attempt at solving this set of equations is done using a 3D numerical model.

The class of numerical model applied is of lesser importance to the usefulness of results than operational skill and experience (Labeur (2009)). Some common dangers occurring while using numerical models are: numerical blindness (garbage in, garbage out) and equifinality (right result for the wrong reasons). Good Modelling Practice (GMP) is followed here to avoid the occurrence of these dangers.

GMP is a guideline that standardizes the use of modelling software within Dutch water management. It aims at the diligent use of models to make modelling studies more reproducible and transferable (van Waveren et al. (1999)). It comprises of a roadmap in using numerical models for water management purposes which will be followed throughout this chapter. GMP broadly consists of the following steps: create a log, describe the problem (Section 1.3), define the objective (Section 1.4), analyse the context and requirements (Chapters 2, 3) then choose (Section 4.2), describe (Section 4.3, Section 4.6) calibrate and validate (Chapter 5) the model, execute simulation runs (Subsection 4.6.2), interpret the results and report (Chapters 6, 8). A full description of GMP can be found in Appendix D. Calibration and sensitivity analyses of model schematizations used here (Section 4.2) have been executed and improved on several occasions see e.g. Uittenbogaard et al. (2005), Kranenburg (2015).

4.2 Model selection

The significance of the HV-HD system to Dutch society has been recognised in a variety of studies in the past (e.g. Tönis et al. (2002), van Koningsveld et al. (2008), Buitenhuis and Dieperink (2019)). Ample (numerical) models are thus available but only a limited number of these models can (accurately) describe salinity transport in the HV-HD. A numerical model that is used to answer the research questions (Section 1.4) must comply with the following:

- Able to reproduce hydrodynamics RMB
- Able to reproduce spatiotemporal salinity transport
- Include the geographical scope (Figure 1.3)

Salt intrusion in estuaries can be a highly 3D physical phenomenon (Geyer and MacCready (2014)). Lateral and vertical mixing processes may play a role in the up-estuary propagation of salinity, especially in relatively wide (W≫d) basins with erratic bathymetry (Saveneije (2006)). This applies to the scope area (Figure 1.3) which is characterised by: a relatively wide profile (B=650-2500m), spatially variable bottom profile of 6-14m depth and marked by approx. 30 pits of 15-30m depth (ter Maat (2015)). Furthermore, salt intrusion into estuaries is dominated by transport in the lower part of the water column (Section 2.1). Locally deeper bottom features, e.g. tidal gullies, thus promote salt intrusion. Sources of turbulence (Subsection 2.3.4) and accommodation space for mixing in the lateral and vertical suppress (along-estuary) intrusion.

Modelling of horizontal salt intrusion depends on the right description of inhibiting physical processes in the vertical and lateral direction (Subsection 2.3.4) and inclusion of baroclinic terms that may be dominating dispersion of salinity especially around slack waters when residual and tidal flow are of the same order (Geyer and MacCready (2014)). Preference must therefore be given to a numerical model with a locally refined grid and accurate bathymetric description. Two developed available numerical models are Zeedelta (RWS) and OSR-NSC (PoR). The former lacks a sufficiently refined bottom description (Communications: Deltares) which is disadvantageous in accurately describing salinity transport. OSR-NSC originally excluded the HV-HD from its topographical description. In 2016, Deltares expanded the OSR-NSC model to include the HV-HD (Kranenburg and Schueder (2015)). This model (OSR-HV) complies with the three decision parameters, see Table 4.1 and is employed here. At the time of writing, another eligible model (DCSM-FM) for reproducing salinity in the RMB was under development, see Section 8.2.

Table 4.1: Decision parameters and outcomes for Zeedelta, OSR-NSC and OSR-HV

Model	Hydrodynamics	Salinity	Haringvliet
Zeedelta	✓	**x**	✓
OSR-NSC	✓	✓	**x**
OSR-HV	✓	✓	✓

4.3 Model description

The OSR-HV model is a geographically expanded version of the 3D OSR-NSC model, that describes the hydraulics of the Rotterdam wet infrastructure. OSR-NSC has been calibrated on multiple occasions (Kranenburg (2015)) and has been used to describe small-scale salinity transport into HV during a 1997 intrusion test (Jacobs et al. (2003)). The expanded version includes the HV-HD and an additional portion of the North Sea southwest of the HV sluices (Figure 4.1). The total grid-size is (M;N)=(648;1925) of which ≈37% are active cells. The fact that $4.6 \cdot 10^5$ cells per layer are used to model hydrodynamics and salinity transport make OSR-HV a relatively computationally demanding model. CPU usage in this study averaged 0.4 real-time days per simulated day working on 20 processors in a Linux remote SSH Beowulf-type cluster. SIMONA software is used which is subdivided into WAQUA (2D) and TRIWAQ (3D) to run OSR-HV. The model allows for nesting in a spatially larger model to generate open boundary conditions for hydrodynamics and salinity transport (Section 4.5, Section 8.2).

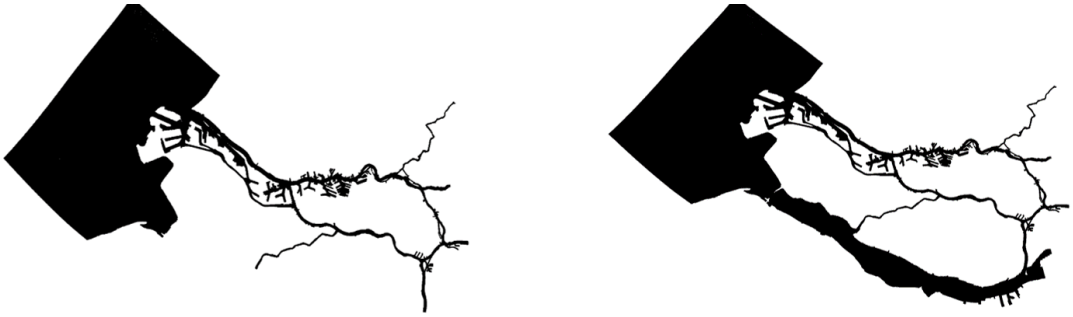

(a) (b)

Figure 4.1: OSR-NSC original grid (a) and OSR-HV grid (b)

Wind forcing is retrieved from KNMI open source data (HoH station). Bathymetry of the RMB (xyz samples) has been obtained for Aug '19. Upstream open boundaries are based on RWS data at Lobith and Lek. Marine open boundaries have been generated using harmonic series. Boundary conditions for salinity have been implemented using representative sets from OSR-NSC 2DH (North Sea model). These data are bundled in the SIMONA input file (siminp), checked (WAQPRE), processed (WAQPRO) and results may be processed in e.g. MatLab afterwards, see Figure 4.2.

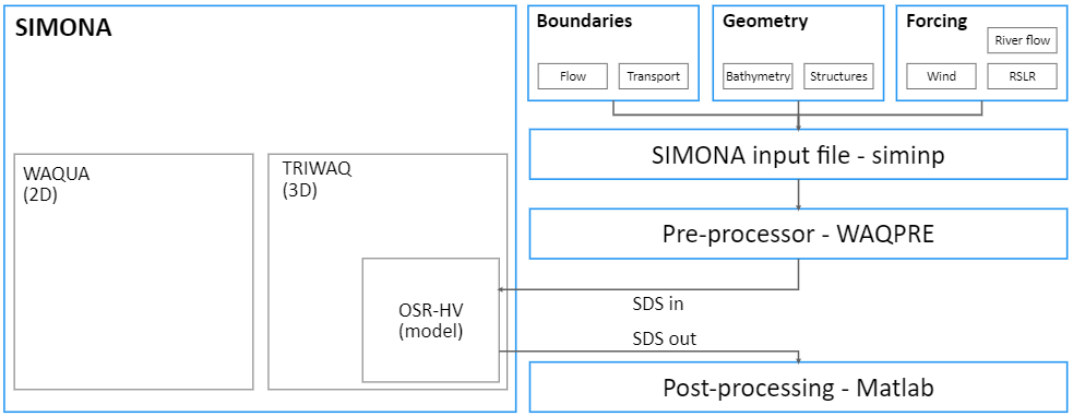

Figure 4.2: Position of OSR-HV in modelling hierarchy

The basic workings of WAQUA/TRIWAQ are essentially the same, however TRIWAQ uses an approach that is not depth-integrated and thus needs discretization of the vertical. This is done using 'terrain-following' discretization also known as σ-layering (Rijkswaterstaat (2005)) rather than z-layering, which preserves layer thickness along grid lines, see Figure 4.3. A total of 10 of these layers is applied. The σ-layering in the OSR-HV model is chosen as non-equidistant with relatively thinner layers lower in the water column to refine salinity transport there. Horizontal discretisation is done using a curvilinear grid, elaboration on considerations regarding the numerical grid is found in Appendix F.

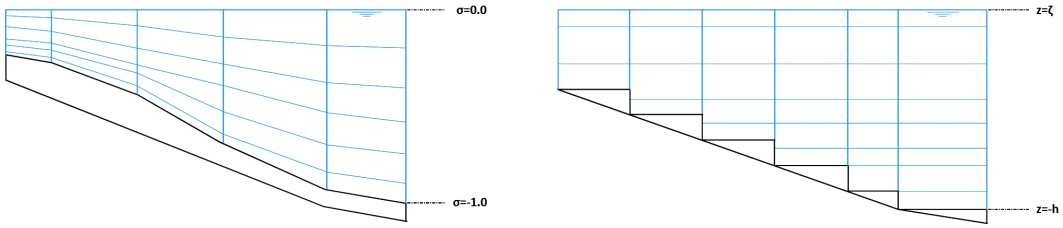

Figure 4.3: Terrain following or σ-layering (L) and z-layering (R)

Table 4.2 shows the state variables that need to be known at the start of a simulation. In principle, only a global estimate of these initial fields will suffice for running simulations. After some time, the effect of the initial conditions will dissipate causing the problem to be wholly defined by the boundary conditions. Unrealistic estimates of initial conditions will result in extensive spin-up times for the model though (van Kester et al. (2001)). Especially a mismatch between initial salinity profile and boundary conditions may cause extensive spin-up times as steep baroclinic pressure gradients give rise to steep water level gradients and generate distortion waves that propagate into the domain (Deltares (2020)). A choice has been made to use initial conditions for HW at HoH corresponding to landward flow in the NWW. Maximum stratification in the nearshore amounts to 13 PSU between surface (18 PSU) and bottom level (31 PSU) and diminishes offshore. Boundary conditions are generated accordingly to minimize spin-up.

The grid of OSR-HV contains an expansion w.r.t. that of OSR-NSC (Section 4.2) along the southern to western marine boundary to model salinity and flow in the HV front delta more accurately (communications: PoR), see Figure 4.4. The grid expansion comprises of two marine zones which are assigned a vertically uniform salinity with a characteristic value. Therefore, some initial distortion waves have been observed. Furthermore, the HV-HD is assigned a characteristic river background salinity of 0.3 PSU (Subsection 3.2.1). This constitutes to a conservative value (Section 5.2). The initial fields in the original model domain are based on a 1997 HV salt intrusion test (Jacobs et al. (2003)). Boundary output on stratification, flow and water levels for boundary conditions are available for the entirety of 1997 which has been used as a source of boundary conditions for predictive scenarios here (Section 4.6).

Table 4.2: Initial conditions used in this study and supplied to OSR-HV. All fields from larger domain OSR-NSC output (see Kranenburg and Schueder (2015)) at maximum water level (HW).

State variable	Domain OSR-NSC	Grid extension	Value	Unit
Flow (u)	Field: 1997 intrusion test	Set value	0	m/s
Flow (v)	Field: 1997 intrusion test	Set value	0	m/s
Water levels (h)	Field: 1997 intrusion test	Set value	NAP+1.25	m
Salinity (S)	Field: 1997 intrusion test	Set values	0.3, 18-30, 30-33	PSU

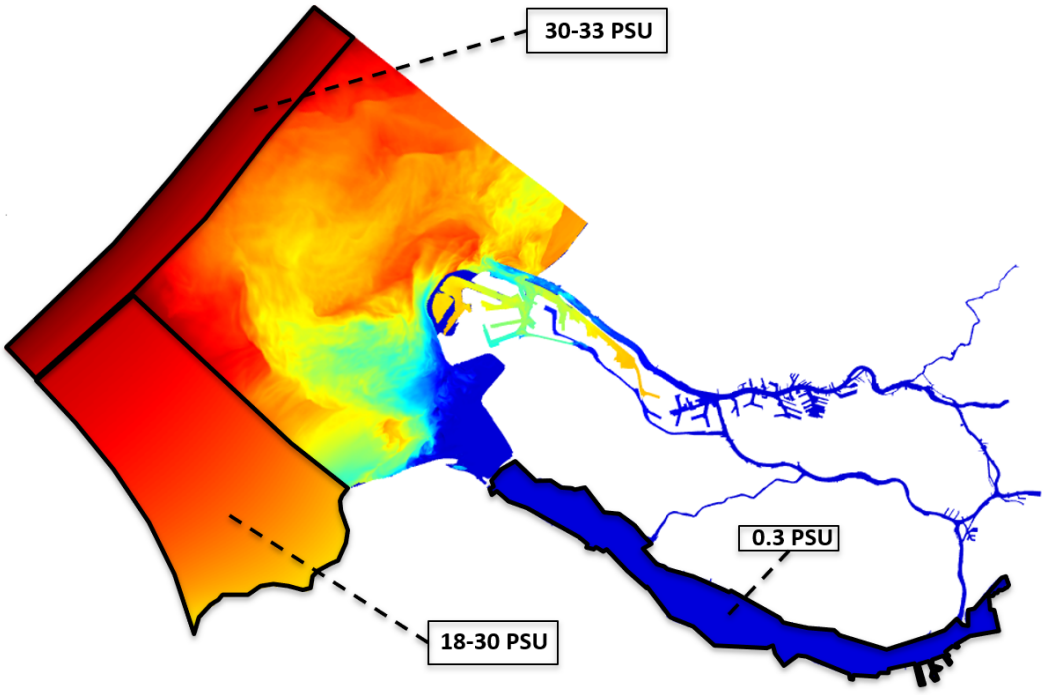

Figure 4.4: Initial surface salinity field OSR-HV (ebb tide) composed of 1997 intrusion test field (at LW) and more homogeneous salinity values in grid extensions

The timescale of spin-up for tidal flow (T_{tide}) is proportional to the prescribed bed friction through Equation 4.2 (van Kester et al. (2001)). Where the Chézy coefficient (C) is inversely proportional to bed friction. Qualitatively, this means that distortion waves caused by initial conditions die out relatively quickly for shallow (small C) and fast-flowing (large U) model areas, such as rivers. Equation 4.2 should be regarded as a first estimate for flow spin-up. Salinity in stratified flows generally takes longer to spin-up due to the need to resolve more numerous gradients Deltares (2020). This is affirmed by validation results (Chapter 6).

Spin-up time thus depends on the local parameters near the marine open boundaries. In OSR-HV: H≯40 m, U=0.2 m/s (mean, from data), g=9.81 m/s^2. Also, the model uses a typical global Manning roughness coefficient of n=0.020 m$^{-1/3}$s (Limerinos (1969), Deltares (2020)). Equation 4.3 describes the length scale over which the intervention (Delta21) exerts influence on the flow field (van Kester et al. (2001)) for a transport problem. In OSR-HV, the open boundaries are positioned at 20-23 km of the Delta21 works which exceeds. Problems may arise north of Maasvlakte II though where a marine open boundary is found at 6 km of the point of outflow. Reproduction of ROFI dynamics (de Boer (2009)) is poor here which affects accuracy of salinity predictions for the entire RMB (Subsection 3.2.1). Equation 4.2 uses an absolute tidal velocity at the start of simulation of |U|=0.31 m/s (Appendix G). For Equation 4.3, a maximum surface velocity of U_{max}= 1.20 m/s near HoH was found to occur at ebb tide (spring phase) after T=31d for Q_{Lobith}=2100 m^3/s The results from rules-of-thumb in Equations 4.1-4.3 are well-reflected by water level results (Appendix I) which show spin-ups of anywhere between 1-2 tidal cycles and O(1.0) cm water level inaccuracies at the northeast boundary situated in the Rhine ROFI (**??**). More typical near-boundary maximum surface velocities amount to 0.6 m/s. This shows that the current model domain requires northward extension (by ≈11-28km) to better replicate Rhine ROFI dynamics (Section 8.2).

$$C = \frac{H^{1/6}}{n} \leq 92.5\ m^{-1/2}s \tag{4.1}$$

$$T_{tide} = \frac{HC^2}{g|U|} \leq 1.75 \cdot 10^5\ s \mathrel{\widehat{=}} 4 \text{ tidal cycles (M2)} \tag{4.2}$$

$$L_{tide} = \frac{2}{\pi} \cdot T_{tide} \cdot U_{max} = \frac{2}{\pi} \cdot 44580 \cdot 0.6 - 1.2 = 17 - 34\ km \tag{4.3}$$

The eastern part of the domain is demarcated using open boundaries as well. Three river branches form open upstream boundaries (Figure 4.6). Input at Lek (L), Beneden Merwede (BM) and Moerdijk bridge (MB) is specified as 'automatic distribution of discharge' or 'Q_{ad}'. This type of boundary distributes discharges over the cross-section such that the higher flow velocities (u) are found in the conveying channel and lower velocities on the floodplains. The alternative would be a uniform distribution of discharge laterally, which would yield an unrealistic distribution of velocities, see Figure 4.5. The input from Hollandsche Ijssel, the northernmost branch in Figure 4.6, is set to zero which is a conservative approach (Kranenburg and Schueder (2015)).

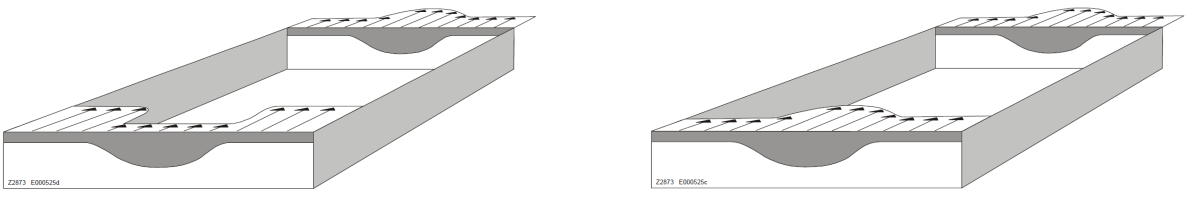

Figure 4.5: Uniform Q-boundary (L), Automatically distributed Q-ad boundary (R) by van Kester et al. (2001)

Figure 4.6 visualises the positioning and type of boundary condition for flow and transport in OSR-HV. North Sea boundaries (NS1, NS2 & NS3) consist of 142 1D velocity points perpendicular to the local

grid cell. Additionally, 14 water level points bring the total to 156 points. Velocity and salinity boundaries are specified for each of 10 σ-layers. Water levels account for the entire water column. A mix of velocities and a few water levels ensures the proper replication of water levels at the open boundaries (Kranenburg and Schueder (2015)). This, in turn, is important for replication of residual currents in the front delta of HV which play a significant role in sub-tidal salinity transport (Rijkswaterstaat (2005)), Deltares (2020)). Additionally, internal boundaries may be defined at (left-to-right): HV sluices, Spui South and Dordtse Kil. In this study, only HV sluices have been adapted in line with different sluicing programs, see Appendix B. Internal boundaries at Spui and Dordtse Kil find their use mostly in calibration purposes such as in Kranenburg and Schueder (2015) and Kranenburg (2015).

Figure 4.6: Boundary conditions in the OSR-HV grid

A pronounced disadvantage of using OSR-HV is that, despite the inclusion of the Eckart Equation of State (EoS) for water density in SIMONA (Zijlema (1998)), it uses a constant water temperature. This omits the effect of temperature fluctuations on buoyancy and thus stratification (Subsection 3.2.4). This may or may not be a justified approximation depending on the relative importance of temperature and salinity on baroclinicity. The implications of this are treated in Chapter 7.

4.4 Model settings

This paragraph treats physical (Subsection 4.4.1) and numerical settings (Subsection 4.4.2) of OSR-HV. Justification for these settings is provided using literature, reference is made to Kranenburg and Schueder (2015) and Kranenburg (2015) for more on these settings regarding OSR-HV specifically.

4.4.1 Physical settings

Vertical mixing quantities are assumed to be of lower order of magnitude than those in the horizontal (L,W≫d). Turbulence production (k), and dissipation (ε) terms can therefore be described in non-conservative form and are solved by a k-ε model for turbulence closure (Deltares (2020)). The magnitude of the horizontal eddy viscosity coefficient (ν_h) affects the exchange of lateral momentum and thereby indirectly that of salinity in the RMM for WAQUA/TRIWAQ models (Uittenbogaard et al. (2005)). Difficulties arise in that ν_h has no direct physical basis and is a function of both local flow parameters and flow history (Blazek (2015)). ν_h is provided to siminp (Appendix H) as a constant value which is a far-reaching simplification though a necessary one regarding computational demand. A higher ν_h denotes more conversion of kinetic (advective) energy into potential energy through dissipation by turbulence. According to Uittenbogaard et al. (2005), ν_h decreases with decreasing Q_f, increasing width and for fine-meshed models (like OSR-HV). Here, ν_h is taken as 1.00 m^2/s in line with findings

from Kranenburg and Schueder (2015) and Kranenburg (2015) which corresponds well with the mean aspect ratio of the HV (W/d≈100).

According to Geyer and MacCready (2014), over half of the subtidal along-channel salt flux (Subsection 2.3.4) in tidally energetic systems is attributable to diffusion. Vertical diffusion is solved by the k-ε model (Appendix E), Instabilities in the vertical transfer of mass and momentum are represented by constant horizontal eddy viscosity and diffusion coefficients (Geyer and MacCready (2014)). Horizontal diffusion is assigned a global value of 0.01 m^2/s and locally higher values varying from 0.2-1.0 m^2/s (Kranenburg and Schueder (2015), Kranenburg (2015)) in landward direction (Appendix F). Diffusion through the HV sluices is set to zero to limit exaggeration of salinity transport through the dam (Kranenburg and Schueder (2015)).

Finally, bed shear stress (τ_b) is locally computed using a 3D Chézy coefficient (Zijlema (1998)) which follows from a user-defined constant Manning coefficient (n). Lyu and Zhu (2018) recognises though, that n gradually decreases for increasing tidal amplitude. The Manning coefficient is therefore assigned a global value of 0.020 but varies locally between 0.016-0.026 in line with findings of Kranenburg (2015).

Table 4.3: Parameters included in previous sensitivity analyses and calibration rounds of OSR-HV. Global denotes background values. Values may vary locally (Appendix F).

Symbol	Parameter	Unit	Global	Plausible range	Source
ν_h	Horizontal eddy viscosity	m^2/s	1.00	0.50-1.50	Uittenbogaard et al. (2005)
$D_{x,y,HV}$	(Hor.) diffusion coefficient HV	m^2/s	0.01	0.1-1	Kranenburg (2015)
n	Manning coefficient	$m^{-1/3}s$	0.020	0.01 - 0.03	Lyu and Zhu (2018)

4.4.2 Numerical settings

The ADI scheme employed in WAQUA is unconditionally stable though coupling to the transport equation (Appendices E and F) may introduce inaccuracies through spurious oscillations (Zijlema (1998)). The timestep (Δt) is defined at 1/16th of a minute. Smaller Δt lead to no significant gain in accuracy. Coarsening the timestep (to e.g. Δt=1/8th minute) leads to non-physical oscillations. Moreover, no significant gain in accuracy was found by refining the vertical to e.g. σ=20 for the similar OSR-NSC model (Section 4.2). Smoothing between the initial conditions and open boundaries is done for the first day of simulation (tlsmooth=1440 min.). More numerical parameters are found in Table 4.4 and elaboration on the numerical workings of OSR-HV is found in Appendix F.

Table 4.4: Numerical constants applied for OSR-HV in this study

Numerical constant	Value	unit
Timestep (Δt)	0.0625	$min.$
No. of σ-layers (non-equidist.)	10	-
Max. iterations continuity (itercon)	40	-
Max. iterations momentum (itermom)	20	-
Convergence criterion vel. (iteraccurvel)	0.0002	-
Time-smoothing (tlsmooth)	1440	min
Hydrodynamical implicitness parameter (θ_h)	0.5	-
Transport implicitness parameter (θ_S)	0.5	-
Critical drying depth	0.10	m

4.5 Model adaptations

The default OSR-HV model is based on a 1997 salt intrusion assessment at the HV sluices. Hence, changes must be made to the model bathymetry (Subsection 4.5.1), open boundary conditions and internal boundary conditions (Subsection 4.6.1) before it can serve as a predictive tool for salt intrusion into the current (2020) and Delta21 (2100) HV.

4.5.1 Bathymetry

The bathymetry file was updated to include changes to the system made between 1997-2020. Major changes are summarized in Table 4.5 though all bathymetric changes have been included through the use of depth samples. Dredging of nautical channels in the RWW promotes salt intrusion there which could in turn increase backward salt intrusion through the Spui into the HV (Figure 3.6). Room for the River (Dutch: Ruimte voor de Rivier) interventions between 2006-2019 (Rijke et al. (2012)) are assumed not to affect macro physical phenomena within this study as hydrodynamics in the upstream domain are mostly affected during flooding of flood plains (Dutch: uiterwaarden). Such scenarios are not assessed here.

Table 4.5: 1997-2020 major bathymetric changes in lower RMB

System feature	Adaptation	Effect on hydrodynamics
North Sea	Morphological change	Macro-level changes in flow patterns (Hollebrandse et al. (2005))
Maasvlakte II	Constructed	Meso-scale changes in flow patterns (Stolk and Dijkshoorn (2009))
New Waterway	Dredged	Stronger gravitational circulation RWW (Section 2.3)
Beerdam	Removed	Brackish Hartelkanaal
Botlek 'thorn'	Removed	Removal of 500.000 m^3 of sediment and increased depth

Delft3D QUICIN module has been used to adapt and smoothen the interpolation of the 1997 depth file using 2019 XYZ-samples . Hereafter, Matlab has been used to convert the Delft3D format depth file (.dep) to one compatible with TRIWAQ (.box). The result is shown in Figure 4.7, notice the addition of Maasvlakte II as an elevated bottom (light blue, NAP+6.00m) rather than land boundary (yellow). The northern section of the North Sea underwent slight changes to the nearshore depth contours in the period 1997-2019.

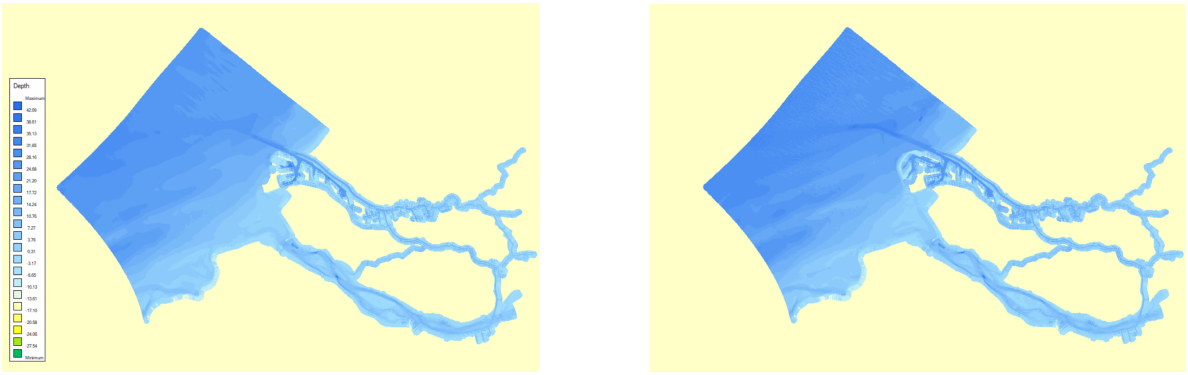

(a) OSR-HV - 1997 bathymetry

(b) OSR-HV - 2020 bathymetry

Figure 4.7: Bathymetric changes (1997-2020) implemented into OSR-HV for validation using Dec '19 Kierbesluit data

More changes to the bathymetry are done to perform an assessment of post-Delta21 scenarios, also see Appendix A. Especially the addition of a shipping lane (NAP-8.00m) is of importance as estuarine circulation strengthens non-linearly with depth (MacCready (2004)) thereby exceedingly adding to salt intrusion. Reconnection of Oostvoorne Lake with the marine environment is also suggested but not made definitive yet (Lavooij and Berke (2019)) and therefore excluded from this study. The Energy Storage Lake (24 km^2) and Tidal Lake are enclosed by a dune system thereby sheltering the HV from direct North Sea impact. A storm surge barrier (sill: NAP-7.00m) closes the Tidal Lake from the North Sea for NAP+3.00m at HoH (communications: Delta21). Also, the HV bridge sill, which forms the boundary between HV and HD, is raised to NAP-3.00m in an attempt to block salt advected over the bottom into the HD. Inclusion of these features is central to answering the research questions (Section 1.4). The last column of Table 4.6 qualitatively indicates what the expected effect of the bathymetric changes is to salt intrusion.

Table 4.6: Adaptations to the RMB system included in Delta21. Note: as per Lavooij and Berke (2019), no decision has been made on dredging works in and around Oostvoorne Lake.

System feature	Adaptation	Effect	Included	Intrusion
Energy Storage Lake	Construction	Further diversion northward flow	✓	↘
Tidal Lake	Construction	Retainment fresh water HV	✓	↘
Raised sill HV bridge	Construction	Block salt advection	✓	↘
Sill Delta21 storm surge barrier	Construction	Block salt advection	✓	↘
Navigation channel	Dredging	Increased navigability HV	✓	↗
Oostvoorne Lake	Dredging	Recreational value	**x**	-

Hydro- and morphodynamics in and around the Energy Storage Lake are outside the scope of research (Section 1.4). Therefore, the Delta21 dune system has been modelled as a closed boundary. Delta21 geometry has been obtained from Appendix A and has been redrawn (ARCGIS, Luchtfoto Actueel Ortho 25cm - Landelijke Voorziening Beeldmateriaal - EPSG:28992). This is shown in Figure 4.8a. Delft3D QUICIN has been used to import the geometry and approximate it using grid-following thin dam elements. This creates a closed lake system. The exported '.thd' file is reformatted to comply with SIMONA input (Dutch: 'schotjes'). See Figure 4.8b.

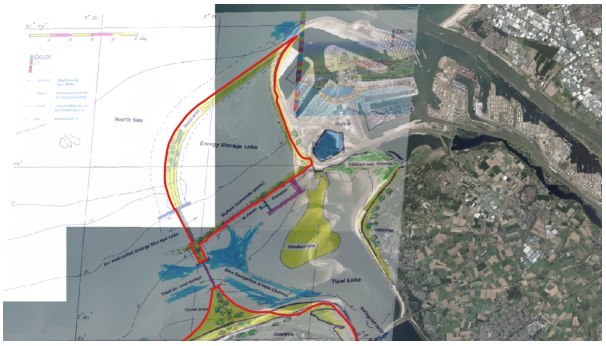

(a) Earth projection of Delta21 concept sketch

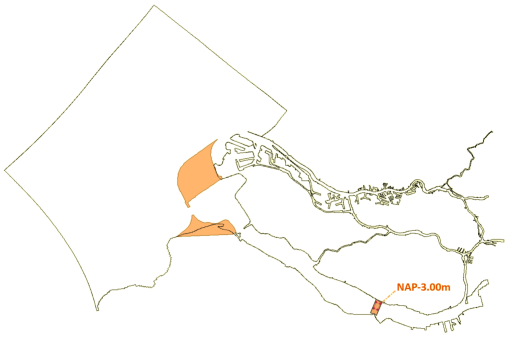

(b) Projection implemented in Delft3D-QUICIN as flow-blocking elements. Notice the raised sill (NAP-3.00m) of HV bridge

Figure 4.8: Representation of Delta21 interventions by thin dam flow-blocking elements. These adaptations provide the basis for predictive scenarios after model validation.

4.6 Input

Subsection 4.6.1 treats the description of marine, riverine and internal open boundaries. Elaboration on generation of marine boundary conditions can be found in Appendix G. Subsection 4.6.2 proceeds to describe relevant model scenarios for this study.

4.6.1 Boundary conditions

The 3 North Sea boundaries (Figure 4.6) are a mix of prescribed water levels and (boundary perpendicular) velocities (Figure 4.6). SLR (Subsection 3.2.2) constitutes to ≈2-4% (35-85cm, ter Maat (2014)) increase of the water column and is therefore asssumed to only affect water level boundary points. Moreover, an assessment is done to check whether North Sea velocities are significantly affected by residual flows from wind and baroclinic effects (see Appendix G). UTide (MatLab tool) has been used to convert velocities and water levels (tot. 1434) of the 1997 intrusion test data to harmonic series, i.e. it performs a harmonic analysis. Reconstruction of the velocity signal then visualizes the contribution of tides and residual flow respectively (Appendix G). Furthermore, salinity is described for every boundary point and over 10 σ-layers (tot. 1550) to define the transport problem. It shows that vertical the salinity

gradient can be significant with $\Delta\rho_{1,2}$ ≈7 PSU near the surface which is especially the case in the area influenced by the Rhine ROFI (NS3, Figure 4.6).

External riverine model boundaries in the east comprise of: Lek, Beneden Merwede and Moerdijk Bridge (Figure 4.6). These are defined by a discharge, refer to Tables 4.7 and F.3. Known discharge distributions (Figure 4.9) are used to generate timeseries from Lobith historical time-series. The discharge distributions over the different branches for mean (Q_{Lobith} = 2100 m^3/s) and low (Q_{Lobith} = 1000 m^3/s) discharge are taken from (Asselman et al. (2018), ten Brinke (2013)). This way, Q_{Lobith} can be divided over the 3 external boundary branches in giving: Q_{MB}, Q_{BM}, Q_L. The Waal splits into the Beneden Merwede (Q_{BM}/Q_{Waal}=38%) and Nieuwe Merwede. The Nieuwe Merwede is then joined by the Meuse. Jointly, these two contributors define the upstream discharge boundary at the Moerdijk bridge (Q_{MB}/Q_{Waal}=62%). The Ijssel and approx. 1% sources/sinks complete the hydrological balance of the RMB. Discharge sinks (e.g. water demand, evaporation) are assumed constant with decreasing Q_{Lobith}. The selected Q_{Lobith} are derived from Lavooij and Berke (2019) and ter Maat (2014), elaboration follows in Appendix H.

Table 4.7: Distribution of Q_{Lobith} over Nieuwe Merwede (Moerdijkbrug, MB), Beneden Merwede (BM) and Lek. Contributions by the Meuse are included in Q_{MB}. All Q in m^3/s

Q_{Lobith}	Q_{Waal}	Q_{Lek}	Q_{Ijssel}	Q_{Loss}	$Q_{MB/Q_{Waal}}$	$Q_{BM/Q_{Waal}}$
2100 (100%)	1428 (68%)	378 (18%)	273 (13%)	≈1%	886/1428	542/1428
1000 (100%)	680 (68%)	180 (18%)	130 (13%)	≈1%	422/680	258/680

Important to note is that the discharge distribution between the Lek, Moerdijk bridge and Beneden Merwede differs little from the pre-closure situation. This can be seen by comparing Figure 3.5 (pre-1970) and Figure 4.9 (post-1970). In Figure 3.5, the northern branches (Lek+Beneden Merwede) add up to 44% and the southern branches (Moerdijk bridge) to 56% of the volume debouched into the North Sea, approx. the same as in Figure 4.9. The main differences are attributed to Q_{Lek} but historical series have been used to model this open boundary without relying on fixed hydrological relations.

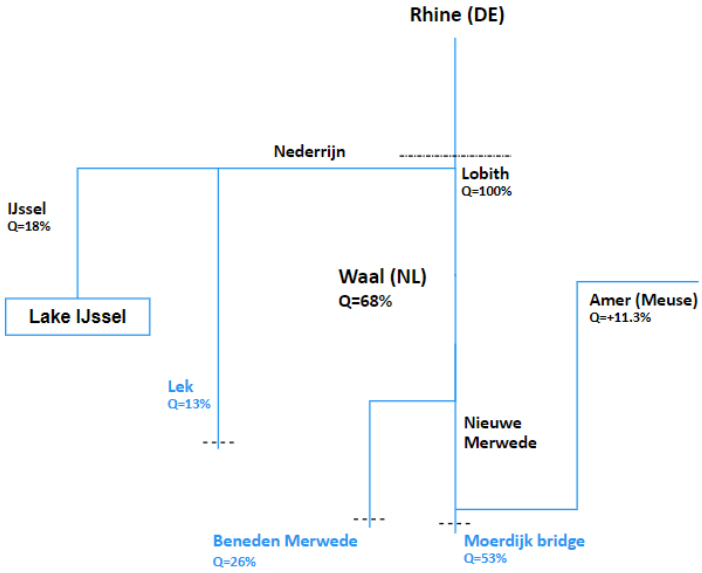

Figure 4.9: Discharge distribution of the relevant upstream boundaries expressed in % of Q_{Lobith} for the range of 1000-2100 m^3/s, note: $Q_{total}=Q_{Rhine}+Q_{Meuse}$=111.3% Q_{Lobith}

The HV sluices function as the key internal boundary condition (Figure 4.6) using either the current (2020) sluicing program (HOP) or the Delta21 program (Appendix B). The original model used the pre-Kierbesluit program known as LPH84, which only sluiced at ebb to 'rinse' the HV-HD basin. Additionally, in Delta21, a new storm surge barrier is situated downstream of the HV sluices (Figure 1.1b). This storm

surge barrier (A_c=13000 m^2) has been modelled as a permanently opened barrier. No storm scenarios are assessed in which threshold of closure (NAP+3.00m) is triggered (Appendix H).

Table 4.8: Parameters of interest for Delta21 storm surge barrier shown in Appendix A. Sill situated one metre above approach depth (NAP-8.00m)

Delta21 Storm surge barrier (to be named)		
Length	2000	m
Sill level	NAP-7.00	m
Conveyance area	13.000	m^2
Closure threshold	NAP+3.00	m

4.6.2 Model scenarios

Relevant scenarios for prediction of salt intrusion post-Delta21 have been composed and run while bearing identified model weaknesses found in Paragraphs 5.1-5.3 in mind. Figure 4.10 shows the chronology of model runs that have been performed. Model validation is done using boundary conditions from November-December 2019 (see Chapter 5). Subsequently, the same conditions are applied to the altered geometry according to the Delta21 plans, (Appendix A). Next, 4 scenarios are tested using boundary conditions corresponding to climate scenarios for the year 2100 (ter Maat (2014)). Finally, the effect of partially opening the HV sluices is assessed.

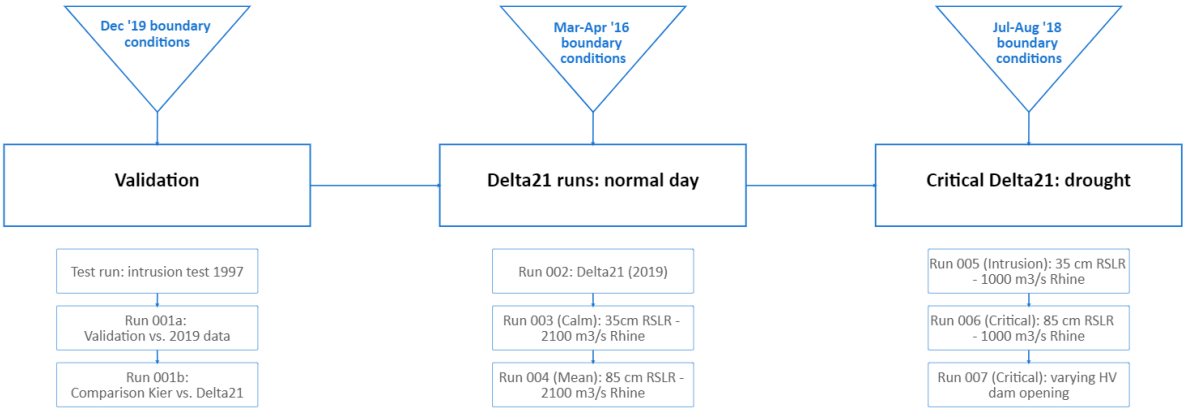

Figure 4.10: Sequence of model runs used to answer the research questions

Boundary conditions for predictive model run scenarios (year: 2100) are based on Bruggeman et al. (2011) for SLR along the Dutch coast. Extreme storm surge scenarios (e.g. Katsman et al. (2011)) have not been included as combined occurrence of drought and storm conditions would trigger closure of the HV sluices to prevent extreme salt intrusion (Lavooij and Berke (2019)). Backward salt intrusion then takes over as the dominant mechanism of intrusion into the HV but is spatially limited (Subsection 3.2.1). Wind forcing (Subsection 3.2.3) is included by imposing spatially uniform wind forcing as measured at HoH (z=10m). Extreme low Rhine river discharge predictions reach as low as 420 m^3/s in Bruggeman et al. (2011). Lavooij and Berke (2019) however, states that the HV sluices are closed for Q_{Lobith}<1000 m^3/s at HW thus forming the lower boundary for discharge. In total, 4 relevant scenarios are aggregated.

Bruggeman et al. (2011) distinguishes 4 scenarios for the Netherlands based on climate-change and socio-economic pressure. In Figure 4.11a, 'Rapid climate change' implies 85 cm SLR alongside a mean temperature increase of 4 °C and 'Moderate climate change' implies 35 cm SLR with 2 °C mean increase of temperature in 2100. Note that low-likelihood but high impact scenarios along the Dutch coast predict 1.1m or even higher SLR by 2100 (Oppenheimer et al. (2019), Church and White (2006)) but this is heavily dependent on the Antarctic Icesheet contribution to SLR which in turn depends on

continued growth of carbon emissions (Haasnoot et al. (2020)). A choice is made here to apply a range of high likelihood (35-85cm) scenarios. The relative position of MSL is further affected by land subsidence mostly due to groundwater extraction which causes oxidization of peat layers in the Netherlands (van Koningsveld et al. (2008), Herrera-García et al. (2021)). Bruggemann et al. (2013) incorporates this effect in their climate assessment. Adopting the same subdivision as in Bruggeman et al. (2011), 4 scenarios for salt intrusion in the HV can be distinguished. North Sea levels and Rhine discharge are decoupled unlike in Bruggeman et al. (2011) to better isolate the buoyancy and mixing terms that are assessed here (Chapter 2). Figure 4.11 visualises this. Salt intrusion is expected to worsen especially due to extremely low discharges, this explains the denomination of the scenarios on the right.

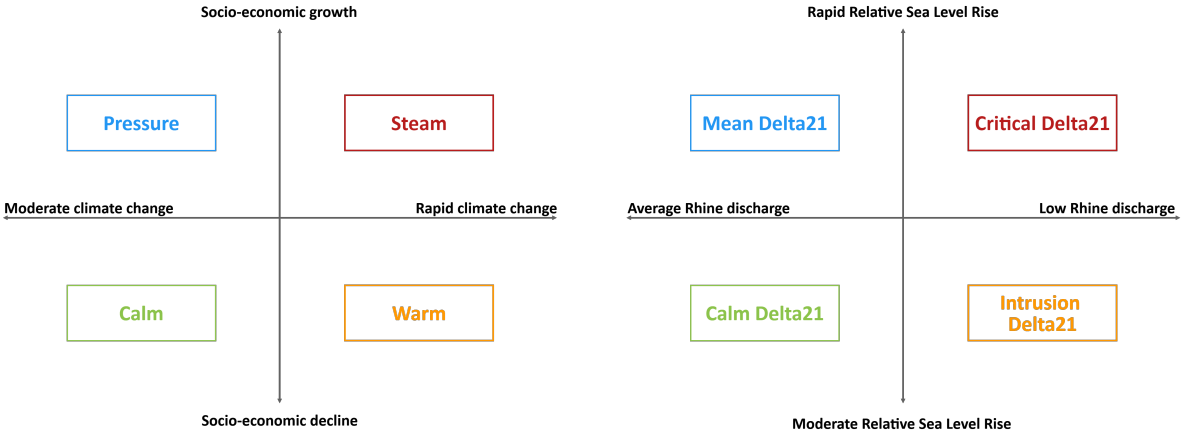

Figure 4.11: (a) Dutch Delta climate scenarios for 2100 adapted from Bruggeman et al. (2011). (b) Same sub-divison applied to study salt intrusion HV-HD using Rhine discharge and SLR as parameters

Now, using Figures 4.10a and 4.10b, the totality of model runs can be listed (Table 4.9). The first three runs have been used to confirm proper workings and reproduction of physics of the OSR-HV model (Chapter 5). Then, the four Delta21 scenarios are prescribed and simulated. Finally the effect of not fully opening the HV sluices is assessed. A brief explanation of the figures in (Table 4.9) is repeated:

- Q_{Lobith}<1000 m^3/s - HV sluices closure threshold (Lavooij and Berke (2019))
- Q_{Lobith} = 2100 m^3/s yearly mean in 2100 CE (ter Maat (2014))
- MSL+0.35m + tide + wind 2100 ('Calm/Pressure', Bruggemann et al. (2013))
- MSL+0.85m + tide + wind 2100 ('Warm/Steam', Bruggemann et al. (2013))

Table 4.9: Summary of model runs used to answer the research questions

Run #	Denomination	Q_{Lobith} [m^3/s]	SLR [cm]	Reference period data
001	Test run	2031	0	09/02/97 - 18/03/97
002	Validation run	1946	0	01/12/19 - 01/01/20
003	Delta21 test run	1946	0	01/01/19 - 01/01/20
004	Delta21 'Calm'	2100	35	19/03/16 - 19/04/16
005	Delta21 'Mean'	2100	85	19/03/16 - 19/04/16
006	Delta21 'Intrusion'	1000	35	17/07/18 - 17/08/18
007	Delta21 'Critical'	1000	85	17/07/18 - 17/08/18
008	20% HV sluice opening	1000	85	17/07/18 - 17/08/18

The Kierbesluit (Figure B.4) has constituted to 15.5 days of opening at $\bar{A}_c$=25 m^2 or put differently: 0.4% opening for 2.7% of time (Data: RWS). Jacobs et al. (2003) performed an in-field analysis of 15% opened HV sluices during 9 tides in 1997 at Q_{Lobith}=2200 m^3/s. Neither of these tests resulted

in extensive up-estuary migration of salinity. A final point of interest within the research scope (SQIII, Section 1.4) therefore is to assess the effect of a non-binary configuration of the HV sluices on salt intrusion given Delta21 Critical conditions (Q_{Lobith}=1000 m^3/s, Figure 4.10). It is theorised that salt intrusion may be suppressed to an exceeding degree by partial closure of the HV sluices while securing ecological restoration as well.

An important aspect to salt intrusion is the turbulent mixing energy budget (Subsection 2.3.4). Salt intrusion will be spatially more limited when the turbulent kinetic energy budget is 'spent' further west in the HV-HD. Jacobs et al. (2003) recognise that the HV sluices can induce flow transitions depending on the water level difference over the dam (Δh) and the degree to which it is opened (a), see Equation 4.4.

The modelling of a hydraulic jump and associated mixing within the HV sluices requires smaller scale non-hydrostatic modelling which has not been performed here. Exploration of reducing the HV sluices A_c remains a point of interest though given the reluctance and inertia to full opening of the HV sluices (Marks et al. (2014)). Therefore, Paalvast et al. (1998) and Equation 4.4 are used to find the threshold of critical flow (Fr=1) at approx. a=2.0m (30%). Furthermore, Jacobs et al. (2003) found that for a constant conveyance area (here: 1800 m^2) depth-limiting all 17 sluice caissons is more effective than width-limiting by full closure of some sluice caissons. Width-limiting has therefore not been further explored here.

$$Fr = \frac{u}{\sqrt{ga}} = \frac{\sqrt{2g\Delta h}}{\sqrt{ga}} \tag{4.4}$$

The last modelled scenario applies a = 1.1m (20%) for HV sluices and 'Delta21 Critical' imposed conditions (Appendix H). A sluice program that imposes 1.1m gate opening for all 17 sluice caissons theoretically corresponds to a supercritical flow regime (Fr>1) for approx. 4 out of 6 hours of flood tide for an ideal, sinusoidal semi-diurnal, tide and average 10 cm wind surge. Figure H.4 visualises a conceptualized tide (lower panel) based on tidal predictions (UTide) for Jul-Aug 2100. Further studies into non-hydrostatic modelling of hydrodynamics within the HV sluices are recommended to represent the increased mixing on HW (Section 8.2).

Spatially uniform wind (U_{10} [m/s]) has been applied to the model domain. Hourly-averaged velocity and direction time-series have been obtained from KNMI open source data at HoH. Historical periods corresponding to Lobith discharges Q=1000, 2100 m^3/s (Table 4.9) correspond to e.g. mid July-August 2018 and mid March-April 2016 respectively. The wind time-series for these periods are enclosed in Appendix H, directional plots are shown in Figure 4.12. Especially westerly winds are known to drive up-estuary intrusion via wind effects such as water level set-up (Subsection 3.2.3), also refer to Figure 4.12c. The choice for Jul-Aug 2016 as source for historical data is further motivated by the fact that it contains a period of forceful wind (U_{10}=13.9-17.1 m/s) with $U_{10,max}$ = 17.0 m/s on August 9th.(ter Maat (2014)).

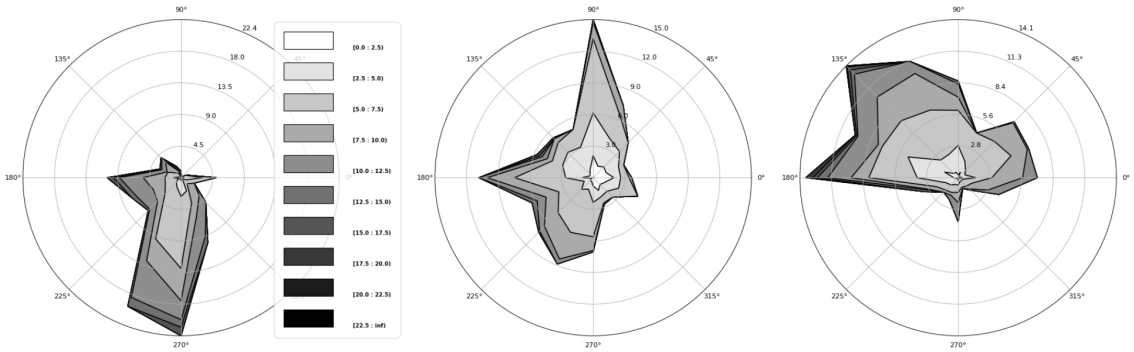

(a) Validation period Dec '19

(b) Delta21 Calm/Mean scenarios based on Mar-Apr 2016

(c) Delta21 Intrusion/Critical scenarios based on Jul-Aug 2018

Figure 4.12: Windroses for three reference periods used in this study based on 10-min. averaged u_{10} [m/s] (HoH data).

4.7 Output

Output of the data validation study (Section 5.2) is described at fixed locations in the HV front delta (HV10) and HV basin (Spui-Middelharnis). Output from validation of the model domain containing Delta21 geometry (Section 5.1) has been done using 12 additional marine observation stations (ns1-ns11, nsrofi) for water levels, velocities and salinity, these are shown in Figure 4.13. Furthermore, anomaly maps are used to show the magnitude of salinity difference due to differences in geometry. The coordinate system for all maps is the Dutch RD (Rijksdriehoeks) system. Orientation of RD_x is west to east and RD_y from south to north.

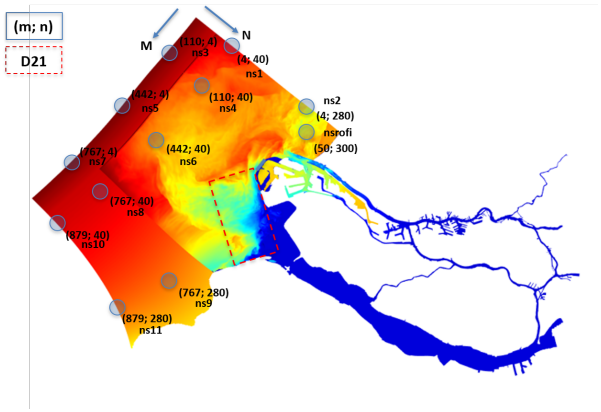

Figure 4.13: Additional observation stations to assess influence of Delta21 on marine boundaries regarding water level, salinity and flow velocity (projected on initial salinity field). Delta21 interventions marked with red dashed line.

Outcomes of the numerical scenarios (Subsection 4.6.2) are first compared for a transect running along the southern HV-HD (Figures 6.2-6.3) to compare magnitudes of salt intrusion across scenarios at LWS/HWS and surface/bottom (Figures 6.4-6.7). Salinity anomaly maps of the entire model domain at HWS for 35 vs. 85cm SLR and 1000 vs. 2100 m^3/s are shown (Figures 6.8-6.11) to isolate and analyze the two main environmental parameters (SLR, Q_f) used in this study. Section 6.3 continues the result analysis by using the transect mentioned above to visualize stratification patterns in HV-HD post-Delta21 (Figures 6.14-6.15). This is in line with recommendations made by Kranenburg (2015) who state that predictive scenarios in OSR-HV are best assessed at the level of macro-intrusion rather than individual stratification profiles. The same figures as mentioned above are produced for the last scenario which explores reduction of the conveyance area of the HV sluices. Chapter 6 finalises with an aggregation of results with more focus on stakeholder assets in the HV-HD.

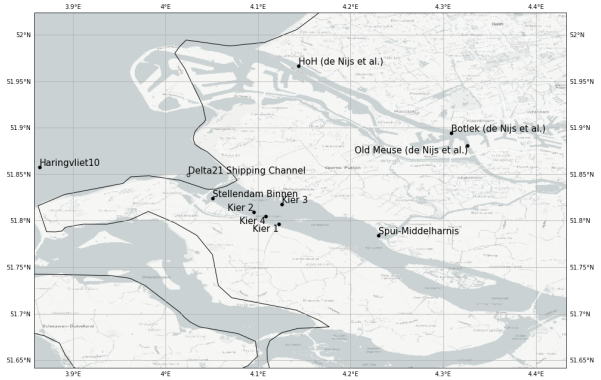

Figure 4.14: Locations within the RMB used in data and geometry validation studies of OSR-HV. Coordinates enclosed in Appendix I.

5

Model validation

OSR-HV has been extensively calibrated and validated in the past for situations without Maasvlakte II (Communications: Deltares). Performance after construction of Maasvlakte II, post-Kierbesluit and post-Delta21 is however uncertain. Therefore, model validation has been done in threefold. First, the effects of Delta21 interventions on North Sea hydrodynamics and salinity transport are assessed by comparing results for water levels, salinity and velocities between the domain including and excluding Delta21 (Section 5.1). This way, it is explored whether the domain is sufficiently large to dissipate distortions by the altered geometry. Results from a larger model domain have been included in Appendix I to show gain in accuracy for the Rhine ROFI. Secondly, salinity reproduction qualities of OSR-HV are assessed by comparing model results to salinity data post-Kierbesluit (Section 5.2). Finally, reproduction of salinity transport in the Rotterdam Waterway is compared to literature (Section 5.3).

5.1 Influence Delta21 geometry

Delta21 proposes major adaptations to the coastal layout of the RMB (Section 1.1). Headlands, such as in Delta21, are known to affect 3D flow structures and the tidal signal (Lieberthal et al. (2019)). At the time of writing (2020), no model studies regarding hydrodynamic and salinity transport response of the RMB to Delta21 had been conducted. Gaining greater insight in requirements for the numerical schematization of a model to describe salinity transport post-Delta21 is therefore deemed necessary. Twelve North Sea observation stations (Figure 4.13) have been used to compare time-series in the marine domain and along boundaries. Maps are assessed at the end of 31 days of simulation, or approx. one spring-neap cycle (Table 3.4).

Salinity is unaffected for stations ns1, ns3-ns9 comparing unaltered and Delta21 geometry. Stations ns10-11 show distortions of the salinity fluctuations. This is attributed to the new orientation of the estuary mouth which is directed to the southwest rather than west (Appendix A) which forces periodic freshwater discharge further south. Significant differences have been observed in salinity between for stations ns2, nsrofi (Appendix I, Figures I.3b-I.3l). These anomalies (max. $\pm$ 5 PSU) in salinity between unaltered and Delta21 geometry are attributed to numerical effects arising from the position of the northern open boundary NS1 (Figure 4.6). Alongshore expansion of the model domain is therefore recommended in Section 8.2.

The salinity values imposed by NS1 are likely to dictate a regime that is more saline than the actual ROFI (Subsection 3.2.4) due to underestimation of coastal surface water dilution. Therefore, a spatially

larger model of the Dutch coast (DCSM-FM, Delft3D) was run to establish the recommended position of marine open boundaries to further investigate effects of Delta21 on hydrodynamics and salinity transport. Reproduction of water levels and salinity using DCSM-FM can be found in Appendix I. In OSR-HV, the northern open boundary is situated at a minimum of 6 km from the RWW mouth. Results show that the Rhine ROFI significantly influences surface salinity to about 30-40 km in alongshore direction, diluting North Sea water (33 PSU) to 26-28 PSU. Beyond this area, surface salinity motion is more harmonic and can therefore be better prescribed by an open boundary. Results from DCSM-FM show that Rhine ROFI surface salinity is consistently estimated to be higher (0-2 PSU) with Delta21 geometry than without it. This is evidence for a geometry-induced redistribution of surface salinity. Higher surface salinity in the ROFI is indicative of less dilution or larger geographical spreading of freshwater, of which the latter is the more logical conclusion. The Delta21 energy storage lake (Section 1.2) is thought to cause this effect given that it is the largest seaward feature of Delta21.

Figures 5.1 and 5.2 show the bottom and surface salinity anomaly between a situation containing Delta21 geometry. Reference case is the same set of validation conditions described in Section 5.2. The images show that anomalies are relatively small on the fully marine domain and boundaries further from shore. The dark jet-like anomaly (+5-6 PSU) running through the Delta21 geometry is attributed to the locally deeper shipping lane which promotes the downward transport and horizontal advection of salinity. The shipping channel furthermore limits the influence of lateral mixing. This, in turn, causes bottom salinity to be much larger just east of the HV sluices for the same (Kierbesluit) sluicing program. Zero-anomaly is found in the east of HV-HD likely due to limited intrusion length.

The forcing applied in Figures 5.1 and 5.2 is described in Appendix H. As expected, anomalies are higher along the southern bank of the HV-HD due to preferential intrusion (Subsection 3.2.1). The Delta21 geometry seems to capture a significant volume of fresher water upon outflow from the HV (x=435.000, y=60.000) Finally, the ROFI originating from the Rotterdam Waterway seems to be reproduced poorly (x=55-65.000, y=450.000). Negative anomalies dominate the surface (i.e. fresher) whereas positive anomalies (i.e. saltier) are found at the bottom indicating sharper stratification for bathymetry including Delta21. Overall, surface salinity anomalies are greater than bottom salinity anomalies. This is possibly due to the larger relative impact of Delta21 on the flow field near the surface.

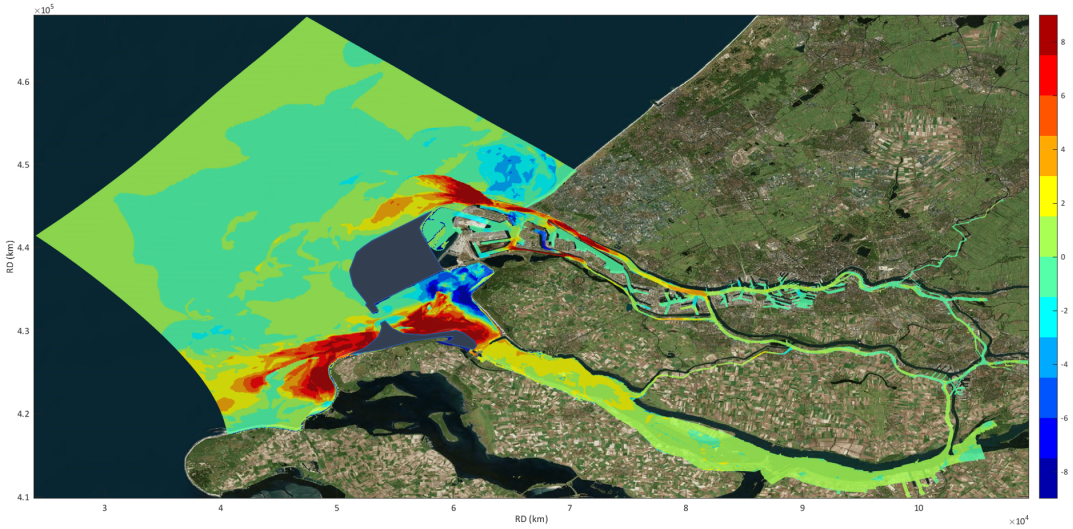

Figure 5.1: Surface salinity (k=1) anomaly map of scenarios unaltered vs. Delta21 geometry at HWS

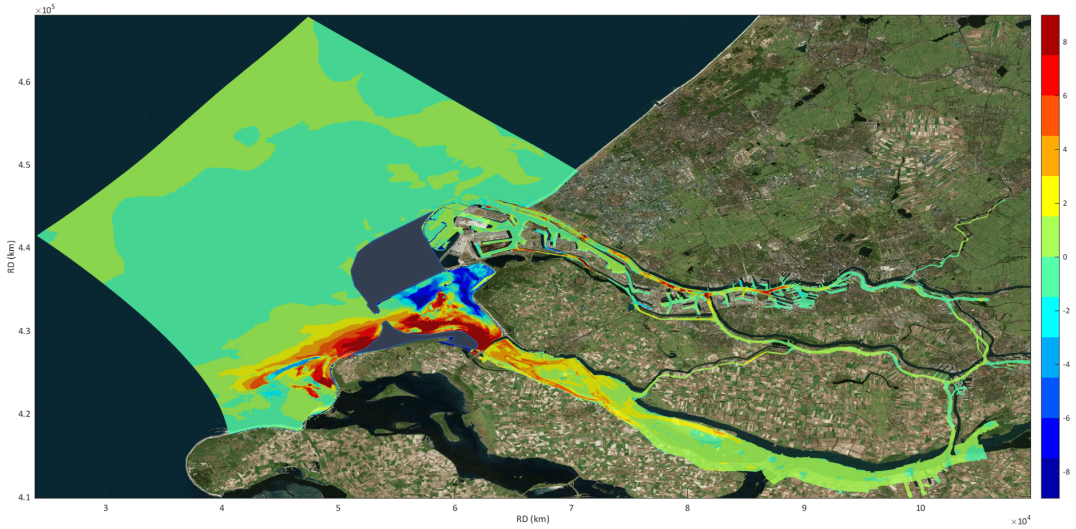

Figure 5.2: Bottom salinity (k=10) anomaly map of scenarios unaltered vs. Delta21 geometry at HWS

A remarkable feature of both Figures Figure 5.1 and Figure 5.2 is the apparent capture of fresher water south of Maasvlakte II. The volume of captured freshwater is attributed to the onset of rotational flow in the HV front delta (Section 6.2) which separates (saline) inflow at flood from fresher outflow at ebb. This effect is aggravated by the presence of a shipping channel in Delta21 which physically separates more saline water from freshwater outflow from the HV. Figure 5.3 visualizes the vertical salinity profiles at 4 tidal stages at the marked location in Figure 4.14. This location has shown to be up to 5-6 PSU more saline due to the presence of Delta21 (Figures 5.1 and 5.2). The presence of higher salinity near the Delta21 shipping channel can be seen in every tidal phase though is most apparent at flood tide.

It can be seen in Figure 5.3 that the water column at 'Delta21 Shipping Channel' (Figure 4.14) achieves full mixing over a tidal cycle, likely due to limited depth. Turbulent kinetic energy (mixing) shows to be relatively high here, see Appendix J. Sharp stratification develops at ebb tide especially for Delta21 geometry albeit with a halocline higher up in the water column. For the unaltered geometry, the increase of bottom salinity from HWS to LW stands out. This is indicative of a residual near-bed flood current during ebb. Results show a 0.05 m/s landward current at k=8 which diminishes towards the bed whereas the k=1 to k=7 are dominated by ebb velocities of O(-0.1) m/s. This internal flow structure is not seen in Delta21 geometry, this is attributed to the availability of more turbulent kinetic energy due to flow expansion (i.e. deceleration) near the new estuary entrance (Appendix A) which allows for more vertical mixing on flood tide. Baroclinic flows are consequently lower in magnitude due to locally weaker stratification.

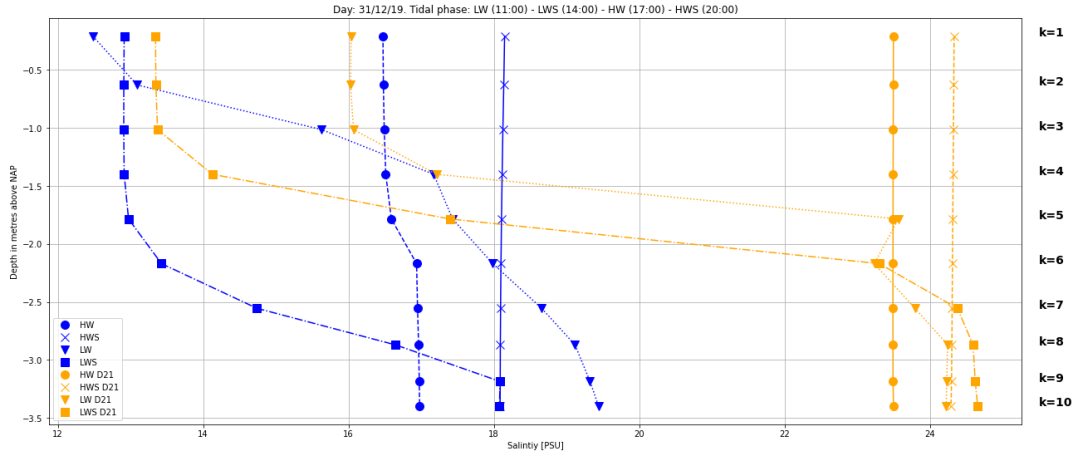

Figure 5.3: Salinity [PSU] vs. depth at the interface of in- and outflow in the HV front delta for unaltered vs. Delta21 geometry cases, location marked in Figure 4.14 as 'Delta21 Shipping Channel'

Conclusion: Anomalies in salinity reproduction can for some instances be explained by differences in hydrodynamics induced by Delta21 geometry though correct reproduction at [40.000; 420.000] and [55-65.000; 450.000] is unlikely due to the proximity of open boundaries to two ROFI. Leading to the conclusion that mappings of salinity resulting from predictive runs (Appendix H) are best treated relative to one another rather than as absolute results. The focus is therefore on macro-scale patterns of salinity intrusion as stated in the objective (Section 1.4).

5.2 Salinity data

Performance of OSR-NSC nested in a larger domain containing the HV-HD has been documented in Kranenburg and Schueder (2015), Kranenburg (2015). It is recognised here that descriptions of salinity in the southern half of the domain (e.g. Bernisse) are consistently overestimated mainly due to excessive transports through the HV sluices. Moreover, the model underestimates the degree of stratification in the lower half of the water column. Users of the model are thus warned for the reliability of effect studies like conducted here. Kranenburg and Schueder (2015) however, conducted their study before initiation of the Kierbesluit and for different discharge regimes which has a marked effect on the salinity distribution in western HV. Therefore, an additional validation has been executed here.

The Kierbesluit came in effect in January 2019 (Communications: RWS) and the first tests using relatively large and persistent HV sluice openings ran from October 2019 - February 2020 (Communications: RWS). These tests resulted in slight salinity intrusion east of the HV sluices (Figure 5.6). No tests during e.g. the dry summer of 2018 ((Huismans (2018), Mens (2018)) were conducted. This is in line with the strategy of Implementing Deductively (Dutch: Lerend Implementeren). This strategy is used to test the salinity response of the HV basin at high Q_{Lobith} (>2000 m^3/s) and to gradually extend tests to periods of more unfavourable meteo-hydraulic conditions. The HV sluices were set ajar most persistently between 01/12/2019 - 10/12/2019 (Data: RWS). Therefore, a validation study of HV salinity intrusion is based on this period. Opening of HV sluices in this period mainly affected salinity in the western part of the HV. The nature of salinity transport is expected to deviate most explicitly from the full-closure situation (Subsection 3.2.1) in the HV front delta and near the Spui. The former due to the introduction of the HV sluices as regulator of salinity, the latter through the weakening of backward salinity intrusion through Spui (Subsection 3.2.1) due to a diminished water level gradient between the HV and HoH. Therefore, validation of OSR-HV has been done through assessment of salinity reproductive qualities in the HV front delta and Spui southern entrance (Figure 4.14). Numerical simulations commenced 25/11/19 to allow for spin-up of the state variables (Table 4.2).

Looking at Figure 5.4, it is apparent that salinity is consistently underestimated between approx. 1/12/19 - 3/12/19. These are likely to be lingering effects from initial conditions imposed in the HV-HD (Figure 4.4). The vertical line separates simulation periods before and after (satisfactory) salinity spin-up. Water levels and flow were found to be spun-up in 2-3 simulation days, salinity in 6-7 days. The dotted lines in Figures 5.4 and 5.5 show the calculated absolute numerical error in PSU. The error at the surface is estimated at $\approx$1.2/30=4%. At the bottom $\approx$2.5/31=8%. Some of the numerical results cannot be directly attributed to physical behaviour (e.g. numerical dip 6/12/20) and may be due to simplified representation of baroclinic terms (Subsection 4.6.1). The overshoot of salinity (Figure 5.4, 8/12/2020) coincides with near-closure of the HV sluices (observed in data Figure 5.6) and vertical mixing is overestimated, causing transport of bottom salinity to the surface. Numerical output in the front delta shows to be generally less saline throughout the vertical though. Conversely, in the area east of the HV sluices, higher values of salinity are found throughout the water column. These two facts indicate an exaggerated response to forcing from the HV sluices in both seaward and landward direction. Consequently, vertically averaged salinity is lower at seaside and vice versa. This has been observed by Kranenburg and Schueder (2015) too. Mixing is especially too intense near the bottom resulting in an underestimation of stratification which also becomes apparent when comparing Figures 5.4 and 5.5.

Figure 5.5 shows the bottom salinity for the same offshore location. Data shows to be consistently

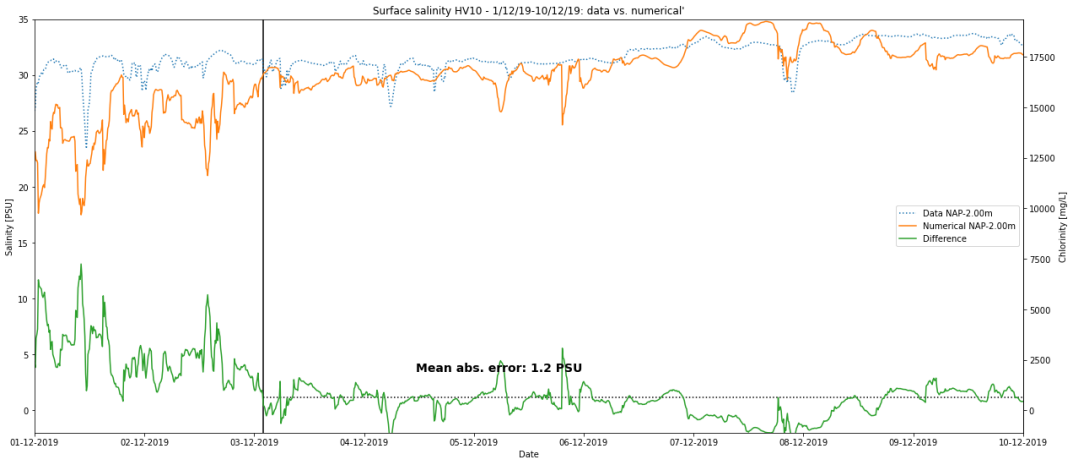

Figure 5.4: Surface salinity (k=1) HV front delta (10 km seawards). Numerical vs. RWS data at HV front delta (Figure 4.14). Differences plotted and absolute error of 1.2 PSU calculated from approx. 3/12/19 onwards.

more saline (31-32 PSU vs. 28-29 PSU). This underestimation of stratification has been observed by Kranenburg and Schueder (2015) too. Errors during spin-up (lower left of Figure 5.5) are lower than at the surface due to smaller differences in salinity forcing further away from the HV. The mean absolute error is higher than for surface salinity though (2.5 vs. 1.2 PSU). The data shows that, at this location, the water column is well-mixed which is line with the expectation for the North Sea during winter months (Subsection 2.3.4).

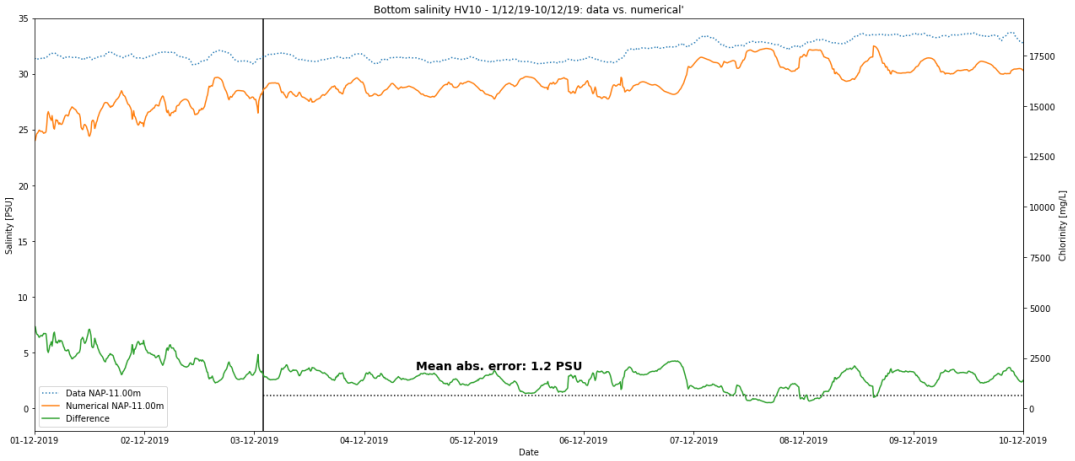

Figure 5.5: Bottom salinity (k=10) HV front delta (10km seawards). Numerical vs. RWS data at HV front delta (Figure 4.14). Differences plotted and absolute error of 2.5 PSU calculated from approx. 3/12/19 onwards.

The previous results suggest that salinity east of the HV sluices is likely to be overestimated and stratification underestimated. This is in agreement with Kranenburg and Schueder (2015) and Kranenburg (2015). Figure 5.6 shows the measured salinity/chlorinity for 1/12/19-10/12-19. It can be observed that salinity peaks twice per day at flood, thereby following the tidal signal. A distinct bias can be seen in the bottom concentrations where numerical simulations fall back to approx. 0.6 PSU vs. 0.25 PSU for the actual data. This is attributed to the vertical position of the chlorinity measurements (NAP-11.00m) which may not perfectly coincide with σ=10 (Appendix F). Moreover, the relation between Rhine discharge and background salinity (Subsection 3.2.1) may be misrepresented. The modelled HV sluices responds faster and stronger relative to the actual physical response as can be seen by the broader and higher numerical peaks, this has been found by Kranenburg (2015) too. The decrease in salinity upon reversal of the tidal signal is modelled more truthfully. The second data peak at 3/12/20 in Figure 5.5 has not been reproduced. The source of this inaccuracy has not been determined but is likely

due to local salinity forcing by e.g. wind, baroclinic effects or local scour excluded from the numerical representation. The last two numerical peaks in Figure 5.5 especially show that downward salinity transport is likely exaggerated by OSR-HV. A selection of individual vertical profiles (data vs. numerical) have been included in Appendix I. These profiles describe locations situated between those of Figures 5.4-5.7 and can be found in Figure 4.14.

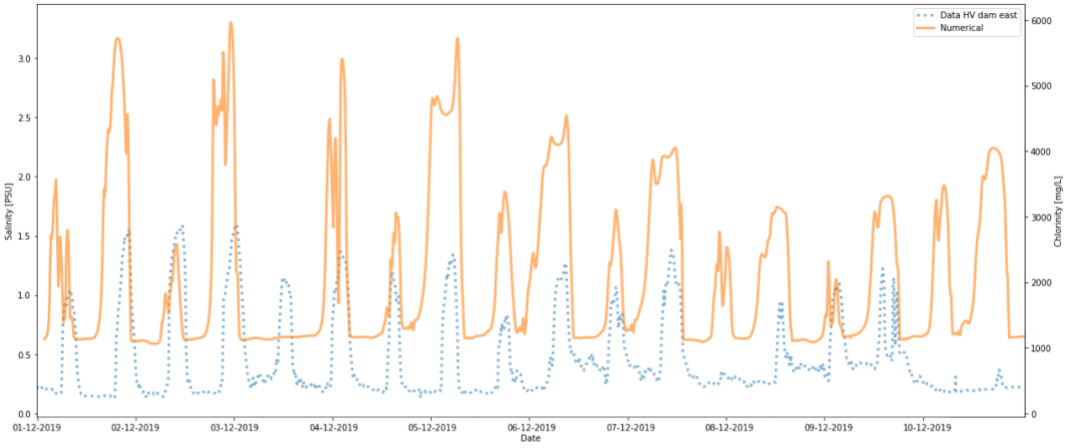

Figure 5.6: Bottom salinity (k=10) HV. Numerical (dotted) vs. RWS data at Spui-Middelharnis (Figure 4.14). Period: 1/12/20-11/12/20 during which the HV sluices were opened at flood. Note semi-diurnal salinity response and exaggerated numerical reproduction. Mean abs. error approx. 1.0 PSU. Approx. +0.35 PSU bias by conservative estimate of background concentration.

Surface salinity reproduction near the Spui southern entrance is visualized in Figure 5.7. It can be seen that the imposed background concentration of 0.30 g/L Cl^- persists for some time in the model. Exaggerated vertical mixing does not protrude into the upper water column, this is in line with the findings of Kranenburg (2015). Dilution appears to come to a halt on December 6th after which a bias of +0.25 PSU remains, comparable to the bias in Figure 5.6. Based on these results it can be argued that a background concentration of 0.05-0.10 g/L Cl^- would suffice for the Spui. Changes in conditions such as landward wind (Figure 4.12) or below-average river discharge can however quickly raise salinity concentrations in the lower RMB reaches (Subsection 3.2.1). A background concentration of 0.30 g/L Cl^- is therefore deemed a conservative estimate for predictive scenarios.

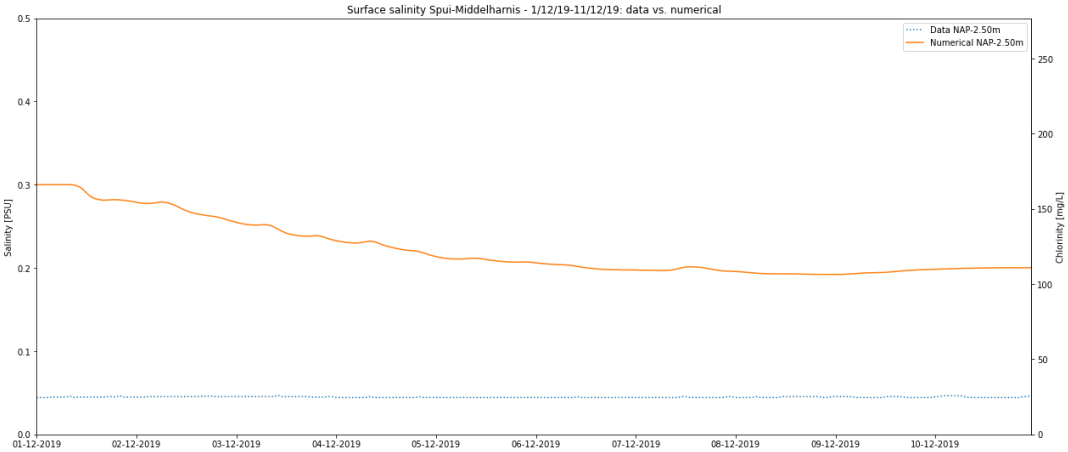

Figure 5.7: Surface salinity (k=1) HV. Numerical (dotted) vs. RWS data at Spui-Middelharnis (Figure 4.14). Period: 1/12/20-11/12/20 during which the HV sluices were opened at flood (data: RWS). Note that the initial background concentration for numerical runs was set to 0.30 PSU irrespective of depth which causes for slight overestimation at the surface. Data shows no influence of salinity at this part of the domain.

Conclusion: salinity spin-up is extensive (approx. 25/11-3/12) despite alignment of boundary and initial conditions (HW). Results thereafter show mean absolute errors of 1.2-2.5 PSU with consistently underestimated bottom salinity at sea and vice versa. This is indicative of exaggerated vertical mixing. Turbulent kinetic energy profiles confirm this (Appendix J). The tidal signal is markedly reproduced at relatively low salinity (O(1.0) PSU). A river background concentration of 0.30 PSU is conservative for the current (2020) RMB as many surface locations within HV-HD show lower measured salinity than modelled numerically (Q_{Lobith}=1986 m^3/s). Future scenarios involve lower Q_f and/or higher turbulent forcing. These altered boundary conditions (Subsection 4.6.1) are assumed to dominate salinity at locations tested here instead of the background salinity concentration.

5.3 Rotterdam Waterways

The intertwined nature of the RMB (Figure 1.3) requires sufficiently accurate reproduction of hydrodynamics and salinity transport in the RWW to avoid non-physical behaviour at internal boundaries such as Spui and Dordtse Kil. Hydrodynamics and salinity transport in the RWW (Figure 1.3) are well-studied subjects (e.g. Pietrzak et al. (1991), de Nijs et al. (2011), Kranenburg (2015)). The comparison made here is based on findings by de Nijs et al. (2011), SPM is excluded from this comparison. The locations indicated as HoH, Botlek harbour and Old Meuse are included in Figure 4.14. Salinity field observations were obtained in de Nijs et al. (2011) (both Eulerian and Lagrangean). Period of simulation was 27/02/2006-11/04/2006 using Delft3D software. The same k-ε model for turbulence closure (Appendix E) has been applied by de Nijs et al. (2011).

Table 5.1: Comparison main salinity transport characteristics in RWW by de Nijs et al. (2011) used to assess performance of OSR-HV here

Physical process	Field observations de Nijs et al.	Simulated de Nijs et al.
Stratification		
Intrusion type	Stable salt wedge	Instable salt wedge
Pycnocline position	Lower half water column	Extended into upper part water column
Intrusion length (ebb)	2 km up-estuary from HoH	5 km up-estuary from HoH
Intrusion length (flood)	Old Meuse, 17 km up-estuary from HoH	Eem-Waalhaven (RD_x = 89 km)
Bifurcation	New-Old Meuse at 2nd half of flood	New-Old Meuse at 2nd half of flood
Tides		
Asymmetry	Longer ebb tide	Longer ebb tide
Low Water Slack (LWS)	Baroclinic up-estuary exchange flow	Near-bed flood current at ebb (HoH)
High Water Slack (HWS)	Baroclinic up-estuary exchange flow	Near-bed flood current at ebb (Botlek)
Advection		
Forcing	Barotropic, baroclinic	Barotropic, baroclinic
Residual flow	Along-channel baroclinic residual flow	Present but less pronounced
Flow maximum	From bed to pycnocline during flood	From bed to pycnocline during flood
Mixing		
Turbulence	Suppressed by pycnocline at flood	Less distinct suppression

Figure 5.8 shows the maximum extent of bottom salinity intrusion which is found at HWS (31/12/19-20:00). In OSR-HV the periodical movement of salinity in and out the RWW is observed too, higher surface salinity indicates underestimation of stratification. Maximum intrusion length is slightly further than in de Nijs et al. (2011), though note that different boundary conditions are applied. Retreat of the salt wedge under the imposed conditions occurs to approx. RD_x=75 km, much closer to the Old-New Meuse bifurcation. This explains why bifurcation of the salt wedge occurs somewhat earlier (at the end of the 1st half of flood) in this model study. Ebb tides (HoH) are found to be distinctly longer due to smaller ebb velocities as well. In OSR-HV, O(0.01) m/s near-bed flood currents are found to be present around HWS as far as Eem harbour (x=88km, Figure 5.8). Baroclinic flows are largely absent during the tidal period though, which is not supported by field observations (Table 5.1). The overall current pattern shows that bed turbulence suppression by stratification occurs in OSR-HV as well but to a lesser degree due to less sharp stratification.

The main difference between findings of de Nijs et al. (2011) and validation in this study, being the bandwidth of minimum and maximum intrusion length, is attributed to lower imposed freshwater discharge at the upstream boundaries ($Q_{up} \approx$ 800 vs. 1000 m^3/s). The underestimation of up-estuary intrusion near HWS is in part resolved by spatially increasing horizontal diffusion coefficients in up-estuary direction (Appendix F) as recommended by Kranenburg (2015). Post-delivery of salinity by baroclinic exchange from the old port branches (x=78-90km) is observed on ebb tide.

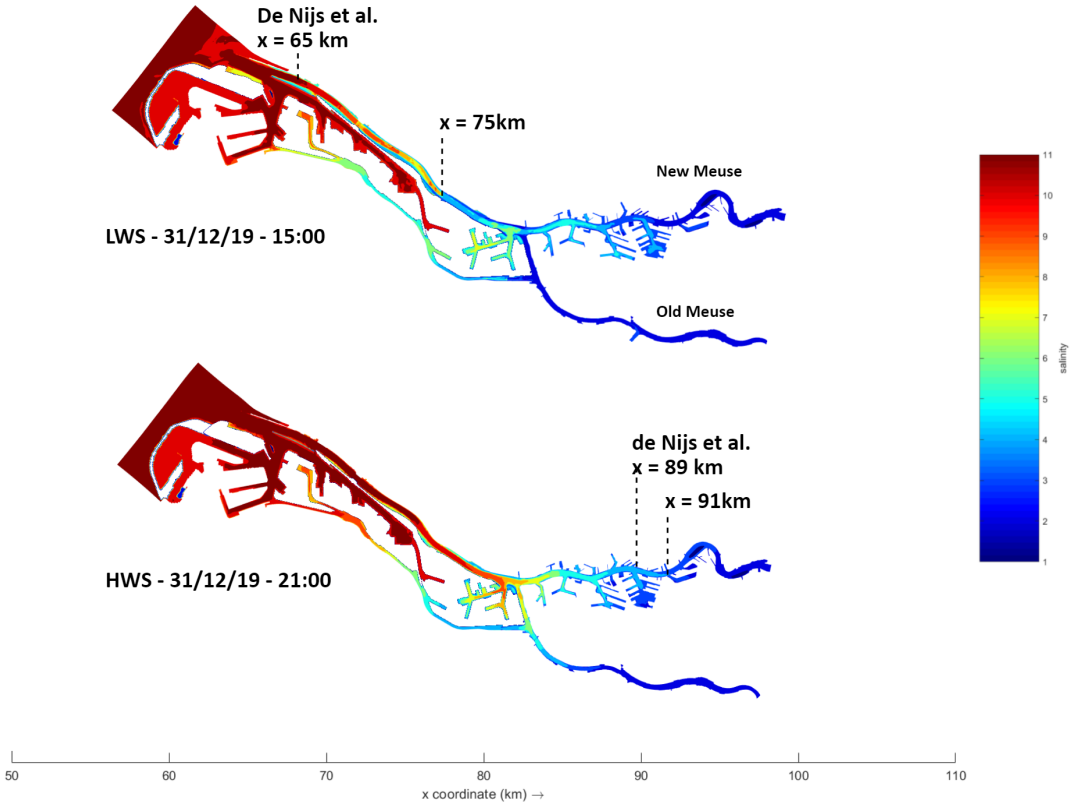

Figure 5.8: Bottom salinity (k=10) in PSU at LWS (top) and HWS (bottom) for after T=31d at $\bar{Q}_{Lobith} = 1986\ m^3/s$ zoomed in on RWW. Results from de Nijs et al. (2011) indicated alongside numerical results from the validation study performed here. Retreat in OSR-HV is likely underestimated by presence of too much salinity in the system. Note that de Nijs et al. (2011) modelled at higher upstream Q which in part explains shift in intrusion bandwidth.

Reproduction of RWW salinity transport is found to be satisfactory though vertical mixing may be overestimated causing the salinity intrusion bandwidth to be underestimated. Landward baroclinic flow countering ebb flow is present but likely modelled to be weaker than in practice ($O(10^{-2})$ vs. $O(10^{-1})$ m/s) due to underestimation of stratification. Finally, de Nijs et al. (2011) recognises two weaknesses in their model causing artificial vertical velocity and diffusion near steep geometries such as port basins (see ADI problem, Appendix F) and the hydrostatic assumption (Appendix E). The ADI scheme and hydrostatic assumption are applied in OSR-HV too and are likely to be of similar influence on model results. Finally, internal wave phenomena are known to play a significant role in the transport of mass and momentum and generation of turbulent kinetic energy (and thereby mixing) in stratified estuaries (Pietrzak and Labeur (2004)). Internal wave phenomena are not resolved in hydrostatic numerical approximations such as used here (Appendix E) and deserve further investigation (Section 8.2).

6

Results

First, modelled scenarios are repeated for clarity (Figure 6.1). Then, numerical results for salinity are assessed along a longitudinal transect of the HV-HD (Section 6.1). Timeseries have been generated at 10-minute intervals for the entire simulation period. Map output (Section 6.2) has been generated for each 48 hrs in the first 30 days and hourly for the last day of simulation. This way, formation of a dynamic salinity equilibrium may be tracked (Section 1.4) as well as salinity dynamics over the last tidal cycles. Stratification is treated in Section 6.3 using along-estuary transects. Finally, effects of height-limiting HV sluices (20%) on salinity are assessed in Section 6.4. More numerical results may be found in Appendix J. Numerical results have been used to draw up an expectation of the post-Delta21 HV-HD estuary regarding its current functionalities (Subsections 3.1.2-3.1.4) in Section 6.5.

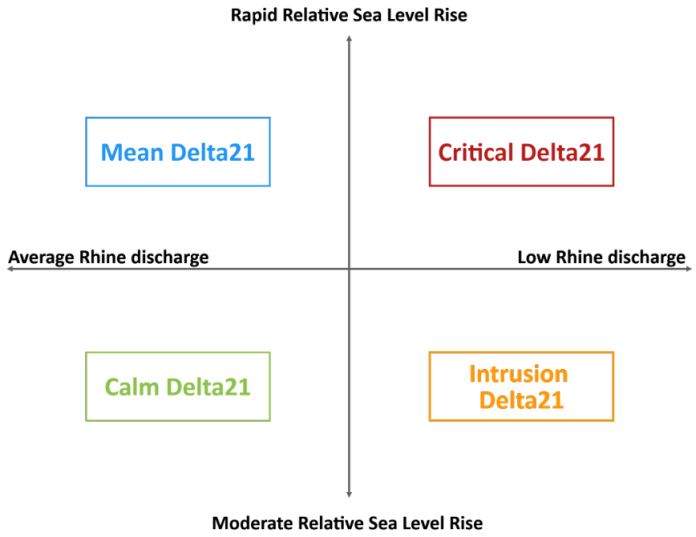

Figure 6.1: Modelled scenarios. Moderate-Rapid SLR: 35-85 cm. Low-Average Rhine discharge: 1000-2100 m^3/s. Scenarios based on ter Maat (2014). Image repeated from Section 4.3

6.1 Scenario comparison

Salinity has been plotted from the HV sluices to the up-estuary open river boundary at Moerdijk bridge for scenarios 001 (Delta21 geometry) and 002-006 at both LWS and HWS which represent the points in time of minimum and maximum intrusion. Surface and bottom salinity have been plotted as well, yielding a total of four figures with 5 transects (validation+4 scenarios) each. The maximum length of intrusion is defined as the point where salinity remains permanently below 1 PSU. The longitudinal position where salinity falls below this threshold has been demarcated in each of the figures using 'Δx=..km'.

Transects in Figures 6.4-6.7 are chosen along a gridline near the southern bank of HV-HD (Figure 6.2). This deserves further explanation as it has not been treated in the theory of Chapter 2. Earthly rotation is known to affect flow on oceanic scales through the Coriolis (pseudo-)force (Pietrzak and Katsman (2019)), but can be of importance at estuary mouths too (see e.g. de Boer (2009)). The length scale at which Coriolis can affect hydrodynamics is known as the Rossby radius of deformation (R_D). It is defined as the ratio of the deep water phase speed ($c = \sqrt{gH}$) and Coriolis parameter (Equation 6.1), i.e. it denotes the relative magnitudes of flow and Earthly rotation (Equation 6.2). For stratified flows however, internal phase speeds at density interfaces can be defined through the principle of reduced gravity (Equation 2.4), a measure for the relative difference in density between two layers expressed as a reduction in gravitational acceleration. This results in an *internal* Rossby radius of deformation (Equation 6.3).

Some typical numbers have been applied to Equations 6.2-6.3 to show that onset of rotational flow is likely to play a role for stratified flows in the HV front delta. Incoming (flood) flow is therefore deflected to the right (Northern Hemisphere) causing salinity to be, initially, transported predominantly on the southern bank. This is supported by results (e.g. Figure 6.10) and literature on pre-closure tidal movement (Ferguson (1971), Paalvast et al. (1998)).

$$f = 2\Omega \sin \phi \tag{6.1}$$

$$R_D \equiv \frac{(gH)^{1/2}}{f} = \frac{\sqrt{10 \cdot 20}}{10^{-4}} \approx 142\ km \tag{6.2}$$

$$R_I \equiv \frac{(g'H)^{1/2}}{f} = \frac{(gH(\frac{\rho_1 - \rho_2}{\rho_0}))^{1/2}}{f} = \frac{\sqrt{10 \cdot 10 \cdot \frac{1030-1000}{1000}}}{10^{-4}} = 10 - 20\ km \tag{6.3}$$

Figure 6.4 shows that surface salinity just east of the HV sluices (x=63-66km) is dictated by the ebbing discharge preceding LWS as Q=1000 m^3/s scenarios (red, yellow) show up to 15 PSU higher salinity locally. SLR shows a distinct influence here (x=63-66km) as well judging the red vs. yellow and blue vs. green lines. From x=66-71km salinity shows weak dependence on marine forcing giving the alignment of red/yellow and blue/green lines. This is attributed to the choice of marine boundary conditions (Subsection 4.6.1) rather than to a physical phenomenon. Remarkably, SLR of 85 cm (red, blue lines) shows a lasting spike of salinity across the Spui southern entrance, which is directed to the west (see Figure 6.2). This is indicative of additional salinity feed from the Spui through the Old Meuse.

Steep spikes in salinity near x=82km and x=86km are observed in each of Figures 6.4 -6.7. Location x=82km is found to be a relatively deep zone (NAP-10.00m) following a permanently emerged transect (NAP+1.40m) on the foreshore of Tiengemeten (island, Figure 6.2) at x=79-81.5km. This deeper zone functions as a salinity trap which explains a sudden spike here. Location x=86km is situated at the raised HV bridge sill (Section 4.5) causing an abrupt change in bathymetry from NAP-8.00m to NAP-3.00m and back to NAP-8.00m over the course of approx. 300m. This results in the spikiness seen in Figures 6.4 -6.7 at x=86km. Salinity preceding the HV bridge sill may furthermore exhibit erratic trends given the presence of Ventjagersplaat (Figure 6.2) which is a tidal flat (van Veen (1929)) that became partly submerged/emerged due to execution of Delta works (Subsection 3.1.1).

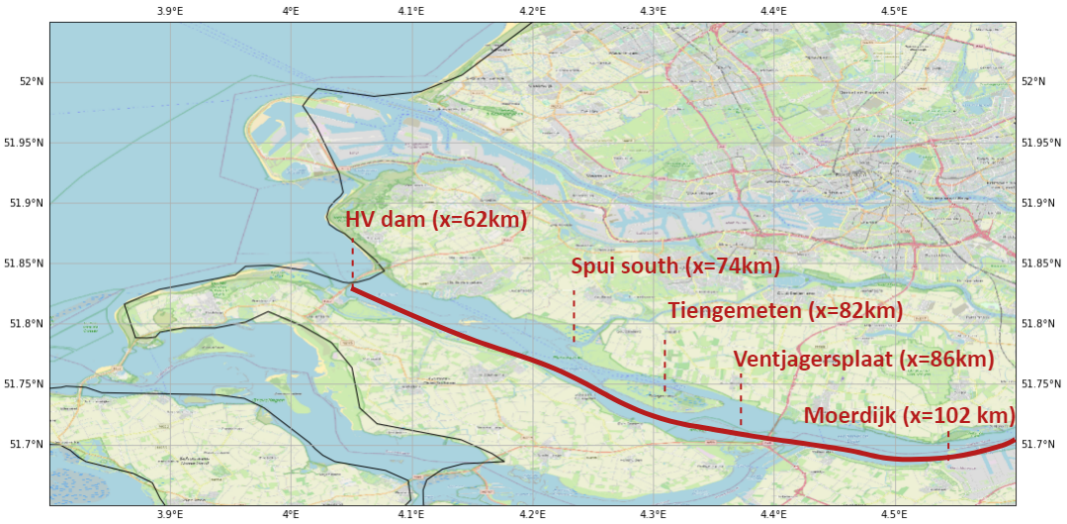

Figure 6.2: Area map showing longtidunal transect used to generate Figures 6.4-6.7

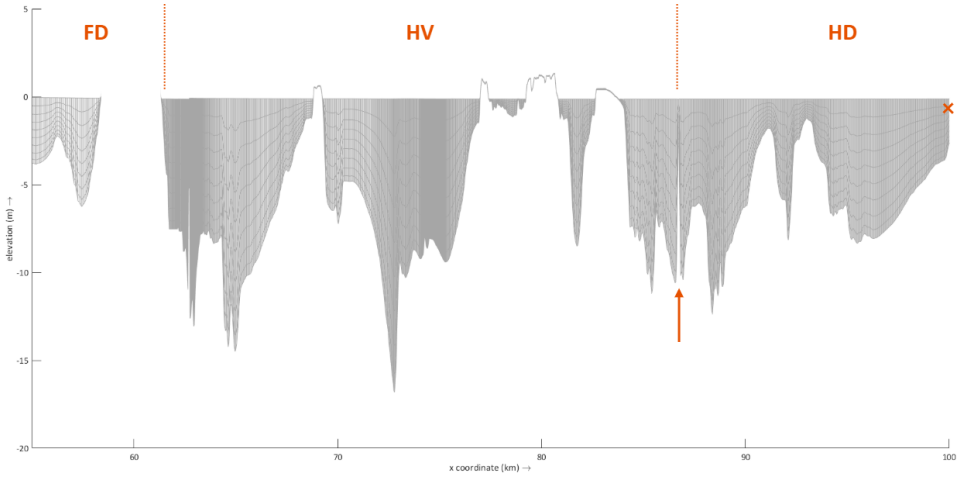

Figure 6.3: 2D hydrodynamic grid of transect shown in Figure 6.2.Arrow (↑): raised HV bridge sill (NAP-3.00m). Cross (x): new surface water intake Strijensas opposite Moerdijk ports. FD: Front delta, HV: Haringvliet, HD: Hollands Diep.

Figure 6.5 shows how surface salinity changes during an entire flood cycle compared to Figure 6.4. Most notable is that the 'base' intrusion is more extensive judging the point of maximum intrusion of the most optimistic scenario (green line). Salinity at the estuary mouth is higher for all scenarios but diminishes more steeply. The influence of Spui on salinity is less distinct than at LWS (Figure 6.4) due to the landward directed flood velocities preceding HWS. Surface salinity east of Spui differ little compared to LWS as ebb flow mainly takes places along the northern HV bank whereas the transect in this figure is taken from the southern (flood) bank. The same spikes at x=82km and x=86km are observed. Surface salinity increase at the HV mouth during a tidal cycle is limited for low discharge scenarios comparing red/orange lines in Figures 6.4-6.5. This is attributed to a combination of poor washout of salinity on ebb tide at Q=1000 m^3/s and the layout of HV sluice caissons (Figure B.2) which stimulate well-mixed conditions in the first kilometer east of the HV sluices at flood. This is affirmed by presence of high turbulent kinetic (Figure J.1b) energy across the entire water column at flood. Conversely, at ebb, mixing is high in the front delta (Figure J.1a).

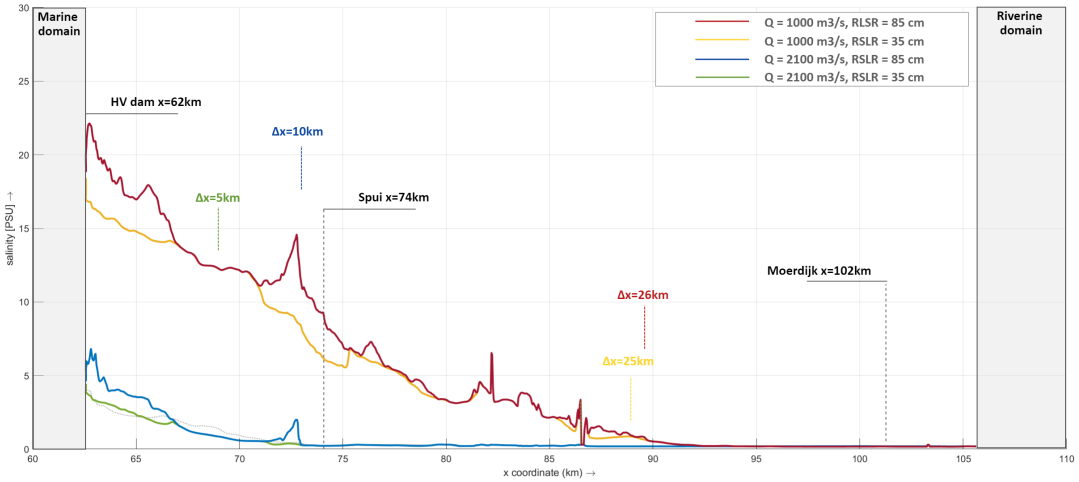

Figure 6.4: Longitudinal surface (k=1) salinity profiles HV for scenario runs: Delta21 geometry (grey dotted), Delta21 Calm (green), Delta21 Mean (blue), Delta21 Intrusion (orange) and Delta21 Critical (red) at LWS

Salinity appears to not fully retreat out of the HV-HD basin at LWS judging Figure 6.4. This is attributed to the relatively deep bathymetry of the western HV (NAP-10.00 to NAP-20.00m) compared to the sill of the HV sluices (NAP-5.50m). This height difference is less pronounced comparing the front delta and the sill of the HV sluice. A remarkable feature is the feedback of salinity from Spui (x=74km) in all scenarios, which is expressed as a peak slightly to the west (x=72-73 km). Bottom salinity intrusion (in km) at Q=1000 m^3/s is twice that at Q=2100 m^3/s and several kilometres farther when increasing RLSR.

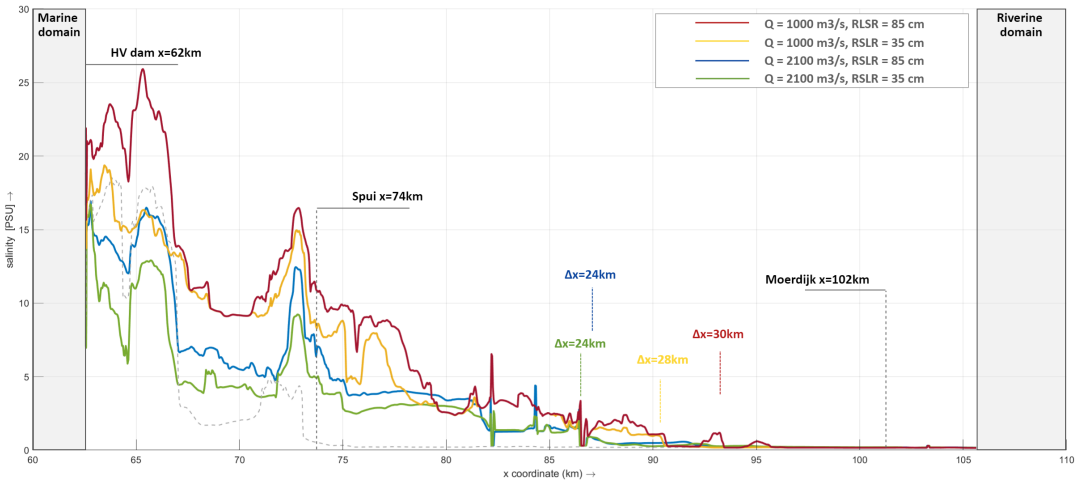

Figure 6.6: Longitudinal bottom (k=10) salinity profiles HV for scenario runs: Delta21 geometry (grey dotted), Delta21 Calm (green), Delta21 Mean (blue), Delta21 Intrusion (orange) and Delta21 Critical (red) at LWS

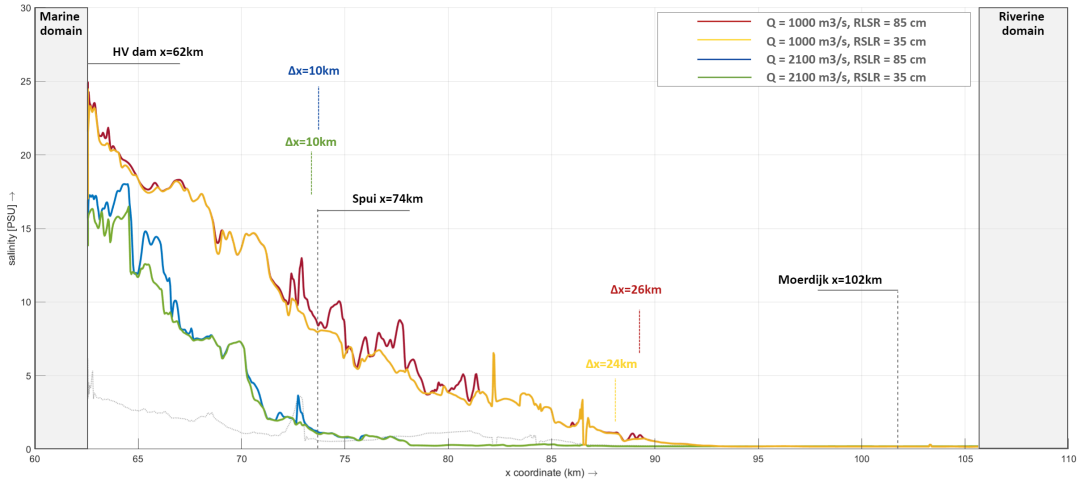

Figure 6.5: Longitudinal surface (k=1) salinity profiles HV for scenario runs: Delta21 geometry (grey dotted), Delta21 Calm (green), Delta21 Mean (blue), Delta21 Intrusion (orange) and Delta21 Critical (red) at HWS

Downward salinity trends are approx. -1 PSU/km (red, yellow) and -1.25 PSU/km (blue, green) until the point of maximum intrusion which is a steeper decline than pre-closure which amounted to -0.4 PSU/km (15 to 3 g/L Cl^-, see Figure 3.5). Bottom salinity for Q=2100 m^3/s (green, blue) can be lower at HWS than at LWS west of Spui. This is attributed to the relatively high southward discharge through Spui and the feedback of salinity into the western HV associated with it. Salinity feedback from the Spui is lower (red) or absent (yellow) as Spui discharge diminishes in periods of drought.

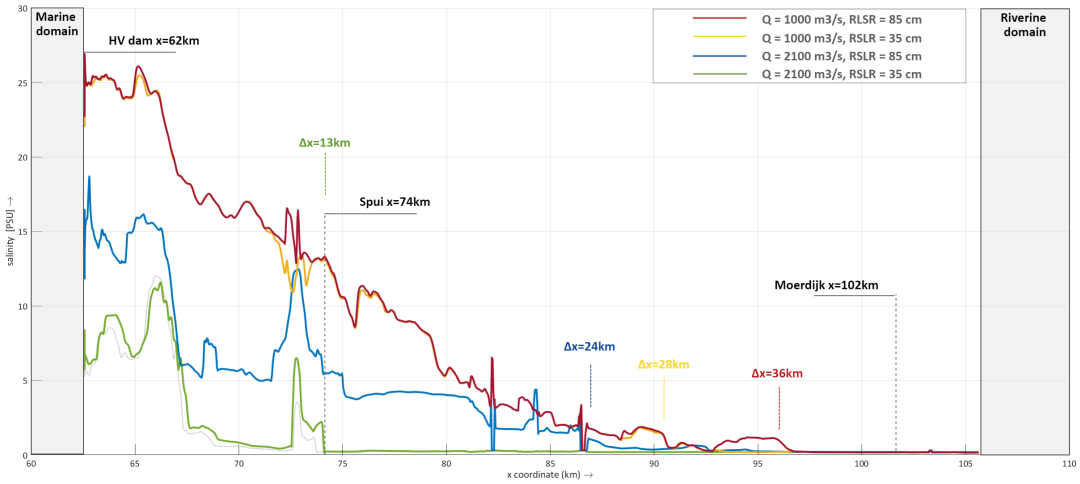

Figure 6.7: Longitudinal bottom (k=10) salinity profiles HV for scenario runs: Delta21 geometry (grey dotted), Delta21 Calm (green), Delta21 Mean (blue), Delta21 Intrusion (orange) and Delta21 Critical (red) at HWS

6.2 Salinity maps

Map output has been printed to show the system-wide salinity intrusion extremes and overall patterns. Here, anomaly maps are used to further investigate the effects of SLR (35 vs. 85 cm) and discharge (Q=1000 vs. 2100 m^3/s). Maximum intrusion is reached for scenario 'Delta21 Critical' (red lines Figures 6.4-6.7). Therefore, 'Delta21 Critical' is taken as lead scenario and compared to both Delta21 'Intrusion' and 'Delta21 Mean' scenarios to isolate the effects of SLR (35 vs. 85cm) and discharge (1000 vs. 2100 m^3/s) respectively. Maps are selected for surface (σ=1) and bottom (σ=10) positions corresponding to 6% and 97% of water depth respectively (Appendix F). This allows for quick assessment of salinity influences on freshwater intake and ecology (Subsections 3.1.2, 3.1.4). In time, maps are taken at HWS which, after investigation, constituted to the point in time of maximum intrusion length. This agrees with both theory and field data (de Nijs et al. (2011)). Up-estuary salinity transported persisted in the westernmost part of HV for at least 1h after HWS at bottom level. This is attributed to weak baroclinic flows at the bed dominating the flow profile in the lower water column.

In Figure 6.8, it can be seen that zones of higher salinity (+1.5-2 PSU) have formed in the old HV front delta at the surface. These zones are positioned at the fringes of the Delta21 shipping channel. Increasing marine forcing from 35 to 85 cm SLR leads to higher surface and bottom (Figure 6.9) salinity further up-estuary in both the RWW and HV-HD though the patterns are more complex in case of HV-HD which is attributed to higher three-dimensionality of flow there. The 8km difference of maximum intrusion length between Delta21 'Critical' and Delta21 'Intrusion' (Figure 6.7) can be seen comparing Figures 6.8 and 6.9 as well. The higher salinity appears to be largely confined to the southern bank. Salinity intrusion at HWS to beyond the bifurcation point Old Meuse-Spui (Figure 5.8) explains the relatively high feedback of salinity at ebb tide into the western HV observed in e.g. Figure 6.6.

Especially surface salinity Figure 6.8 shows to be markedly fresher at 35 cm SLR for, predominantly, zones along coastal boundaries and Delta21 shipping channel. This is attributed to greater downward transport of salinity at 85 SLR causing deep features to be more saline and shallow features fresher in the 85 cm SLR scenario compared to 35 cm SLR.

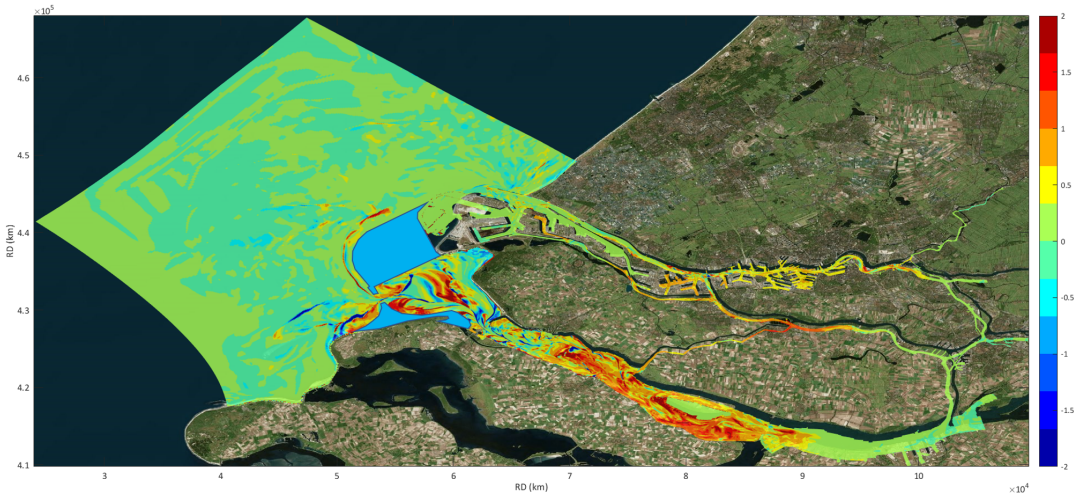

Figure 6.8: Surface salinity (k=1) anomaly map of scenarios Delta21 Critical vs. Delta21 Intrusion - Q=1000 m^3/s and 85 vs. 35 cm SLR at HWS after 30d of simulation

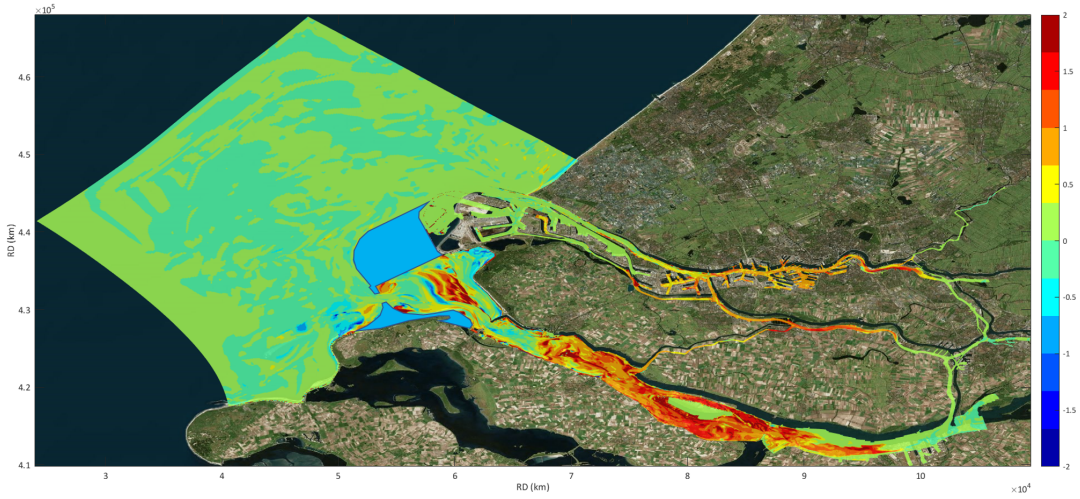

Figure 6.9: Bottom salinity (k=10) anomaly map of scenarios Delta21 Critical vs. Delta21 Intrusion - Q=1000 m^3/s and 85 vs. 35 cm SLR at HWS after 30d of simulation

Figures 6.10 and 6.11 show salinity difference for upper-end SLR scenarios (85cm) and Q=1000 vs. 2100 m^3/s. Notice the salinity ranges on the colorbars on the right which span $\pm$ 20 PSU instead of $\pm$ 2 PSU as in Figures 6.8 and 6.9 indicating that, for this model set-up, the problem is dominated by Q_f rather than SLR. It is to be expected that raising Q_f further causes an increase of relative importance of SLR. Line of thought is that the estuarine physics then change to that of the salt wedge type by stabilization of the pycnocline which limits horizontal intrusion as well as mixing. This can be seen by inspecting the rate of change for parameters in the equation for the estuarine Richardson number (Equation 2.6). For an arbitrary projected rise in sea level, ε and u_T will not vary significantly whereas the annual variability of Q_{Lobith} in 2100 amounts to 760-15.000 m^3/s (ter Maat (2014)). Sharper stratification at higher q_f may thus allow for less breakdown of pycnoclines in up-estuary direction. Horizontal movement of the salt wedge is then dominated by marine forcing i.e. a superposition of the local tide, stratification, wind and MSL (Section 3.2). Note that the relatively weak influence of SLR here is partly thought to be an artefact of numerical schematization applied (Subsection 4.6.1).

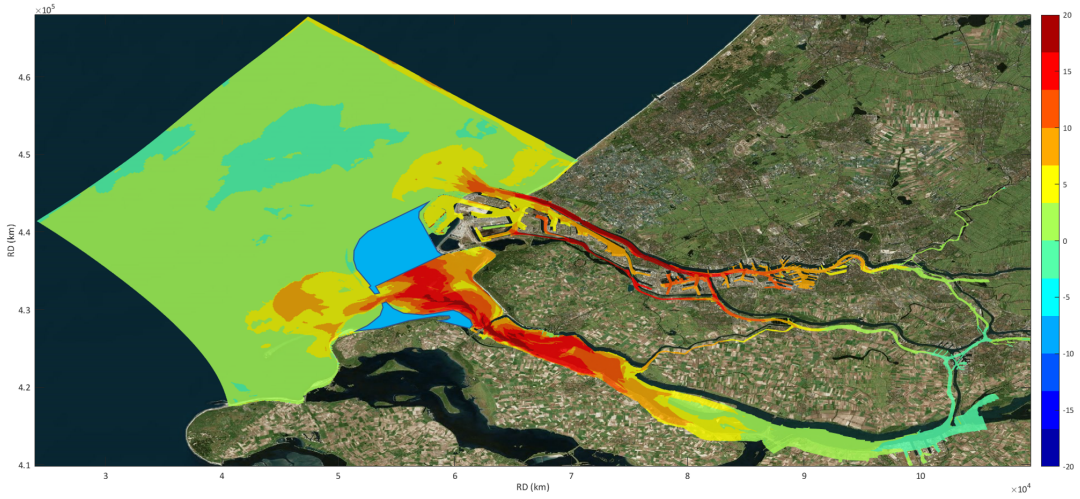

Figure 6.10: Surface salinity (k=1) anomaly map of scenarios Delta21 Critical vs. Delta21 Mean - Q=1000 vs. 2100 m^3/s and 85 cm SLR at HWS after 30d of simulation

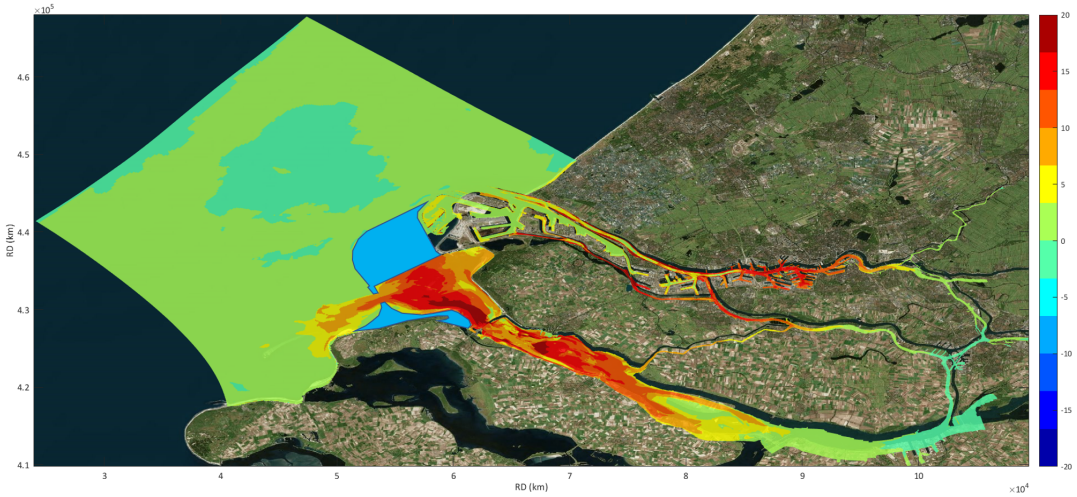

Figure 6.11: Bottom salinity (k=10) anomaly map of scenarios Delta21 Critical vs. Delta21 Mean - Q=1000 vs. 2100 m^3/s and 85 cm SLR at HWS after 30d of simulation

On a final note, the effectiveness of raising the HV bridge sill from approx. NAP-8.00m to NAP-3.00m (Section 4.5) is visualised. Judging Figure 6.12, salinity of 5-6 PSU approaches the sill at HW for Q_{Lobith}=1000 m^3/s and 85cm SLR. A combination of weakened tidal flow and intensified freshwater flow at the surface appears to be effective in duliting the incoming salinity. Spillover of salinity quickly diffuses and progresses along the southern bank of HD to the Moerdijk ports (Figure 1.3). The raised sill therefore seems effective in hindering further intrusion though feasibility of this intervention remains to up for debate.

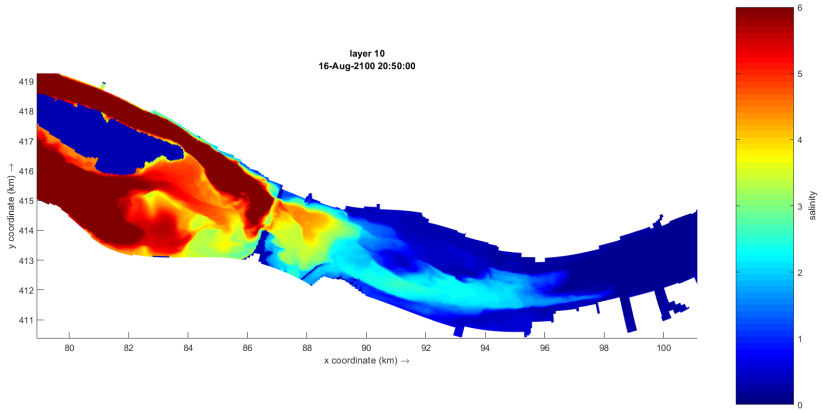

Figure 6.12: Salinity map Delta21 Critical - Q=1000 m^3/s and 85 cm SLR at HWS after 30d of simulation: zoomed in on domain Tiengemeten-Moerdijk (Figure 1.3). The HV bridge sill (NAP-3.00m) and surroundings (NAP-8.00m) can be seen between x=84-88km

6.3 Stratification

Figure 6.13 shows two locations within the HV of comparable depth which are situated 4.5 and 12 km up-estuary respectively. The horizontal velocities on the right show that tidal flow weakens from ≈0.8 m/s to 0.6 m/s moving from the HV sluices to Spui South entrance (Figure 4.14). The green line on the right shows an idealised sine depicting pre-closure average horizontal tidal velocities (1.40 m/s) just east of where the HV sluices are now. A perfect sine was selected to stress the skewness of the current tidal signal, which shows a significantly longer ebb tide.

HWS occurs slightly earlier in time for the up-estuary location and vice versa for LWS. Influences from

wind, complex geometry and flow from Spui appear to play a role especially down-estuary and on ebb tide where the the evolution of horizontal velocity is more erratic. Ebb flow (u<0) on average lasts for 7.5h whereas flood flow (u>0) only lasts for 4.5h. Tidally averaged absolute velocities amounted to 0.78 m/s post-Delta21 for the entire simulation (after flow spin-up). This is significantly higher than the 0.60 m/s pre-1970 (Paalvast et al. (1998)). Tidal flow through the estuary mouth is therefore stronger post-Delta21 but the profile quickly widens from approx. 1000 to 2500-3000m causing the extraction of kinetic energy from the mean flow to be higher comparing pre-closure and post-Delta21. Consult Appendix J for more on velocity vectors, turbulent kinetic energy en cross-channel quantities.

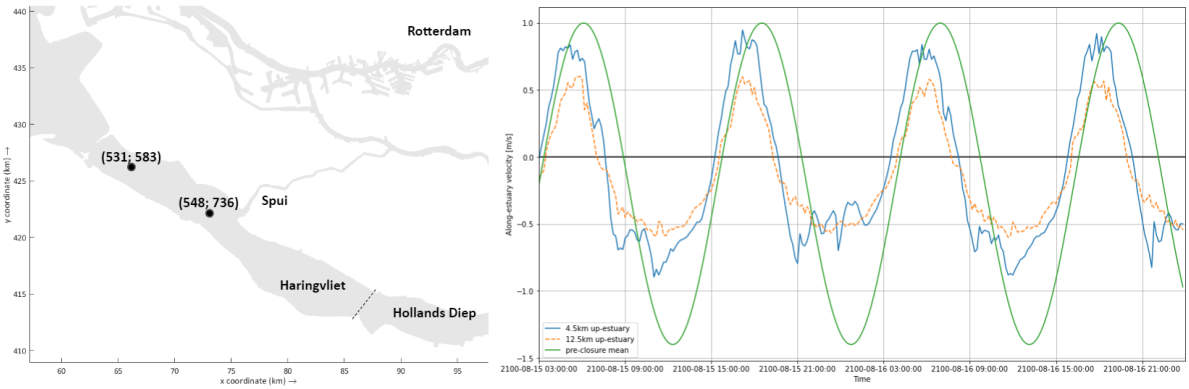

Figure 6.13: Horizontal surface (k=1) velocities (along-estuary) for two marked locations in HV post-Delta21 (fully opened, 85 cm SLR) and near-mouth pre-closure mean tidal velocity represented by perfect sine function.

Figure 6.14 shows that at Q=1000 m^3/s salinity is poorly washed out from locally deeper zones at ebb tide. This is confirmed by inspecting results of transect within HV-HD at different timestamps. The converse effect takes places on flooding tide where diminished horizontal velocities cause intrusion no further than x=90km. The old HV front delta (x=55-59km) is subject to high mixing on flood tide. Partial mixing is achieved east of the HV sluices (x=61k-69km). The following salinity regimes (Subsection 3.1.4) are thus found along the southern bank of the HV on flood tide in case of critical conditions: polyhaline (x=61-73km), mesohaline (x=73-80km) and oligohaline (x=80-90km) which gives the estuarine domain a maximum length of 29km. Restratification on ebb tide is low but not absent as can be seen x=61-76km. Observation point (531; 583) shows distinct stratification of 12 to 25 PSU. Note that the drying of grid points around x=78, x=80 and x=83km at LWS in Figures 6.14-6.15 produces odd interpolations locally but is not an effect of (additional) numerical inaccuracies.

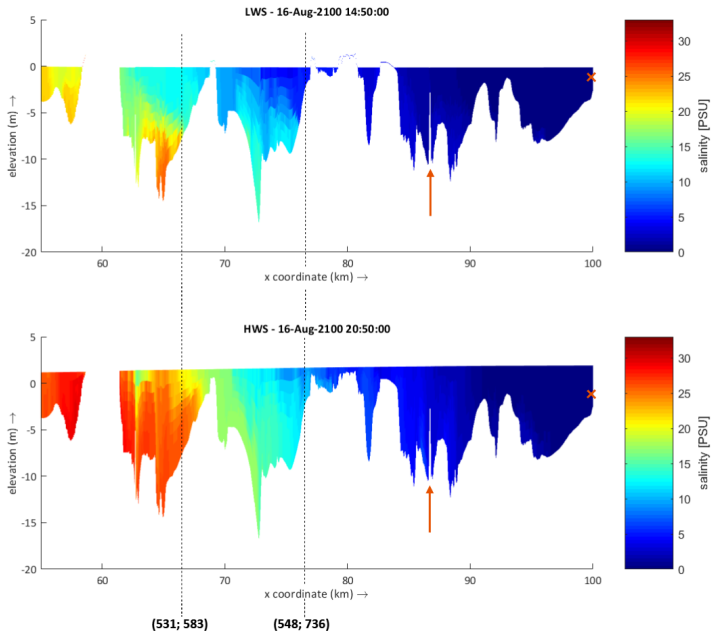

Figure 6.14: Salinity contour along-estuary transects (shown in Figure 6.2) at LWS (top) and HWS (bottom) for Q=1000 m^3/s and SLR 85cm, locations from Figure 6.13 marked. Note the non-resolved zone x=59-61km due to non-flooded cells south of HV sluices. T=31d. Arrow (↑): raised HV bridge sill (NAP-3.00m). Cross (x): new surface water intake Strijensas opposite Moerdijk ports.

Figure 6.15 displays the situation with mean discharge (Q_{Lobith}=2100 m^3/s) and moderate SLR (35cm). This transect better reflects the position of halines on a 'normal' day post-Delta21. Salinity is washed out more easily into the front delta on ebb tide though deeper zones (x=63-64km) capture salinity nevertheless. On flood tide the southern front delta is subject to intense mixing over its relatively shallow depth (4-5m) though not as much as in Figure 6.14. The high salinity marine water is almost entirely buffered from x=61-68km. The following salinity regimes (Subsection 3.1.4) are thus found along the southern bank of the HV on flood tide in case of critical conditions: polyhaline (up to x=69km), mesohaline (x=69-74km) and oligohaline (x=74-79km) which gives the estuarine domain a maximum length of 18km (excluding HV ROFI).

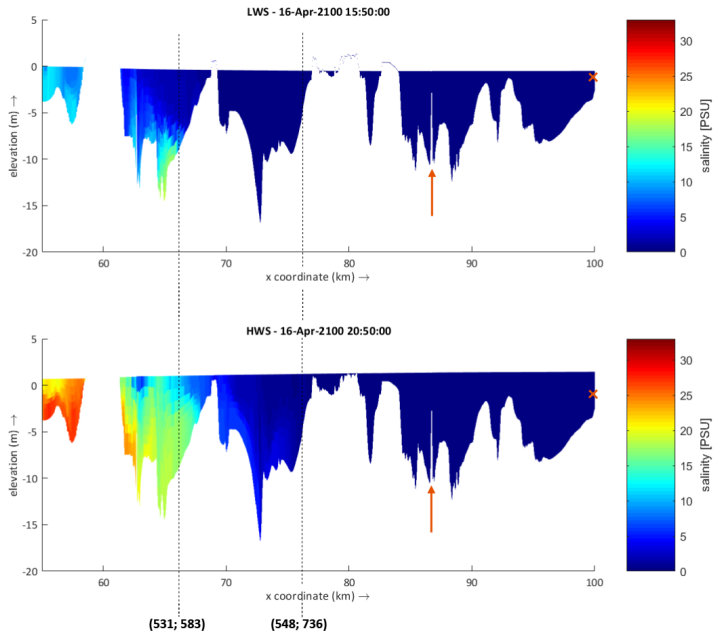

Figure 6.15: Salinity contour along-estuary transects (shown in Figure 6.2) at LWS (top) and HWS (bottom) for Q=2100 m^3/s and SLR 35cm, locations from Figure 6.13 marked. Note the non-resolved zone x=59-61km due to non-flooded cells south of HV sluices. T=31d. Arrow (↑): raised HV bridge sill (NAP-3.00m). Cross (x): new surface water intake Strijensas opposite Moerdijk ports.

6.4 Partially opened Haringvliet

Finally, numerical results of applying 'Delta21 Critical' conditions using 80 % height limitation of the HV sluices (Section 4.6) are discussed. Figure 6.16 shows the cumulative discharge through the HV sluices for simulations 'Delta21 Critical' using full and partial opening. At full opening, this implies that $\bar{Q}_{HV}$=448 m^3/s whereas $\bar{Q}_{HV}$=335 m^3/s for partial opening. Subsequently, continuity demands that a redistribution of discharge takes places which results in a shift from 55/45 to 66/34 discharge ratio beteen RWW/HV.

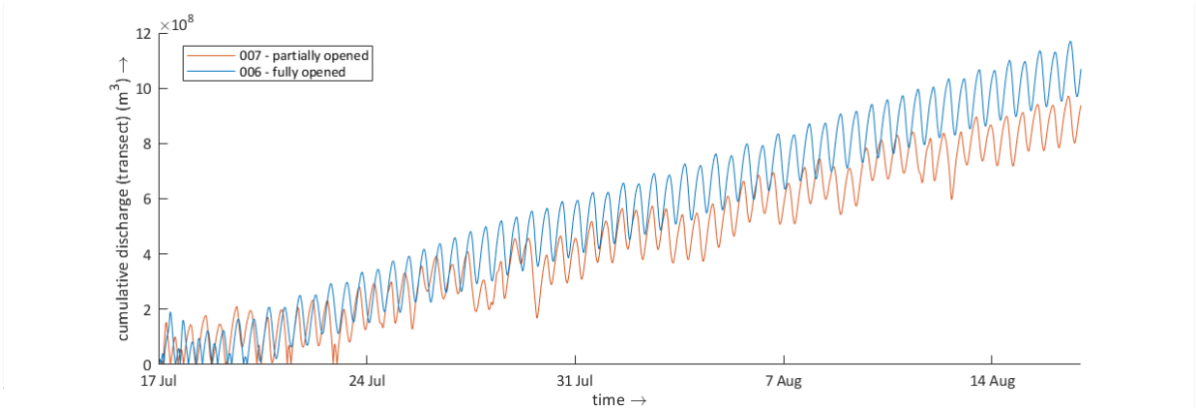

Figure 6.16: Cumulative discharge [m^3] through HV sluices (17 units) for simulation period 17/07/2100-17/08-2100 - Q_{Lobith}=1000 m^3/s, SLR=85cm. Partially opened (average 20%) vs. fully opened.

Figure 6.17 shows that the Old Meuse and RWW remain significantly fresher (-1 to -7 PSU) at the surface (k=1) for the case where the HV sluices are opened only partially. This is attributed to a discharge redistribution between the northern and southern RMB branches in favour of the RWW which strength-

ens the salt wedge behaviour due to increased tidal shear there. Salinity within the HV-HD is 1-4 PSU fresher comparing 20% and 100% opened HV sluices which is a relatively small reduction given 80% limitation of A_c. This small reduction in salinity is indicative of the formation of an equilibrium under drought flow conditions ($\bar{Q}_{\text{Lobith}}$=1000 m^3/s) given enough time (here: T=31d). These conditions result in extensive vertical and lateral mixing in the western HV which is exacerbated by post-supply from Spui on ebb tide. Extensive salinity intrusion is however, not observed as tidal straining (Subsection 2.3.2) is weak despite the presence of distinct horizontal density gradients due to low tidal velocity shear (de Boer (2009)) in the HV-HD.

Advection through the Delta21 shipping lane (Appendix A) is weakened as tidal flow through the HV sluices is diminished at 20% opening. This affects the availability of kinetic energy in the front deltas leading to zones of up to 8 PSU fresher water compared to 100% opening. Occasional spots of higher salinity are observed as well, these are attributed to hydrodynamically calmer conditions (at A_c=0.2$A_{c,max}$) which allows for more stratification in deep features compared to A_c=$A_{c,max}$. Deep features further upstream (e.g. x=86km) are unaffected by salinity intrusion and therefore remain fresher. Overall, the reduction in salinity can be observed nearly up to L_{max} at x=96km (Figure 6.7) as well. This indicates that the intrusion length is unaffected but the tidally transported salinity volume is lower.

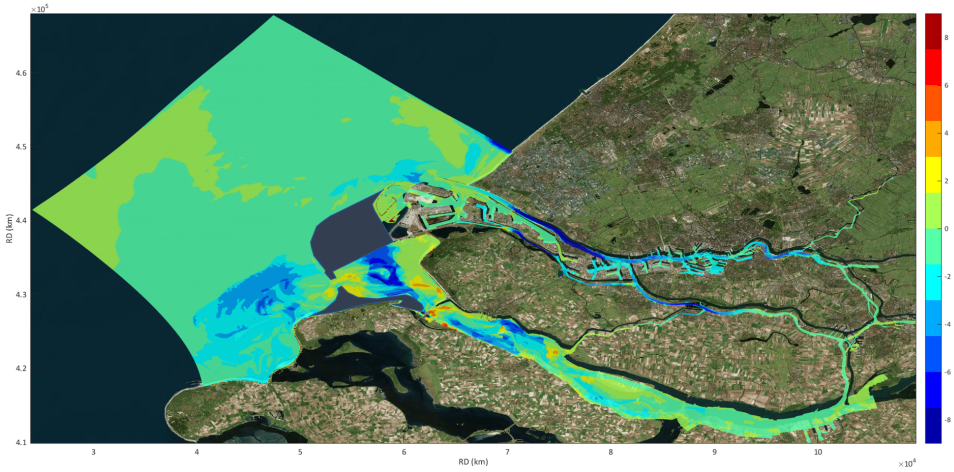

Figure 6.17: Surface salinity (k=1) anomaly map of scenarios Delta21 Critical full vs. partial HV sluices opening - Q=1000 m^3/s and 85 cm SLR at HWS after 30d of simulation

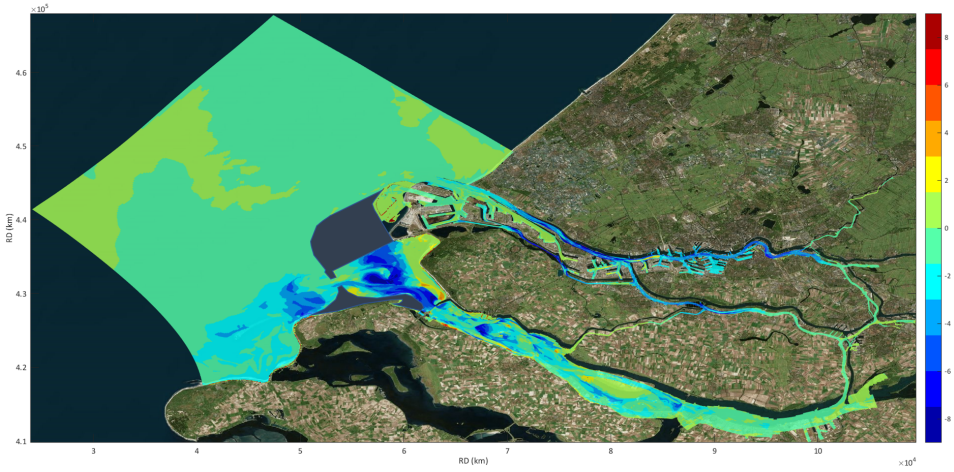

Figure 6.18: Bottom salinity (k=10) anomaly map of scenarios Delta21 Critical full vs. partial HV sluices opening - Q=1000 m^3/s and 85 cm SLR at HWS after 30d of simulation

Figure 6.19 shows largely the same behaviour as in Figure 6.14. Less stratification is observed around x=75km. The development of a similar distribution of salinity in the basin as for fully opened HV sluices indicates a 'history effect' from marine forcing in the preceding month. Outwash of salinity is low due to limited Q_f which dominates the problem. The development of a similar salinity structure in x=61=68 km appears to be dominated by high mixing in the HV front delta. Salinity reaches past the raised HV bridge sill (↑) despite weakened tidal dynamics, from Δh=1.30 m to 1.00 m near Moerdijk (Paalvast et al. (1998)). This may be an indication that non-physical vertical diffusion and flow takes places near the sill due to abrupt adaptation of bottom geometry. Investigation into effectiveness of anti-creep methods may deserve attention here (Section 8.2).

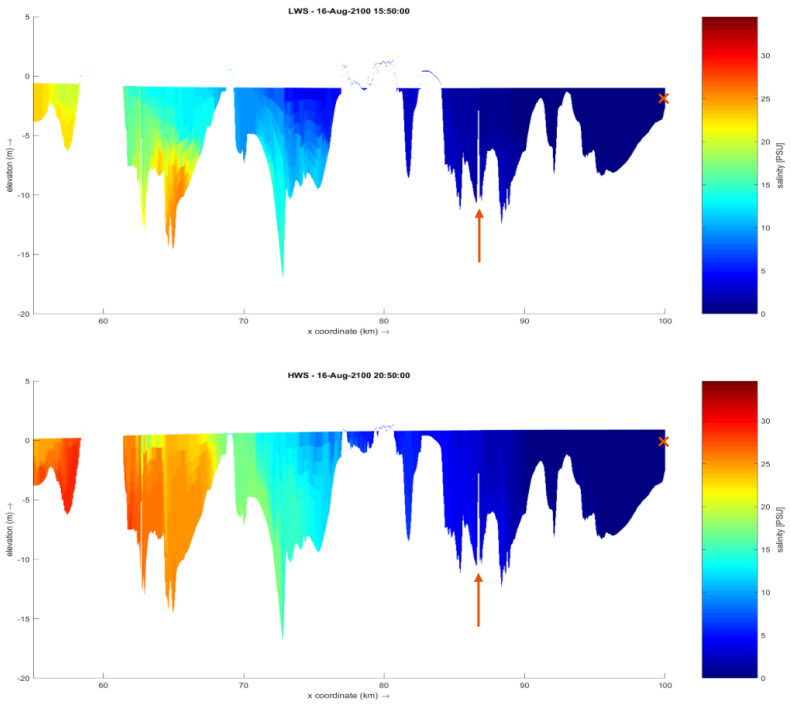

Figure 6.19: Salinity contour along-estuary transects (shown in Figure 6.2) at LWS (top) and HWS (bottom) for Q=1000 m^3/s and SLR 85cm and partially opened HV sluices. Note the non-resolved zone x=59-61km due to non-flooded cells south of HV sluices. T=31d. Arrow (↑): raised HV bridge sill (NAP-3.00m). Cross (x): new surface water intake Strijensas opposite Moerdijk ports.

6.5 Result aggregation

The results discussed in the previous paragraphs of this chapter are aggregated to determine the expected estuarine character of the HV-HD post-Delta21. Herein, geographical limitation is applied as shown in the lower part of Figure 3.1. SLR is set at 85 cm. Figures 6.20a-6.20b show the difference in salinity, tidal regime, freshwater intake and storage between current (Kierbesluit) and future (Delta21) situations. The last 4 figures show spatial distributions of bottom salinity using haline regimes defined in Paalvast et al. (1998) and Wijsman et al. (2018) at HWS/LWS for Q=1000/2100 m^3/s. Figures 6.20a and 6.20b show the total (expected) maximum extent of salt intrusion under the Kierbesluit and Delta21 respectively. Figures 6.21a-6.21d elaborate on expected spatial distributions of salinity at 85cm SLR and varying Q_f for LWS/HWS.

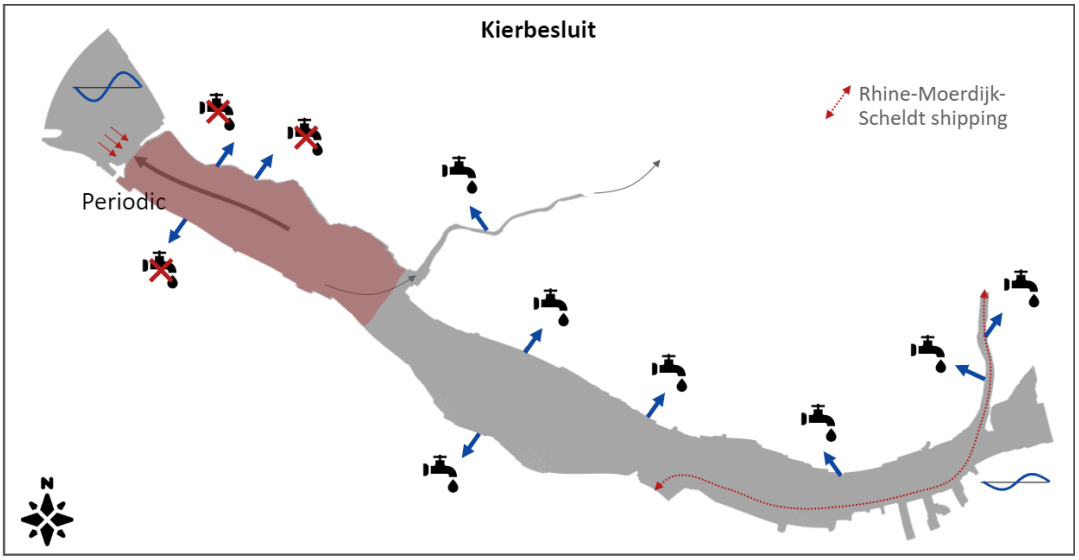

The situation at the time of writing. Periodic ebb sluicing is used to control Haringvliet-Hollands Diep water levels. Sporadic opening (Dutch: Kieren) of Haringvliet sluices allows for some intrusion of salinity though not beyond the virtual line (0.3 g/L Cl) of Middelharnis-Spui south. The basin is 'rinsed' before opening the HV sluices at flood. This warrants continued freshwater intake at marked locations. The three westernmost intakes have been closed as part of the Kierbesluit. Flow through the Spui is directed northwards to the North Sea via Old Meuse and Nieuwe Waterweg. MWL at Moerdijk, during validation period Dec '19, was NAP+0.35m. Mean tidal ranges amount to 2.15m in Haringvliet front delta to 0.50m at Moerdijk. Various species of fish have been observed to pass Haringvliet sluices since the start of Kierbesluit in Jan '19 but ecological (re-)development is poor due to absence of morphodynamics and (periodic) emergence of tidal flats.

(a) Situation sketch HV-HD during Kierbesluit. Red shading marks maximum extent salinity intrusion as agreed in Kierbesluit.

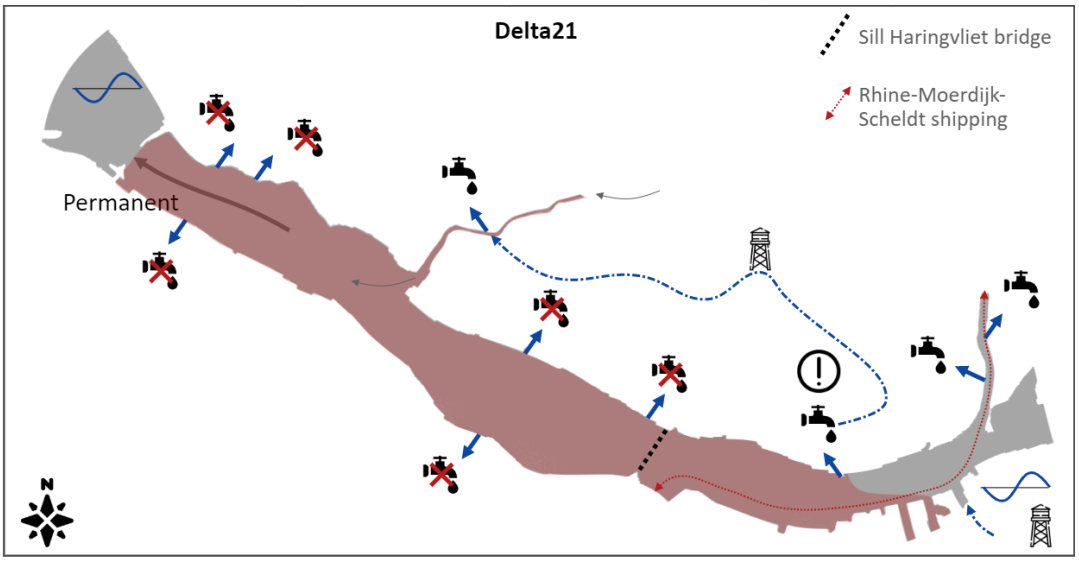

The situation post-Delta21. The Haringvliet-Hollands Diep has become a permanently discharging estuary. The semi-diurnal tidal signal is not able to completely wash out salinity and diffusion in the west of the basin is widespread. Extent of salinity intrusion depicted for the range LWS-HWS during forceful up-estuary (13.9-17.1 m/s) and Q=1000-2100 m3/s at Lobith. Three more agricultural water intakes require closure for the majority of the year. Supply to now freshwater-deprived areas in Voorne-Putten is done by a new water route from the east at Strijensas. Extra storage is added at Binnenbedijkte Maas and Roode Vaart (water tower icons). A scenario of 85 cm SLR, Q=1000 m3/s and high freshwater demand may lead to salinity norm exceedance at the Strijensas intake as well, though it is estimated that this constitutes to a few days per year and can be anticipated by manual closure of the HV sluices. Flow through the Spui is directed southwards which supplies extra salinity from Old Meuse to HV. MWL at Moerdijk, during drought, is NAP-0.20m (65 cm lower). Mean tidal ranges amount to 1.50m in HV front delta to 1.35m at Moerdijk. This is likely to hinder shipping on route Rotterdam-Moerdijk-Scheldt.

(b) Situation sketch HV-HD post-Delta21. Red shading marks numerically estimated maximum extent salinity intrusion.

Figure 6.20: Maximum salinity bandwidths Kierbesluit (2020) vs. Delta21 (2100) by numerical estimation

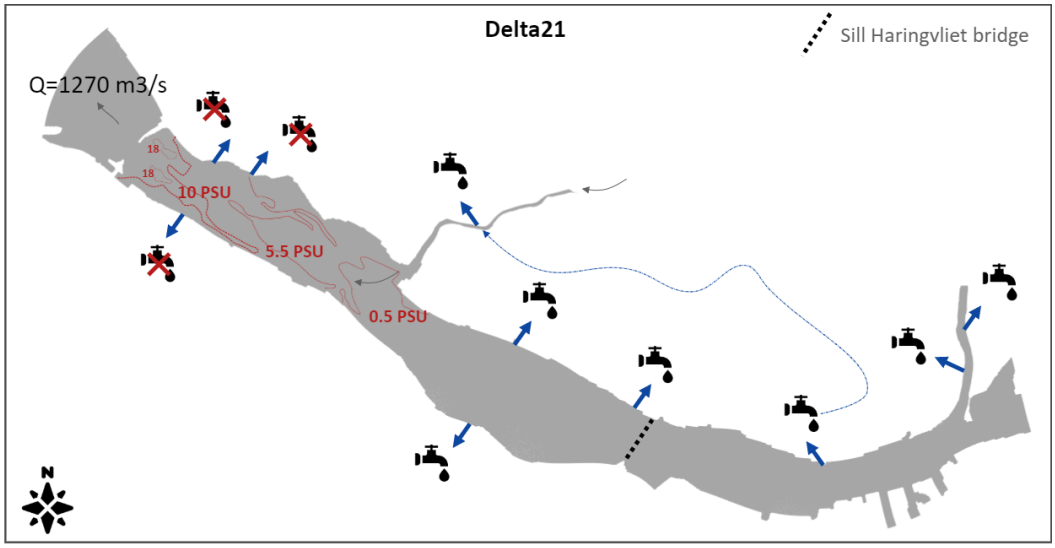

Mean discharge (Q=2100 m3/s) and ebb tide cause salinity to be transported to just near Spui south entrance. The mesohaline (5.5-18 PSU) and oligohaline (0.5-5.5 PSU) regimes are shifted to the west of Haringvliet and former front delta. East of the Haringvliet sluices, only deep pits capture saline water (>18 PSU). Intake of fresh water may therefore continue at Spui Bernisse at LW for discharges (Lobith) exceeding 2100 m3/s. Live monitoring of salinity influx at Spui south and bifurcation Old Meuse-Spui will be needed though as local turbulent mixing may cause exceedance of salinity norms in Spui.

(a) Salinity regime sketch HV-HD post-Delta21 for $Q_{Lobith} = 2100\ m^3/s$ at LWS.

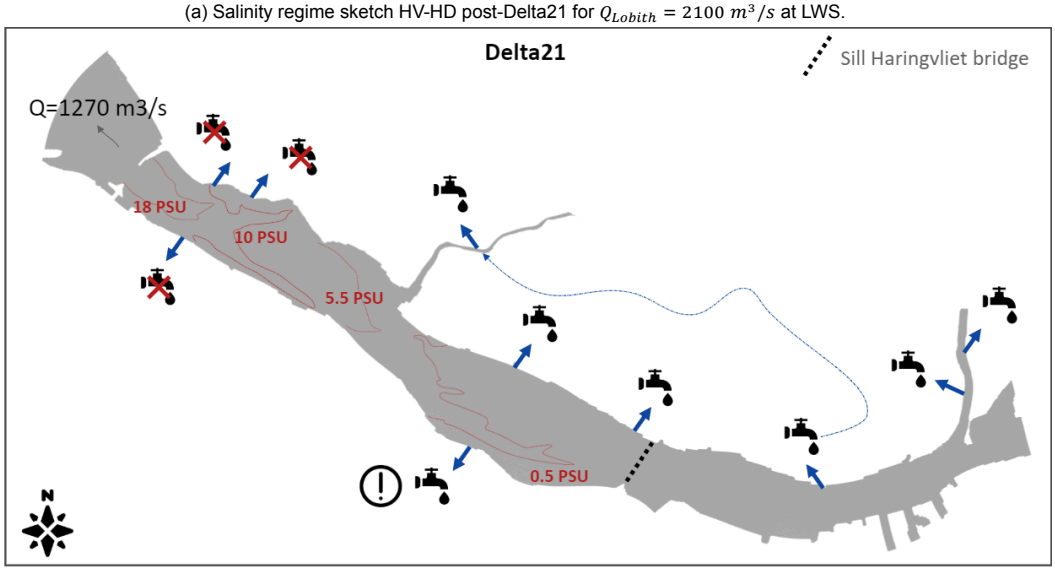

Mean discharge (Q=2100 m3/s) and flood tide cause more salinity intrusion than anticipated in the Kierbesluit. The extent of intrusion and mixing is however much lower than in scenarios of drought due to more efficient flushing of the system during ebb tide. Up-estuary diffusion is therefore limited in Hollands Diep. Outwash of salinity down-estuary, in the Haringvliet, remains low especially due to robustness here (2600m wide) which gives rise to lateral and vertical mixing on flood tide. Salinity at Spui may still reach norm-exceeding levels due to supply of salinity by the Old Meuse (north). Alternative supply from Strijensas is not at risk and can therefore deliver freshwater to Bernisse (Spui). Water levels are higher than for drought scenarios causing the inundation of more tidal flats and therefore more propagation of salinity over these flats e.g. in the Haringvliet and at Tiengemeten (island). Marine salinities (>31 PSU) are not encountered in the vicinity of the Haringvliet front delta due to dilution by captured fresh water.

(b) Salinity regime sketch HV-HD post-Delta21 for $Q_{Lobith} = 2100\ m^3/s$ at HWS.

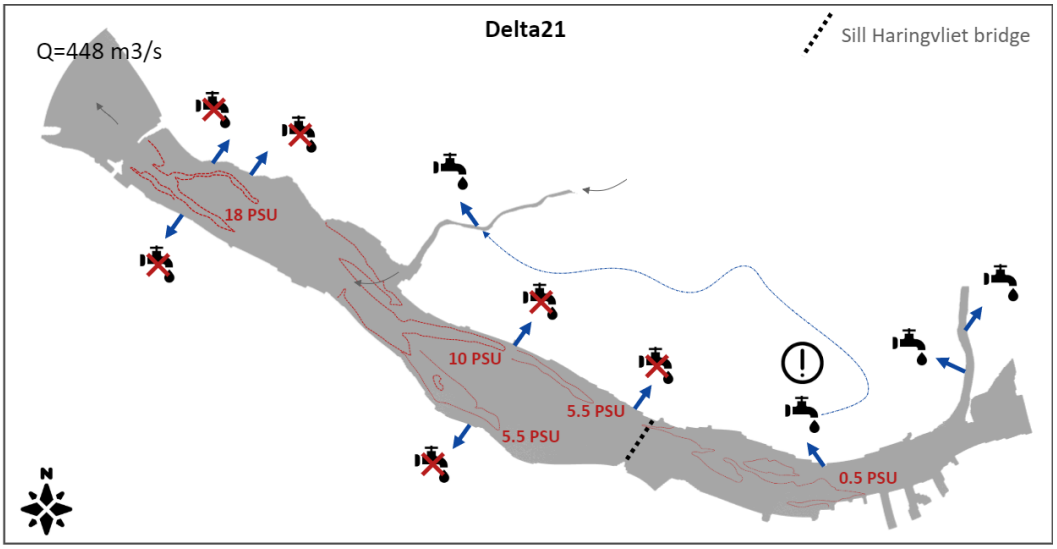

Low discharge (Q=1000 m3/s) and ebb tide cause marine salinity (>31 PSU) to be washed out of the Haringvliet front delta. A polyhaline regime (18-31 PSU) reaches approx 6 km up-estuary and can be seen to circumnavigate historical tidal flats through deeper gullies. Spui exhibits strong north-to-south flow which admixes 7-8 PSU bottom salinity intro the retreating Haringvliet water on the northern bank. Retreat of salinity is strongest along the northern bank but down-estuary directed velocities are too weak to transport already diffused salinity out of the system efficiently. The oligohaline regime (0.5-5.5 PSU) is therefore hardly affected and likely aided in being sustained by the raised Haringvliet bridge sill.

(c) Salinity regime sketch HV-HD post-Delta21 for $Q_{Lobith} = 1000\ m^3/s$ at LWS.

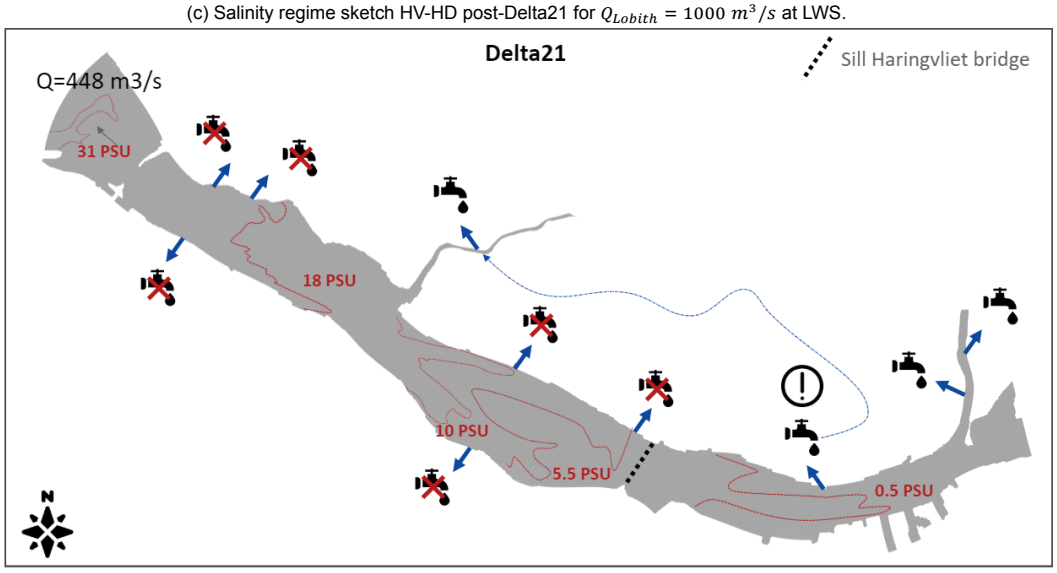

Low discharge (Q=1000 m3/s) and flood tide cause marine salinity (>31 PSU) to reach the Haringvliet front delta. A polyhaline regime (18-31 PSU) is found to extend approx. 10 km up-estuary along the southern bank of HV. Spui exhibits weak north-to-south flow at approx. 8-9 PSU bottom salinity. Propagation of salinity shifts to concentrate on the northern Haringvliet bank where the mesohaline (5.5-18 PSU) regime extends furthest. The large indent in the 5.5 PSU isohaline is due to Tiengemeten (island). The oligohaline regime (0.5-5.5 PSU) crosses the raised Haringvliet sill and converges back to the southern bank in the Hollands Diep extending to the westernmost Moerdijk port.

(d) Salinity regime sketch HV-HD post-Delta21 for $Q_{Lobith} = 1000\ m^3/s$ at HWS.

Figure 6.21: Aggregated numerical results for HV-HD showing numerical approximation of bottom salinity spreading applied to freshwater, ecology and shipping

6.6 Result discussion

The main findings of the numerical study concerning climate scenarios (post-Delta21) relate to macroscopic intrusion patterns in the RMB. Analysis of numerical results have confirmed expectations that the overall estuarine character of HV-HD post-Delta21 shows: relatively high flood mixing at the estuary mouth with slight re-stratification on ebb tide (Subsection 2.3.2, Section 6.3), marked lateral redistribution of salinity (Section 2.3, Appendix J) and poor outwash of salinity caused by diminished tidal flow compared to the pre-closure estuary (Subsection 3.2.2, Section 6.2). Capture of salinity in deep pits appears to be an evident result though vertical admixing and convection between the main channels and deep pits must be questioned using the current vertical discretization (σ-layers, Section 4.3).

Another result that deserves attention is that at the range of Q_{Lobith} assessed here, Q=1000-2100 m^3/s, the salinity spreading appears to be dominated by discharge judging the 5-15 PSU anomalies between scenarios of equal SLR but different Q_{Lobith}, see Figures 6.10-6.11. Anomalies for constant discharge and varying SLR (35-85cm) are 0-2 PSU in the HV basin (6.8-6.9) and therefore of lower order using this model schematization. Important to note is that the position of MSL is however unchanging when looking at short timescales which makes the effects of SLR on salt intrusion more permanent than that of discharge which can vary significantly on a weekly timescale.

The main limitations to the results arise from the description of marine boundary conditions (Subsection 4.6.1). The marine boundary points (156x10 salinity, 142x10 velocity, 14 water levels) require a description that rightly represents the coupled nature of these state variables while remaining unaffected by system properties such as freshwater discharge. Especially the latter is doubtful as was shown in Section 5.1. The secondary salinity peak visible in Figure 6.6 is therefore likely to be an overestimation of the forced salinity on ebb tide near Spui south as this peak is a direct consequence of salinity forced through HoH->New Waterway->Old Meuse. Implementation of stratification profiles from a larger (2DH) North Sea model as is done here has its own associated limitations for which reference is made to Kranenburg and Schueder (2015).

Another limitation is that the computational demand of OSR-HV has not allowed for simulation of multiple months within this study and therefore largely excludes additional forcing effects of the spring-neap tidal cycle (Table 3.4). Simulation periods further exclude large variations in freshwater discharge regime and storm events which are known to affect the dynamic salinity equilibrium significantly (ter Maat (2015)).

The results presented in Section 6.4 should be treated as an exploratory assessment of a HV sluice configuration that may be suggested as a compromise between Kierbesluit (A_c=0.05$A_{c,max}$) and Delta21 (A_c=$A_{c,max}$) by applying approx. 20% of the available cross-section. Results (Figures 6.17-6.18) show that height-limitation of HV sluices allows for less intrusion into the post-Delta21 tidal lake (Appendix A) and thereby limiting intrusion into HV-HD. Limitation of this assessment is that enhanced mixing due to transition of flow (subcritical->supercritical) within HV sluices is not reproduced due to use of the hydrostatic approximation (Appendix E).

Finally, despite the 3D nature of OSR-HV, analysis of results mostly relies on inspection of 2D fields and time-series due to limitations in available visualisation tools. The relatively large quantity of numerical output data (per model run) may therefore cause loss/omission of information between dimensions of space (ξ, η, σ) and time (t).

7

Discussion

This chapter discusses: the applicability of OSR-HV as a salinity-predicting tool Section 7.1, the way in which model validation (Section 7.2) and scenario simulation (Section 7.3) should be viewed in light of the objectives. The chapter concludes with the main residual uncertainties in this study (Section 7.4) which will be elaborated on in Section 8.2.

7.1 OSR-HV model

Replication of in-field salinity time-series and vertical profiles has proven to be possible using OSR-HV (Kranenburg and Schueder (2015), Kranenburg (2015)). Replication is found to be challenged by the description of transports through the HV sluices which cause for added complexity with respect to an open sea connection such as encountered in the RWW. Setting diffusion through the HV sluices to zero added to higher replication quality (Kranenburg (2015)) but did not resolve all difficulties in describing estuarine salinity in HV-HD. Further calibration by locally reducing the imposed wind forcing in the coastal region has been dropped due to its doubtful physical basis.

The description of system geometry (Section 4.5), barotropic signal and freshwater forcing (Subsection 4.6.1) allow for studying the macro features of exchange flow between the North Sea and HV-HD which is markedly influenced by the geometry of the tidal channel structure and the balance between the locally asymmetrical tide and buoyant input. Predictive modelling using OSR-HV has to be treated as a conservative estimate for vertical profiles as both transports through HV sluices and pycnocline breakdown are systemically overestimated. Outwash of basin salinity on ebb tide may consequently be larger than modelled as well which adds to the conservative projections surrounding the basin-wide diffusion of salinity resulting from predictive runs, which has an equal implication for all research questions (Section 1.4).

7.2 Validation study

Validation of a model requires an assessment of reproduction quality of state variables. This is preferably done using historical data. Data on salinity transport through HV sluices is however scarce due to basin closure in 1969-70 (Ferguson (1971)). Kranenburg and Schueder (2015) relied on a 1997 intrusion test. Ample data was collected on this field study though the time-span was limited at 10 tidal cycles. In January 2019, the Kierbesluit (Paalvast (2016)) came in effect. The period in which the

HV sluices were opened most persistently is found in December 2019 (tot. 10 days). The period for validating salinity reproductive quality of OSR-HV used here is therefore markedly longer than that of Kranenburg and Schueder (2015) but less data monitoring locations were available within the confines of the HV-HD basin.

The validation data in this study has been taken just west and east of the HV sluices to assess performance near the closure work. Therefore, in view of time, assumption were made regarding model capabilities of OSR-HV in/around RWW. Assessment of Delta21 geometry (Section 5.1) and a literature comparison (Section 5.3) have shown that this cannot be assumed given the current layout of the numerical domain. This mainly appears to have implications for retreat of the salt wedge in the RWW at ebb tide which is underestimated. Salinity forcing on the northern branches may therefore be excessive and must be kept in mind when analysing the southern branches.

Salinity data that was used has been obtained from various stations in/around HV (Figure 4.14). Some limitations include the fact that nearly every station provides a total of 3 measurements over depth. Linear interpolation of spatial was therefore required (Appendix I) which becomes exceedingly inaccurate for zones of larger depth.

The overall underestimation of stratification in the data validation study (Section 5.2, Appendix I) points at overestimation of transfer of momentum in the vertical. The application of spatially homogeneous wind forcing is thought to be an important factor in the destruction of stratification. A local reduction in the coastal wind field has been applied before but has no physical basis and was therefore not applied here (communications: Deltares). This results in a combination of overestimated salinity transports and stratification breakdown east of HV sluices. Graphically, this is expressed as an overestimation of vertically averaged salinity and less distinct stratification in the HV-HD basin. Typical salinity differences between data and numerical approximation appear lower in the western HV (Figures I.7a-I.7h) compared to near Spui South (Figure 5.6). This is thought to be an effect of extra salinity forced from HoH through Old Meuse and Spui.

Outcome of the validation study therefore is that the model schematization used here gives rise to inaccuracies mostly in the northwestern part of the domain (Rhine ROFI, HoH, RWW). Some of these inaccuracies translate into local salinity inaccuracies in vertical profiles for the eastern HV near Spui. Overall, the salinity response of HV-HD appears to be accurate with mistakes of O(0.1) PSU and slightly less stratified vertical profiles. The assumption that the nature of salinity forcing imposed by the Kierbesluit ($A_{c,max}$=0.05A_c) is similar to that of large-scale intrusion encountered post-Delta21 (A_c=$A_{c,max}$) has to be made when prospective scenarios are run.

7.3 Scenario simulation

This study makes use of climate projections for the year 2100 (80 years from the time of writing). Studying physical phenomena on these timescales creates large uncertainties, some of which can be accounted for and others that need to be either identified and accepted or deserve attention for further research.

Especially SLR (Subsection 3.2.2) and its inclusion in the marine open boundaries (Appendix G) cause for uncertainty in the description of RMB salinity description. Bruggemann et al. (2013) has been taken as the lead source on SLR and Rhine-Meuse discharge along the Dutch coast for the year 2100 CE. The authors in this report concede that their scenarios constitute to a 'modest, plausible bandwidth of autonomous developments'. The official scenarios for global mean SLR by Church et al. (2013) use upper-end scenarios of 1.25m though their estimate for the Dutch coast amounts to 0.22-0.78m (Figure 7.1). The scenarios used in Bruggemann et al. (2013), and this study, are therefore to be treated as indicative. The reader is also alerted that extreme and unforeseen events between 2020-2100 may render such scenarios useless see e.g. Taleb (2007) for a description of 'unknown unknowns'.

The main numerical uncertainties arise from description of the marine boundary conditions in this study. SLR appears as a second order effect when salinity anomaly results are analysed (Figures 6.8, 6.9). The effect of SLR is likely to be suppressed by its relatively weak inclusion in the open marine boundaries where harmonic tidal velocities dominate the imposed signal. Inclusion of more water level points

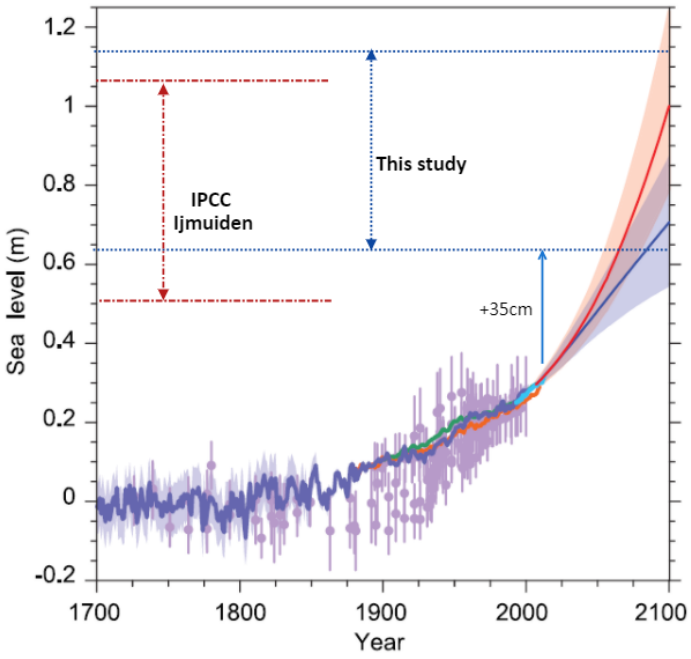

Figure 7.1: Image from Church et al. (2013) showing historical data and extrapolation for 2013-2100 of global mean sea level. Local estimate at Dutch coast from Church et al. (2013) (red) and Bruggemann et al. (2013) (blue) indicated too.

in favour of velocity points at the downstream open boundaries may however compromise the objective of accurately representing salinity dynamics. The effects of SLR are significant ($\pm$ O(1.0) PSU) in the current model schematization though. Results are best treated as comparative and have contributed to insight in a situation with opened HV sluices when looking at macroscopic behaviour induced by basin geometry and structures which is in line with the objectives formulated in Section 1.4.

Another important residual uncertainty is the exclusion of temperature as a parameter in the EoS in TRIWAQ. This gives rise to a misrepresentation of the vertical density profile especially in periods of high insolation which causes thermal gradients in the water column to contribute to stratification and flows. Exclusion of a temperature model appears to be justified for the validation period (Dec '19). Scenarios are based on discharge regimes of the RMB which relate to precipitation (dry/wet periods) as a parameter. Predictive capability of OSR-HV may however still be benefited by inclusion of a temperature model.

Some general limitations of the model include the vertical schematization using σ-layers which perform poorly in steeply sloping bed features due to misalignment with local pycnoclines (Deltares (2020)). Models that can make use of spatially varying vertical schematizations like DCSM-FM (communications: RHDHV) may therefore be able to better replicate salt dynamics in systems like HV-HD. Moreover, vertical accelerations are unaccounted for in OSR-HV by imposing the hydrostatic approximation (Appendix E). This prevents a proper hydrodynamic description of e.g. observed vertical flows near the HV sluices (Jacobs et al. (2003)) and internal wave phenomena (Pietrzak et al. (1991)).

Finally, the representation of the post-Delta21 coastal layout by means of flow-blocking elements (Section 4.5) without smoothly transitioning of bathymetry is a simplification that needs to be kept in mind. As stated in Appendix A, the basic geometry of Delta21 is still subject to changes as well.

7.4 Residual uncertainties

Figure 7.2 shows the main uncertainties that remain in this study. Recommendations for further research follow in Section 8.2. Note that Figure 7.2 is not aimed at being complete but does show a hierarchy of issues that need to be resolved, if possible at all, to greatly increase predictive capabilities of the post-Delta21 system.

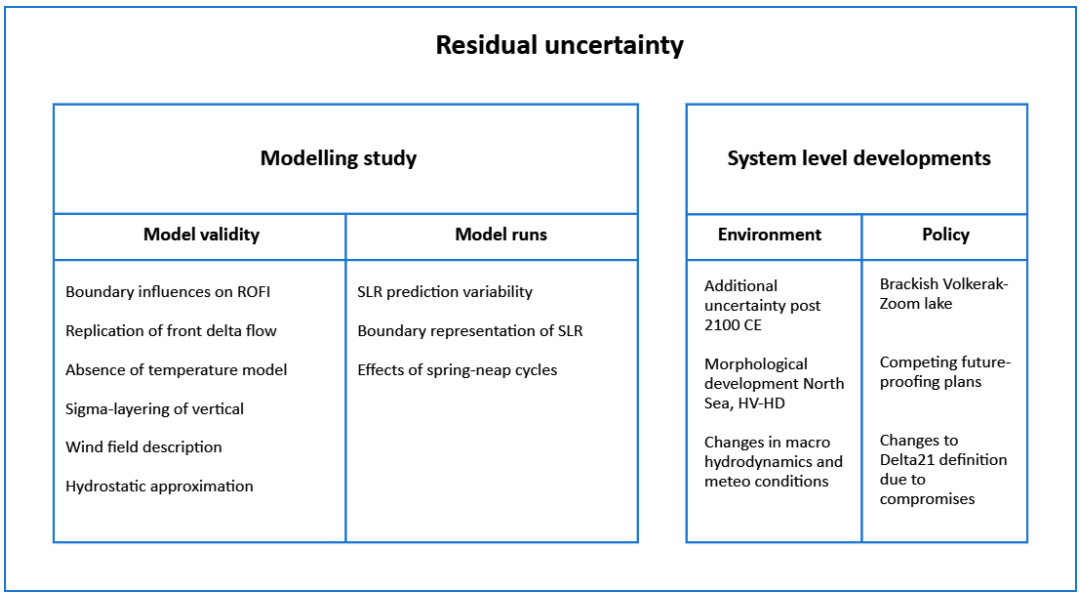

Figure 7.2: Main residual uncertainties that follow from this exploratory salinity study on HV-HD post-Delta21. The emphasis is placed on accuracy gain by adjustments to the modelling study as these factors can be more readily influenced.

8

Conclusions

This research is aimed at exploring the effects of Delta21 interventions on the movement of salinity in the HV-HD basin. To that end, the research questions as formulated in Section 1.4 are answered as complete as possible based on acquired numerical results (Chapter 6).

8.1 Findings

Key points:

- HV-HD exhibits semi-diurnal partially mixed estuarine behaviour with re-stratification on ebb tide
- Maximum bottom salinity intrusion reaches Moerdijk ports, less than pre-closure due to diminished tidal velocities at the estuary mouth
- Freshwater discharge dominates salinity intrusion length for the range Q_{Lobith}=1000-2100 m^3/s in HV-HD but SLR is non-negligible
- Exploratory assessment of partially opening HV sluices shows little effect regarding salinity in HV-HD and significant effect on RWW due to discharge redistribution

Research Question: *How does opening of the Haringvliet sluices impact the spatiotemporal advection and diffusion of salinity in the Haringvliet-Hollandsch Diep for relevant climate projections post-Delta21?*

Bearing model weaknesses in mind (Section 8.2), it may be concluded that salinity intrusion into the HV-HD given the proposed climate scenarios (Section 4.6) is likely to be less extensive than pre-closure. The average historical intrusion of salinity up to Biesbosch at HW (Subsection 3.1.4) is not found. This is attributed to the changed nature of the estuary mouth. Constriction of the HV mouth ($A_{c,new} = 0.35A_{c,old}$) is likely creating conditions giving rise to tidal pumping (Subsection 2.3.2) in which outwash of salinity is hampered by mouth geometry whereas influx of salinity is jet-like. Moreover, in Delta21 model runs, more tidal kinetic energy is dissipated at the doubly-constricted estuary mouth than pre-closure. The amount of tidal kinetic energy available is virtually unchanged compared to pre-1970 though. Therefore, enhanced mixing in both the HV front delta and zones east of HV sluices should occur which is is indeed apparent from numerical results (Figure I.1). Further east, the formation of steeper pycnoclines is observed (e.g. Figure 6.14) which indicates presence of the estuarine circulation,

albeit weak (Section 2.2). Salinity intrusion follows a preferential path along the southern bank of HV-HD in line with historical observations. Flow from Spui to the HV (via Old Meuse) is a significant source of salinity especially at Q=2100 m^3/s. This is likely triggered by southward (ebbing) flow and a much more saline Old Meuse due to SLR (here: 85cm).

Despite exaggeration by OSR-HV (Section 5.2), vertical mixing is likely to play a significant role post-Delta21. Sharp restratification is observed at ebb tide in the former HV front delta (now tidal lake) but restratification within the HV-HD appears weak at tested freshwater discharges (Q=1000, 2100 m^3/s). Lateral mixing is mostly observed in the westernmost part of the HV at Q=1000 m^3/s (drought) scenarios (e.g. Figure 6.9). SLR extends the influence of lateral mixing in up-estuary direction (also: Figure 6.9). The former constitutes the buffering function of the western HV causing the intrusion length to be limited to ≈36km upstream. Mixing is mainly observed in the HV, intrusion along deep bottom features (old tidal channels) continues within HD. This behaviour is in line with expectations drawn up using Richardson and Simpson numbers in Section 2.2. The estuarine character of HV-HD develops seawards for increasing Q_f.

On flood tide, extensive mixing occurs in the HV front delta mainly due to the presence of a shipping channel included in the Delta21 definition. The altered geometry of the estuary mouth gives rise to a pattern of advective acceleration-deceleration which generates significantly more turbulence than in the unperturbed estuary mouth. This gives the HV-HD a markedly different estuarine character than the RWW which shows to correspond more to a salt wedge regime. This difference also becomes apparent by comparing the velocity profiles over depth between the two estuaries (Appendix J) where baroclinic modes show to be either absent or weak in case of HV-HD.

In conclusion, full opening of the HV sluices after 2100 creates an estuarine character that corresponds best with that of 'partially mixed' (refer to Figure 2.1) with noticeable re-stratification during ebb tide in the westernmost part of the HV. In the current schematization, Q_f dominates the salinity intrusion length. SLR, despite not being the dominant forcing parameter, affects the entire water column resulting in +1-2PSU comparing lower and upper end SLR scenarios. The maximum intrusion length remains unaffected which indicates that SLR is mainly responsible for increased mixing.

SQI: *On what timescales does the new dynamic equilibrium form, if it forms at all?*

A dynamic equilibrium may never fully form due to a strong estuary response to forcing by river, wind and tide. The HV-HD however is a relatively robust (wide, deep) sea arm with a double estuary mouth (in Delta21) which significantly affects tidal energy penetration into the post-closure basin. Nevertheless, a distinct semi-diurnal salinity response is found in the west of the HV where tidal velocities are comparable to those of the pre-closure estuary. Salinity map output shows formation of a region with a tidally averaged near-constant salinity near ports of Moerdijk. This is likely to be the mean-to-maximum extent of salinity intrusion. More extensive salinity intrusion may occur under rare circumstances of strong up-estuary winds and low freshwater discharge such as during westerly summer storms. Such rare events can be a reason to manually close the HV sluices or Delta21 storm surge barrier.

Assessment of discharges exceeding $\bar{Q}_{\text{Lobith}}$=2100 m^3/s falls outside of the scope of this study but numerical results show exceedingly large outwash of salinity in the upper water column by raising discharge. It is therefore likely that the HV during periods of high precipitation and alpine snow melt develops an equilibrium more seaward and salinity dynamics more reminiscent of the RWW and corresponding ROFI. Lastly, stagnant saline zones are likely to develop in deep features (up to NAP-35.00m) found along both banks of the HV-HD. The salinity equilibria described here result in a transition zone from marine (33 PSU) to riverine (0 PSU) conditions of 18-29km upstream of the HV sluices depending on the applied boundary conditions This would result in the addition of (on average) 40 km^2 of estuariny at Q_{Lobith}=2100 m^3/s.

SQII: *Is the extent of salinity intrusion acceptable with regard to existing regional regulations, and if not, are mitigation strategies viable?*

Intake standards for surface water salinity are sensitive at 0.1-0.2 PSU (150-300 mg/L Cl^-). Model accuracy given boundary conditions as defined here is deemed insufficient to resolve salinity at this resolution. A best estimate can still be formulated looking at surface salinity timeseries in upstream reaches of the HD. Those unaffected by salinity intrusion show no departure from the imposed river

background concentration. Comparing Figures 3.3 and 5.1 it can be seen that most irrigation water intakes will require supply from sources further inland post-Delta21. Relocation of Bernisse intake to Strijensas is deemed sufficient in most scenarios given its position on the northern bank of HD. Closure of inland reservoirs to prevent salinity fluxes from Spui and Old Meuse will be needed for the greater part of the year. Irrigation water intake may be at risk during dry months though due to increased agricultural water demand and increased salinity intrusion into the RMB in low precipitation periods. Redundancy must be then be present in the form of e.g. POA, Klimaatbestendige Wateraanvoer (KWA), see (Mens (2018)) and buffering bodies such as Roode Vaart (Lavooij and Berke (2019)). Continued freshwater intake along HV-HD post-Delta21 is advised to take place along the northern banks to reduce risk of shutdown due to excessive salinity intrusion.

Acceptability of salinity intrusion is not merely related to drinking water standards here. Those benefited by economical operation of Moerdijk ports are affected too. Estuarine Turbidity Maxima (ETM) are known to coincide with the maximum salinity intrusion length (de Nijs et al. (2010)). Low Q_f scenarios show this point of maximum intrusion to be in the vicinity of Moerdijk ports. Presence of elevated SPM concentrations near port entrances typically drive baroclinic exchange of sediment with the port basins. This raises port OPEX as a result of increased dredging maintenance. Salt intrusion may need to be spatially more limited to satisfy requirements set by port operators in the Moerdijk area.

Raising the HV bridge sill to NAP-3.00m appears to be superfluous given the modelled circumstances. It is recommended here to not include this adaptation in Delta21 definition as it may prove a costly endeavour to raise the sill (approx. 200x1200x5m). Whereas the yield would be -1 to -4 PSU salinity for <30 d/y in the lower half of the water column at Moerdijk. Moreover, the effects of the raised sill would also enable unwanted capture of salinity in up-estuary direction. A combination of HV sluices closure and alternative water supply schemes is advised under the infrequent circumstances of prolonged intrusion east of the HV bridge.

SQIII: *What are the effects on salinity intrusion of varying the conveyance cross section of the Haringvliet dam?*

A first exploration was done to assess the effect of extending the Kierbesluit by 80% reduction of the HV sluices conveying cross-section. It is concluded that height-limiting of the HV sluices numerically resulted in relatively little reduction of horizontal salinity intrusion. It it theorised that flood currents are able to follow the historical flood tidal channels of the HV without too much dissipation of turbulent kinetic energy even at limited A_c of the HV sluices thereby reaching similar L_{max} at somewhat lower salinity due to lower influx of salinity. Freshwater discharge dominates the evolution of salinity in HV-HD. Therefore, HV sluices are of less impact in regulating salinity evolution during e.g. drought. Post-supply of salinity by Spui on ebb tide appears to cause poor outwash of salinity in tidally-averaged sense. Two-sided closure of the Spui may be helpful to secure freshwater storage for the region of Voorne-Putten. Freshwater supply from the east can then be realised as recommended in Lavooij and Berke (2019). Rinsing of the HV basin as is done as part of the current sluice program (Appendix B) can be effective to wash out diffused salt for a limited period. It is deemed unlikely that this practice is effective post-Delta21 due to large salt fluxes per flood cycle and increased intrusion from Spui.

8.2 Recommendations

Any numerical representation of the physical world is subject to both the consequences of simplifications made to mimic the system and the changes of the system itself. Therefore, recommendations for further research are included regarding modelling strategy and environmental factors. This list is an elaboration on Figure 7.2 and should be read as a hierarchy.

Modelling

- **Figure 7.2 - Boundary influences on ROFI**. The RMB branches and Dutch coastal zone form an interconnected system. Accurate reproduction of salinity in these areas relies on capturing the correct spatiotemporal fluxes of mass transport. OSR-HV currently employs shore normal boundaries that are likely to be too close to the RWW and HV estuary mouths (Subsection 4.6.1). Consequently, proper replication of state variables near discharging bodies (HV and Rotterdam

Waterway) is prevented and in turn the model domain is influenced by non-physical behaviour due to imposed boundary conditions within the area where Regions of Freshwater Influence develop.

- **Recommendation**: Extend the marine numerical domain to properly replicate near-coast ROFI development. Relocations of the southern North Sea boundary 20km southward and northern North Sea boundary 25 km northward are deemed necessary. The offshore North Sea boundary was found to be largely unaffected and therefore requires no relocation.

- **Figure 7.2 - Replication of front delta flow**. Absolute results must be treated prudently as especially model predictive capacity of salinity in the vertical shows to be low due to exaggerated vertical mixing. This in turn influences the vertical suppression of turbulence and baroclinic pressure gradients. Relative results of scenario runs are deemed trustworthy due to the small variation in parameters between scenarios. Schematization of open boundary conditions using numerically nested salinity profiles and harmonic velocities introduces inaccuracies regarding residual flows in the HV front delta. The barotropic mode is reproduced more faithfully.

  - **Recommendation**: A data campaign on front delta (tidal velocities, water levels and salinity) may aid in strengthening modelling capabilities of salinity transport across HV sluices. This campaign should take place at a, preferably lengthy, interval of opened HV sluices at flood.

- **Figure 7.2 - Absence of temperature model**. Water temperature is taken as a constant (10 °C) which is a simplification of the EoS through omission of contribution by temperature variability. This also affects the baroclinic pressure term in the SWE and therefore affects mass transport

  - **Recommendation**: include meteo-data, especially for drought scenarios, such as insolation, cloud cover and air temperature and/or specify a space-varying water temperature field on North Sea to include effects of temperature on density (thermal stratification, thermal wind).

- **Figure 7.2 - Sigma-layering of vertical**. Non-physical vertical diffusion and flow is likely to occur due to steep bottom gradients near HV bridge and in deep pits in the western HV basin. Another disadvantage of using σ-grids arises from the misalignment of vertical layers with pycnoclines. This causes for underestimation of stratification, especially halfway the water column where stratification may be pronounced and σ-layers are relatively thicker (Figure 4.3).

  - **Recommendation**: Implement anti-creep method after total computational demand has been brought down. Another option is to apply spatially varying vertical discretization where erratic bathymetry is described using z-layers and gentle bathymetry by sigma-layers. Such functionality is not yet available in TRIWAQ.

- **Figure 7.2 - Wind field description**. Wind forcing is taken to be geographically uniform. On average, this is conservative as Hook of Holland station generally yields larger wind speeds than recorded further inland. Mixing by wind in the HV-HD may thus be overestimated purely considering wind forcing. Wind set-up towards the coast may be underestimated though due to higher wind speeds at sea.

  - **Recommendation**: apply a space-varying wind field based on data originating from multiple environments to model wind shear stress and wind setup more accurately

- **Figure 7.2 - Hydrostatic approximation**. OSR-HV uses the hydrostatic approximation. Non-hydrostatic behaviour may occur within HV sluices (hydraulic jump) which is relevant to mixing phenomena of incoming water during flood tide and therefore relevant for predicting intrusion patterns.

  - **Recommendation**: Apply non-hydrostatic model schematization to better resolve flow near structures and vertically accelerating flow caused by (internal) waves and flow transitions.

- **Figure 7.2 - SLR prediction variability.** Climate change scenarios may differ across various research groups. Moreover, global assessments (Church and White (2006), Church et al. (2013), Oppenheimer et al. (2019)) are updated annually causing some pronounced differences with scenarios used here (ter Maat (2014)) particularly in terms of confidence intervals.

- **Figure 7.2 - Boundary representation of SLR.** Salinity replication relies on a sound representation of the flow field. Water level points are included in the offshore boundaries (Figure 4.6) to ensure sound replication of water levels. These water level points have been used to incorporate SLR. Tidal velocities remain unaltered (model assumption). Therefore, a change in MSL is represented by 14/156 boundary points in OSR-HV which may lead to additional marine forcing that is too weakly represented in the model.
- **Figure 7.2 - Effects of spring-neap cycles.** Simulation periods constituted to 31 days (Appendix H) which fully captures one spring-neap tidal cycle (T=14.5d). This makes distinguishing the effects of spring tides a difficult task. Table 3.4 shows that these effects may be considerable (of the order of SLR) for the Dutch coast.
    - **Recommendation**: Simulate longer periods to filter the effects of spring-neap cycles on salinity spreading in HV-HD. This may require additional simplifications to the model due to the already sizable computational demand.

Environment

- **Figure 7.2 - Additional uncertainty post-2100 CE.** Climate scenarios used here are taken for the year 2100 CE. Climate change trends however, are likely to persist during construction lifetime of Delta21 (2100-2200). Projections of e.g. 2200 AD are however both scarce and associated with additional (extreme) uncertainties and therefore not used for practical reasons.
- **Figure 7.2 - Morphological development North Sea, HV-HD.** Ongoing morphological developments, as of 2020, include bed erosion of Old Meuse, Spui, Noord and Dordtsche Kil. Further scouring of these branches allows for strengthened salinity fluxes between RWW and HV-HD post-Delta21. Upon opening the HV sluices, regained tidal dynamics are likely to cause scouring of the existing network of tidal channels in the HV-HD basin as well. Residual currents due to deepening are often associated with additional landward dispersion of salinity (MacCready (2004)). Moreover, engineering works that are not planned as per 2020 may be implemented in intermediate decades which can alter local hydrodynamics far more than climatic factors. (van Koningsveld et al. (2008)).
    - **Recommendation**: A separate morphological study may provide a more realistic geometry to assess post-2100 hydrodynamics. This study requires a focus on wave-tide interaction inside the HV-HD.
- **Figure 7.2 - Changes in macro hydrodynamics and meteo conditions.** Multi-decadal timescales introduce uncertainties surrounding: North Sea morphology (Tönis et al. (2002)), evolution of the tidal signal (Hollebrandse et al. (2005)) and stratification behaviour due to SLR, rising mean global temperature and river runoff variability. This study is used to establish an idea of the dynamic salinity equilibrium using (Section 1.4) relatively constant forcing conditions whereas the weather system post-Delta21 may be much more erratic and thereby does not allow for a stabilizing trend in the salinity profiles.
    - **Recommendation**: Subsequent hydrodynamic/salinity studies of Delta21 should elaborate on forcing events such as summer storms and fast outwash of salinity by river floods.

Policy & Legislation

- **Figure 7.2 - Brackish Volkerak Zoom lake**. Turning Volkerak Zoom lake saline as well is being considered to counter cyanobacteria blooms (Mens (2018)). Execution of this plan constitutes to another salinity influx boundary along the HV-HD.
    - **Recommendation**: Anticipate by including scenarios with an internal source of salinity at the location of the Volkerak sluices.
- **Figure 7.2 - Competing future-proofing plans.** Several measures meant for the security of fresh water resources and flood safety are already under development. These may all affect

decision-making on the future of the HV. To name a few: Wateraanvoer Roode Vaart, Kleinschalige Wateraanvoer (KWA), POA, Plan Sluizen.

- **Figure 7.2 - Changes to Delta21 definition due to compromises.** Delta21 is an under-development concept which aims at being universally applicable around the world. Layout of the plans for the Dutch southwestern delta are subject to changes as insight in processes, like salinity intrusion, becomes greater over time. Compare e.g. Figure A.1 and Figure A.2 which are sketches of Delta21 in 2019 and 2021 respectively. The 2019 layout has been used here.

Other considerations

These following recommendations do not play a pronounced role in the numerical description of the RMB for salinity intrusion though deserve a mention as well.

- Seaward Delta21 works (Appendix A) are likely to have an offshore-steering effect on the HV contribution to the Rhine ROFI (Subsection 3.2.4) due to reorientation of the estuary mouth. This is relevant for marine ecology and pollutant transport. Negative ecological effects for the south-eastern North Sea may thus be more severe than positive ecological effects for the HV which would render Delta21 as non-beneficial for the environment at large.
  - **Recommendation**: Assess the evolution of the Rhine ROFI in presence of Delta21. This requires a Dutch coastal model such as DCSM-FM mentioned in Section 7.2.
- Lyu and Zhu (2018) found that the Manning roughness coefficient may vary spatially in estuaries. Depth is the dominant parameter.
  - **Recommendation**: Consider application of spatially varying Manning coefficient (n) in HV-HD based on field measurements post-Kierbesluit.
- Spin-up times for flow and especially salinity are extensive which yields large computational time before generating useful results.
  - **Recommendation**: So-called 'hot start' or 'restart' runs may be generated for each climate scenario. This allows repeated simulation of scenarios with decimated spin-up. This has not been attempted here due to time limitations.

A

Delta21

Figure A.1 shows the basic geometry of seaward proposed interventions by Lavooij and Berke (2019) to future-proof the lower RMB.

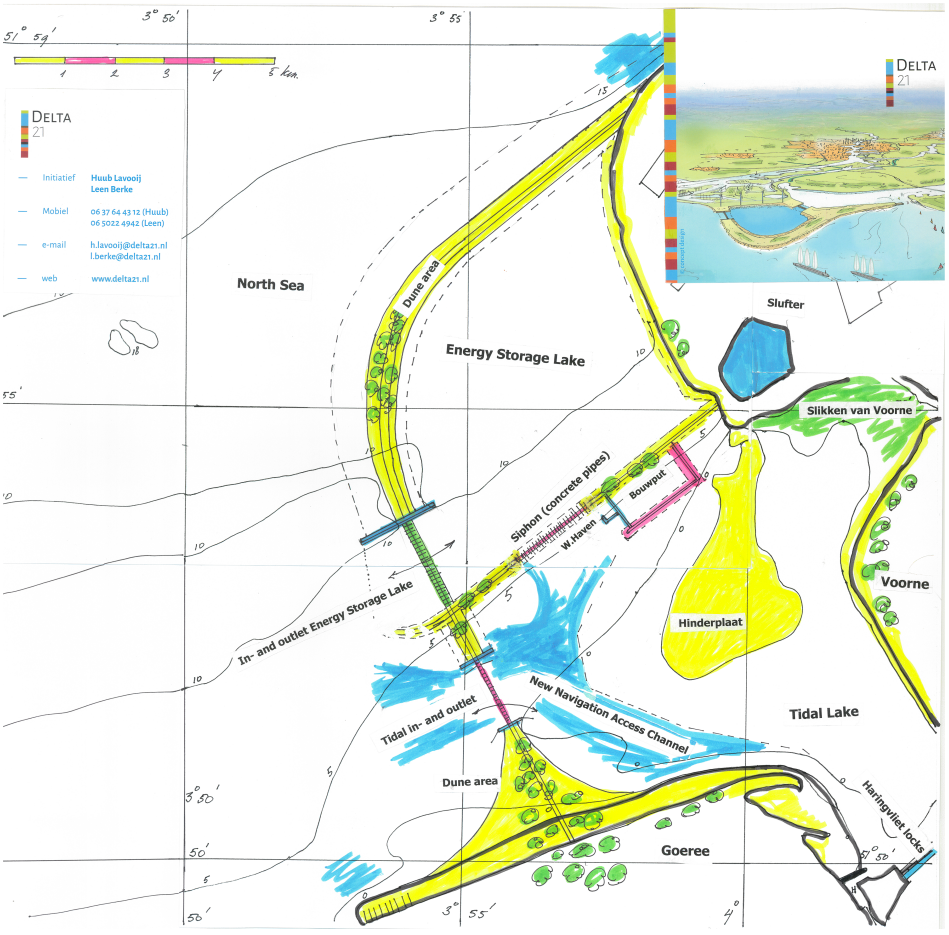

Figure A.1: Concept of the Delta21 North Sea area (Lavooij and Berke (2019)). Geometry used in this study.

Figure A.2 shows an updated (2021) sketch of the Delta21 concept in the RMB. Layout has, in part, been updated following results from this study.

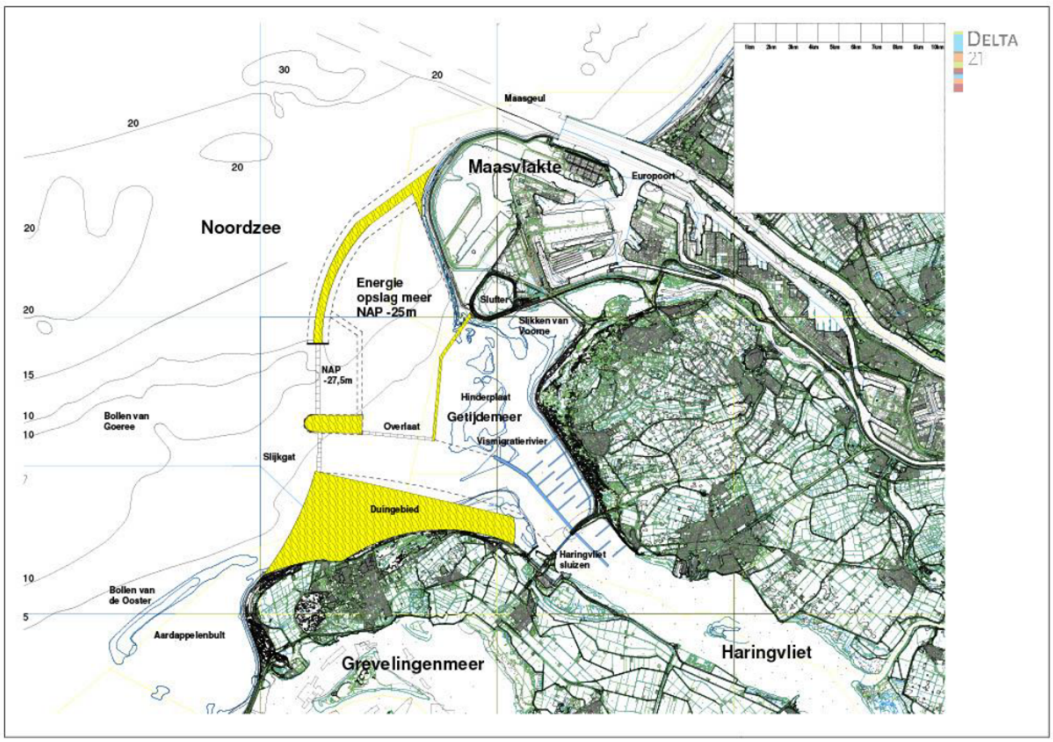

Figure A.2: Adapted geometry (2021) based on results in this study and other theses within Delta21.

B

Haringvliet sluices

Figures B.1-B.2 shows a conceptual cross-section of one HV sluice caisson (tot. 17) when (partially) opened at flood. Acceleration and deceleration (left) first mix incoming sea water. Further deceleration (right) mixes water just east of the element and is transported downwards. An element functions as an (im)perfect weir or spillway depending on the cross-dam water level gradient for a fully opened dam.

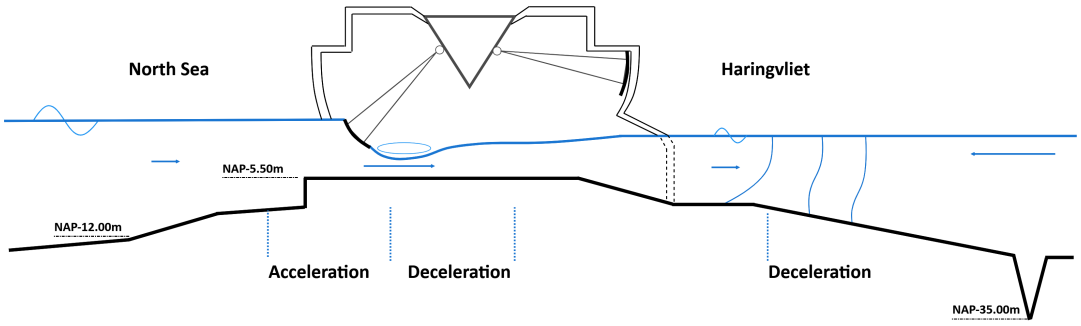

Figure B.1: Conceptual cross-section of single sluice caisson HV sluices - evolution of flow in spillway regime (Fr>1)

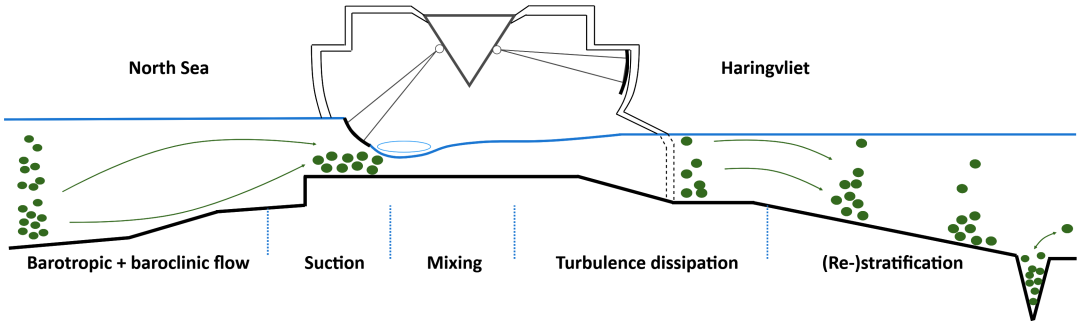

Figure B.2: Conceptual cross-section of single sluice caisson HV sluices - evolution of salinity in spillway regime (Fr>1)

Three HV sluicing programs are distinguished in this study. Before Jan '19, the 'Sluicing program

Haringvliet sluices' (Dutch: Lozingsprogramma Haringvlietsluizen 1984 (LPH84)) was in effect. The program meant complete closure of the HV sluices at flood and opening of salinity drains at ebb (Q=7 m^3/s), see Figure B.3. Recently, after decades of decision-making inertia (Marks et al. (2014)), Haringvliet sluices Operational Program (Dutch: Haringvliet Operationeel Programma (HOP)) came in effect (Figure B.4). Delta21 pursues a more natural system still by only closing HV sluices during prolonged drought (Figure B.5).

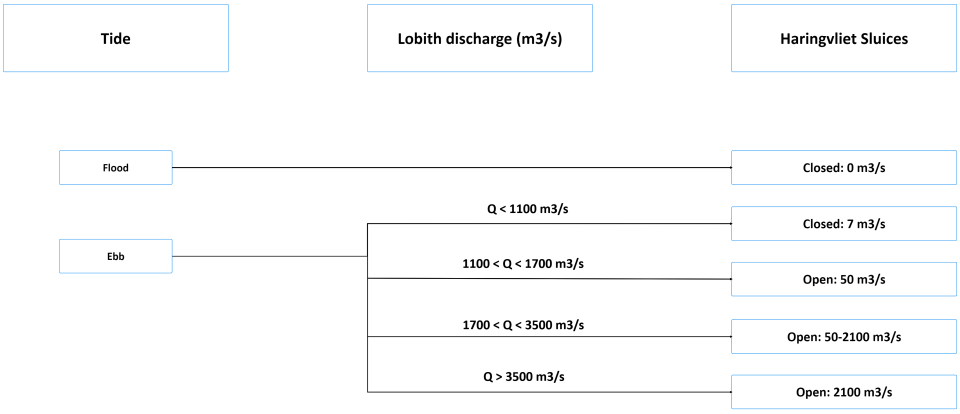

Figure B.3: Haringvliet Sluicing Program 1984 (Dutch: Lozingsprogramma Haringvlietsluizen 1984 (LPH84))

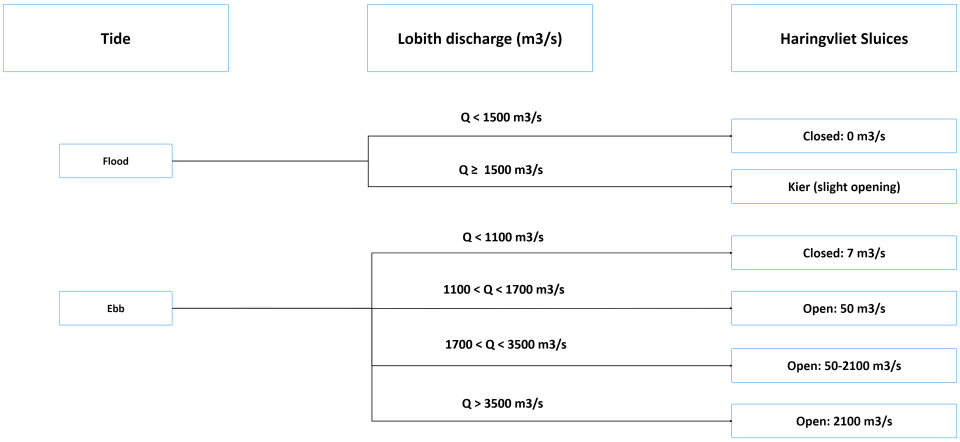

Figure B.4: Current (2020) operational program of the HV sluices (HOP)

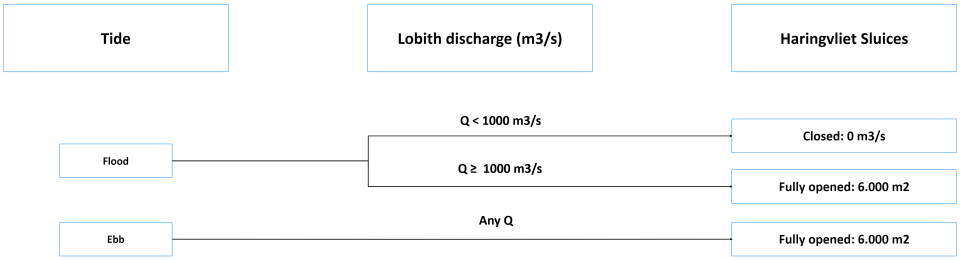

Figure B.5: Delta 21 operational program of the HV sluices

C

Dutch coastal ecology

Figure C.1 shows current (2020-21) protected Natura2000 areas in the RMB. Delta21 proposes to execute engineering works south of Maasvlakte II and in the HV for the benefit of ecology.

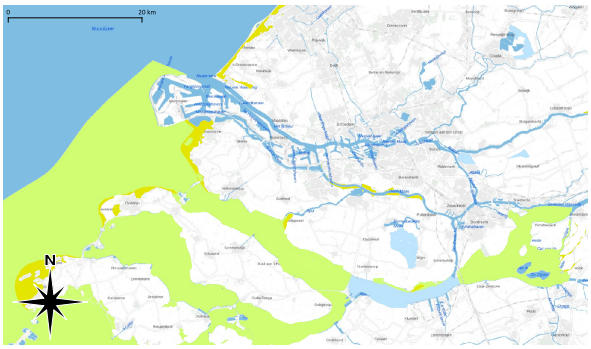

Figure C.1: Natura2000 areas: North Sea, Haringvliet, Grevelingen, Eastern Scheldt and Biesbosch in green (aquatic/intertidal) and yellow (terranean)

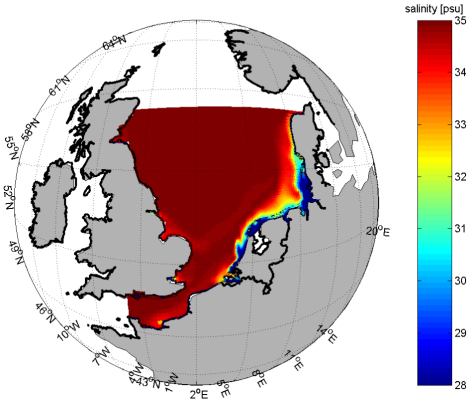

Figure C.2: Rhine ROFI depicted within North Sea domain. Further contribution to the ROFI originates from Ems-Dollard estuary (Germany). Results from Delft3D on ZUNO coarse grid. Image by Deltares.

D

Good Modelling Practice

Table D.1 is borrowed from Rijkswaterstaat (2005) and summarizes the guidelines issued in van Waveren et al. (1999). It was originally meant for use in corporations and governments but applies to academic work too. Some intermediate (detailed) steps have been left out.

The choices for software, space/time discretization and numerical approaches were done in one step by relying on OSR-HV as model. Sensitivity analyses and calibration rounds may be found in publications like Uittenbogaard et al. (2005) and Kranenburg and Schueder (2015), Kranenburg (2015).

Table D.1: Actions to comply with Good Modelling Practice

#	Activity
1	**Start a log and continue to use it**
2	**Setup of the modelling study**
2.1	Describe the problem
2.2	Define the objective
2.3	Analyse the context and agree on accountability
2.4	Formulate requirements
2.5	Create a work plan
3	**Setup of the model**
3.1	Choose starting point: data analysis, system analysis or conceptual model
3.2	Analyse the data
3.2.1	Determine basic information needed to create and run the model
3.2.2	Determine model analysis tools
3.2.3	Determine availability of (meta)data
3.3	Analyse the system
3.4	Create a conceptual model
3.5	Choose from existing software
3.6	Choose a time and space discretisation
3.7	Choose a numerical approach
3.8	Implement the model
3.9	Verify the model
4	**Analyse the model**
4.1	Make a plan-of-action for the analysis activities
4.2	Do a global analysis of the model
4.2.1	Do a standard input run
4.2.2	Do the global-behaviour test
4.2.3	Check the mass balances
4.2.4	Do a robustness test
4.3	Perform sensitivity analysis
4.4	If possible, perform a formal identification
4.5	Calibrate the model
4.6	Perform a reliability analysis
4.7	Validate the model
4.8	Determine the scope of validity
5	**Use the model**
5.1	Make a plan-of-action for the simulation runs
5.2	Perform the simulation runs
5.3	Check the results
6	**Interpret the results**
6.1	Describe the results
6.2	Discuss the results
6.3	Describe the conclusions
6.4	Check whether the objective is met
6.5	Summarize the results
6.6	Analyze the consequences for the research questions
7	**Report and archive**
7.1	Report in the target audience language
7.2	Make the study reproducible (archive)

E

Mathematical description

The Shallow Water Equations (SWE) combined with a transport relation (advection-diffusion) and turbulence closure model (k-ε) form the mathematical basis of TRIWAQ. The set of equations are shortly repeated here, reference is made to (Zijlema (1998), Deltares (2020)) for the precise description of the equations. The final set is solved on the numerical grid by OSR-HV to resolve hydrodynamics and salinity transport.

The Shallow Water Equations (SWE) form a set of partial differential equations (PDE) derived from these Navier-Stokes equations that is able to describe estuarine systems like the RMB. The key system property here is that horizontal dimensions (L,B) are far larger than the water depth (h). A series of (justified) assumptions and simplifications allow for more efficient solving of the equations, these are discussed below.

$$\frac{\partial \bar{u}}{\partial t} + \frac{\partial \bar{u}\bar{u}}{\partial x} + \frac{\partial \bar{u}\bar{v}}{\partial y} + \frac{\partial \bar{u}\bar{w}}{\partial z} + \frac{1}{\rho}\frac{\partial \bar{p}}{\partial x} - f\bar{v} - \frac{1}{\bar{\rho}}\left[\frac{\partial \tau_{xx}}{\partial x} + \frac{\partial \tau_{xy}}{\partial y} + \frac{\partial \tau_{xz}}{\partial z}\right] = f_1 \tag{E.1}$$

$$\frac{\partial \bar{v}}{\partial t} + \frac{\partial \bar{u}\bar{v}}{\partial x} + \frac{\partial \bar{v}\bar{v}}{\partial y} + \frac{\partial \bar{v}\bar{w}}{\partial z} + \frac{1}{\rho}\frac{\partial \bar{p}}{\partial y} + f\bar{u} - \frac{1}{\bar{\rho}}\left[\frac{\partial \tau_{yx}}{\partial x} + \frac{\partial \tau_{yy}}{\partial y} + \frac{\partial \tau_{yz}}{\partial z}\right] = f_2 \tag{E.2}$$

$$\frac{\partial \bar{w}}{\partial t} + \frac{\partial \bar{u}\bar{w}}{\partial x} + \frac{\partial \bar{v}\bar{w}}{\partial y} + \frac{\partial \bar{w}\bar{w}}{\partial z} + \frac{1}{\rho}\frac{\partial \bar{p}}{\partial z} + g - \frac{1}{\bar{\rho}}\left[\frac{\partial \tau_{zx}}{\partial x} + \frac{\partial \tau_{zy}}{\partial y} + \frac{\partial \tau_{zz}}{\partial z}\right] = f_3 \tag{E.3}$$

Table E.1 summarizes all steps that are made to arrive at the simplified set of SWE used here. It also describes the addition of equations for constituent transport and vertical mixing whereas the momentum equation in z-direction is reduced to the hydrostatic balance (Equation E.5) in the absence of significant wave action and widespread complex flow patterns in the vertical due to e.g. civil engineering structures. Also note that water level (h) is defined as local depth (d) plus water level elevation (ζ), see Equation E.4.

$$h = d + \zeta \tag{E.4}$$

$$\frac{\partial p}{\partial z} = -\rho g \tag{E.5}$$

Table E.1: Assumptions that applied to the Navier-Stokes equations resulting in 3D SWE with mass transport coupling

Basis	Action(s)	Affected term(s)	Result
Scale of interest	Reynolds averaging	All	RANS
Incompressibility	$\frac{D}{Dt} = 0$ in continuity eq.	Cont. eq.	ρ omitted in cont.
Hydrostatic pressure	Baroclinic, barotropic term	Pressure terms	Simplified p_z
Hydrostatic pressure	Set vertical accelerations to zero	Equation E.3	No accelerations in z
Boussinesq approximation	Replace ρ by constant ρ_0	ρ in E.1, E.2	Simplified p_x, p_y
Eddy viscosity concept	Define eddy viscosities ν_h, ν_v	Turbulent stresses	Simplified τ_{ij}
Eddy viscosity concept	Introduce k-ε model	New equations (2)	Inclusion vertical mixing
Transport physics	Introduce conv.-diff. equation	New equation	Inclusion of transport
Thermodynamics	Introduce EoS: $\rho = \rho(S,T)$	New equation	S,T-flow coupling

This way of space discretization can however yield an inaccurate description of processes near the bottom, especially for non-stably stratified systems with strong tidal forcing. Hence, the OSR-HV model, makes use of a boundary-fitted schematization of the vertical. This implies using a discretization of the vertical known as σ-layering. Curvilinear grids are often preferred to allow for local refining of resolution in areas of interest. This also applies to the OSR-H grid. The previous result is transformed further by switching from horizontal Cartesian coordinates (x,y) to curvilinear coordinates (ξ, η). The basis of the transformation is given in Equations E.6 and E.7. Also, the product of the transformation coefficients ($g_{\xi\xi}, g_{\eta\eta}$) is defined through Equation E.8. Source and sink terms can be found on the right hand side of Equations E.9 and E.10, these consist of discharges (q_{in}), extractions (q_{out}), precipitation (P) and evaporation (E), also see Equation E.11.

$$g_{\xi\xi} = \left(\frac{\partial x}{\partial \xi}\right)^2 + \left(\frac{\partial y}{\partial \xi}\right)^2 \tag{E.6}$$

$$g_{\eta\eta} = \left(\frac{\partial x}{\partial \eta}\right)^2 + \left(\frac{\partial y}{\partial \eta}\right)^2 \tag{E.7}$$

$$g_* = g_{\xi\xi} \cdot g_{\eta\eta} \tag{E.8}$$

The order of the equations is again: local and global continuity (Equations E.9, E.10), horizontal momentum conservation (Equations E.12, E.13) including external sources/sinks of momentum (M_ξ, M_η), pressure decomposition into barotropic and baroclinic terms (Equation E.14), conversion of turbulent stresses (Equations E.15, E.16 and E.17) for use in the transport relation (Equation E.18). Again, a source and sink term (S_c) is included (Equation E.19) as well. Decay processes are excluded here as salinity is an abiotic constituent which is not reduced by biological factors. Finally, the k-ε model is described by Equations E.20 and E.21. The hydrostatic balance remains unaltered (Equation E.5).

$$\frac{\partial \zeta}{\partial t} + \frac{1}{\sqrt{g_*}}\frac{\partial [hu\sqrt{g_{\eta\eta}}]}{\partial \xi} + \frac{1}{\sqrt{g_*}}\frac{\partial [hv\sqrt{g_{\xi\xi}}]}{\partial \eta} + \frac{\partial \omega}{\partial \sigma} = H\,(q_{in} - q_{out}) \tag{E.9}$$

$$\frac{\partial \zeta}{\partial t} + \frac{1}{\sqrt{g_*}} \frac{\partial [hU\sqrt{g_{\eta\eta}}]}{\partial \xi} + \frac{1}{\sqrt{g_*}} \frac{\partial [hV\sqrt{g_{\xi\xi}}]}{\partial \eta} = Q \tag{E.10}$$

$$Q = H \int_{-1}^{0} (q_{in} - q_{out})\, d\sigma + P - E \tag{E.11}$$

$$\frac{\partial u}{\partial t} + \frac{u}{\sqrt{g_{\xi\xi}}} \frac{\partial u}{\partial \xi} + \frac{v}{\sqrt{g_{\eta\eta}}} \frac{\partial u}{\partial \eta} + \frac{\omega}{h} \frac{\partial u}{\partial \sigma} - \frac{v^2}{\sqrt{g_*}} \frac{\partial \sqrt{g_{\eta\eta}}}{\partial \xi} + \frac{uv}{\sqrt{g_*}} \frac{\partial \sqrt{g_{\xi\xi}}}{\partial \eta} = -\frac{1}{\rho_0 \sqrt{g_{\xi\xi}}} P_\xi + F_\xi + \frac{1}{h^2} \frac{\partial}{\partial \sigma} \left(\nu_V \frac{\partial u}{\partial \sigma} \right) + fv + M_\xi \tag{E.12}$$

$$\frac{\partial v}{\partial t} + \frac{u}{\sqrt{g_{\xi\xi}}} \frac{\partial v}{\partial \xi} + \frac{v}{\sqrt{g_{\eta\eta}}} \frac{\partial v}{\partial \eta} + \frac{\omega}{h} \frac{\partial v}{\partial \sigma} + \frac{uv}{\sqrt{g_*}} \frac{\partial \sqrt{g_{\eta\eta}}}{\partial \xi} - \frac{u^2}{\sqrt{g_*}} \frac{\partial \sqrt{g_{\xi\xi}}}{\partial \eta} = -\frac{1}{\rho_0 \sqrt{g_{\eta\eta}}} P_\eta + F_\eta + \frac{1}{h^2} \frac{\partial}{\partial \sigma} \left(\nu_V \frac{\partial v}{\partial \sigma} \right) - fu + M_\eta \tag{E.13}$$

$$P_\xi = \rho_0 g \frac{\partial \zeta}{\partial \xi} + gh \int_\sigma^0 \left(\frac{\partial \rho}{\partial \xi} + \frac{\partial \rho}{\partial \sigma} \frac{\partial \sigma}{\partial \xi} \right) d\sigma', \quad P_\eta = \rho_0 g \frac{\partial \zeta}{\partial \eta} + gh \int_\sigma^0 \left(\frac{\partial \rho}{\partial \eta} + \frac{\partial \rho}{\partial \sigma} \frac{\partial \sigma}{\partial \eta} \right) d\sigma' \tag{E.14}$$

$$F_\xi = \frac{1}{\sqrt{g_{\xi\xi}}} \frac{\partial \tau_{\xi\xi}}{\partial \xi} + \frac{1}{\sqrt{g_{\eta\eta}}} \frac{\partial \tau_{\xi\eta}}{\partial \eta}, \quad F_\eta = \frac{1}{\sqrt{g_{\xi\xi}}} \frac{\partial \tau_{\eta\xi}}{\partial \xi} + \frac{1}{\sqrt{g_{\eta\eta}}} \frac{\partial \tau_{\eta\eta}}{\partial \eta} \tag{E.15}$$

$$\tau_{\xi\xi} = \frac{2\nu_H}{\sqrt{g_{\xi\xi}}} \left(\frac{\partial u}{\partial \xi} + \frac{\partial u}{\partial \sigma} \frac{\partial \sigma}{\partial \xi} \right), \quad \tau_{\eta\eta} = \frac{2\nu_H}{\sqrt{g_{\eta\eta}}} \left(\frac{\partial v}{\partial \eta} + \frac{\partial v}{\partial \sigma} \frac{\partial \sigma}{\partial \eta} \right) \tag{E.16}$$

$$\tau_{\xi\eta} = \tau_{\eta\xi} = \nu_H \left\{ \frac{1}{\sqrt{g_{\eta\eta}}} \left(\frac{\partial u}{\partial \eta} + \frac{\partial u}{\partial \sigma} \frac{\partial \sigma}{\partial \eta} \right) + \frac{1}{\sqrt{g_{\xi\xi}}} \left(\frac{\partial v}{\partial \xi} + \frac{\partial v}{\partial \sigma} \frac{\partial \sigma}{\partial \xi} \right) \right\} \tag{E.17}$$

$$\frac{\partial hc}{\partial t} + \frac{1}{\sqrt{g_*}} \left\{ \frac{\partial [\sqrt{g_{\eta\eta}} huc]}{\partial \xi} + \frac{\partial [\sqrt{g_{\xi\xi}} hvc]}{\partial \eta} \right\} + \frac{\partial \omega c}{\partial \sigma} = \frac{h}{\sqrt{g_*}} \left\{ \frac{\partial}{\partial \xi} \left(D_H \frac{\sqrt{g_{\eta\eta}}}{\sqrt{g_{\xi\xi}}} \frac{\partial c}{\partial \xi} \right) + \frac{\partial}{\partial \eta} \left(D_H \frac{\sqrt{g_{\xi\xi}}}{\sqrt{g_{\eta\eta}}} \frac{\partial c}{\partial \eta} \right) \right\} + \frac{1}{h} \frac{\partial}{\partial \sigma} \left(D_V \frac{\partial c}{\partial \sigma} \right) + hS_c \tag{E.18}$$

$$S_c = (q_{in} c_{in} - q_{out} c) + q_{tot} \tag{E.19}$$

$$\frac{\partial k}{\partial t} + \frac{u}{\sqrt{g_{\xi\xi}}} \frac{\partial k}{\partial \xi} + \frac{v}{\sqrt{g_{\eta\eta}}} \frac{\partial k}{\partial \eta} + \frac{\omega}{h} \frac{\partial k}{\partial \sigma} = + \frac{1}{h^2} \frac{\partial}{\partial \sigma} \left(D_k \frac{\partial k}{\partial \sigma} \right) + P_k + P_{kw} + B_k - \varepsilon \tag{E.20}$$

$$\frac{\partial \varepsilon}{\partial t} + \frac{u}{\sqrt{g_{\xi\xi}}}\frac{\partial \varepsilon}{\partial \xi} + \frac{v}{\sqrt{g_{\eta\eta}}}\frac{\partial \varepsilon}{\partial \eta} + \frac{\omega}{h}\frac{\partial \varepsilon}{\partial \sigma} = \frac{1}{h^2}\frac{\partial}{\partial \sigma}\left(D_\varepsilon \frac{\partial \varepsilon}{\partial \sigma}\right) + P_\varepsilon + P_{\varepsilon w} + B_\varepsilon - c_{2\varepsilon}\frac{\varepsilon^2}{k} \tag{E.21}$$

Note that the k-ε model (E.20 and E.21) makes use of derivatives written in the non-conservative form. This approach is justified by the assumption that the production (P_ε), buoyancy flux (B_ε) and dissipation terms (ε) dominate over the turbulence quantities (de Nijs et al. (2011), Deltares (2020)).

The set of equations is completed by defining how variations in density (ρ) should be modelled. Nowadays, water density is preferably described by the UNESCO equation of state (EoS). Equation E.22 describes a combined polynomial of salinity (S) and temperature (T) with the reference density of pure water (Equation E.23) as base value (Millero and Poisson (1981)). In this study, salinity is assumed to dominate density in the EoS and therefore constant water temperature of 10 °C is applied to the Equations E.23-E.24.

$$\rho(S,T) = \rho_0 + AS + BS^{3/2} + CS \tag{E.22}$$

$$\rho_0 = 999.84 + 6.79\times 6.792^{-2}\cdot T - 9.10\times 10^{-3}\cdot T^2 + 1.00\times 10^{-4}\cdot T^3 - 1.12\times 10^{-6}\cdot T^4 + 6.54\times 10^{-9}\cdot T^5 \tag{E.23}$$

$$\begin{gathered} A = 8.2449\times 10^{-1} - 4.0899\times 10^{-3}\cdot T + 7.6438\times 10^{-5}\cdot T^2 - 8.247\times 10^{-7}\cdot T^3 + 5.388\times 10^{-9}\cdot T^4 \\ B = -5.72466\times 10^{-3} + 1.0227\times 10^{-4}\cdot T - 1.6546\times 10^{-6}\cdot T^2 \\ C = 4.8314\times 10^{-4} \end{gathered} \tag{E.24}$$

The resulting system of SWE has a hyperbolic (or wave-like) character in the horizontal direction. This means that fluid motion is described by characteristic planes for 2D and 3D problems. The number of in-going characteristics at the boundaries determine where and how many boundary conditions are needed (van Kester et al. (2001)). At the time of writing (2020-21), direct numerical simulation (DNS) which resolves all fluid motions was not feasible due to the extreme computational demand. Therefore, operators of numerical models are responsible for applying simplifications of physical processes. In 3D hydrodynamic mass transport modelling these are dominated by: boundary conditions, (horizontal) eddy viscosity, (horizontal) diffusion coefficients, external forcing (wind, bottom friction), bathymetry, discharge coefficients (barriers) and numerical settings.

F

OSR-HV model

A more detailed description of the OSR-HV numerical model is supplied below. Properties of SIMONA regarding functionalities, grid, physical features, hydrodynamics and computational methods will be treated, in that order. The appendix is an aggregation of information found in the SIMONA user documentation, mostly Zijlema (1998), van Kester et al. (2001) and Rijkswaterstaat (2005).

SIMONA

OSR-HV is run in the SIMONA (SImulatie MOdellen NAtte waterstaat) program. This program was developed by RWS in the 1980s to warrant the consistency and quality of modelling studies across different departments and in time (Rijkswaterstaat (2005)). First, WAQUA was conceived for doing depth-averaged (2D) model runs. Then, as complexity of these calculations increased as well, TRIWAQ (3D) was developed to allow for layering in the vertical. Input to SIMONA is done through bundling of data, conditions and numerical settings in an ASCII-format file called siminp. This siminp file is structured in a hierarchy of blocks and sub-blocks demarcated by preprogrammed keywords. Siminp is read by the pre-processing unit and converted to a binary SIMONA Datastorage (SDS) file. Error messages are generated instead of the SDS file in case of an improper siminp file (Zijlema (2006)).

Grid

The geographical scope is small relative to the dimensions of the Earth (<1° lat/lon), meaning the plane on which the geographical area of interest is found may be assumed flat. The RMB is however, a (semi-)natural system with curved geometry which motivates the choice for a curvilinear grid in the horizontal rather than a rectilinear or spherical one (Rijkswaterstaat (2005)). SIMONA allows manual construction of a grid but in practice the RGFGRID tool is applied to generate grids. This tool ensures that requirements regarding grid smoothness ($\pm 20\%$ neighbouring cell size) and orthogonality (85-95°intersect) are met (Zijlema (1998)). Cell sizes in the OSR-HV grid are 20-50 m.

A choice between two types of discretization remain for the vertical: an equidistant z-layering or a terrain-following σ-layering (Figure 4.3). Z-layering approaches the bathymetry as a staircase. It has the advantage that the PDE that need to be solved by the model do not need coordinate conversion. Density driven flows can be well described by z-layering if the system is weakly forced (i.e. non-tidal or micro-tidal). A weak forcing implies that the system is more stably stratified causing pycnoclines to be thinner and more horizontal. The σ-coordinate system, due to its curvature, is more suitable to describe the system at hand as it is meso-tidally forced (Deltares (2020)) and stratification is periodically instable in the SIPS regime. Smaller (relative) thicknesses are applied near the bottom to gain accuracy here. This is depicted in Table F.1. The σ-coordinates are defined positive upwards and each layer is assigned

Table F.1: Non-equidistant sigma layering - OSR-HV

Layer no.	% of depth
1	12.0
2	12.0
3	11.0
4	11.0
5	11.0
6	11.0
7	11.0
8	9.0
9	9.0
10	6.0

a fractional value relative to local water depth. The free surface is taken as the origin of the σ-axis i.e. $\sigma(\zeta)$=0 and σ(-d)=-1. Main advantage is that it reaches a high resolution in shallow areas which is expressed in an accurate description of water levels. Disadvantage is that σ-layering causes an effect called artificial creep in which non-physical transports in the vertical occur due to curvature of the grid in presence of large bottom density gradients (Deltares (2020)) and/or steeply sloping geography (Zijlema (1998)). An anti-creep method is applied here to counteract this effect. Moreover, the PDE solved by the numerical model need conversion from z to σ-coordinates.

The lef-to-right direction is defined by an m-axis running from m=0 to m=MMAX. Velocity u is defined along this axis. Similarly, the bottom-to-top direction is defined by an n-axis running from n=0 to n=NMAX and velocity v aligns with this axis. Grid staggering is applied to represent the coupled physics of water level gradients and fluxes. The staggered grid arrangement can best be imagined as a mesh subdivided in water columns (quadrangles) across the system that experience in- and outflow a the center of their interfaces. The corner points represent varying water levels.

TRIWAQ solves the SWE (Appendix E) for each of the 10 σ-layers on a staggered grid cell arrangement. Water level points (ζ) are found half a grid cell to either side of velocity points (u,v) in such a grid arrangement. Depth points are then defined at the center of the water levels and velocities. This configuration of grid cells is possible because the water levels are defined by discharge fluxes (hu, hv) at the face of the respective cells. Conversely, the velocities are defined by the pressure gradient (Δh) over the cell interfaces. This way, the grid reflects the coupled physics of water levels and flow velocities better than it does in a co-located grid arrangement (Zijlema (2019), Deltares (2020)). Diffusion coefficients are defined at water level points (Rijkswaterstaat (2008)), see Figure F.1. The grid enclosure captures all active cells. These cells then serve as control volumes which experience fluxes at the centre of their interfaces, fluxes through the enclosure are zero by definition.

A curvilinear grid is applied to allow for spatial deviations in grid resolution. Areas of less interest can then be described by a more coarse grid and vice versa. A curvilinear grid does, however still impose requirements on orthogonality and local resolution differences of the (m,n)-mesh (Deltares (2020)). Moreover, it alters the set of PDE by changing to another coordinate system (Appendix E).

The layout of the applied grid and timestep (1/8th min.) result in a distribution of Courant numbers according to Figure F.2. The implicit description used in TRIWAQ does not impose limitations on the Courant number for stability (Zijlema (1998), Deltares (2020)). Large Courant numbers ($\gg$1) may however result in inaccuracies. Figure F.2 shows that C of O(100) can be found in areas such as tidal flats, beaches and shallows (blue colored). Numerical output is likely to be of relatively poor quality there. Courant numbers of 1-20 are typically found on the North Sea and HV and C<1 in the coastal zone with exception of the Delta21 shipping lane. The latter may introduce some inaccuracies to the numerical approximations in the HV front delta. Courant numbers are somewhat higher in the

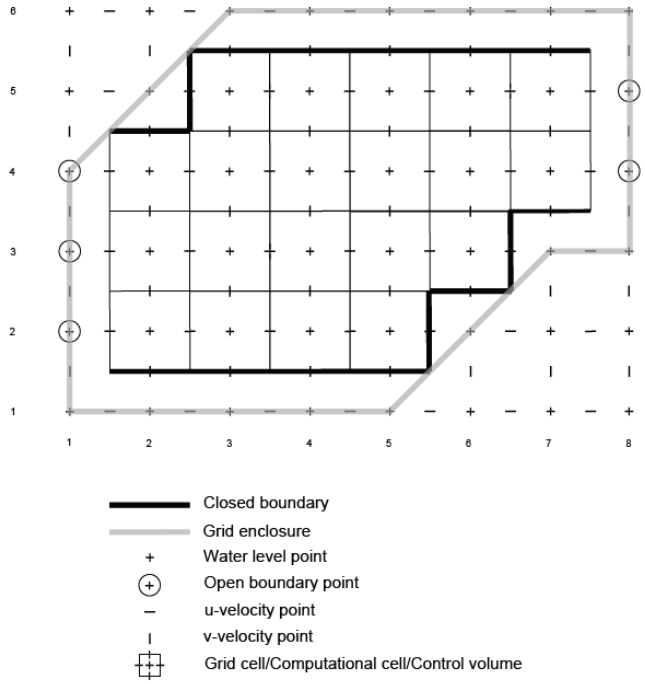

Figure F.1: Grid used for solving SWE in WAQUA/TRIWAQ. Notice the staggered configuration of h and u,v. Closed boundary=land boundary. Inactive cells are situated between the grid enclosure and closed boundary.

Rotterdam Waterways.

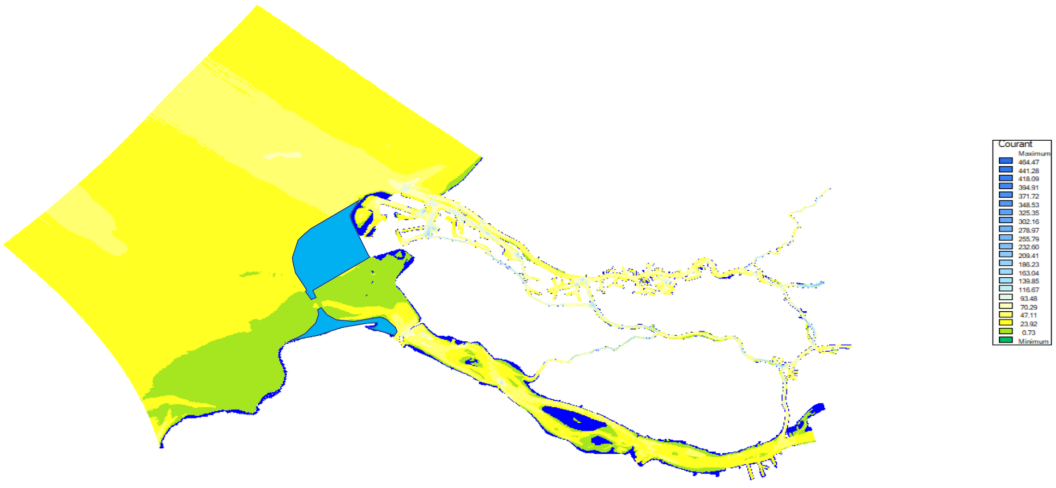

Figure F.2: Courant numbers (C) for Delta21 bathymetry. Notice Delta21 shipping channel which cause larger values of C in the near-coast. Blue values (C of O(100)) are present in sporadically flooded or non-flooded domains.

Physical features

Table F.2 summarizes global constants imposed upon the model domain. Initial water level for HV-HD is chosen larger than mean HW to prevent excessive influx of salinity during spin-up. Wind stress coefficient (C_D) and air density (ρ_a) are applied in Equation F.1 to calculate wind stress (τ_w) which is used for surface boundary conditions (Zijlema (1998)). Bed boundary conditions are defined using a 3D Chézy coefficient (C_{3D}) which follows from adapting C_{2D}. This procedure is described in detail in Zijlema (1998) and is not repeated here. Horizontal diffusion across the HV sluices ($D_{h,Hvs}$) is set to zero due to excessive salinity transport through the closure work (Kranenburg (2015)).

Table F.2: Physical global constants that have been supplied to TRIWAQ to simulate 3D hydrodynamics and salinity transport in the RMB. Locally, values may differ

Physical constant	**Symbol**	**Value**	**Unit**
Gravitational acceleration	g	9.81	$[m/s^2]$
Marine water background density	ρ	1000	$[kg/m^3]$
Freshwater reference density	ρ	1000	$[kg/m^3]$
Global water level (HV-HD)	h	1.25	$[m]$
Water temperature	T	10	[°C]
Marine salinity (North Sea)	S	33	$[PSU]$
Air density	ρ_a	1.205	$[kg/m^3]$
Wind stress coefficient	C_D	0.0026	-
Longitudinal Manning coefficient	n_x	0.020	$[m^{-1/3}s]$
Lateral Manning coefficient	n_y	0.020	$[m^{-1/3}s]$
Hor. diffusion coefficient	D_h	0.01	$[m^2/s]$
Hor. diffusion coefficient (HV sluices)	$D_{h,HVs}$	0.00	$[m^2/s]$
Hor. eddy viscosity coefficient	ν_h	1.00	$[m^2/s]$

$$|\tau_w| = \rho_a C_d W_{10}^2 \tag{F.1}$$

$$C_{2D} = \frac{(\zeta + d)^{\frac{1}{6}}}{n_{x,y}} \tag{F.2}$$

An important model adaptation compared to OSR-NSC is the description of locally varying diffusion coefficients in the upstream domain (Kranenburg and Schueder (2015), Kranenburg (2015)). This was done in a recalibration round by Svašek Hydraulics, the creators of the original OSR-NSC model to better match salinity concentrations in the upstream domain. The exact description of the new diffusion coefficients is shown in Figure F.3.

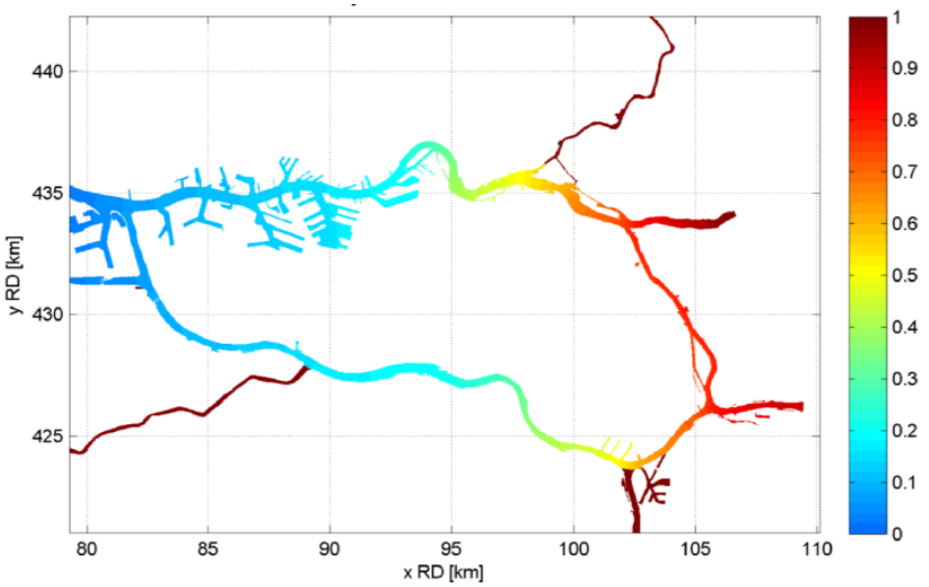

Figure F.3: Zoomed plot (Spui-Old Meuse-RWW-Noord-Dordtsche Kil) of horizontal diffusion coefficients [m^2/s] assigned locally higher values in the east of the RMB near riverine open boundaries as recommended by Kranenburg and Schueder (2015)

The RMB land boundary file (.rrb) is used to make cells that are not flooded in the simulation inactive. The remaining boundaries are open boundaries for flow and transport listed in Table F.3. DK and SS

Table F.3: Default flow and transport boundary conditions of OSR-HV

Figure 4.6	Location	Flow	Transport	Model code
L	Lek	Discharge (Q-ad)	Discharge (Q-ad)	P8013-14
DK	Dordtsche Kil	Discharge (Q-ad)	-	P8025-8026
HV	Haringvliet	Discharge (17x)	Irregular timeseries (17x)	P8050-8082
SS	Spui South	Discharge (Q-ad)	-	P8090-8091
BM	Ben. Merwede	Discharge (Q-ad)	Discharge (Q-ad)	P8094-95
NS1	North Sea	Water level/velocities	Timeseries	P9000-9047
NS2	North Sea	Velocities	Timeseries	P9048-9108
NS3	North Sea	Velocities	Timeseries	P9109-9155
MB	Moerdijk bridge	Discharge (Q-ad)	Discharge (Q-ad)	P10001-2

Table F.4: Barriers included in OSR-HV as internal boundaries

Civil structure	Location	Type	Model code
Maeslantkering	New Waterway	Storm surge barrier	P501-502
Hollandsche Ijssel Lock	Hollandsche Ijssel	(Shipping) lock	P503-504
Hollandsche Ijssel Barrier	Hollandsche Ijssel	Storm surge barrier	P505-506
Rozenburg Lock	Caland channel	(Shipping) lock	P507-508
Hartel Lock	Hartel channel	(Shipping) lock	P509-510
HV Sluices (17x)	North Sea	Closure work	P511-544
Hartel Barrier North	Hartel channel	Storm surge barrier	P545-546
Hartel Barrier South	Hartel channel	Storm surge barrier	P547-548

are internal boundaries that contribute to flow only. Hence, no transport input is defined for these two boundaries. The first columns refer to the markers included in Figure 4.6.

A number of barriers have been included in OSR-HV. These serve as internal boundary conditions and are listed in Table F.4. These barriers have their own time-dependent operating programs. Storm surge barriers are opened for all simulations in this study as storm conditions are not assessed (Section 4.6).

The following figures show depth contours (0-30 m min/max.) of the entire OSR-HV hydrodynamic grid (Figure F.4a), HV-HD (Figure F.4b) and RWW (Figure F.4c). Note that depths may locally exceed 30m but the scale is chosen to allow for better differentiation between 10-20m depths. Moreover, Maasvlakte II is modelled as a permanently emerged grid section and Delta21 geometry (Appendix A) is closed of from hydrodynamics influences which make the modelling of Delta21 energy lake (Appendix A) more analogous to an actual lake.

Computational methods

Integration is done per half timestep on a staggered grid. Advantage of this method is that it prevents wiggling of the solution (no need for numerical dissipation) and saves in computational cost. The main disadvantage though, is that it requires interpolation of the state variables. The state variables are: streamwise flow velocity (u), lateral flow velocity (v), elevation of the water surface (ζ) and contituent concentrations (c). WAQUA/TRIWAQ employs an Alternating Direction Implicit (ADI) scheme. This scheme is unconditionally stable and second order accurate in space and time. Moreover, its computational efficiency due to grid staggering and ability to solve both steady state and time-dependent problems make it suitable for solving the SWE. A tri-diagonal system of equations for water levels results from substituting the momentum equations in continuity equation. The computed water levels are then substituted back into the momentum equations to find the velocities Deltares (2020). Also, it is mass conserving which is an important feature for describing constituent transport. Mass conservation is mathematically expressed through inclusion of constituent concentrations (c) in the PDE derivatives rather than as a constant.

The ADI scheme alternates which horizontal term (u,v) is integrated explicitly/implicitly for each half timestep. Figure F.5 uses subscripts i,j for directions x,y respectively. The x,y directions can be changed for polar or curvilinear horizontal coordinates depending on which coordinate system is used. This will

not affect the execution of the scheme as the employed coordinate system is incorporated in the SWE. Furthermore, each integration step includes integration over a whole number of assigned σ-layers, denoted by subscript n.

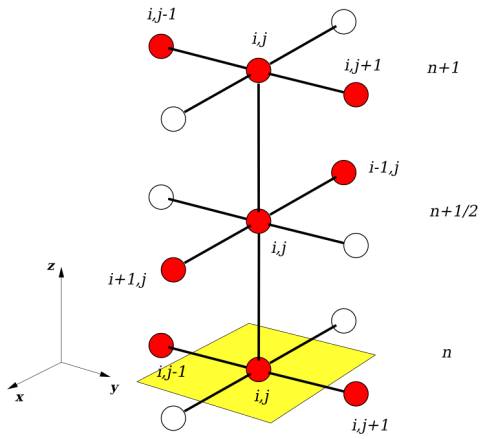

Figure F.5: Stencil of numerical scheme: ADI - work © Sidney.hy.li / Wikimedia Commons / CC-BY-SA-3.0

For 2D calculations (WAQUA) the scheme is unconditionally stable and no second order artificial viscosity is needed to counter inaccuracies. TRIWAQ however, couples the equation for salinity transport to that of momentum. This introduces a weak stability stability condition based on the Courant number of internal waves (Equation F.3). Note that $g' = \varepsilon g$ is of O(10^{-1}). This is no CFL condition, as the scheme is implicit (Zijlema (1998)).

$$C_{wave} = 2\Delta t \sqrt{g'H\left(\frac{1}{\left(\Delta\xi\sqrt{g_{\xi\xi}}\right)} + \frac{1}{\left(\Delta\eta\sqrt{g_{\eta\eta}}\right)}\right)} \tag{F.3}$$

These inaccuracies are known as the ADI-problem and occur upon applying Courant numbers according to Equation F.4 combined with a flow field that is not aligned with the local grid lines. Such situations arise in or near complex geometries. Such geometries contain at least 2 angles of 90 °. Stelling (1983) gives the example of a 'zig-zag' channel. This equally applies to coastlines that are misaligned with the local grid.

$$C_{\text{wave}} \geq 4\sqrt{2} \tag{F.4}$$

The horizontal viscosity term (ν_h) is time-integrated by use of the Crank-Nicolson scheme. This may produce oscillations. The stability condition is given by Equation F.5. This condition, combined with the geographical scope, is the main reason for the extensive runtime of OSR-HV as it poses the strictest limitation on Δt.

$$\Delta t \leq \frac{1}{\nu_H}\left(\frac{1}{\left(\Delta\xi\sqrt{g_{\xi\xi}}\right)^2} + \frac{1}{\left(\Delta\eta\sqrt{g_{\eta\eta}}\right)^2}\right)^{-1} \tag{F.5}$$

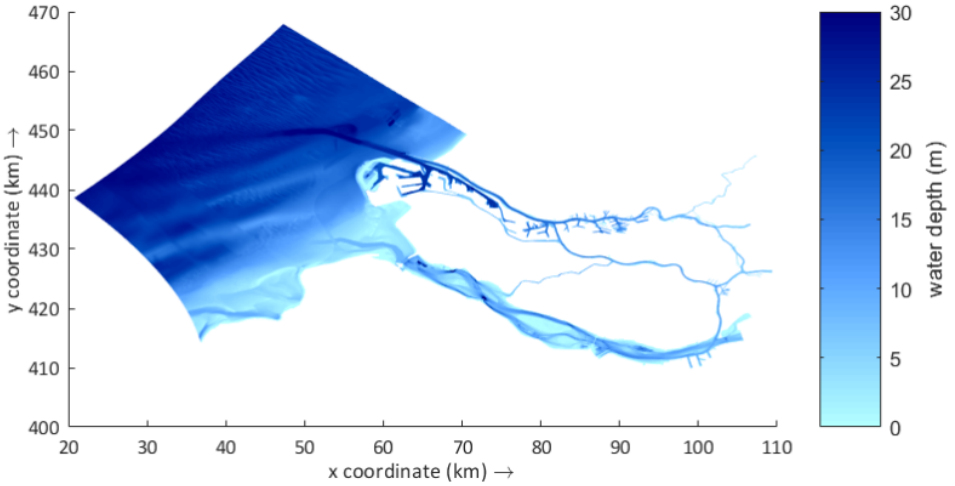

(a) Bathymetry of the OSR-HV hydrodynamic grid. Notice Delta21 shipping channel (x=50-60km, NAP-8.00m) in the HV front delta and the deep (30-40m) entry to PoR (x=50-60 km, north)

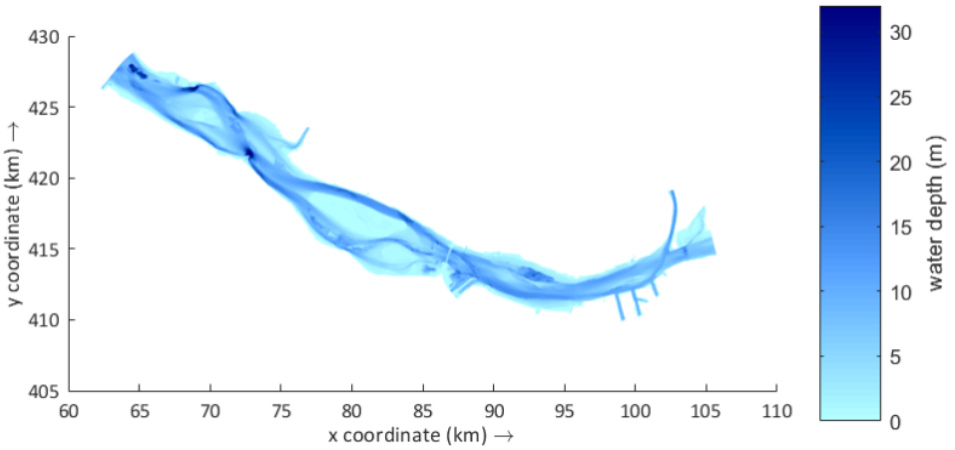

(b) Bathymetry of the OSR-HV hydrodynamic grid: HV-HD. Notice the distinct estuarine features which have been preserved from the pre-1970 era. Ports of Moerdijk visible (x=98-102 km) as well as Spui south (x=75 km) and Dordtse Kil (x=103 km)

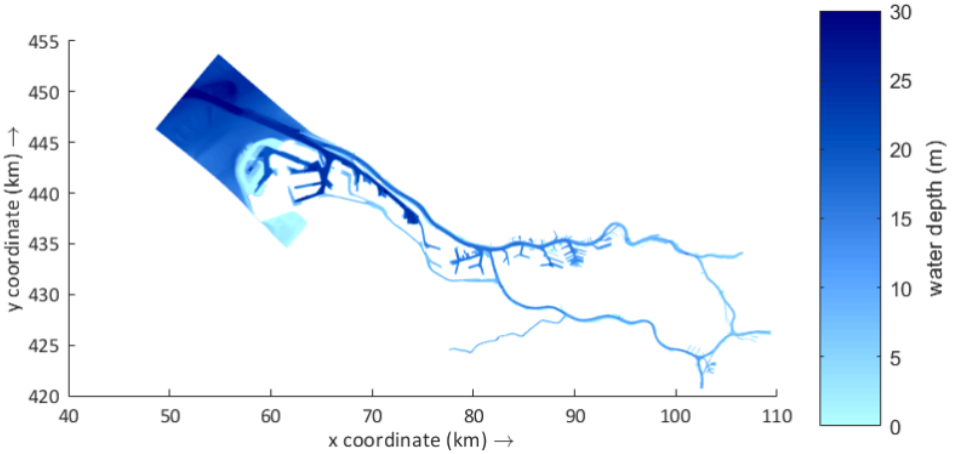

(c) Bathymetry of the OSR-HV hydrodynamic grid: greater Rotterdam wet infrastructure. Maasvlakte I as land boundary, Maasvlakte II extension as dry points (x=55-65 km)

G

Harmonic series generation

Information in this appendix is based on Codiga (2011). UTide is a harmonic analysis program to be executed in MatLab. The tool can analyse 1D (water level) or 2D (u,v-velocities) oceanic time-series and return a decomposition of the harmonic tidal constituents. It can reconstruct these components into a purely harmonic tidal velocity signal. Velocity boundaries of OSR-HV are inspected using UTide to separate the harmonic signal from non-harmonic contributions to the North Sea flow velocities. The latter are dominated by baroclinic and wind-induced currents. OSR-HV employs 142 single-velocity (U) boundary points over 10 σ-layers each. The command '*coef = ut_solv(t_raw, u_raw, v_raw, lat, cnstit,[optional])*' uses the syntaxes from Table G.1. The main result consists of up to 76 tidal components, of which 58 were identified for the scope area (Figure 1.3).

Table G.1: UTide input structure using OSR-HV

Syntax	**Type**	**Specification**
time_raw	1D datenumber vector	Period of simulation in 10s of min.
u_raw	1D velocity vector	U_{OSR} (142x10)
v_raw	1D velocity vector	set to zeros(N)
lat	Decimal value	51.98°N
csntit	Text string	'auto' - determine automatically
Optional(s)	Command	'DiagnPlot' - creates visual diagnostics

UTide output is composed of: tidal constituent, current ellipse major axis length (Lsmaj), minor axis length (Lsmin), angle (Theta) and Greenwich phase lag (g) incl. 95% confidence intervals (ci). Apart from the main results, auxilliary and diagnostic results are generated that elaborate on variances, correlations, noise etc. Subsequently, a reconstruction module (*ut_reconstr*) converts the harmonic components back into velocities. The difference in velocity input and output is a non-harmonic component which is attributed to meteorological effects and/or stratification. Table G.2 shows (curtailed) results of the analysis of the HoH tidal record for validation period 01/12/19-10/12/19 (Section 5.2).

Table G.2: Contributions of tidal components resulting from UTide analysis of tidal signal at HoH between 01/12/19-10/12/19. Output set reduced to three main parameters: contribution to total energy, amplitude component and phase. 58 components identified in total.

Component name	Percent energy [%]	Amplitude [m]	Phase [°]
M2	84.89045	0.7610	61.2
M4	6.847773	0.1680	114.4
N2	2.228651	0.1010	38.2
S2	1.052657	0.1860	121.0
L2	0.910449	0.0500	83.6
K2	0.529601	0.0520	116.9
O1	0.411389	0.1100	176.6
MS4	0.350355	0.0980	166.1
MM	0.301231	0.0340	167.6
K1	0.098812	0.0720	347.2
MN4	0.097122	0.0600	90.9
M8	0.093577	0.0420	137.8

Residual flow is found to be of O(+0.01) m/s on flow of -0.2 to 0.2 m/s. Most of the residual flow in winter months coincide with storm events. Though for offshore locations (e.g. P9048) residual flows are present year-round and cannot be neglected as they are of order of $|u|$=0.1 m/s on a total flow of $|u|$=0.5 m/s, see Figure G.1.

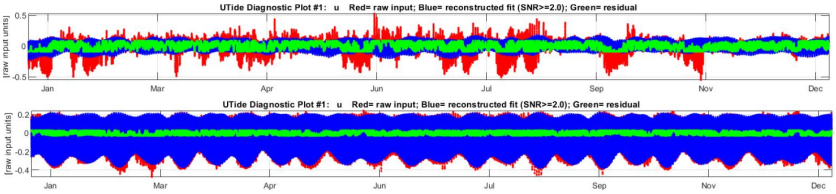

Figure G.1: Residual flow (green) vs. harmonic flow (blue) for boundary P9048 (top) vs. P9155 (bottom) at surface level as analysed by UTide. Residual flows can be neglected for offshore point P9155 whereas nearshore point P9048 shows significant contribution of non-harmonic effects to the flow profile.

Figure G.2 shows the representation of marine velocities as purely harmonic series which yields relatively larger velocities in the upper water column than for the full signal. For vertically well-mixed conditions in winter and in the absence of storms, a harmonic velocity profile is found to be a good approximation (based on 1997 data). Figure G.2 shows offshore tidal velocities generated by UTide for the period of the validation study.

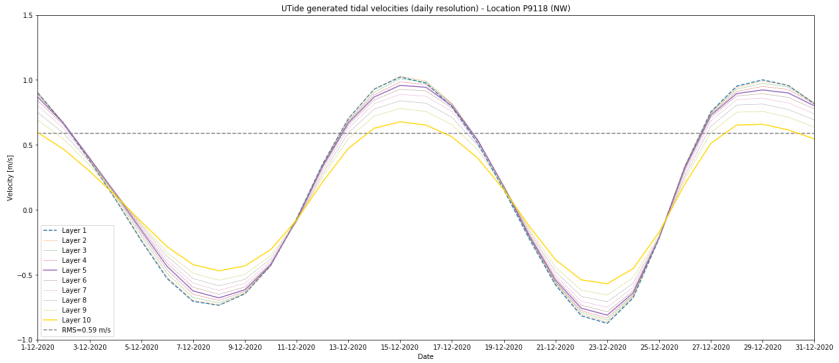

Figure G.2: Example of UTide generated harmonic velocities on marine open boundary

H

Model run details

The following tables specify the input that is given per model run. Situations mimicking the predictive scenarios have been simulated using historical data from dry/mean periods in the past.

Test run - 001		
Purpose: observe and confirm model functionalities		
Reference date	25/12/1995	T_0
Simulation period	09/02/1997 - 18/03/1997	T_{start} -T_{end}
River boundaries	From nesting	$\bar{Q}_{Lobith} = 2031\ m^3/s$
North Sea boundaries	From nesting	h (12x), u (142x10)
Wind forcing	25/12/1995 - 01/01/1998	KNMI HoH
HV sluice programme	Ebb sluicing closure work	LPH'84

Validation run - 002		
Purpose: assess salinity reproducing qualities of unaltered geometry		
Reference date	01/06/2018	T_0
Simulation period	01/12/2019 - 01/01/2020	T_{start} -T_{end}
River boundaries	Data, hydrological relations	$\bar{Q}_{Lobith} = 1946\ m^3/s$
North Sea boundaries	Data, UTide reconstruction	h (12x), u (142x10)
Wind forcing	01/01/2018 - 01/01/2020	KNMI HoH (Figure 4.12a)
HV sluice programme	Kierbesluit, closure work	HOP

Delta21 validation run - 003		
Purpose: assess influence of changed system geometry on salinity		
Reference date	01/06/2018	T_0
Simulation period	01/01/2019 - 01/01/2020	T_{start} -T_{end}
River boundaries	Data, hydrological relations	$\bar{Q}_{Lobith} = 1946\ m^3/s$
North Sea boundaries	Data, UTide reconstruction	h (12x), u (142x10)
Wind forcing	01/01/2018 - 01/01/2020	KNMI HoH (Figure 4.12a)
HV sluice programme	Kierbesluit, closure work	HOP

Delta21 'Calm' - 004		
Purpose: assess lower bound expected intrusion 2100		
Reference date	01/06/2100	T_0
Simulation period	Average month (31d)	T_{start} -T_{end}
River boundaries	Data: 19/03/2016 - 19/04/2016	$\bar{Q}_{Lobith} = 2100\ m^3/s$
North Sea boundaries	UTide forecasting	h (12x), u (142x10)
Wind forcing	Data: 19/03/2016 - 19/04/2016	KNMI HoH (Figure 4.12b)
HV sluice programme	Delta21	100% opened

Delta21 'Mean' - 005		
Purpose: assess mean expected intrusion 2100		
Reference date	01/06/2100	T_0
Simulation period	Average month (31d)	T_{start} -T_{end}
River boundaries	Data: 19/03/2016 - 19/04/2016	$\bar{Q}_{Lobith} = 2100\ m^3/s$
North Sea boundaries	UTide forecasting	h (12x), u (142x10), from nesting
Wind forcing	Data: 19/03/2016 - 19/04/2016	KNMI HoH (Figure 4.12b)
HV sluice programme	Delta21	100% opened

Delta21 'Intrusion' - 006		
Purpose: assess dry month intrusion 2100		
Reference date	01/06/2100	T_0
Simulation period	Dry month (31d)	T_{start} -T_{end}
River boundaries	Data: 17/07/2018 - 17/08/2018	$\bar{Q}_{Lobith} = 1000\ m^3/s$
North Sea boundaries	stratified+35cm SLR	h (12x), u (142x10)
Wind forcing	Data: 17/07/2018 - 17/08/2018	KNMI HoH (Figure 4.12c)
HV sluice programme	Delta21	100% opened

Delta21 'Critical' - 007		
Purpose: assess upper bound expected intrusion 2100		
Reference date	01/06/2100	T_0
Simulation period	Dry month (31d)	T_{start} -T_{end}
River boundaries	Data: 17/07/2018 - 17/08/2018	$\bar{Q}_{Lobith} = 1000\ m^3/s$
North Sea boundaries	stratified+85cm SLR	h (12x), u (142x10)
Wind forcing	Data: 17/07/2018 - 17/08/2018	KNMI HoH (Figure 4.12c)
HV sluice programme	Delta21	100% opened

Alternative HV sluice opening - 008		
Purpose: assess effectiveness of old HV sluices as Delta21		
Reference date	01/06/2100	T_0
Simulation period	Dry month (31d)	T_{start} -T_{end}
River boundaries	Data: 17/07/2018 - 17/08/2018	$\bar{Q}_{Lobith} = 1000\ m^3/s$
North Sea boundaries	stratified+85cm	h (12x), u (142x10)
Wind forcing	Data: 17/07/2018 - 17/08/2018	KNMI HoH (Figure 4.12c)
HV sluice programme	Kierbesluit+	20% opened

Wind time-series are visualized in Figures H.1, H.2 and H.3. All dataset contain events of forceful wind (13.9-17.1 m/s). Validation period (Figure H.1) and Calm/Mean Delta21 scenarios (Figure H.2) contain storm-like events (17.2-20.7 m/s) but directionality (Figure 4.12) does not align with the estuary axis for the majority of time.

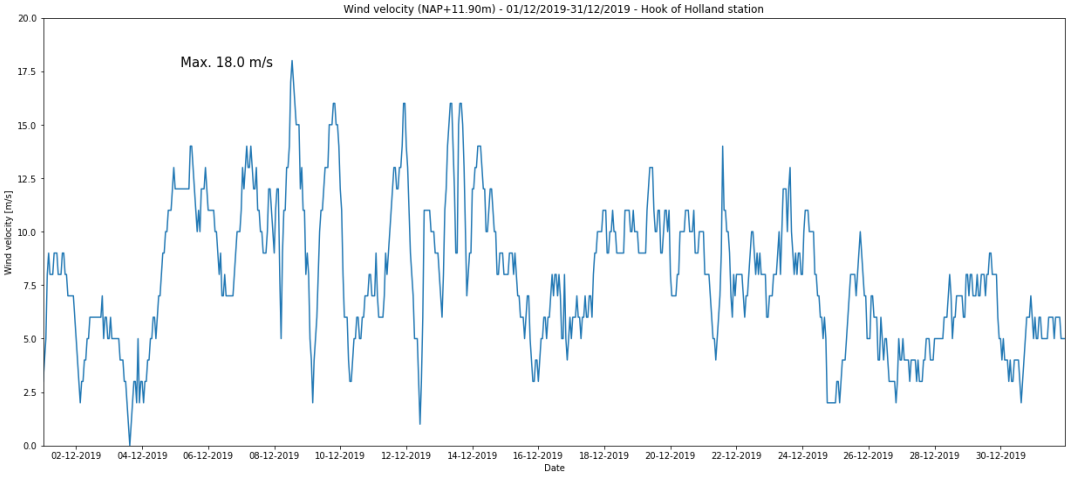

Figure H.1: Wind time-series validation period (Dec 2019)

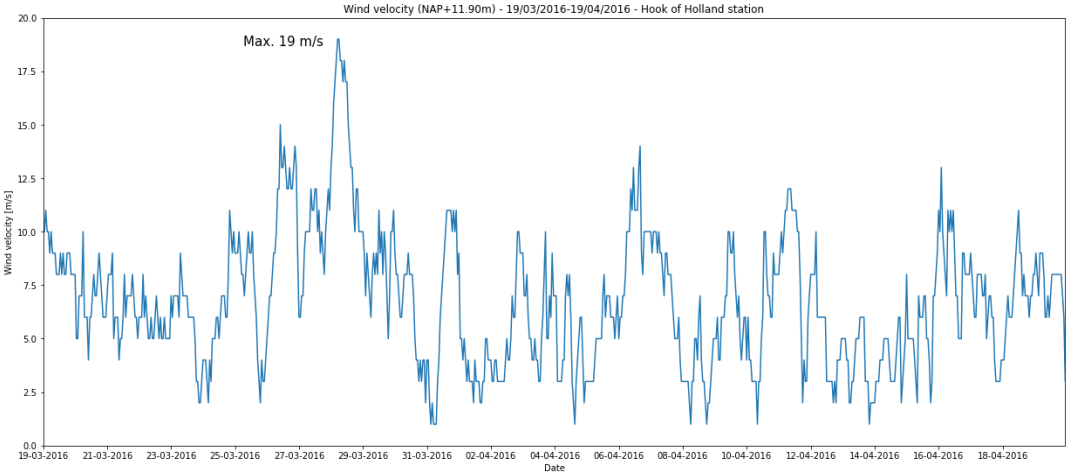

Figure H.2: Wind time-series Calm/Mean Delta21 scenarios based on Mar-Apr 2016

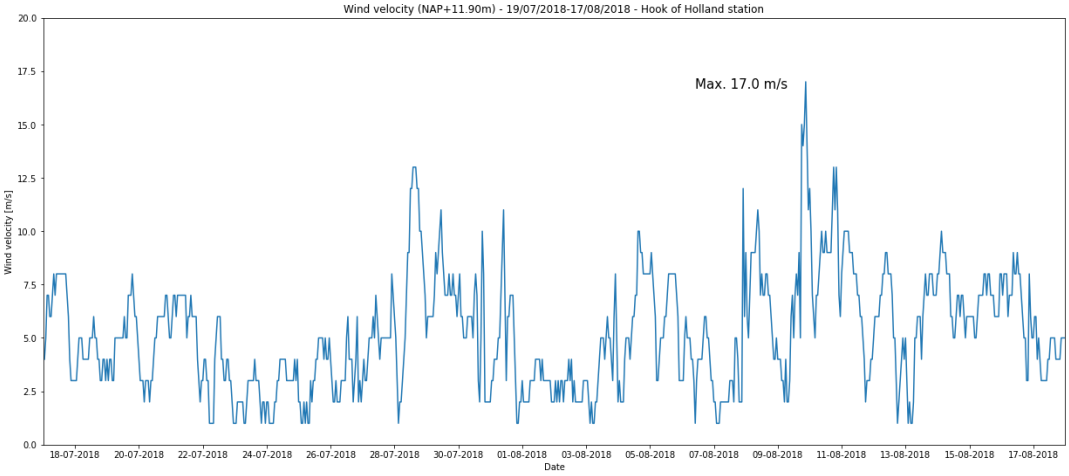

Figure H.3: Wind time-series Intrusion/Critical Delta21 scenarios based on Jul-Aug 2018

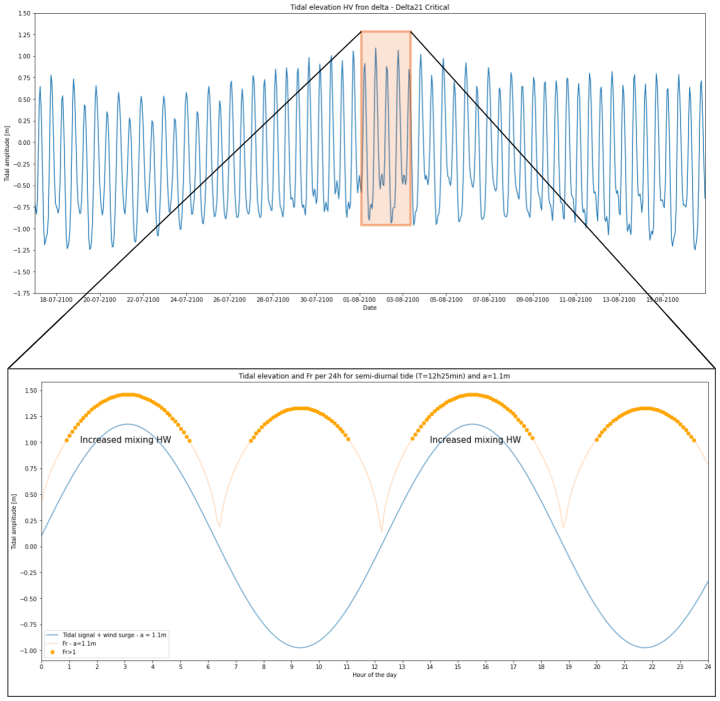

Figure H.4: **Upper panel:** Predicted tidal signal HV front delta (Delta21 'Critical') for period 18/07-18/08 (2100 CE). **Lower panel:** Tidal elevation and Froude numbers for a (simplified) semi-diurnal tide and 1.1m opening of all 17 units of HV sluices (20%). Increased landward mixing is theoretically achieved for Fr>1 on flooding tide, this is a recommendation for further research (Section 8.2)

Validation

Figure 4.13 shows observations stations that have been added for model validation purposes. The numerical results in these locations are treated in Section I.1. Figure 4.14 shows existing stations used for data validation. Coordinates of these locations are shown in Table I.1.

Table I.1: Data monitoring locations used in the validation study, see Section 5.2, Section 5.3. Categorical split between locations in HV and RWW by de Nijs et al. (2011)

Data validation			
Station name	**Location**	**Latitude [°]**	**Longitude [°]**
Haringvliet10	HV front delta	51.857411	3.863943
Spui-Middelharnis	Spui South entrance	51.784515	4.229720
Stellendam Binnen	HV 1km up-estuary	51.824313	4.051066
Kier4	HV 3km up-estuary	51.805058	4.108201
Kier2	HV 4km up-estuary	51.809438	4.095240
Kier3	HV 5km up-estuary	51.817522	4.125738
Kier1	HV 6km up-estuary	51.796711	4.122349
RWW de Nijs et al. (2011)			
HoH	HoH-NWW	51.966611	4.143377
Botlek	Port entrance	51.894313	4.308479
Old Meuse bifurcation	New/Old-Meuse	51.880835	4.326280

I.1 Influence Delta21 geometry

Figure I.1 shows turbulent kinetic energy production [m^2/s^2] in the HV front delta at HW for Q=1000 m^3/s at 85 cm SLR. It shows that production is high in the Delta21 shipping channel which causes high vertical mixing as stratification breaks down. Turbulent kinetic energy production quickly diminishes closer to the HV sluices.

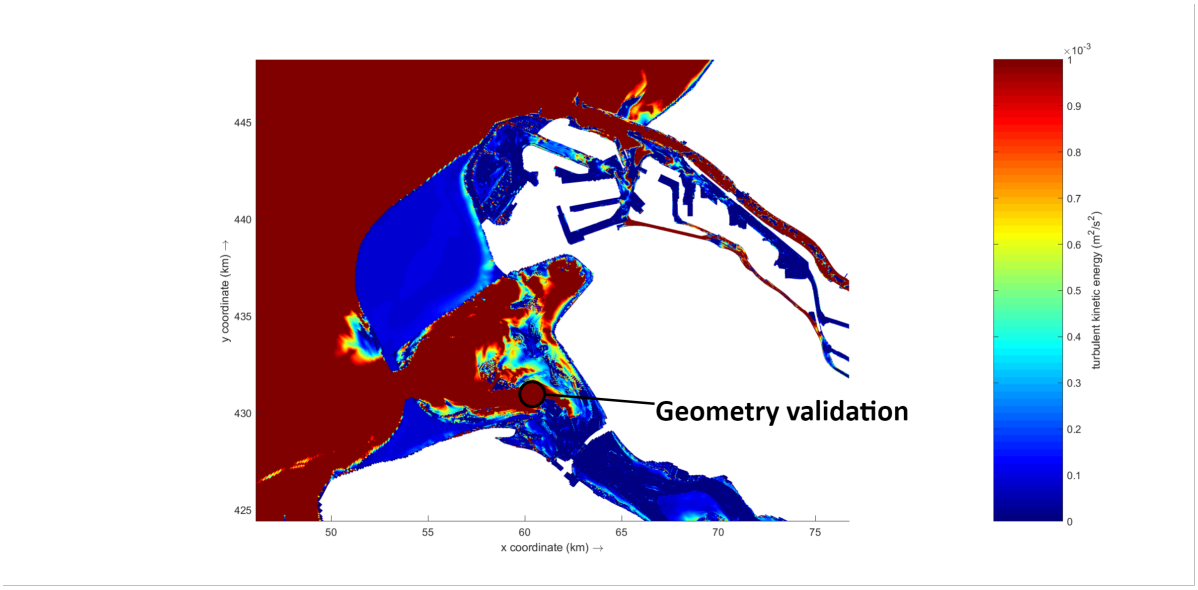

Figure I.1: Turbulent kinetic energy HV front delta at HW on 31/12/19 shows to be concentrated along Delta21 shipping channel (red protrusion) before being damped in presence of fresher water from HV-HD (blue zone)

Figures I.2a-I.2d show surface velocities at peak LW/HW comparing unaltered and Delta21 geometries. It becomes clear that the maximum ebb flow velocities that would normally concentrate on the seaward tip of Maasvlakte II (Figure I.2b) show the same behaviour on the seaward bank of the Delta21 energy storage lake (Figure I.2d). Flood velocities into the tidal lake show to be stronger than ebb velocities exiting the tidal lake at the new Delta21 storm surge barrier (compare Figures I.2c-I.2d). Also note the select pathway in which the main ebb flow is focused for both Figures I.2a and I.2c. This contributes to the salinity buffering function of the tidal lake described in Section 5.1.

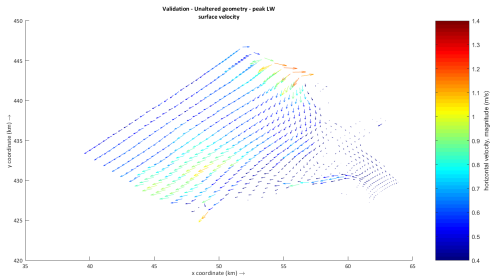

(a) Validation: surface velocities unaltered geometry at peak LW

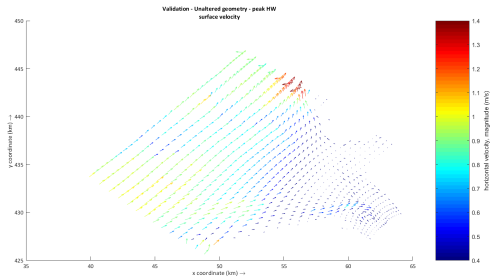

(b) Validation: surface velocities unaltered geometry at peak HW

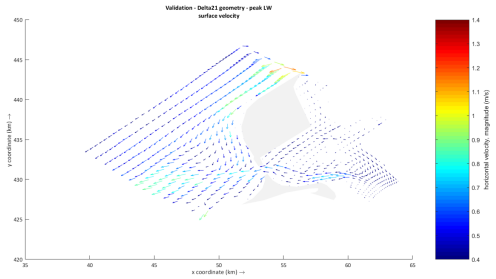

(c) Validation: surface velocities Delta21 geometry at peak LW

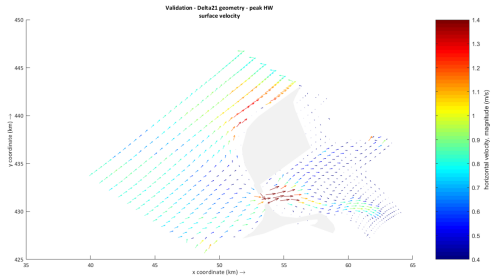

(d) Validation: surface velocities Delta21 geometry at peak HW

Figure I.2: Surface velocities (k=1) for the HV front delta comparing unaltered and Delta21 geometries at peak LW/HW

Figures I.3a-I.3l show surface salinity vs. time for all stations in Figure 4.13 during validation period

1/10/12-31/10/12. Top panels show output for unaltered geometry, middle panels for altered geometry (same conditions) and lower panels show differences. Differences are low for offshore locations but significant for stations: ns2 (I.3b) and nsrofi I.3l. Therefore, water level differences have been included for these stations in Figures I.3m-I.3n. These plots show that water levels are generally similar except near the end of simulation (29 Dec). The poor reproduction of salinity in the altered geometry case can therefore not be wholly ascribed to difference in water levels. It is likely that the altered near-shore geometry affects alongshore tidal transport of salinity and therefore salinity in the Rhine ROFI close to the northern boundary (NS1, Figure 4.6).

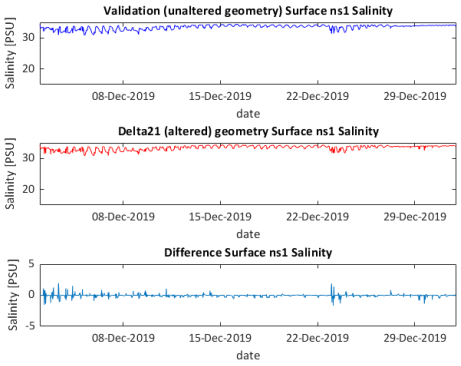

(a) Surface salinity at station ns1: Validation, Delta21 and difference

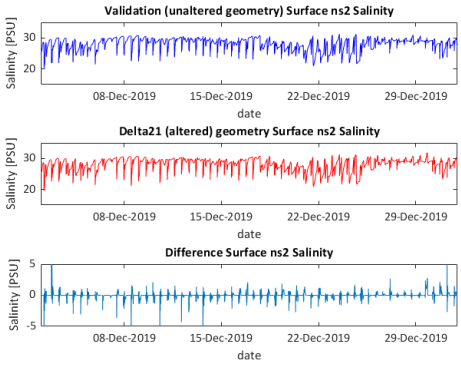

(b) Surface salinity at station ns2: Validation, Delta21 and difference

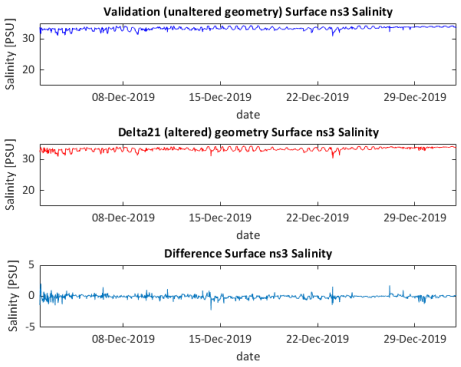

(c) Surface salinity at station ns3: Validation, Delta21 and difference

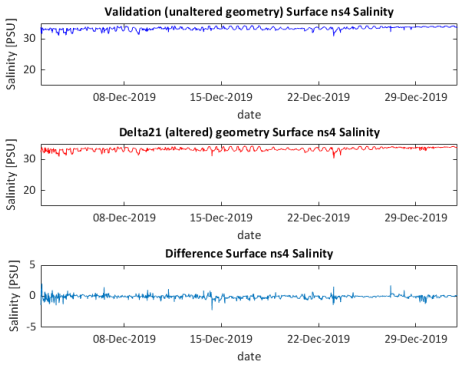

(d) Surface salinity at station ns4: Validation, Delta21 and difference

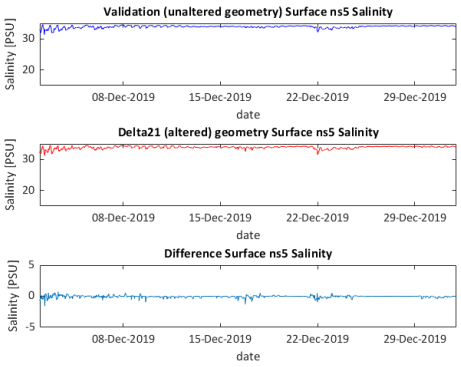

(e) Surface salinity at station ns5: Validation, Delta21 and difference

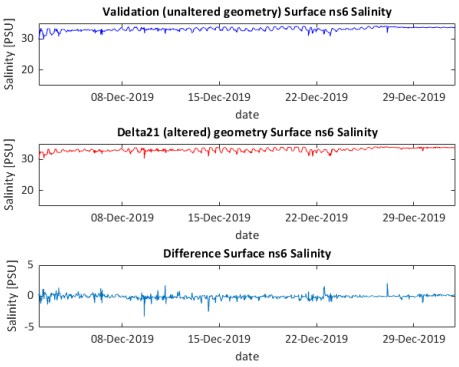

(f) Surface salinity at station ns6: Validation, Delta21 and difference

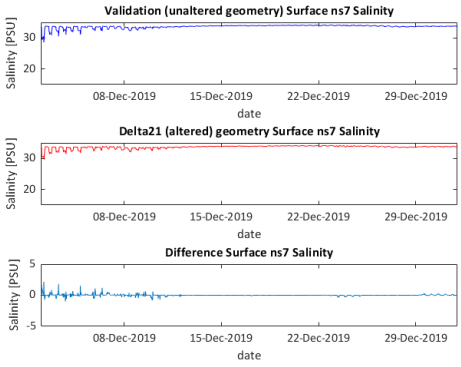

(g) Surface salinity at station ns7: Validation, Delta21 and difference

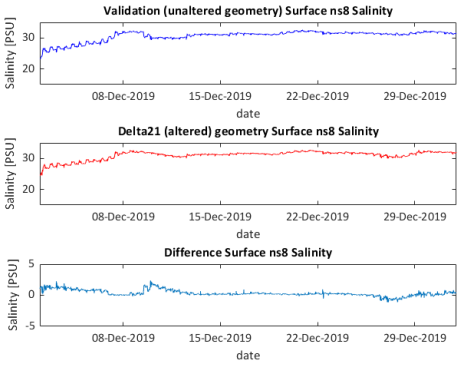

(h) Surface salinity at station ns8: Validation, Delta21 and difference

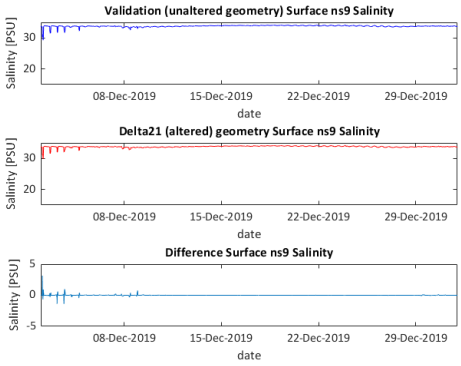

(i) Surface salinity at station ns9: Validation, Delta21 and difference

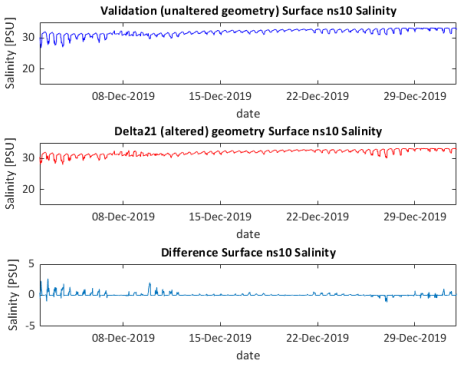

(j) Surface salinity at station ns10: Validation, Delta21 and difference

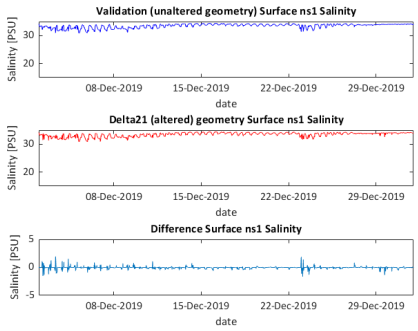

(k) Surface salinity at station ns11: Validation, Delta21 and difference

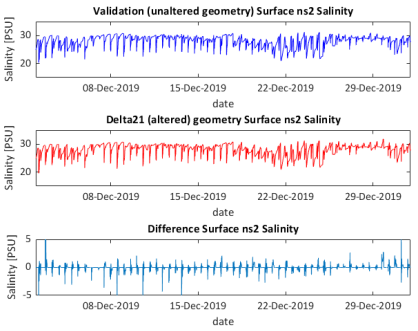

(l) Surface salinity at station nsrofi: Validation, Delta21 and difference

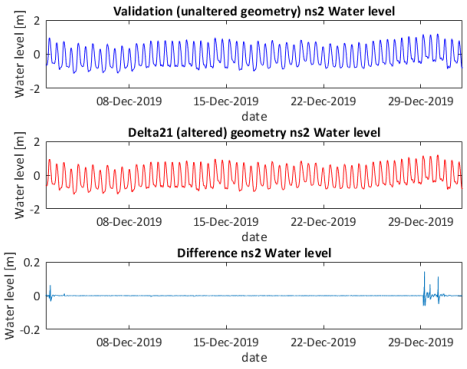

(m) Water level at station ns2: Validation, Delta21 and difference

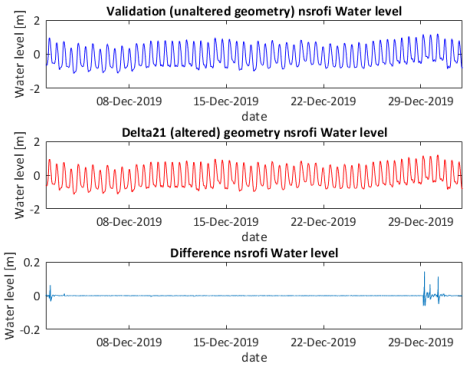

(n) Water level at station nsrofi: Validation, Delta21 and difference

Figure I.4 shows monitoring locations included in running Delta21 geometry in the larger DCSM-FM model. The four locations plotted in Figures I.5-I.6 are: HARVT10, Nieuwe Waterweg-Vaargeul, Nieuwe Waterweg Noord and STRAINS_M18 in that order. NieuweWaterweg Noord corresponds to observation station ns1 (Figure 4.13). HARVT10 also indicated in Figure 4.14.

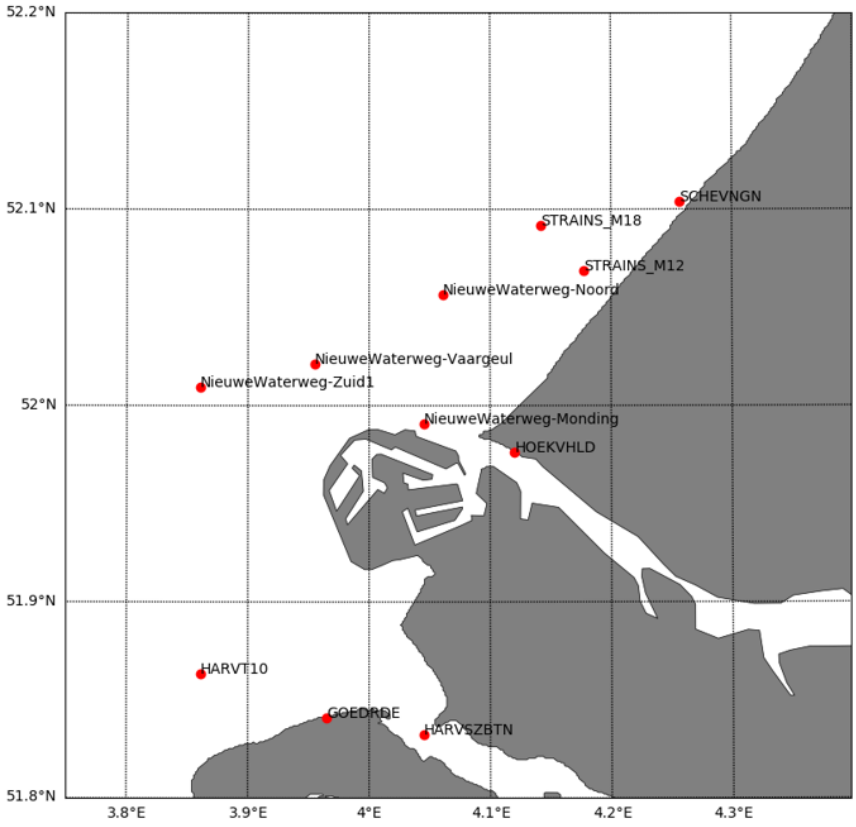

Figure I.4: Monitoring locations Figures I.5-I.6. Courtesy of Lennart Keyzer (TUD)

Figure I.5 shows water level comparisons between altered and unaltered geometries for the locations described above using the larger DCSM-FM model which has a grid that roughly coincides with the geographical extent of Figure I.4. It can be seen that for this larger grid, water levels at, especially, NieuweWaterweg-Noord are well-reproduced.

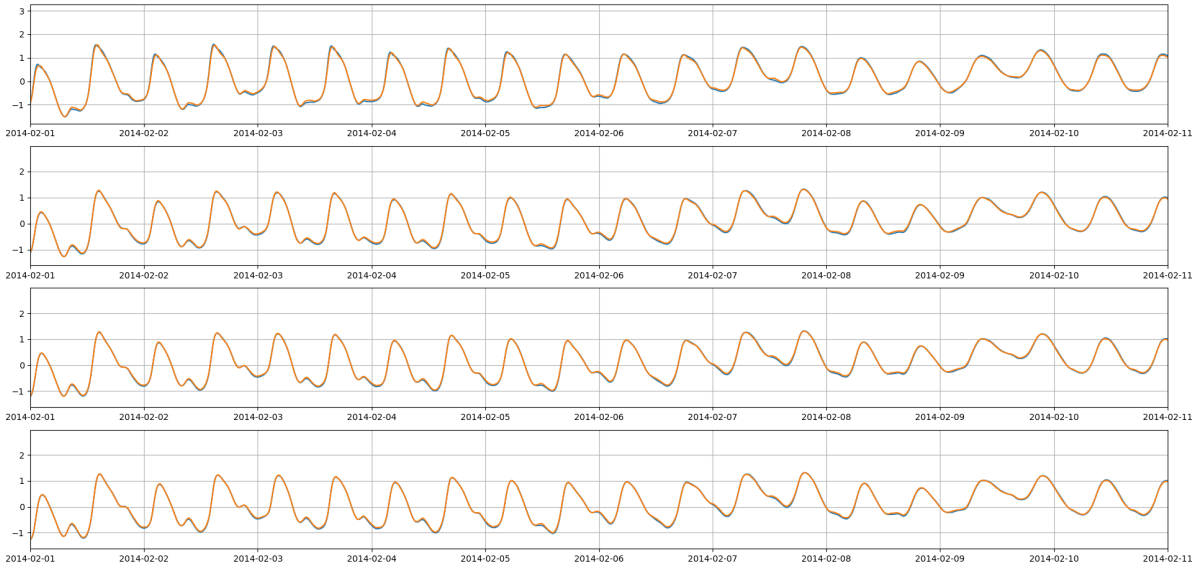

Figure I.5: Water levels DCSM-FM with and without Delta21 seaward structures at locations HARVT10, NieuweWaterweg-Vaargeul, NieuweWaterweg-Noord and STRAINS_M18 from Figure I.4. Courtesy of Lennart Keyzer (TUD).

Figure I.5 shows salinity comparisons between altered and unaltered geometries for the locations described above using the larger DCSM-FM model. It can be seen that salinity still shows different numerical approximations comparing the two geometries. Salinity trends are however reproduced well. HRVT10 (top panel) is not reproduced due to modelling of HV sluices as permanently closed.

Judging the blue line in Figure I.6, surface salinity is estimated to be consistently higher (+0-2 PSU) in presence of Delta21 for stations in the Rhine ROFI (Figure C.2). This suggests that the Delta21 geometry has an effect of spreading water from the ROFI over a larger marine domain causing less dilution of near-coast surface salinity. This in turn may have pronounced implications for marine ecology which should be considered in the scope of Delta21.

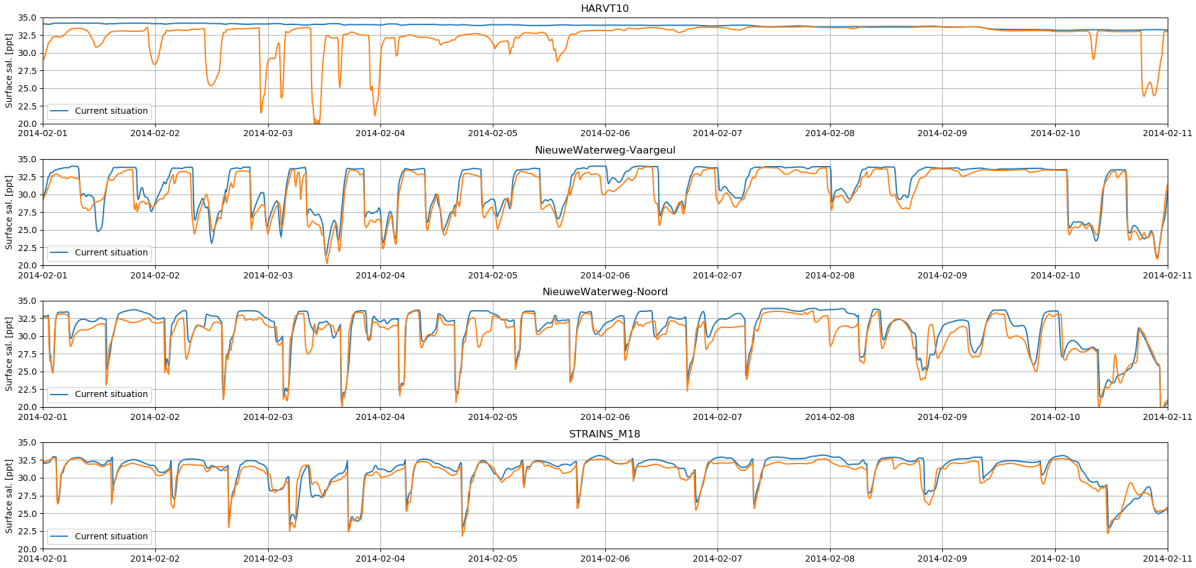

Figure I.6: Surface salinity DCSM-FM at locations HARVT10, NieuweWaterweg-Vaargeul, NieuweWaterweg-Noord and STRAINS_M18 from Figure I.4. Courtesy of Lennart Keyzer (TUD).

I.2 Data validation

Figures I.7a-I.7h show vertical salinity profiles on December 9th 2019 at the start (LWS) of the 15th tidal cycle in the validation period (1/12/19-10/12/19). Data has been linearly interpolated (blue dotted) between 3-5 points per vertical profile. Location coordinates can be found in Table I.1. Figures I.7a-I.7c are taken in deep pits in the west of Haringvliet (see Figure F.4b). Predictive capability in these features is assumed low due to non-physical flows arising from sigma-layering (Appendix F). Figures I.7d-I.7h denote locations approx. 1km apart along the northern bank of HV (up-estuary). It can be seen that salinity is generally over-predicted by O(0.1) PSU. Bottom salinity is overestimated.

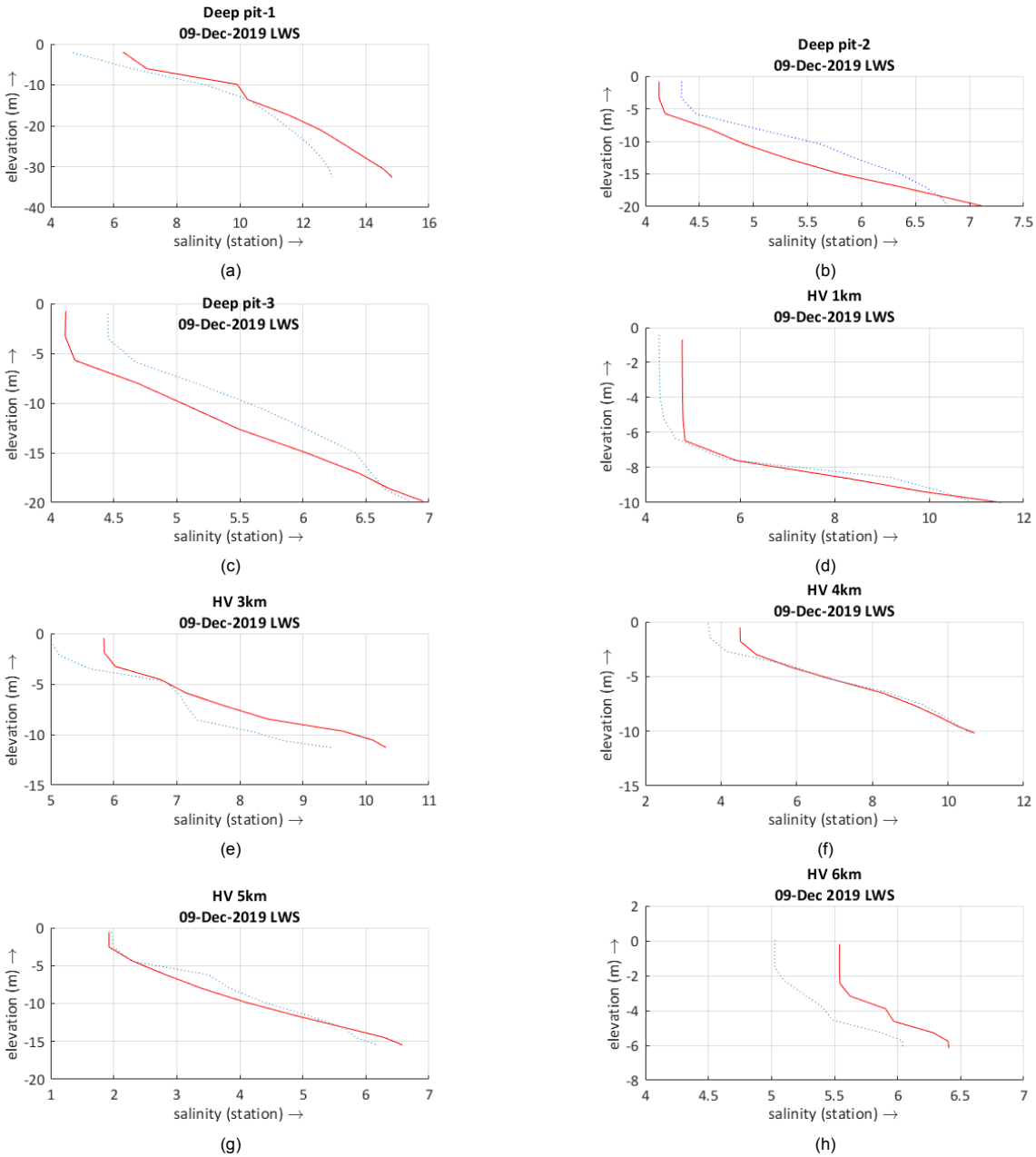

Figure I.7: Vertical salinity profiles Haringvliet basin at LWS. Blue dotted: data RWS. Red line: Numerical result OSR-HV. Typical differences amount to 0.50-0.75 PSU. Locations can be found in Figure 4.14.

J

Results

Turbulent kinetic energy

Comparing J.1a and J.1b, it can be seen that the offshore profile climbs steeply towards the HV front delta which causes vertical penetration of turbulent kinetic energy. On ebb tide, turbulent kinetic energy is low within HV-HD. On flood tide, turbulent kinetic energy can be seen to penetrate the entire HV and part of HD.

Horizontal velocity vs. time

Figures J.2a-h show horizontal velocities (x-direction) at the 8 locations marked in Figures 4.14 and 6.13 being: HoH, Botlek and Old Meuse from (de Nijs et al. (2011)), P(531; 583), P(548; 736) and two validation locations in the HV front delta. Notice that Figures J.2a, J.2c-J.2g display unidirectional velocities meaning the forcing is characterised as barotropic. Tidal velocities weaken noticeably between J.2f-J.2g which constitutes 8km up-estuary flow in the HV. Figures J.2a-J.2c are situated in/near the RWW and show more skewness than the other 5 tidal signals. Figure J.2b shows distinctly different behaviour with bottom flood velocities during ebb tide. The latter indicates the activation of baroclinic modes (O(0.05) m/s). This behaviour is largely absent in HV-HD which explains the difference in estuarine behaviour between RWW and HV-HD. Locations within the HV (Figures J.2h, J.2f, J.2g) show to have relatively weak bottom ebb currents (green bands), no distinct baroclinic modes and a more

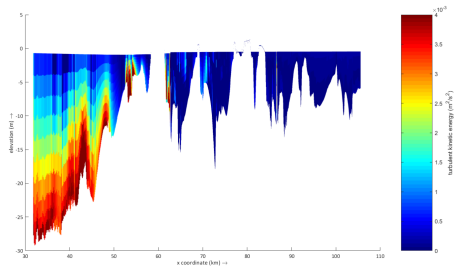

(a) Turbulent kinetic energy $[m^2/s^2]$ per σ-layer in cross-section from Figure 6.2 during maximum down-estuary velocities (LW) at Q_{Lobith}=1000 m^3/s, SLR=85cm.

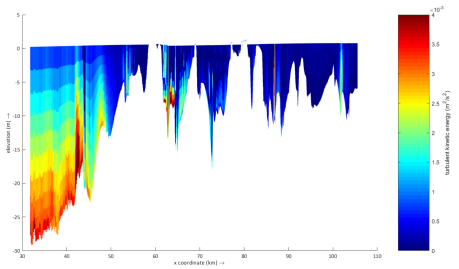

(b) Turbulent kinetic energy $[m^2/s^2]$ per σ-layer in cross-section from Figure 6.2 during maximum up-estuary velocities (HW) at Q_{Lobith}=1000 m^3/s, SLR=85cm.

symmetrical tidal signal. This in part explains the behaviour of limited intrusion (weak residual currents) and limited outwash (weak ebbing).

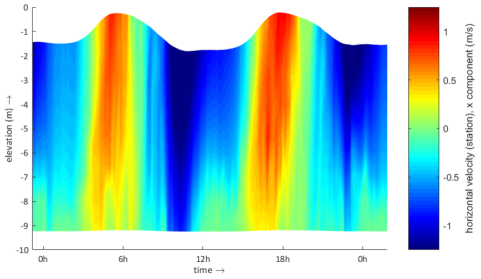

(a) HoH de Nijs et al. (2011) - velocities in x-direction vs. local depth for Q_{Lobith}=1000 m^3/s, SLR=85 cm. T=31d.

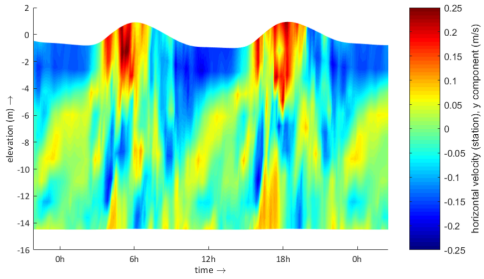

(b) Botlek de Nijs et al. (2011) - velocities in x-direction vs. local depth for Q_{Lobith}=1000 m^3/s, SLR=85 cm. T=31d.

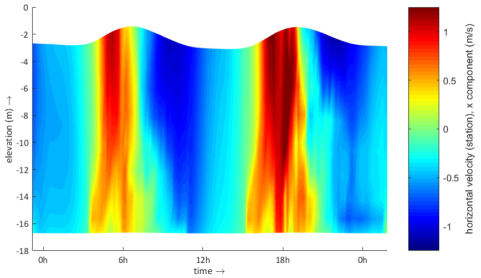

(c) Bifurcation Old/New Meuse de Nijs et al. (2011) - velocities in x-direction vs. local depth for Q_{Lobith}=1000 m^3/s, SLR=85 cm. T=31d.

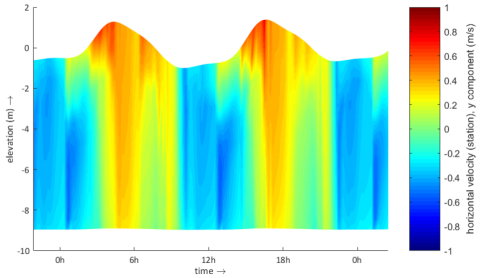

(d) Data validation front delta - velocities in x-direction vs. local depth for Q_{Lobith}=1000 m^3/s, SLR=85 cm. T=31d.

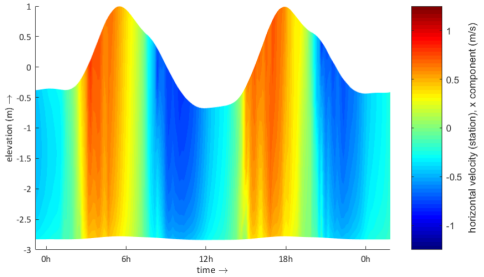

(e) Geometry validation - velocities in x-direction vs. local depth for Q_{Lobith}=1000 m^3/s, SLR=85 cm. T=31d.

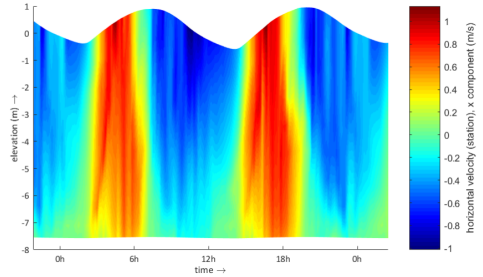

(f) P(531; 583) - velocities in x-direction vs. local depth for Q_{Lobith}=1000 m^3/s, SLR=85 cm. T=31d.

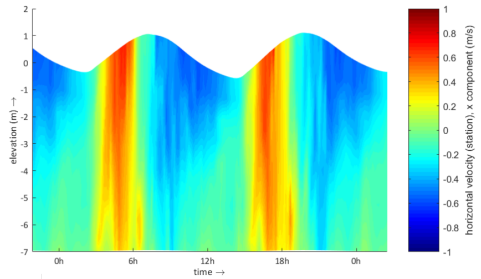

(g) P(548; 736) - velocities in x-direction vs. local depth vs. local depth for Q_{Lobith}=1000 m^3/s, SLR=85 cm. T=31d.

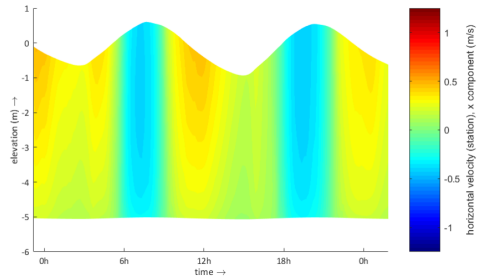

(h) Spui south - velocities in x-direction vs. local depth for Q_{Lobith}=1000 m^3/s, SLR=85 cm. T=31d.

Figure J.2: Horizontal velocity (along-estuary) vs. time (24h) for 8 locations described in Figures 4.14 and 6.13. Scales may vary between figures to better visualize differences within a single image.

Salinity vs. time - Q_{Lobith}=1000 m^3/s

Figures J.4a-h show salinity at the same 8 locations as above. Stratification develops between HoH and Botlek (Figures J.3a-J.3b). Flood velocities push the pycnocline upward in Figure J.3c whereas mixing appears low which points at low tidal straining in the northern branches. Offshore of HV, over half the water column becomes fresher at LWS but mixing on flood is high. The occurrence of stratification in the HV front delta (Figure J.3e) varies per ebb cycle mostly due to stronger influence from turbulent effects (i.e. bottom, wind). The previous influences stratification east of HV sluices (Figure J.3f) though this effect diminishes quickly when moving up-estuary (Figure J.3g). Overall salinity at Spui south (Figure J.3h) is much higher compared to Figure J.4h which is attributed to the change in discharge regime through Spui between $Q_{Lobith} = 1000, 2100\ m^3/s$.

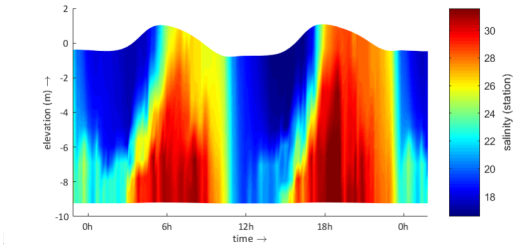

(a) HoH de Nijs et al. (2011) - salinity vs. local depth for Q_{Lobith}=1000 m^3/s, SLR=85 cm. T=31d.

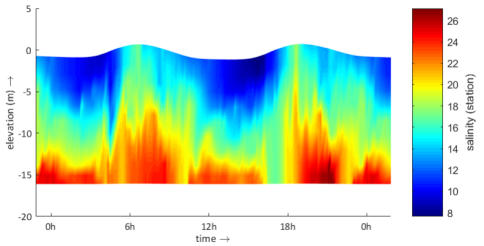

(b) Botlek de Nijs et al. (2011) - salinity vs. local depth for Q_{Lobith}=1000 m^3/s, SLR=85 cm. T=31d.

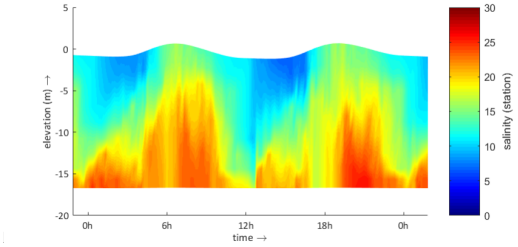

(c) Bifurcation Old/New Meuse de Nijs et al. (2011) - salinity vs. local depth for Q_{Lobith}=1000 m^3/s, SLR=85 cm. T=31d.

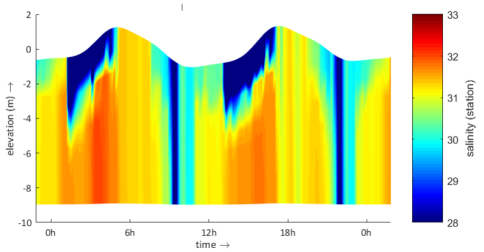

(d) Data validation front delta - salinity vs. local depth for Q_{Lobith}=1000 m^3/s, SLR=85 cm. T=31d.

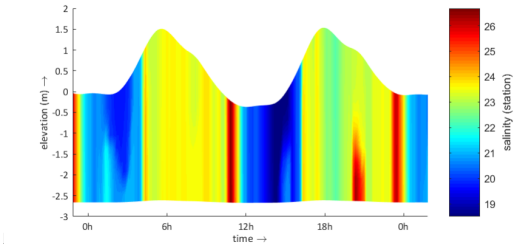

(e) Geometry validation - salinity vs. local depth for Q_{Lobith}=1000 m^3/s, SLR=85 cm. T=31d.

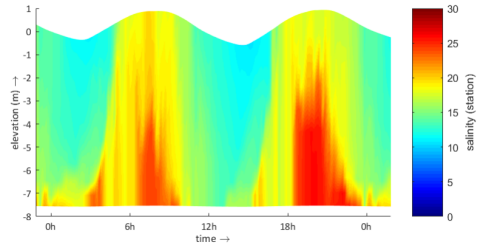

(f) P(531; 583) - salinity vs. local depth for Q_{Lobith}=1000 m^3/s, SLR=85 cm. T=31d.

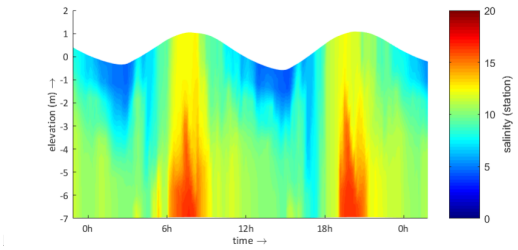

(g) P(548; 736) - salinity vs. local depth vs. local depth for Q_{Lobith}=1000 m^3/s, SLR=85 cm. T=31d.

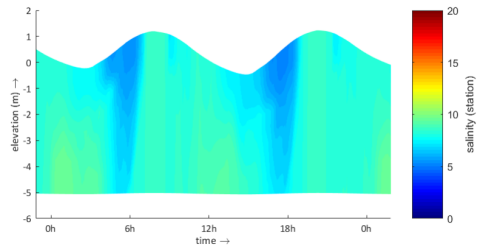

(h) Data validation Spui south - salinity vs. local depth for Q_{Lobith}=1000 m^3/s, SLR=85 cm. T=31d.

Figure J.3: Salinity vs. time (24h) for 8 locations described in Figures 4.14 and 6.13. Scales may vary between figures to better visualize differences within a single image. Q_{Lobith}=1000 m^3/s, SLR=85 cm. T=31d.

Salinity vs. time - Q_{Lobith}=2100 m^3/s

Figures J.4a-h show salinity at the same 8 locations as above. Salinity is washed out completely for approx. 1h on ebb tide at HoH (Figure J.4a). The salt wedge can be observed during the second half of flood approx. 16 km up-estuary at Botlek (Figure J.4b). A large part of the saline flux is transport south through Old Meuse (Figure J.4c). Offshore of HV (Figure J.4d), a dilute surface zone can be observed which is admixed around HWS. Closer to the HV dam (Figure J.4e), the pattern is more complex though near homogeneous in the vertical which points at greater influence of vertical and lateral mixing. Downward transport of salinity is apparent comparing Figure J.4f-g. Mixing intensity appears stronger near Spui south (Figure J.4h).

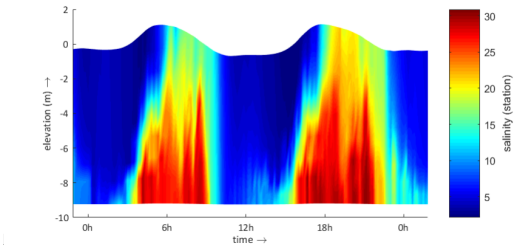

(a) HoH de Nijs et al. (2011) - velocities in x-direction vs. local depth for Q_{Lobith}=2100 m^3/s, SLR=85 cm. T=31d.

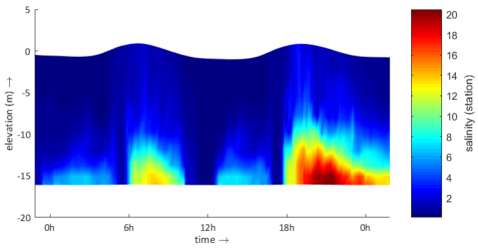

(b) Botlek de Nijs et al. (2011) - salinity vs. local depth for Q_{Lobith}=2100 m^3/s, SLR=85 cm. T=31d.

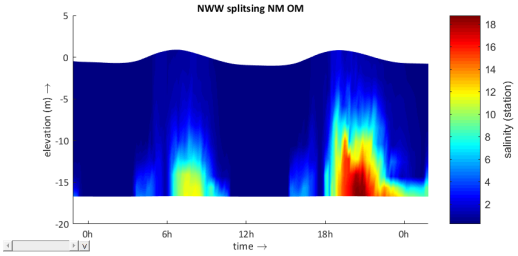

(c) Bifurcation Old/New Meuse de Nijs et al. (2011) - salinity vs. local depth for Q_{Lobith}=2100 m^3/s, SLR=85 cm. T=31d.

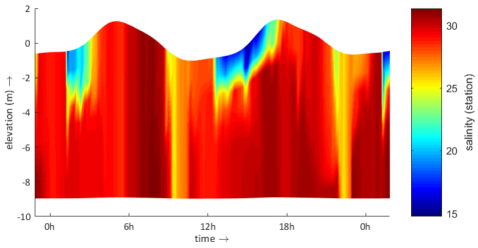

(d) Data validation front delta - salinity vs. local depth for Q_{Lobith}=2100 m^3/s, SLR=85 cm. T=31d.

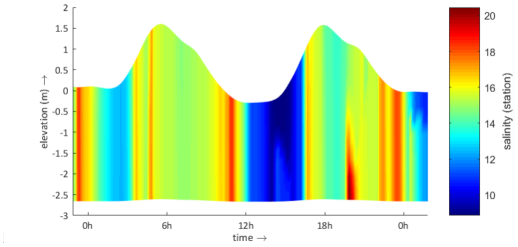

(e) Geometry validation - salinity vs. local depth for Q_{Lobith}=2100 m^3/s, SLR=85 cm. T=31d.

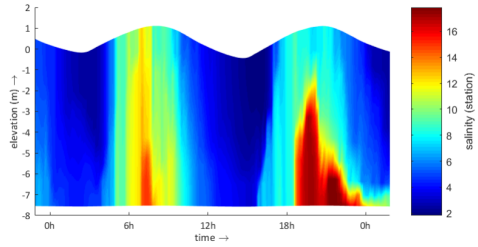

(f) P(531; 583) - salinity vs. local depth for Q_{Lobith}=2100 m^3/s, SLR=85 cm. T=31d.

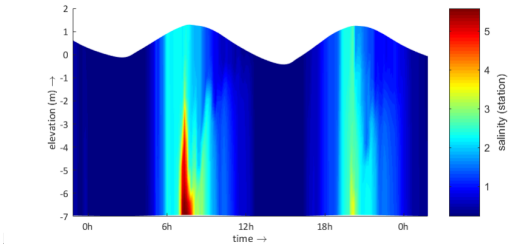

(g) P(548; 736) - salinity vs. local depth vs. local depth for Q_{Lobith}=2100 m^3/s, SLR=85 cm. T=31d.

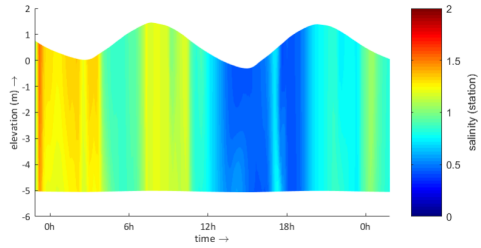

(h) Data validation Spui south - salinity vs. local depth for Q_{Lobith}=2100 m^3/s, SLR=85 cm. T=31d.

Figure J.4: Salinity vs. time (24h) for 8 locations described in Figures 4.14 and 6.13. Scales may vary between figures to better visualize differences within a single image. Q_{Lobith}=2100 m^3/s, SLR=85 cm. T=31d.

Velocity vector fields

Horizontal velocities in the HV at the onset and maximum of flood tide are inspected (Figures J.5a-J.6b) to establish an idea about flow evolution near the HV sluices and Spui southern entrance. Figures J.5a-J.5b show horizontal surface velocities in the western HV at the start and peak of flood tide for Delta 21 'Mean' scenario (Q_{Lobith}=2100 m^3/s, SLR=85cm). J.5a demonstrates how the secondary peak of Figures 6.4-6.7 is obtained. At the start of HW, basin velocities are shifting to a mean up-estuary orientation. Strong local up-estuary velocities near HV sluices show that higher water levels at sea drive landward flow. HV basin water levels are still relatively low and therefore cause the north-to-south pressure gradient between Old Meuse-Spui-HV to persist until LWS and sometime thereafter. The relatively narrow and deep geometry of Spui ($W_{Spui}/d_{Spui} \approx 20$) contribute to this behaviour.

Largely the same behaviour is observed at low flow (Figures J.6a-J.6b) though up-estuary velocities are considerably higher with approx. +20 cm/s at the surface. Tidal pumping (Section 2.3) near HV sluices is evident in Figure J.6b. Also note the strong lateral velocities downstream of HV sluices. These may be indicative of enhanced mixing of water before it enters the basin. Also note that the height of 'layer 1' varies with the tidal deflection. It can thus be seen that ebb flow is directed from shallow zones into the tidal channel structure and subsequently offshore whereas flood flow concentrates around these shallow features. Flood flow and residual outflow from Spui appear to nearly balance out. The relatively weak net flood flow is directed from south-to-north through Spui.

Finally the same timestamps of Figures J.5a-J.6a are assessed for a vertical channel cross-section at RDx=74km approx. at the southern boundary of these respective figures. The profile here, as can be deduced from Figures J.7a-J.8b, consists of two tidal channels and a shoal in the centre. It is becomes apparent that the lateral circulation (Subsection 2.3.3) does not dominate at this location, this is likely due to heterogeneity of the profile (not perfectly parabolic) and the effects of rotation and flow over the shoal (see e.g. Lyu and Zhu (2018)).

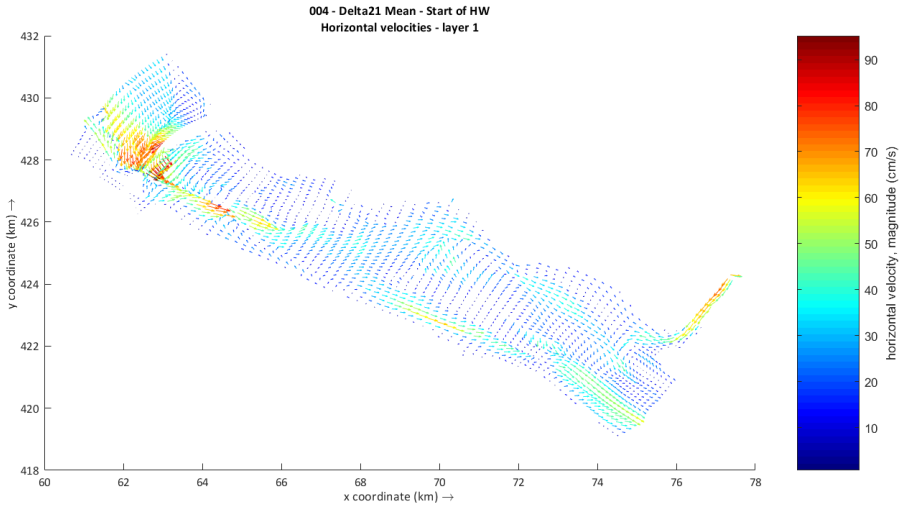

(a)

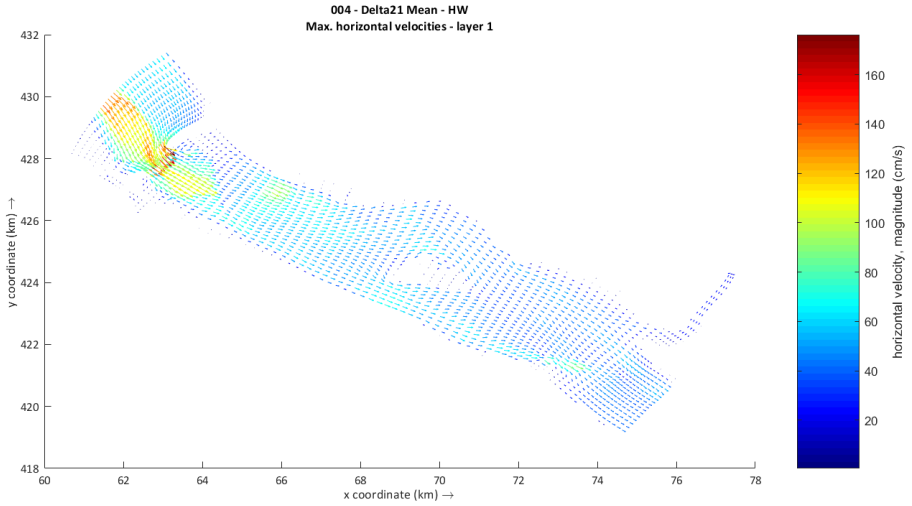

(b)

Figure J.5: Horizontal surface velocities western HV. Delta21 Mean scenario: SLR=85cm, Q_{Lobith}=2100 m^3/s. HV sluices at x=62-64km, Spui southern entrance at x=75-76km. **(a)**: start of HW, flow has reversed at sea and partially in the basin. Spui flow still directed southwards. **(b)**: maximum up-estuary flow concentrated in Delta21 shipping channel and diminished flow through Spui.

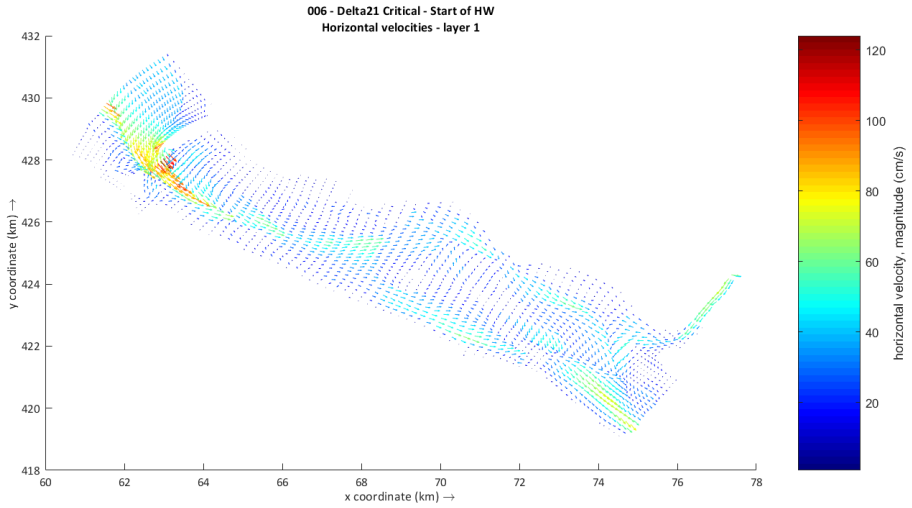

(a)

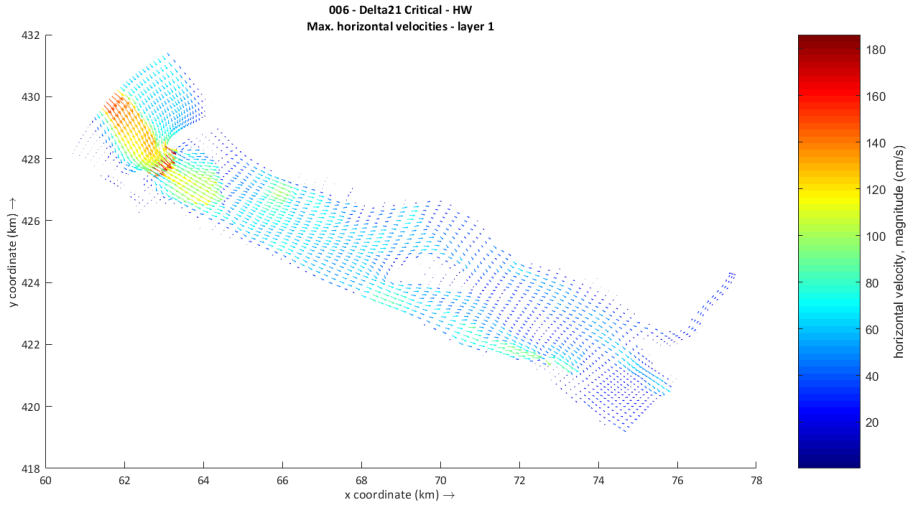

(b)

Figure J.6: Horizontal surface velocities western HV. Delta21 Critical scenario: SLR=85cm, Q_{Lobith}=1000 m^3/s. HV sluices at x=62-64km, Spui southern entrance at x=75-76km. **(a)**: start of HW, flow has reversed at sea and partially in the basin. Spui flow still directed southwards. (**b)**: maximum up-estuary flow concentrated in Delta21 shipping channel and diminished flow through Spui.

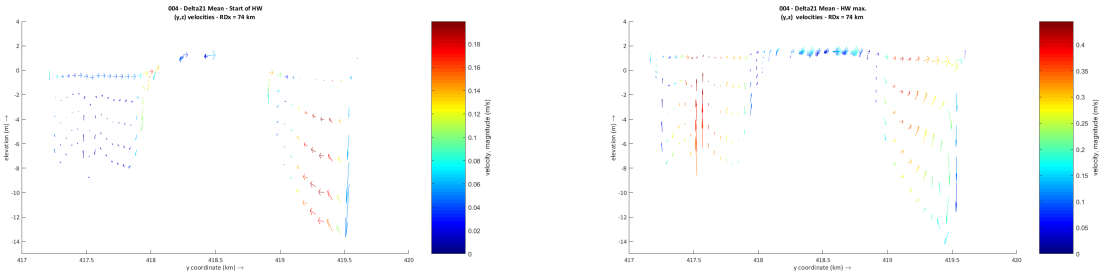

(a) (b)

Figure J.7: Cross-sectional velocities (y,z) at RDx = 74km (lower boundary (x,y) vector plots). Double tidal channel and shallow shoals in the centre of the cross-section. Delta21 Mean scenario: SLR=85cm, Q_{Lobith}=2100 m^3/s. **(a)**: start of HW, surface flow directed to the right for both channels. Continuity drives relatively strong lateral flow for channel on the right. **(b)**: maximum up-estuary flow is deflected over the shoal towards southern bank (y=419.5km).

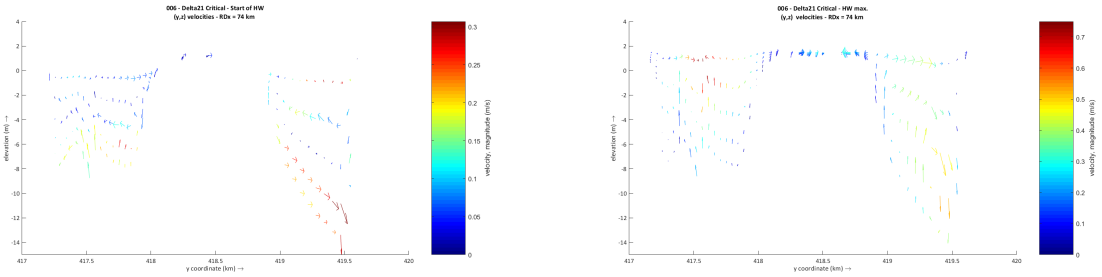

(a) (b)

Figure J.8: Cross-sectional velocities (y,z) at RDx = 74km (lower boundary (x,y) vector plots). Double tidal channel and shallow shoals in the centre of the cross-section. Delta21 Critical scenario: SLR=85cm, Q_{Lobith}=1000 m^3/s. **(a)**: start of HW, strongly heterogeneous vertical velocity distribution though surface flow is uniformly deflected to the right. **(b)**: surface flow convergence in left channel and towards shoal. Deflection towards southern bank in the flood tidal channel on the right.

Bibliography

N. Asselman, P. de Grave, and D. Wagenaar. Afvoerverdeling Rijntakken na 2050: lijkt een wijziging kosteneffectief of niet? Technical report, Deltares, https://puc.overheid.nl/rijkswaterstaat/doc/PUC_160766_31/, 2018.

J. Blazek. *Computational fluid dynamics: principles and applications*. Butterworth-Heinemann, 2015.

J.C.H. Blom and E. Lamberts. *History of the Low Countries*. Bergahn Books, 1999.

J. Bosboom and M.J.F. Stive. *Coastal Dynamics I*. Delft Academic Press, 2015.

W. Bruggeman, M. Haasnoot, S. Hommes, A. te Linde, R. van der Brugge, B. Rijken, E. Dammers, and G.J. van den Born. Deltascenario's; verkenning van mogelijke fysieke en sociaaleconomische ontwikkelingen in de 21ste eeuw op basis van knmi'06 en wlo-scenario's, voor gebruik in het deltaprogramma 2011-2012. *Planbureau voor de Leefomgeving/Deltares, Rapport*, pages 1205747–000, 2011.

W. Bruggemann, E. Dammers, G.J. van den Born, B. Rijkens, B. van Bemmel, A. Bouwman, K. Nabielek, J. Beersma, B. van den Hurk, N.B.P. Polman, V.G.M. Linderhof, C. Folmer, F. Huizinga, S. Hommes, A. te Linde, R. Didde, and M. Roukema. *Deltascenario's voor 2050 en 2100 : nadere uitwerking 2012-2013*. Deltares, 2013.

Y. Buitenhuis and C. Dieperink. Governance conditions for successful ecological restoration of estuaries: lessons from the Dutch Haringvliet case. *Journal of Environmental Planning and Management*, 62(11):1990–2009, 2019.

H. Burchard and R.D. Hetland. Quantifying the contributions of tidal straining and gravitational circulation to residual circulation in periodically stratified tidal estuaries. *Journal of Physical Oceanography*, 40(6):1243–1262, 2010.

J.A. Church and N.J. White. A 20th century acceleration in global sea-level rise. *Geophysical research letters*, 33(1), 2006.

J.A. Church, P.U. Clark, A. Cazenave, J.M. Gregory, S. Jevrejeva, A. Levermann, M.A. Merrifield, G.A. Milne, R.S. Nerem, P.D. Nunn, A.J. Payne, W.T. Pfeffer, D. Stammer, and A.S. Unnikrishnan. Sea level change. Technical report, PM Cambridge University Press, http://drs.nio.org/drs/handle/2264/4605, 2013.

D.L. Codiga. Unified tidal analysis and prediction using the UTide Matlab functions, 2011.

G.J. de Boer. *On the interaction between tides and stratification in the Rhine Region of Freshwater Influence*. PhD thesis, Delft University of Technology, 2009.

A.M.J. de Kraker. Flood events in the southwestern Netherlands and coastal Belgium, 1400–1953. *Hydrological Sciences Journal*, 51(5): 913–929, 2006.

M.A.J. de Nijs, J.C. Winterwerp, and J.D. Pietrzak. The effects of the internal flow structure on SPM entrapment in the Rotterdam Waterway. *Journal of Physical Oceanography*, 40(11):2357–2380, 2010.

M.A.J. de Nijs, J.D. Pietrzak, and J.C. Winterwerp. Advection of the salt wedge and evolution of the internal flow structure in the Rotterdam Waterway. *Journal of Physical Oceanography*, 41(1): 3–27, 2011.

Deltares. *Delft3D-FLOW User Manual*, 2020.

H.A. Ferguson. De afsluiting van het Haringvliet. *Weg-en Waterbouw*, 1971.

W.R. Geyer and P. MacCready. The estuarine circulation. *Annual Review of Fluid Mechanics*, 46(1):175–197, 2014. doi: 10.1146/annurev-fluid-010313-141302. URL https://doi.org/10.1146/annurev-fluid-010313-141302.

W.R. Geyer and R.P. Signell. A reassessment of the role of tidal dispersion in estuaries and bays. *Estuaries*, 15(2):97–108, 1992.

A.E. Gill. Atmosphere-ocean dynamics. *Int. Geophys. Ser.*, 30:662p, 1982.

M. Haasnoot, J. Kwadijk, J. van Alphen, D. le Bars, B. van den Hurk, F. Diermanse, A. van der Spek, G. Essink, J. Delsman, and M. Mens. Adaptation to uncertain sea-level rise; how uncertainty in antarctic mass-loss impacts the coastal adaptation strategy of the netherlands. *Environmental Research Letters*, 15(3):034007, 2020.

S. Haddout, I. Baimik, A. Maslouhi, M. Igouzal, B. Magrane, and H. Marah. The influence of spring and neap tide on salt intrusion and stratification in Sebou estuary (Morocco). *International journal of river basin management*, 17(1): 131–142, 2019.

G. Herrera-García, P. Ezquerro, R. Tomás, M. Béjar-Pizarro, J. López-Vinielles, M. Rossi, R.M. Mateos, D. Carreón-Freyre, J. Lambert, P. Teatini, E. Cabral-Cano, G. Erkens, D. Galloway, W.C. Hung, N. Kakar, M. Sneed, L. Tosi, H. Wang, and S. Ye. Mapping the global threat of land subsidence. *Science*, 371(6524):34–36, 2021.

F.A.P. Hollebrandse, J.D. Pietrzak, M.J.F. Stive, T.J. Zitman, and J.G. de Ronde. *Temporal development of the tidal range in the southern North Sea*. PhD thesis, Delft University of Technology, Faculty of Civil Engineering and Geosciences, Hydraulic Engineering, 2005.

B. Hong and J. Shen. Responses of estuarine salinity and transport processes to potential future sea-level rise in the Chesapeake Bay. *Estuarine, Coastal and Shelf Science*, 104:33–45, 2012.

Y. Huismans. Zoutindringing in de Rijn- Maasmonding: Knelpunten en effectiviteit stuurknoppen. Deltares, 2018.

HydroLogic. *Inventarisatie Slim Watermanagement Rijn-Maasmonding*. 2015.

P. Jacobs, B.P.C. Steenkamp, and S. de Goederen. *Analyse zoutmetingen inlaatproef Haringvliet in maart 1997*. Ministerie van Verkeer en Waterstaat, Directoraat-Generaal Rijkswaterstaat …, 2003.

C.A. Katsman, A. Sterl, J.J. Beersma, H.W. van den Brink, J.A. Church, W. Hazeleger, R.E. Kopp, D. Kroon, J. Kwadijk, R. Lammersen, J. Lowe, M. Oppenheimer, H. Plag, J. Ridley, H. von Storch, D.G. Vaughan, P. Vellinga, L.L.A. Vermeersen, R.S.W. van de Wal, and Weisse R. Exploring high-end scenarios for local sea level rise to develop flood protection strategies for a low-lying delta, the Netherlands as an example. *Climatic change*, 109(3-4):617–645, 2011.

A.P. Kleinman and F.B. Brown. *Colorado River Salinity, Economic Impacts on Agricultural, Municipal, and Industrial Users*. US Department of the Interior, Water and Power Resources Service, Colorado …, 1980.

F. Klijn, J. ter Maat, and E. van Velzen. Zoetwatervoorziening in Nederland - Landelijke inventarisatie knelpunten in de 21^{e} eeuw. Deltares, 2011.

W.M. Kranenburg. *Evaluatie van het OSR-model voor zoutindringing in de Rijn- Maasmonding (II)*. Deltares, 2015.

W.M. Kranenburg and R. Schueder. *Evaluatie van het OSR-model voor zoutindringing in de Rijn-Maasmonding (I)*. Deltares, 2015.

R.J. Labeur. *Finite element modelling of transport and non-hydrostatic flow in environmental fluid mechanics*. PhD thesis, Delft University of Technology, 6 2009.

H. Lavooij and L. Berke. Update Delta21: 2019. `https://www.delta21.nl/wp-content/uploads/2019/09/UPDATE-DELTA21-29-7-2019.pdf`, 2019.

H.J.R. Lenders, M.A.J. Huijbregts, B.G.W. Aarts, and C.A.M. Van Turnhout. Assessing the degree of preservation of landscape, natural and cultural–historical values in river dike reinforcement planning in the Netherlands. *Regulated Rivers: Research & Management*, 15(4):325–337, 1999.

J.A. Lerczak and W.R. Geyer. Modeling the lateral circulation in straight, stratified estuaries. *Journal of Physical Oceanography*, 34(6):1410–1428, 2004.

E. Lewis. The practical salinity scale 1978 and its antecedents. *IEEE Journal of Oceanic Engineering*, 5(1):3–8, 1980.

B. Lieberthal, K. Huguenard, L. Ross, and K. Bears. The generation of overtides in flow around a headland in a low inflow estuary. *Journal of Geophysical Research: Oceans*, 124(2): 955–980, 2019.

J.T. Limerinos. Relation of the Manning coefficient to measured bed roughness in stable natural channels. *US Geological Survey Professional paper D*, 650:45, 1969.

H. Lyu and J. Zhu. Impact of the bottom drag coefficient on saltwater intrusion in the extremely shallow estuary. *Journal of Hydrology*, 557: 838–850, 2018.

P. MacCready. Toward a unified theory of tidally-averaged estuarine salinity structure. *Estuaries*, 27(4):561–570, 2004.

M. Mahmuduzzaman, Z.U. Ahmed, A.K.M. Nuruzzaman, and F.R.S. Ahmed. Causes of salinity intrusion in coastal belt of Bangladesh. *International Journal of Plant Research*, 4(4A):8–13, 2014.

M. Marchand, F. Klijn, and J. Kind. Handreiking toepassing vergelijkingssystematiek Deltaprogramma. *Deltares report*, 1205040, 2012.

P.K. Marks, L.M. Gerrits, S. Bakker, and E. Tromp. Explaining inertia in restoring estuarine dynamics in the Haringvliet (The Netherlands). *Water policy*, 16(5):880–896, 2014.

T.J. McDougall and P.M. Barker. Getting started with teos-10 and the gibbs seawater (gsw) oceanographic toolbox. *SCOR/IAPSO WG*, 127:1–28, 2011.

M. Mens. Maatregelverkenning voor het deltaprogramma zoetwater. Deltares, 2018.

H Meyer, S Nijhuis, M Pouderoijen, R Campanella, V Zagare, W.V. Dijk, R Broesi, M Marchand, P.Q. Dieu, T Le, D Neumann, J.P. Costa, J.F. de Sousa, C. Thomas, and P. Viganò. *Urbanized deltas in transition*. Techne Press Amsterdam, 2014.

F.J. Millero and A. Poisson. International one-atmosphere equation of state of seawater. *Deep Sea Research Part A. Oceanographic Research Papers*, 28(6):625–629, 1981.

F.T.M. Nieuwstadt, J. Westerweel, and B.J. Boersma. *Turbulence: introduction to theory and applications of turbulent flows*. Springer, 2016.

R.A. Nunes and J.H. Simpson. Axial convergence in a well-mixed estuary. *Estuarine, Coastal and Shelf Science*, 20(5):637–649, 1985.

M. Oppenheimer, B. Glavovic, J. Hinkel, R. van de Wal, A.K. Magnan, A. Abd-Elgawad, R. Cai, M. Cifuentes-Jara, R.M. Deconto, T. Ghosh, J. Hay, F. Isla, B. Marzeion, B. Meyssignac, and Z. Sebesvari. Sea level rise and implications for low lying islands, coasts and communities, 2019.

P. Paalvast. Monitoringsplan ecologie project Kierbesluit. Technical report, 03 2016.

P. Paalvast, W. Iedema, M. Ohm, and R. Posthoorn. MER beheer Haringvlietsluizen. Technical report, RIZA, Over de grens van zoet en zout, 1998.

F.B. Pedersen. *Environmental Hydraulics: Stratified Flows*, volume 18. Springer Science & Business Media, 2012.

C. Pickover. *Archimedes to Hawking: laws of science and the great minds behind them*. Oxford University Press, 2008.

J.D. Pietrzak. An introduction to stratified flows for civil and offshore engineers, May 2020.

J.D. Pietrzak and C.A. Katsman. Physical Oceanography - Lecture Notes, September 2019.

J.D. Pietrzak and R.J. Labeur. Trapped internal waves over undular topography in a partially mixed estuary. *Ocean Dynamics*, 54(3-4):315–323, 2004.

J.D. Pietrzak, C. Kranenburg, G. Abraham, B. Kranenborg, and A. van der Wekken. Internal wave activity in rotterdam waterway. *Journal of Hydraulic Engineering*, 117(6):738–757, 1991.

J.D. Pietrzak, G.J. de Boer, and M.A. Eleveld. Mechanisms controlling the intra-annual mesoscale variability of sst and spm in the southern north sea. *Continental Shelf Research*, 31(6):594–610, 2011.

D.W. Pritchard. What is an estuary: physical viewpoint. *American Association for the Advancement of Science*, 1967.

J. Rijke, S. van Herk, C. Zevenbergen, and R. Ashley. Room for the River: delivering integrated river basin management in the Netherlands. *International journal of river basin management*, 10(4):369–382, 2012.

Rijkswaterstaat. *WAQUA in SIMONA - cursusboek gevorderden*, 2005.

Rijkswaterstaat. *User's Guide WAQPRE*, 2008.

Rijnmond Nieuws. Uitgestorven vis duikt levend op bij Haringvlietdelta . `https://www.rijnmond.nl/nieuws/197630/Uitgestorven-vis-duikt-levend-op,-bij-Haringvlietdelta`, 2020.

B. Roels. *Toon Ambitie voor Zoet, Zout en Zalm! Oostelijk aanvoeren voor het verder openen van het Haringvliet*. `https://www.wwf.nl/wat-we-doen/actueel/blog/bas/zoet-zout-zalm`, 2020.

H.H.G. Saveneije. *Salinity and tides in alluvial estuaries*. Elsevier, 2006.

H.H.G. Savenije. A one-dimensional model for salinity intrusion in alluvial estuaries. *Journal of Hydrology*, 85(1-2):87–109, 1986.

E. Schulz, H.M. Schuttelaars, U. Gräwe, and H. Burchard. Impact of the depth-to-width ratio of periodically stratified tidal channels on the estuarine circulation. *Journal of Physical Oceanography*, 45(8):2048–2069, 2015.

M.E. Scully and W.R. Geyer. The role of advection, straining, and mixing on the tidal variability of estuarine stratification. *Journal of Physical Oceanography*, 42(5):855–868, 2012.

J. Sestak. *Science of heat and thermophysical studies: a generalized approach to thermal analysis*. Elsevier, 2005.

J.H. Simpson. Physical processes in the ROFI regime. *Journal of marine systems*, 12(1-4):3–15, 1997.

J.H. Simpson, J. Brown, J. Matthews, and G. Allen. Tidal straining, density currents, and stirring in the control of estuarine stratification. *Estuaries*, 13(2):125–132, 1990.

M.T. Stacey and D.K. Ralston. The scaling and structure of the estuarine bottom boundary layer. *Journal of Physical Oceanography*, 35(1): 55–71, 2005.

G.S. Stelling. *On the construction of computational methods for shallow water flow problems*. PhD thesis, Delft University of Technology, 1983.

Ad Stolk and Chris Dijkshoorn. Sand extraction Maasvlakte 2 project: license, environmental impact assessment and monitoring. In *EMSAGG Conference, Italy*. Citeseer, 2009.

K. Storm, J. Kuijpers, and C. Harmsen. Eb en weer vloed in het haringvliet. *Landschap-Tijdschrift voor Landschapsecologie en Milieukunde*, 23 (4):199, 2006.

N.N. Taleb. *The Black Swan: The impact of the highly improbable*, volume 2. Random house, 2007.

W. ten Brinke. Fact finding afvoerverdeling Rijntakken. Technical report, Deltares, NL-HaNA, Deltaprogramma, 2.16.133, inv.nr. DC364, 2013.

J. ter Maat. Effecten van maatregelen voor de zoetwatervoorziening in Nederland in de 21e eeuw. Deltares, 2014.

J. ter Maat. Systeemanalyse van de Rijn- Maasmonding voor verzilting. Deltares, 2015.

I.E. Tönis, J.M.T. Stam, and J. Van de Graaf. Morphological changes of the Haringvliet estuary after closure in 1970. *Coastal Engineering*, 44(3): 191–203, 2002.

I. Tulp, N. Tien, and C. van Damme. *PMR Monitoring natuurcompensatie Voordelta : ontwikkeling vis in de Voordelta na instelling bodembeschermingsgebied ter compensatie van de aanleg Tweede Maasvlakte*. Number C089/16 in Wageningen Marine Research rapport. Wageningen Marine Research, 2016.

L. Tuomi, K. Myrberg, and A. Lehmann. The performance of the parameterisations of vertical turbulence in the 3d modelling of hydrodynamics in the baltic sea. *Continental Shelf Research*, 50:64–79, 2012.

R.E. Uittenbogaard, C. Stolker, E.D. de Goede, J.A.T.M. van Kester, H.R.A. Jagers, and J.H.A. Wijbenga. Eddy viscositeit in waqua modellen voor rijntakken en maas. *Q3846*, 2005.

J. van Kester, G. Stelling, A. Bijlsma, and T. van der Kaaij. *Syllabus Randvoorwaarden in WAQUA en TRIWAQ*, 2001.

M. van Koningsveld, J.P.M. Mulder, M.J.F. Stive, L. van der Valk, and A.W. van der Weck. Living with sea-level rise and climate change: a case study of the Netherlands. *Journal of Coastal Research*, 2008(242):367–379, 2008.

J. van Veen. Hellegat: Ontwerp 1929. Technical report, Rijkswaterstaat, Deltadienst, `http://resolver.tudelft.nl/uuid:4a93e962-8149-4380-a2b9-4b4c21a40c`, 1929.

R.H. van Waveren, S. Groot, H. Scholten, F. van Geer, H. Wösten, R. Koeze, and J. Noort. *Vloeiend modelleren in het waterbeheer*, 1999.

W.J. Wallace. *The development of the chlorinity/salinity concept in oceanography*. Elsevier, 1974.

R. Wassmann, N.D. Phong, T.Q. Tho, C.T. Hoanh, N.H. Khoi, N.X. Hien, T.B.T Vo, and T.P. Tuong. High-resolution mapping of flood and salinity risks for rice production in the Vietnamese Mekong Delta. *Field Crops Research*, 236:111–120, 2019.

X. Wei, G.P. Schramkowski, and H.M. Schuttelaars. Salt dynamics in well-mixed estuaries: Importance of advection by tides. *Journal of Physical Oceanography*, 46(5):1457–1475, 2016.

J.R. West and A.P. Cotton. The measurement of diffusion coefficients in the Conwy estuary. *Estuarine Coastal and Shelf Science*, 12(3):323–336, 1981.

J. Wijsman, V. Escaravage, Y. Huismans, A. Nolte, R. van der Wijk, Z.B. Wang, and T. Ysebaert. *Potenties voor herstel getijdenatuur in het Haringvliet, Hollands Diep en de Biesbosch*. Number C008/18 in Wageningen Marine Research rapport. Wageningen Marine Research, jan 2018. doi: 10.18174/440424.

J.A.W. Wit, T.P.M. Chamuleau, H.V. Winter, A.W. Breukelaar, V.A.W. Beijk, and R. Goes. *Andere mogelijkheden voor het Besluit beheer Haringvlietsluizen: een verkennende studie naar verbetering van de vismigratie tussen de Noordzee en het Rijn- en Maasstroomgebied bij het intrekken van het Kierbesluit*. Rijkswaterstaat, 2011.

M. Zijlema. WAQUA/TRIWAQ - two- and three-dimensional shallow water flow model. Technical documentation, 1998.

M. Zijlema. *Quick-start guide Programming in SIMONA*, 2006.

M. Zijlema. Computational modelling of flow and transport - lecture notes, 2019.